

STUDY OF SURFACE WAVE METHODS FOR DEEP SHEAR WAVE VELOCITY
PROFILING APPLIED IN THE UPPER MISSISSIPPI EMBAYMENT

A Dissertation Presented to
the Faculty of Graduate School
University of Missouri – Columbia

In Partial Fulfillment
Of the Requirements for the Degree
Doctor of Philosophy

by

JIANHUA LI

Dr. Brent L. Rosenblad, Dissertation Supervisor

DECEMBER 2008

The undersigned, appointed by the Dean of the Graduate School, have examined the dissertation entitled

STUDY OF SURFACE WAVE METHODS FOR DEEP SHEAR WAVE VELOCITY
PROFILING APPLIED IN THE UPPER MISSISSIPPI EMBAYMENT

presented by Jianhua Li,

a candidate for the degree of Doctor of Philosophy in Civil Engineering ,

and hereby certify that, in their opinion, it is worthy of acceptance.

Professor Brent L. Rosenblad

Professor John J. Bowders, P.E.

Professor William Likos

Professor Eric Loehr, PE

Professor Eric Sandvol

ACKNOWLEDGEMENTS

I would like to express my sincere appreciation to my advisor, Dr. Rosenblad, for introducing me to this interesting area of research and supervising me throughout the entire work. He provided excellent guidance whenever needed, taught me how to think critically, and encouraged me to surmount all challenges. The study would have never been possible without his efforts.

I would also like to thank other three professors in the program of geotechnical engineering. Dr. Bowders has stimulated me by his exceptional enthusiasm for geotechnical engineering. That enthusiasm has been passed to me during the graduate program, and will continue to influence me in my future professional career. I thank Dr. Loehr and Dr. Likos for sharing valuable and interesting knowledge, and their guidance in and out of their classes. It is my great pleasure to have them as members of the committee for this dissertation.

Additionally I truly appreciate Dr. Sandval for serving on my dissertation committee and giving me his valuable advice.

I would also like to thank my fellow colleagues, Jonathan Bailey, Ryan Goetz, and personnel from the University of Texas at Austin for assistance in the field work. Without their assistance this study would have not been possible.

Financial support for the study came from the National Science Foundation as part of the Network for Earthquake Engineering Simulation (NEES) program under grant No. 0530140.

Finally, I would like to dedicate this dissertation to my parents and my wife, Jingwen Guo. What my parents taught me has been a huge treasure in my entire life. My wife's support and understanding has motivated me throughout the course of the study. Thanks to them can not be expressed with words.

TABLE OF CONTENTS

ACKNOWLEDGEMENTS.....	ii
LIST OF FIGURES	ix
LIST OF TABLES	xix
ABSTRACT	xxi
INTRODUCTION	1
1.1. Problem Statement	1
1.2. Research Objectives	3
1.3. Dissertation Overview	5
OVERVIEW OF SURFACE WAVE METHODS AND PAST STUDIES	7
2.1 Introduction	7
2.2 Overview of Surface Wave Methods.....	8
2.2.1 Spectral-Analysis-of-Surface-Waves (SASW) Method	8
2.2.2 Active-Source Frequency-Wavenumber ($f-k$) Method	9
2.2.3 Passive-Source Frequency-Wavenumber ($f-k$) Method	11
2.2.4 Refraction Microtremor (ReMi) Method	12
2.3 Overview of Past Applications of Deep V_s Profiling.....	13
2.4 Overview of Past Comparative Studies	15
TESTING SITES, EQUIPMENT AND PROCEDURES	17
3.1 Upper Mississippi Embayment and New Madrid Seismic Zone	17
3.2 Site Descriptions	21
3.2.1 Site 1: Mooring, Tennessee	22
3.2.2 Site 2: Yarbro, Arkansas	24
3.2.3 Site 3: Gosnell, Arkansas	25

3.2.4	Site 4: Lepanto, Arkansas	27
3.2.5	Site 5: Shelby Farms, Memphis, Tennessee	28
3.2.6	Site 6: East Prarie, Missouri	30
3.2.7	Site 7: Portageville, Missouri	31
3.2.8	Site 8: Glass, Tennessee	33
3.2.9	Site 9: Braggadocio, Missouri	34
3.2.10	Site 10: Tennemo, Tennessee	36
3.2.11	Site 11: Manila, Arkansas	37
3.3	Estimated Lithology at Site Locations	39
3.4	Field Equipment	42
3.4.1	Active Energy Sources	42
3.4.2	Data Acquisition Systems	44
3.5	Field Testing Procedures	46
3.5.1	SASW Testing	46
3.5.2	Active $f-k$ and ReMi Testing	47
3.5.3	Passive $f-k$ Testing	50
	DATA PROCESSING PROCEDURES	53
4.1	Introduction	53
4.2	Data Processing of SASW Measurements	53
4.3	Data Processing of Active $f-k$ Measurements	57
4.3.1	Spatiospectral Correlation Matrix	57
4.3.1.1	Computation of Spatiospectral Correlation Matrix	57
4.3.1.2	Modification of Spatiospectral Correlation Matrix due to Geophone Calibration	58
4.3.1.3	Normalization of Spatiospectral Correlation Matrix	59
4.3.2	Formation of Steering Vector	60

4.3.3	Beamforming	62
4.3.4	Interpretation of Dispersion Curves from Active $f-k$ Measurement.....	64
4.4	Data Processing of Passive $f-k$ Measurements	65
4.4.1	Spatiospectral Correlation Matrix	65
4.4.2	Formation of Steering Vector	67
4.4.3	Beamforming	68
4.4.3.1	Conventional FDBF Method	69
4.4.3.2	Multiple Signal Classification (MUSIC) Method	70
4.4.3.3	Minimum Variance Beamforming (MVBF) Method	74
4.4.4	Interpretation of Dispersion Curves from Passive $f-k$ Measurement.....	76
4.5	Data Processing of ReMi Measurements	77
4.5.1	Slowness-Time Intercept ($p-\tau$) Transformation (Thorson and Claerbout, 1985)	78
4.5.2	Slowness-Frequency ($p-f$) Transformation (McMechan and Yedlin, 1981)	79
4.5.3	Normalization of $p-f$ Images (Louie,2001)	80
4.5.4	Dispersion Curve Picking	82
DISPERSION CURVE COMPARISON BETWEEN SASW AND ACTIVE $f-k$ METHODS		85
5.1	Introduction	85
5.2	Field Performance of NEES Vibrator	85
5.3	Comparison of Dispersion Curves Developed from SASW and Active $f-k$ Methods	87
5.4	Phase Unwrapping Errors	93
5.5	Near-Field Effects on Active $f-k$ Analysis	101
5.5.1	Mitigation of Near-Field Effects	101

5.5.2	Near-Field Effects Criterion Based on Observations	104
5.6	Summary	107
AMBIENT WAVEFIELD CHARACTERISTICS		109
6.1	Introduction	109
6.2	Amplitude and Frequency Content	109
6.3	Direction of the Dominant Energy	115
6.4	Number of Energy Sources	123
6.5	Summary	131
DISPERSION CURVE COMPARISON BETWEEN PASSIVE AND ACTIVE $f-k$ METHODS		133
7.1	Introduction	133
7.2	Comparison of Dispersion Curves Developed from Passive and Active $f-k$ Methods	134
7.2.1	Performance of Conventional FDBF Method	134
7.2.2	Performance of High-Resolution Methods	138
7.2.3	Higher Modes	144
7.3	Factors Affecting the Performance of Passive $f-k$ Methods	144
7.3.1	Array Pattern	145
7.3.2	Effect of Multiple-Source Wavefield	147
7.4	Wavelength Resolution Criteria	151
7.5	Summary	153
DISPERSION CURVE COMPARISON BETWEEN REMI AND ACTIVE $f-k$ METHODS		155
8.1	Introduction	155
8.2	Slowness-Frequency ($p-f$) Spectral Ratio Images	156
8.3	Comparison of Dispersion Curves Developed from ReMi and Active $f-k$ Methods	159

8.4	Factors Influencing ReMi Performance	167
8.5	Summary	171
COMPARISON OF DEEP V_s PROFILES FROM FUNDAMENTAL MODE AND EFFECTIVE VELOCITY INVERSION		172
9.1	Introduction	172
9.2	Data Inversion Procedures	173
9.3	Comparison of Deep V_s from Fundamental Mode and Effective Velocity Inversions	177
9.4	Inversion Model Compatibility	189
9.4.1	Simulation Procedure	189
9.4.2	Simulation Results for Site 5 and Site 8	191
9.4.3	Influence of Depth to Stiffer Soil Layer on Dispersion Curve Estimates.....	195
9.5	Consequence of Inversion Model Incompatibility	202
9.6	Summary	202
CONCLUSIONS AND RECOMMENDATIONS		204
10.1	Introductions	204
10.2	Conclusions	204
10.2.1	Conclusions on Active-Source Measurements	204
10.2.2	Conclusions on Passive-Source Measurements	206
10.2.3	Conclusions on Fundamental Mode and Effective-Velocity Inversion	208
10.3	Recommendations	209
REFERENCES		212
VITA		220

LIST OF FIGURES

Figure	Page
Figure 2.1 Typical configuration for SASW testing.....	8
Figure 2.2 Typical configuration for active-source f - k measurements.....	10
Figure 3.1 Plan view of the upper Mississippi Embayment (Van Arsdale and TenBrink, 2000).....	18
Figure 3.2 Stratigraphic column of sediments in the Mississippi Embayment (Van Arsdale and TenBrink, 2000).....	19
Figure 3.3 Elevation of Paleozoic bedrock relative to mean sea level in the Mississippi Embayment (Romero and Rix, 2001).....	20
Figure 3.4 East-West cross-section through Memphis, Tennessee in the Mississippi Embayment (Hashash and Park, 2001).....	20
Figure 3.5 Eleven site locations in the Mississippi Embayment (map modified from Romero and Rix, 2001).....	21
Figure 3.6 Google Earth image of Site 1 and surrounding major roadways.....	23
Figure 3.7 Google earth image of Site 1 showing array location and orientation (from Bailey, 2008).....	23
Figure 3.8 Google earth image of Site 2 and surrounding major roadways.....	24
Figure 3.9 Google Earth image of Site 2 showing array location and orientation (from Bailey, 2008).....	25
Figure 3.10 Google Earth image of Site 3 and surrounding major roadways.....	26
Figure 3.11 Google Earth image of Site 3 showing array location and orientation (from Bailey, 2008).....	26

Figure 3.12	Google Earth image of Site 4 and surrounding major roadways.....	27
Figure 3.13	Google Earth image of Site 4 showing array location and orientation (from Bailey, 2008).....	28
Figure 3.14	Google Earth image of Site 5 and surrounding major roadways.....	29
Figure 3.15	Google earth image of Site 5 showing array location and orientation (from Bailey, 2008).....	29
Figure 3.16	Google earth image of Site 6 and surrounding major roadways.....	30
Figure 3.17	Google Earth image of Site 6 showing array location and orientation (from Bailey, 2008).....	31
Figure 3.18	Google Earth image of Site 7 and surrounding major roadways.....	32
Figure 3.19	Google Earth image of Site 7 showing array location and orientation (from Bailey, 2008).....	32
Figure 3.20	Google Earth image of Site 8 and surrounding major roadways.....	33
Figure 3.21	Google Earth image of Site 8 showing array location and orientation (from Bailey, 2008).....	34
Figure 3.22	Google Earth image of Site 9 and surrounding major roadways.....	35
Figure 3.23	Google Earth image of Site 9 showing array location and orientation (from Bailey, 2008).....	35
Figure 3.24	Google Earth image of Site 10 and surrounding major roadways.....	36
Figure 3.25	Google earth image of Site 10 showing array location and orientation (from Bailey, 2008).....	37
Figure 3.26	Google earth image of Site 11 and surrounding major roadways.....	38
Figure 3.27	Google Earth image of Site 11 showing array location and orientation (from Bailey, 2008).....	38
Figure 3.28	Estimated soil stratigraphy at Sites 1 through 11, presented in (a) through (k), respectively.....	41
Figure 3.29	Low-frequency NEES vibrator and its theoretical force output (from:	

	http://nees.utexas.edu/Equipment-Liquidator.shtml) as presented in (a) and (b).....	43
Figure 3.30	Instrumented impact hammer and its frequency content as presented in (a) and (b).....	44
Figure 3.31	Digital signal analyzers used for field measurements: (a) VXI analyzer and (b) Data Physics analyzer.....	45
Figure 3.32	Mark Product L-4 high-sensitivity geophone (1 Hz).....	45
Figure 4.1	Cross-power spectrum and coherence function from 300-m spacing at Site 1 with masking (shadowed) of near-field region shown.....	55
Figure 4.2	Unwrapping of cross-power spectrum shown in Figure 4.1.....	55
Figure 4.3	Composite dispersion curve for Site 1 presented in terms of phase velocity versus wavelength.....	56
Figure 4.4	Steered response powers estimated with and without geophone calibration at a frequency of 1.35 Hz for Site 1, Array 2.....	59
Figure 4.5	Steered response powers estimated with different normalization techniques at 5.03 Hz for Site 1, Array 2.....	60
Figure 4.6	Contour plot of steered power spectrum in terms of frequency and wavenumber for Array 1, Site 7.....	63
Figure 4.7	Spectral power spectrum estimates at (a) 4.01 Hz and (b) 6.19 Hz.....	63
Figure 4.8	Dispersion curve estimated from f - k analysis for Array 1, Site 7.....	64
Figure 4.9	Coordinate system used for Array A along with NS-EW directions.....	67
Figure 4.10	FDBF power spectrum estimate at 1.5 Hz for Site 1 shown in (a) 3-D mesh plot and (b) 2-D contour plot.....	70
Figure 4.11	MUSIC power spectrum estimate at 1.5 Hz for Site 1 with a noise subspace dimension of 15, shown in (a) 3-D mesh plot and (b) 2-D contour plot.....	72
Figure 4.12	MUSIC power spectrum estimate at 1.5 Hz for Site 1 with a noise subspace dimension of 12, shown in (a) 3-D mesh plot and (b) 2-D contour plot.....	73

Figure 4.13	Power spectrum estimate using Capon's method at 1.5 Hz for Site 1 shown in (a) 3-D mesh plot and (b) 2-D contour plot.....	75
Figure 4.14	Dispersion curve estimated by conventional FDBF method for Site 1.....	77
Figure 4.15	p-f spectral ratio images of 4 individual noise records for Array 2, Site 9.....	81
Figure 4.16	Comparison of p-f images estimated for Array 1, Site 9 from (a) MATLAB program developed for this study and (b) the commercial SeisOpt ReMi software.....	82
Figure 4.17	Procedures of picking dispersion curves from p-f image.....	84
Figure 4.18	Examples of data quality of power-slowness profiles used for dispersion picking from ReMi.....	84
Figure 5.1	Recording at last receiver of Array 2 at Site 8 showing (a) power spectra with NEES vibrator operating and (b) coherence function between source signal and measured signal.....	86
Figure 5.2	Comparison of dispersion curves developed from SASW and active $f-k$ methods presented in terms of frequency (left column) and wavelength (right column) for Site 1 to Site 11 as (a) to (k).....	89
Figure 5.3	Results from Bertel (2006) showing (a) example V_s profile, and (b) comparison of simulated experimental dispersion curve with theoretical and modal dispersion curves from profile shown in (a).....	94
Figure 5.4	Interpretation of the 61-m pair phase data for example V_s profile (in Figure 5.3) showing (a) continuous phase unwrapping over frequencies 4.6 Hz to 7.6 Hz, (b) phase unwrapping of the lower mode at frequencies less than 4.6 Hz and (c) phase unwrapping of the higher mode at frequencies between 4.6 and 7.6 Hz (from Bertel, 2006).....	95
Figure 5.5	Comparison of simulated experimental and theoretical dispersion curves for example profile (in Figure 5.3a) after the application of correct phase unwrapping shown in Figure 5.4b and 5.4c (from Bertel, 2006).....	95

Figure 5.6	Interpretation of the 200-m pair phase data for Site 3 showing (a) continuous phase unwrapping over frequencies from 1.6 Hz to 4.0 Hz, (b) phase unwrapping of the lower mode at frequencies between 1.6 and 2.4 Hz and (c) phase unwrapping of the higher mode at frequencies between 2.4 and 4.0 Hz.....	96
Figure 5.7	Comparison of dispersion curves developed from SASW and active $f-k$ methods for (a) Site 3, (b) Site 6 and (c) Site 9 after correct interpretation of phase unwrapping.....	97
Figure 5.8	Vs profile inverted from SASW measurements and estimated soil profile for Site 3 (from Bailey, 2008).....	99
Figure 5.9	Vs profile inverted from SASW measurements and estimated soil profile for Site 6 (from Bailey, 2008).....	99
Figure 5.10	Vs profile inverted from SASW measurements and estimated soil profile for Site 9 (from Bailey, 2008).....	100
Figure 5.11	Mitigation of near-field effects by using measurements at last 10 receivers (offset of 100 m) (left column) and using cylindrical wave beamformer (right column) for Sites 2, 3 and 4 in (a), (b) and (c), respectively.....	103
Figure 5.12	Comparison of percent differences corresponding to the two approaches of mitigating near-field effects for Sites 2, 3 and 4 in (a), (b) and (c), respectively.....	104
Figure 5.13	Determination of longest wavelength without near-field effects by comparing dispersion curves from shorter array with those from longer array at Site 8.....	105
Figure 6.1	Time records (left column) and associated Fourier spectra (right column) at Site 1 through Site 11, in (a) through (k), respectively.....	112
Figure 6.2	Plots showing (a) wave directions at Site 1 in terms of back azimuth versus frequency, (b) wave directions in NS-EW coordinate system, and (c) Google Earth image of major roadways close to Site 1 (same as Figure 3.6).....	118
Figure 6.3	Plots showing (a) wave directions at Site 3 in terms of back azimuth versus frequency, (b) wave directions in NS-EW coordinate system, and (c) Google Earth image of major roadways close to Site 3 (same as Figure 3.10).....	119

Figure 6.4	Plots showing (a) wave directions at Site 5 in terms of back azimuth versus frequency, (b) wave directions in NS-EW coordinate system, and (c) Google Earth image of major roadways close to Site 5 (same as Figure 3.14).....	120
Figure 6.5	Plots showing (a) wave directions at Site 9 in terms of back azimuth versus frequency, (b) wave directions in NS-EW coordinate system, and (c) Google Earth image of major roadways close to Site 9 (same as Figure 3.22).....	121
Figure 6.6	Plots showing (a) wave directions at Site 10 in terms of back azimuth versus frequency, (b) wave directions in NS-EW coordinate system, and (c) Google Earth image of major roadways close to Site 10 (same as Figure 3.24).....	122
Figure 6.7	Relative location of x - y coordinate of Array A to NS-WE coordinates at Site 1.....	124
Figure 6.8	Contour plots of power spectra at 1.50 Hz, 2.50 Hz, 3.51 Hz and 5.09 Hz estimated from the MUSIC method at Site 1 using Array A.....	124
Figure 6.9	Relative location of x - y coordinate of Array A to NS-WE coordinate at Site 3.....	125
Figure 6.10	Contour plots of power spectra at 1.75 Hz, 2.50 Hz, 3.59 Hz and 5.10 Hz estimated from the MUSIC method at Site 3 using Array A.....	125
Figure 6.11	Relative location of x - y coordinate of Array A to NS-WE coordinate at Site 5.....	126
Figure 6.12	Contour plots of power spectra at 1.63 Hz, 2.50 Hz, 3.51 Hz and 5.04 Hz estimated from the MUSIC method at Site 5 using Array A.....	126
Figure 6.13	Relative location of x - y coordinate of Array B to NS-WE coordinate at Site 9.....	127
Figure 6.14	Contour plots of power spectra at 1.40 Hz, 2.56 Hz, 3.60 Hz and 5.48 Hz estimated from the MUSIC method at Site 9 using Array B.....	127
Figure 6.15	Relative location of x - y coordinate of Array C to NS-WE coordinate at Site 9.....	128

Figure 6.16	Contour plots of power spectra at 1.36 Hz, 2.56 Hz, 3.60 Hz and 5.48 Hz estimated from the MUSIC method at Site 9 using Array C.....	128
Figure 6.17	Relative location of x - y coordinate of Array B to NS-WE coordinate at Site 10.....	129
Figure 6.18	Contour plots of power spectra at 1.68 Hz, 2.51 Hz, 3.58 Hz and 5.00 Hz estimated from the MUSIC method at Site 10 using Array B.....	129
Figure 7.1	Comparison of dispersion curves developed from the active f - k method and the conventional FDBF passive f - k method in terms of frequency (left column) and wavelength (right column) for (a) Site 1, (b) Site 3, (c) Site 5, (d) Site 9 using Array B, (e) Site 9 using Array C and (f) Site 10.....	136
Figure 7.2	Comparison of dispersion curves developed from active f - k method and MUSIC passive f - k method in terms of frequency (left column) and wavelength (right column) for (a) Site 1, (b) Site 3, (c) Site 5, (d) Site 9 using Array B, (e) Site 9 using Array C and (f) Site 10.....	140
Figure 7.3	Comparison of dispersion curves developed from active f - k method and Capon's passive f - k method in terms of frequency (left column) and wavelength (right column) for (a) Site 1, (b) Site 3, (c) Site 5, (d) Site 9 using Array B, (e) Site 9 using Array C and (f) Site 10.....	142
Figure 7.4	Normalized array patterns for (a) Array A, (b) Array B and (c) Array C. Left: Array geometries. Middle: Normalized array patterns in the (k_x , k_y) plane. Right: Cross-section of array patterns at $k_y = 0$	146
Figure 7.5	FDBF contour power plots for (a) simulated two-source wavefield and (b) simulated three-source wavefield.....	148
Figure 7.6	Power plots estimated from (a) FDBF and (b) MUSIC method at 1.68 Hz for Site 10.....	150
Figure 7.7	Power plots estimated from (a) FDBF and (b) MUSIC method at 1.40 Hz for Site 9.....	151
Figure 8.1	Slowness-frequency (p - f) spectral ratio images estimated using Array 1 (short arrays) for (a) Site 1, (b) Site 5 and (c)-(h) Site 6-Site 11....	157

Figure 8.2	Slowness-frequency (p - f) spectral ratio images estimated using Array 2 (long arrays) for (a) Site 1, (b) Site 5 and (c)-(h) Site 6-Site 11.....	158
Figure 8.3	Comparison of dispersion curves developed from ReMi and active f - k methods shown in terms of frequency for (a) Site 1, (b) Site 5 and (c)-(h) Site 6-Site 11.....	160
Figure 8.4	Comparison of dispersion curves developed from ReMi and active f - k methods shown in terms of wavelength for (a) Site 1, (b) Site 5 and (c)-(h) Site 6-Site 11.....	161
Figure 8.5	Expanded view of ReMi dispersion curves along with active f - k dispersion curves (with estimated 5% error bars) for (a) Site 1, (b) Site 5 and (c)-(h) Site 6-Site 11.....	163
Figure 8.6	Power-slowness profiles of slowness-frequency images (Figure 8.2) at selected low frequencies for (a) Site 1, (b) Site 5 and (c)-(h) Site 6-Site 11.....	165
Figure 8.7	Power-slowness profile through slowness-frequency images (Figure 8.2f) at 2.38 Hz for Site 9.....	167
Figure 8.8	Power plots from passive f - k measurements at Site 1, 5, 9 and 10 (from the top row to the bottom shown in (a), (d), (g) and (j) for low frequencies, (b), (e), (h) and (k) for high frequencies, along with array orientation shown in (c), (f), (i) and (l).....	170
Figure 9.1	Inversion results for Site 1 showing (a) experimental and theoretical dispersion curves and (b) Vs profiles based on SASW (Bailey,2008) and active f - k dispersion curves.....	179
Figure 9.2	Inversion results for Site 2 showing (a) experimental and theoretical dispersion curves and (b) Vs profiles based on SASW (Bailey,2008) and active f - k dispersion curves.....	180
Figure 9.3	Inversion results for Site 4 showing (a) experimental and theoretical dispersion curves and (b) Vs profiles based on SASW (Bailey,2008) and active f - k dispersion curves.....	181
Figure 9.4	Inversion results for Site 5 showing (a) experimental and theoretical dispersion curves and (b) Vs profiles based on SASW (Bailey,2008) and active f - k dispersion curves.....	182
Figure 9.5	Inversion results for Site 7 showing (a) experimental and theoretical	

	dispersion curves and (b) Vs profiles based on SASW (Bailey,2008) and active $f-k$ dispersion curves.....	183
Figure 9.6	Inversion results for Site 8 showing (a) experimental and theoretical dispersion curves and (b) Vs profiles based on SASW (Bailey,2008) and active $f-k$ dispersion curves.....	184
Figure 9.7	Inversion results for Site 10 showing (a) experimental and theoretical dispersion curves and (b) Vs profiles based on SASW (Bailey,2008) and active $f-k$ dispersion curves.....	185
Figure 9.8	Inversion results for Site 11 showing (a) experimental and theoretical dispersion curves and (b) Vs profiles based on SASW (Bailey,2008) and active $f-k$ dispersion curves.....	186
Figure 9.9	Plots showing (a) inverted and modified Vs profiles for Site 5, and (b) comparison of theoretical dispersion curves for inverted and modified Vs profiles.....	187
Figure 9.10	Vs profile in the Memphis, Tennessee area from geophysical logging at deep well MLGW 236, located about 5.5 km from Site 5.....	188
Figure 9.11	Comparison of experimental dispersion curves developed from SASW and active $f-k$ methods presented in terms of wavelength for Site 5.....	188
Figure 9.12	Simulation results for Site 8 (left column) and Site 5 (right column) showing (a) (b) measured and simulated $f-k$ dispersion curves, (c) (d) relative importance of first four Rayleigh modes, along with (e) (f) estimated soil stratigraphy.....	192
Figure 9.13	Comparison of VS profiles from SASW measurements, refraction Measurement (Williams et al, 1999) and SCPT (Mayne, 2000)....	194
Figure 9.14	VS profiles assumed for (a) Case 1, (b) Case 2 and (c) Case 3.....	197
Figure 9.15	Simulation results for Case 1 showing (a) simulated $f-k$ dispersion curve in terms of frequency, (b) relative importance of first five Rayleigh modes and (c) simulated $f-k$ dispersion curve in terms of wavelength.....	199
Figure 9.16	Simulation results for Case 2 showing (a) simulated $f-k$ dispersion curve in terms of frequency, (b) relative importance of first five Rayleigh modes and (c) simulated $f-k$ dispersion curve in terms of	

wavelength.....200

Figure 9.17 Simulation results for Case 3 showing (a) simulated $f-k$ dispersion curve in terms of frequency, (b) relative importance of first five Rayleigh modes and (c) simulated $f-k$ dispersion curve in terms of wavelength.....201

LIST OF TABLES

Table	Page
Table 3.1	Coordinates of site locations.....22
Table 3.2	Lithology of the Mississippi Embayment sediments in the depth range of this study (modified from Van Arsdale & TenBrink, 2000 and Romero & Rix, 2001).....40
Table 3.3	Comparison of characteristics of NEES vibrator and a conventional Vibroseis.....42
Table 3.4	Summary of the measurements performed using traditional SASW testing procedures.....47
Table 3.5	Summary of linear arrays used.....48
Table 3.6	Summary of the measurements performed using active $f-k$ and ReMi procedures.....50
Table 3.7	Description of the three circular arrays.....51
Table 3.8	Summary of data collection using passive $f-k$ procedure.....52
Table 4.1	Receiver pair spacings used for SASW analyses at 11 testing sites.....56
Table 4.2	Parameters for calculation of $\mathbf{R}(f)$ at five sites.....66
Table 4.3	Aliasing limits of circular arrays used for ambient noise measurements.....68
Table 5.1	Comparison of layer resonant frequencies with mode-transition frequencies for Site 3, 6, and 9.....100
Table 5.2	Near-field effect criteria observed from comparing dispersion curves from Array 2 with from Array 1.....106
Table 5.3	Near-field effect criteria observed from comparing dispersion curves from Array 3 with from Array 2.....107

Table 7.1	Description of two simulated multi-source wavefield.....	148
Table 7.2	The λ_{\max} estimated by three empirical criteria.....	152
Table 9.1	Soil profiles for Case 1, Case 2 and Case 3.....	197

STUDY OF SURFACE WAVE METHODS FOR DEEP SHEAR WAVE VELOCITY
PROFILING APPLIED IN THE UPPER MISSISSIPPI EMBAYMENT

Jianhua Li

Dr. Brent L. Rosenblad, Dissertation Supervisor

ABSTRACT

Surface wave methods have become an important tool for non-intrusively and inexpensively determining shear wave velocity (V_s) profiles for many geotechnical earthquake engineering applications. The primary objectives of this study are to (1) compare active-source and passive (ambient vibration) surface wave methods for developing V_s profiles to depths of 200 to 300 m at deep soil sites, and (2) identify the primary factors affecting the reliability and consistency of surface wave methods. This comparative study became possible with the advent of a unique low-frequency field vibrator developed as part of the National Science Foundation's (NSF) Network for Earthquake Engineering Simulation (NEES) program. This vibrator is able to actively excite surface wave energy down to frequencies of less than 1 Hz. Four surface wave methods (two active-source methods and two passive-source methods) were applied in this study, namely: (1) the Spectral-Analysis-of-Surface-Waves (SASW) method, (2) the active-source frequency-wavenumber ($f-k$) method, (3) the passive-source frequency-wavenumber ($f-k$) method and (4) the refraction microtremor (ReMi) method. The focus of this study is on two critical aspects of surface wave methods: (1) development of a reliable surface wave dispersion curve from field measurements, and (2) compatibility between the experimental dispersion

curve and the theoretical model used in the inversion procedure to develop the final V_s profile. Measurements were performed at eleven sites distributed over a distance of about 180 km in the upper Mississippi Embayment in the central United States, where soil deposits are hundreds of meters deep.

Limitations associated with each of the four methods were identified in this study. With respect to the SASW method it was found that potential phase unwrapping problems could cause an erroneous estimate of the dispersion curve. These errors were found to be associated with an abrupt mode transition caused by a strong velocity contrast at a shallow depth. With respect to the active-source $f-k$ approach, it was demonstrated that near-field effects caused by a short near-source offset produced an underprediction of the surface wave dispersion curve at long wavelengths. Recommendations for acceptable source offset distances were developed based on the results from this study. The performance of the passive approaches (passive $f-k$ method and ReMi method) was shown to be strongly dependent on the local ambient wavefield characteristics. Results from a study of the ambient wavefield characteristics at the 11 sites showed high ambient vibration levels at all sites in the frequency range of 1 to 4 Hz. Passive measurements using a circular array provided good comparisons with the active-source methods out to wavelengths of 500 m (2.5 times the array aperture) in most cases. Poor performance at one site was shown to be due to a multi-source wavefield at low frequencies. An improved comparison at this site was achieved by applying high-resolution processing methods. The ReMi method was found to provide good results down to frequencies of 3 to 4 Hz

(wavelengths of 100 to 150 m) but very poor performance at lower frequencies (< 3 Hz). The wavefield characteristics at low frequencies were identified as the primary factor affecting the performance of the ReMi method.

Lastly, deep V_s profiles developed from active-source $f-k$ dispersion curves using a fundamental mode inversion were compared with V_s profiles developed from SASW dispersion curves using an “effective-velocity” inversion. Good agreement between two inversion approaches was shown at most sites, however, large inconsistencies at depth were observed at one site. This inconsistency was shown to be due to incompatibility between the experimental dispersion curve and the fundamental mode model used in the inversion. The local site conditions, specifically the shallow depth of the Memphis Sand formation at this site was identified as the cause of the model incompatibility. Base on the findings from this study, recommendations for procedures to perform deep V_s profiling using surface waves are presented.

CHAPTER 1

INTRODUCTION

1.1 Problem Statement

Many seismically vulnerable regions in the United States and worldwide are located on deep soil deposits which extend to depths of several hundred meters. These deep deposits will affect the propagation of seismic wave energy and thus impact the frequency content and amplitude of surface ground motion. One of the most important parameters for predicting ground response in an earthquake is the small-strain shear wave velocity (V_s) profile. Recent studies have demonstrated the need to characterize V_s profiles of deep sediments to much greater depths than the 30-m depth of conventional geotechnical investigation (Hashash and Park, 2001; Cramer et al., 2004). However, extending the depth of penetration to hundreds of meters becomes prohibitively expensive using conventional borehole methods such as crosshole and downhole measurements.

Surface wave methods offer a non-intrusive and economical approach for evaluating V_s profiles and have been applied extensively in geotechnical earthquake engineering applications for shallow site characterization studies (depths of 30 to 50 m). Since the 1980's, the Spectral-Analysis-of-Surface-Waves (SASW) method (Nazarian and Stokoe, 1984) has been the dominant surface wave approach used in geotechnical engineering applications. In recent years methods based on multi-channel wavefield transformation procedures have been used extensively (Park

et al., 1999; Tokimatsu, 1995; Zywicki, 1999). The profiling depth achieved with any of these methods has been limited by the inability to actively excite the low-frequency energy (1 to 4 Hz) needed to develop deeper profiles. For this reason, methods based on the interpretation of low-frequency ambient vibrations (termed passive or microtremor measurements) which are recorded using a two-dimensional receiver array have been used to supplement higher-frequency active-source measurements (Tokimatsu, 1995; Zywicki, 1999). In the last few years a new passive approach termed the Refraction Microtremor (ReMi) method has been developed that requires only a linear receiver array (Louie, 2001). The convenience and ease of this method have lead to the widespread use of this technique throughout the United States for developing both shallow and deep V_s profiles.

Due to the critical importance of V_s profiles in geotechnical engineering applications, it is important to examine the performance of these methods. However, there have been few direct studies comparing the performance of these different surface wave methods for near-surface characterization and, due to the inability to actively excite low-frequency energy, there have been no studies directly comparing high-quality active source measurements to passive methods for deep V_s profiling. Studies that have been performed are generally lacking in the following respects: (a) variations in V_s profiles obtained from different methods are reported but the factors causing the variations are not identified, (b) studies are often performed at “uncomplicated” sites where the V_s profile varies gradually with depth, and (c) there are no direct comparisons of active and passive measurements for deep V_s profiling

(200 m or greater).

Recently, a one-of-a-kind low-frequency field vibrator capable of generating high-force levels at frequencies down to less than 1 Hz was developed as part of the Network for Earthquake Engineering Simulation (NEES) program funded by the National Science Foundation (NSF) (Stokoe et al. 2004a). With the advent of this equipment it is now possible to actively generate surface wave energy to wavelengths of several hundred meters. This equipment was utilized in this study to perform a comprehensive comparative study of the performance of active-source and passive-source surface wave methods for developing deep V_s profiles.

The study area is the northern Mississippi embayment region of the central United States. This region has very deep soil deposits up to maximum depths of over 1000 m (Van Arsdale and TenBrink, 2000). The Mississippi embayment overlies the New Madrid Seismic Zone (NMSZ), which produced the largest earthquakes in the contiguous U.S. and is the major seismic hazard in this region. The deep V_s profiles resulted from this study will be valuable for site response studies in this region, and the knowledge gained from the study of surface wave methods will be beneficial to other deep soil regions around the world.

1.2 Research Objectives

The goal of this project is to identify and understand the primary factors affecting the reliability and consistency of surface wave methods used for developing deep V_s profiles. The focus of this work is on two critical aspects of surface wave

measurements: (1) development of a reliable surface wave dispersion curve, and (2) compatibility between the experimental dispersion curve and the theoretical model used to fit the experimental data. The following three research objectives are pursued.

1. The first objective is to characterize the ambient wavefield in the Mississippi Embayment. This work focuses on identifying the dominant sources of ambient energy and characterizing several aspects of the ambient wavefield, including: amplitude, frequency content, single or multi-source, and source direction.
2. The second objective is to evaluate the consistency between experimental dispersion curves developed from active-source and passive-source methods and identify factors causing adverse performance. Four different surface wave methods are investigated in this portion of the study, namely, the Spectral-Analysis-of-Surface-Waves (SASW) method, the active-source frequency-wavenumber ($f-k$) method, the passive-source frequency-wavenumber ($f-k$) method, and the refraction microtremor (ReMi) method.
3. The third objective is to investigate the validity of using a fundamental mode theoretical model to fit to the experimental dispersion curve. This assumption is the basis for most commercial surface wave software and is almost universally assumed in published studies of low-frequency passive surface wave measurements. It is expected that this assumption may not be valid for some site conditions.

1.3 Dissertation Overview

Chapter 2 presents a brief overview of four surface wave methods and a literature review of previous surface wave studies with emphasis on applications to deep V_s profiling, and published comparative studies of these methods. Chapter 3 provides a brief overview of the geology of the northern Mississippi embayment, a general description of each test site, including site coordinates and the estimated soil lithology, and a summary of field equipment and field testing procedures. Step-by-step data processing procedures used for each of the four surface wave methods are presented in Chapter 4. In Chapter 5, dispersion curves developed from SASW and active $f-k$ methods are compared for the eleven test sites. The causes of the inconsistencies between the methods are identified and discussed. The performance of the NEES vibrator is also discussed in this chapter. Ambient wavefield characteristics in the Mississippi embayment are presented and discussed in Chapter 6. These characteristics includes: (a) amplitude and frequency content, (b) direction and likely sources of the dominant energy and (c) number of energy sources. Chapter 7 covers the dispersion curve comparison between passive and active-source $f-k$ methods. The issues affecting the reliability of the passive dispersion measurements are identified and discussed. A comparative study of ReMi and active $f-k$ methods for developing low-frequency dispersion curves is presented in Chapter 8. Factors influencing the performance of the ReMi method are identified and discussed. In Chapter 9, deep V_s profiles developed from two different inversion procedures are compared. A simulation procedure is used to explain significant inconsistencies observed in the V_s

profiles at one of test sites. With this, the validity of the assumption of fundamental mode dominance in $f-k$ measurements is discussed. Lastly, Chapter 10 covers a summary of the findings, conclusions drawn from this study, and recommendations for future studies.

CHAPTER 2

OVERVIEW OF SURFACE WAVE METHODS AND PAST STUDIES

2.1 Introduction

Surface wave methods offer a non-intrusive and economical approach for determining V_s profiles for many geotechnical earthquake engineering applications. According to the energy sources used, surface wave methods can be categorized into: active-source and passive-source methods. Active-source methods measure surface waves generated by dynamic sources such as sledge hammers, drop weights, bulldozers and hydraulic Vibroseis equipment, while passive-source methods utilize ambient vibrations caused by natural (ocean wave activity, wind) and man-made (traffic, construction, factories) activities.

In this study, two active-source methods, the Spectral-Analysis-of-Surface-Waves (SASW) method and the active-source frequency-wavenumber ($f-k$) spectral analysis method; and two passive-source methods, the passive-source frequency-wavenumber ($f-k$) spectral analysis method and the refraction microtremor (ReMi) method, are utilized for determining low-frequency surface wave measurements. This chapter first provides a brief overview of each of these four methods, followed by a literature review of related past surface wave studies, with emphasis on applications to deep V_s profiling and comparative studies of surface wave methods.

2.2 Overview of Surface Wave Methods

Surface wave measurements are all based on three important steps as follows:

(1) data collection in the field, (2) data processing to develop an experimental dispersion curve relating phase velocity to frequency or wavelength, and (3) inversion of the experimental dispersion curve, where a one-dimensional V_s profile is developed that provides a matching theoretical dispersion curve to the experimental dispersion curve. The four surface wave methods used in this study differ in the way one or more of these steps are performed. A brief overview of each method is provided below. More detailed information on these methods is discussed in later chapters.

2.2.1 Spectral-Analysis-of-Surface-Waves (SASW) Method

The Spectral-Analysis-of-Surface-Waves (SASW) method was originally proposed and developed in the early 1980's (Nazarian and Stokoe 1984; Stokoe et al. 1989). It uses the phase difference recorded between multiple pairs of vertically-oriented receivers to determine an effective-velocity dispersion curve (Stokoe et al., 1994). The typical SASW setup is shown in Figure 2.1, along with a

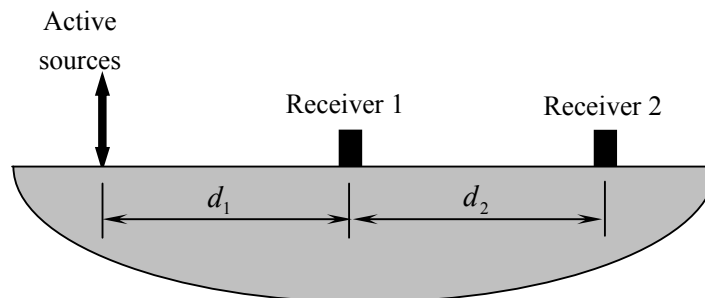


Figure 2.1 Typical configuration for SASW testing

vertical dynamic load as the energy source. In Figure 2.1, d_1 and d_2 are the distance from the source to the closest receiver, and the spacing between two receivers, respectively. Generally, d_1 is kept equal to d_2 for all receiver pairs in order to mitigate near-field effects (Sanchez-Saliner, 1987). Data are typically recorded in terms of frequency domain parameters, such as the cross-power spectrum and the coherence function between two receivers. The wrapped phase angle representing the relative lead or lag (± 180 degrees) between the two receivers is determined from the cross power spectrum. The cumulative phase shift between receivers is then determined from manually “unwrapping” the wrapped phase plot by identifying 360-degree “jumps”. For each frequency, the effective phase velocity is calculated from the cumulative phase difference and receiver spacing. It is important to note that this velocity is not necessarily the same as the fundamental mode velocity, and may contain contributions from higher mode surface waves and body waves. Measurements are performed with several receiver spacings (typically 7 or more) to develop a dispersion curve covering the desired range of wavelengths. An inversion approach, based on an “effective-velocity” dispersion curve, is usually used for SASW analysis to develop the V_s profile. This inversion procedure evaluates the displacements at each receiver pair location and thus simulates the SASW test.

2.2.2 Active-Source Frequency-Wavenumber ($f-k$) Method

With one active energy source, a linear array of multiple receivers, as shown in Figure 2.2, can be used to determine a surface wave dispersion curve. The potential advantages of multi-channel array testing over SASW testing are: (1) it saves time

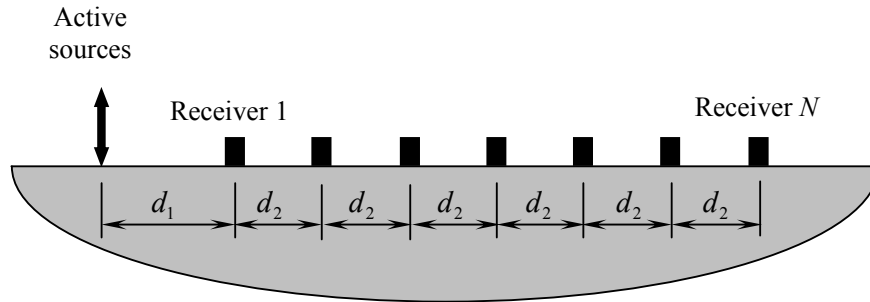


Figure 2.2 Typical configuration for active-source $f-k$ measurements

because a single receiver configuration is used, and (2) it can potentially separate and identify the fundamental mode of the Rayleigh wave from higher modes and body waves (Xia et al. 1999; Foti 2000).

The active-source $f-k$ method is one of several multi-channel array methods and has been widely used for near-surface characterization studies (Tokimatsu, 1995; Gabriels et al., 1987; Beaty, 2000; Foti, 2000; Hebel 2001; Yoon and Rix 2005). Typically 12 to 24 receivers are used in the linear array, and data are recorded simultaneously at all the receivers, either in the time domain or frequency domain. The general approach to data processing procedures in the $f-k$ analysis involves a method to search for propagating waves by assuming a wavenumber (for a given frequency) and shifting and summing the responses in the linear array based on the assumed wavenumber. The procedure is repeated over a range in wavenumbers and the propagating wavenumber is identified by a peak in the array response. These calculations are performed for each frequency of interest to construct the experimental dispersion curve. In some cases, multiple peaks from multiple modes can be identified for a given frequency. The conventional frequency domain beamforming (FDBF) method is a commonly used method to perform this procedure for active-source

measurements. Finally, a fundamental mode inversion is typically used to develop the V_s profile. This inversion procedure is based on an assumption that the dispersion curve represents the fundamental mode of Rayleigh-wave propagation.

2.2.3 Passive-Source Frequency-Wavenumber ($f-k$) Method

The $f-k$ method can also be applied using a two-dimensional (2D) array to search for ambient vibrations. This passive-source $f-k$ method requires a two-dimensional array in order to detect the direction and velocity of the passive energy. This 2-D array could be an “S”, “L”, “X”, triangular or circular shape. But a uniformly spaced circular array has generally proved most efficient (Zywicki, 1999). As compared to active-source methods, the passive $f-k$ approach has two advantageous properties (Tokimatsu et al., 1992a): (1) greater exploration depths can be achieved because ambient energy usually propagates with longer wavelengths, and (2) the assumption of dominance of Rayleigh waves is more likely to be true because the Rayleigh waves are generated by a distant source so that body wave components are negligible.

The data processing procedures for the passive $f-k$ method are similar to those for the active $f-k$ method, except the wavenumber search procedure is performed using wavenumber pairs in the x and y directions. A trial wavenumber pair is used that corresponds to an assumed direction and velocity. The search is performed in two-dimensions and the wavenumber pair with the peak energy is used to calculate both the direction and velocity of the propagating energy at a given frequency. These

calculations are performed for each frequency of interest to construct the experimental dispersion curve. High-resolution f - k methods like the Minimum Variance Distortionless Look (MVDL) method (hereafter referred to as Capon's method) (Capon, 1969), and the Multiple Signal Classification (MUSIC) method (Schmidt, 1986) are often applied for ambient vibration measurements because they can provide an improved ability to separate multiple energy sources than the conventional FDBF f - k method. Like the active-source f - k method, a fundamental mode inversion is typically used to develop the V_s profile.

2.2.4 Refraction Microtremor (ReMi) Method

The refraction microtremor (ReMi) technique (Louie, 2001) is a new method to perform passive-source measurements using a linear array. Due to the use of a linear spread and the lack of a need for an active source, ReMi has been considered to be the most convenient and inexpensive surface wave method, and is currently in widespread use for geotechnical applications.

Ambient vibrations are recorded in the time domain for ReMi measurements. A slant-stack approach (McMechan and Yedlin, 1981) is used to transform the time domain data to the frequency-slowness (p - f) domain. The ReMi analysis yields images of spectral power ratio in the p - f domain by adding only a spectral power ratio calculation to this transformation. This method is based on an assumption that the ambient wavefield is composed of essentially equal energy propagating from all directions. Therefore, the lower bound of dispersion trend in the ReMi image should

be the slowest velocity, representing the fundamental mode propagating along the length of the receiver array. The interpretation of ReMi data is performed by picking the lower bound of the spectral ratio image to estimate the fundamental mode of propagation. Picking of two or three possible dispersion curve values are recommended by Louie (2001). The development of the dispersion curve from ReMi measurements is discussed in greater detail in Section 4.5 of Chapter 4. As with the f - k methods, a fundamental mode dispersion curve is used as the inversion procedure.

2.3 Overview of Past Applications of Deep V_s Profiling

Due to the inability to actively excite the low-frequency energy (1 to 4 Hz) needed to develop deeper V_s profiles, most published studies of active-source surface wave methods are limited to characterization of near-surface sediments (30 to 60 m) (Stokoe et al., 1994; Kavazanjian et al., 1996; Luke and Stokoe, 1998; Bergstrom, 1999; Anderson and Thitimakorn, 2004; Tokimatsu, 1995; Zywicki, 1999). There have been a limited number of active source studies performed to greater depths by using a servo-hydraulic field vibrator (Vibroseyis) source. Brown et al. (2002) applied the SASW method with a Vibroseis source at 10 sites in Southern California achieving a maximum profiling depth of 100 m. V_s profiles were developed for eleven rock sites at Yucca Mountain using a Vibroseis source and the SASW method (Stokoe et al. 2004b). Among the sites measured, six resulted in deep profiles with depths ranging from 150 to 210 m, and the other five sites resulted in V_s profiles ranging from 60 to 130 m. The results were compared to downhole data, which was limited to

the top 60 m.

Passive-source $f-k$ methods have also been widely applied to profile soil structures to depths of less than 100 m in recent years (Tokimatsu et al., 1992b; Bozdag and Kocaoglu, 2005; Giulio et al., 2006). In some studies, the passive $f-k$ method has been combined with active-source methods to extend the exploration depth (Hebeler, 2001; Suzuki and Hayashi, 2003; Yoon and Rix, 2005).

Passive methods have also been used to profile the substructures to much greater depths. Horike (1985) first proposed an exploration technique based on the $f-k$ spectral analysis for the array records of ambient vibrations. With this technique, Horike claimed that geological conditions down to a depth of more than 100 m can be inverted. Ishida et al. (1998), Kawase et al. (1998), Miyakoshi et al. (1998), Satoh et al. (2001), and Scherbaum et al. (2003) performed passive $f-k$ measurements at different sites in USA, Japan and Germany. The exploration depth was over 1000 m in most cases. As with many deep V_s studies, there was no way to verify the results through use of another method.

The ReMi method has been widely used for profiling near-surface (from 30 to 70 m) V_s structure (Louie, 2001; Pullammanappallil et al., 2003; Rucker, 2003; Stephenson et al. 2005; Pei et al., 2005; Thelen et al., 2006; Pei et al., 2007; Pancha et al., 2008). In recent years the ReMi approach has been used to profile to much greater depths. Liu et al. (2005), for example, combined SASW and ReMi methods to characterize V_s profiles for a dozen sites in the Las Vegas basin. The ReMi measurements presented in Liu et al. (2005) yielded surface wave dispersion curves

out to wavelengths of about 1000 m and frequencies as low as 1 Hz. The V_s profiles at several sites were developed to depths of 300 m and greater. The reliability of the ReMi dispersion curves at these long wavelengths was justified in part by the overlap with the SASW results at shorter wavelengths (about 10 to 100 m).

2.4 Overview of Past Comparative Studies

Most of the comparative studies of different surface wave methods are limited to shallow depths (Xia et al, 2002; Pullammanappallil et al. 2003; Stephenson et al. 2005, and Thelen et al. 2006). Comparative studies of deep V_s profiles are rare. Liu et al. (2000) compared the dispersion curve estimated from passive $f-k$ measurements to dispersion curves calculated from a borehole profile at one site. The authors concluded that the dispersion curve from the passive measurement agreed with the borehole results to within 11% when the wavelength was less than 2 times the array aperture (array aperture was 100 m in their study).

Brown et al. (2002) compared V_s profiles developed from the SASW method with nearby downhole seismic results at 10 sites in Southern California to a maximum profiling depth of 100 m. Comparisons showed generally good agreement, with obvious differences at a couple of sites. Tokeshi et al. (2006) compared the V_s profile developed from passive $f-k$ measurements and from P-S logging at one site to a depth of 100 m, and showed very good agreement between them. Lastly, Boore (2006) compared results from several different active and passive techniques performed by different researchers at a site near San Jose, CA. Most of the active methods were

limited to profiling depths of 50 m or less and the passive profiles extended to depths of up to 300 m. It was concluded in the paper that differences from the methods were of little importance in some commonly-used measures of site amplification.

These comparative studies have been limited to the following ways: (1) variations in the V_s profiles obtained from different methods are reported, but the factors causing the variations are not identified (Brown, 2002; Boore, 2006), (2) studies are often performed at fairly simple sites with a gradually increasing V_s profile with depth (Liu et al., 2000; Tokeshi et al., 2006; Boore, 2006), and (3) there are no direct comparisons of active and passive measurements for deep V_s profiling (200 m or greater) due to the lack of an active low-frequency source.

CHAPTER 3

TESTING SITES, EQUIPMENT AND PROCEDURES

3.1 Upper Mississippi Embayment and New Madrid Seismic Zone

The upper Mississippi Embayment is a southwest plunging trough encompassing parts of Arkansas, Missouri, Kentucky, Tennessee and Mississippi in the Central United States, as shown in Figure 3.1. The Embayment is filled with deep sediments of gravel, sand, silt, clay, chalk and lignite ranging in age from Late Cretaceous to recent Cenozoic (Cushing et al., 1964). The general stratigraphy of the sediments in this region, as developed by Van Arsdale and TenBrink (2000), is presented in Figure 3.2. The basement rock is the Knox Dolomite from the Paleozoic era (Cushing et al., 1964). The estimated depth to the bedrock increases southward from approximately 470 m near New Madrid, Missouri to nearly 1000 m near Memphis, Tennessee (Van Arsdale and TenBrink, 2000), as shown in Figure 3.3. A cross-sectional view of the Embayment near Memphis is shown as Figure 3.4. The sediments in the embayment dip gently toward the axis at a rate of 1.9 to 6.6 m/km (Brahana et al., 1987).

The axis of the Embayment is nearly coincident with the underlying Reelfoot rift, which is the most prominent buried structure in the northern Embayment, and appears to reflect Cretaceous reactivation of an ancient rift (Braile et al., 1982). The New Madrid Seismic Zone (Figure 3.1) is a clustered pattern of earthquake epicenters between 5 and 15 km deep and lies mostly within the Reelfoot rift (Hashash and Park,

2001). The NMSZ is the primary seismic hazard in the central United States, and has produced three major earthquakes and several large aftershocks in the winter of 1811-1812 (Johnson and Kanter, 1990; Atkinson and Hanks, 1995).

Cramer (2001) and Tuttle et al. (2002) estimate that the NMSZ is able to produce large earthquakes ($> M7$), like the 1811-1812 event, at mean-recurrence intervals of about 500 years. This potentially large event could result in significant loss of life and property, especially in the Memphis metropolitan area. The presence of the very deep sediments in this region will alter the frequency content and

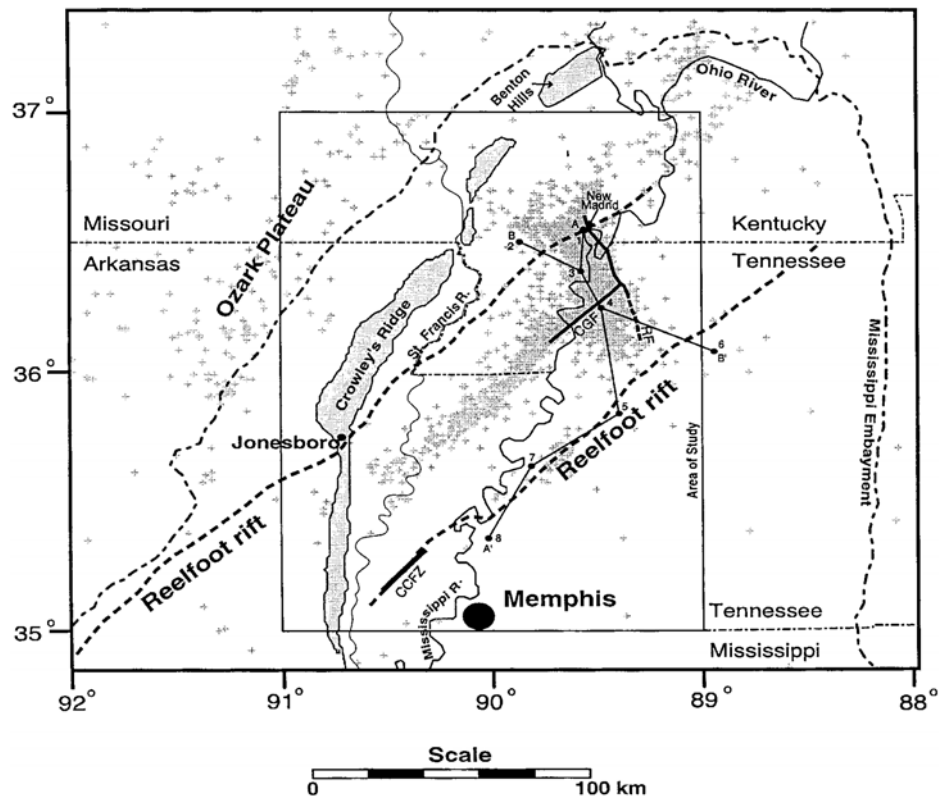
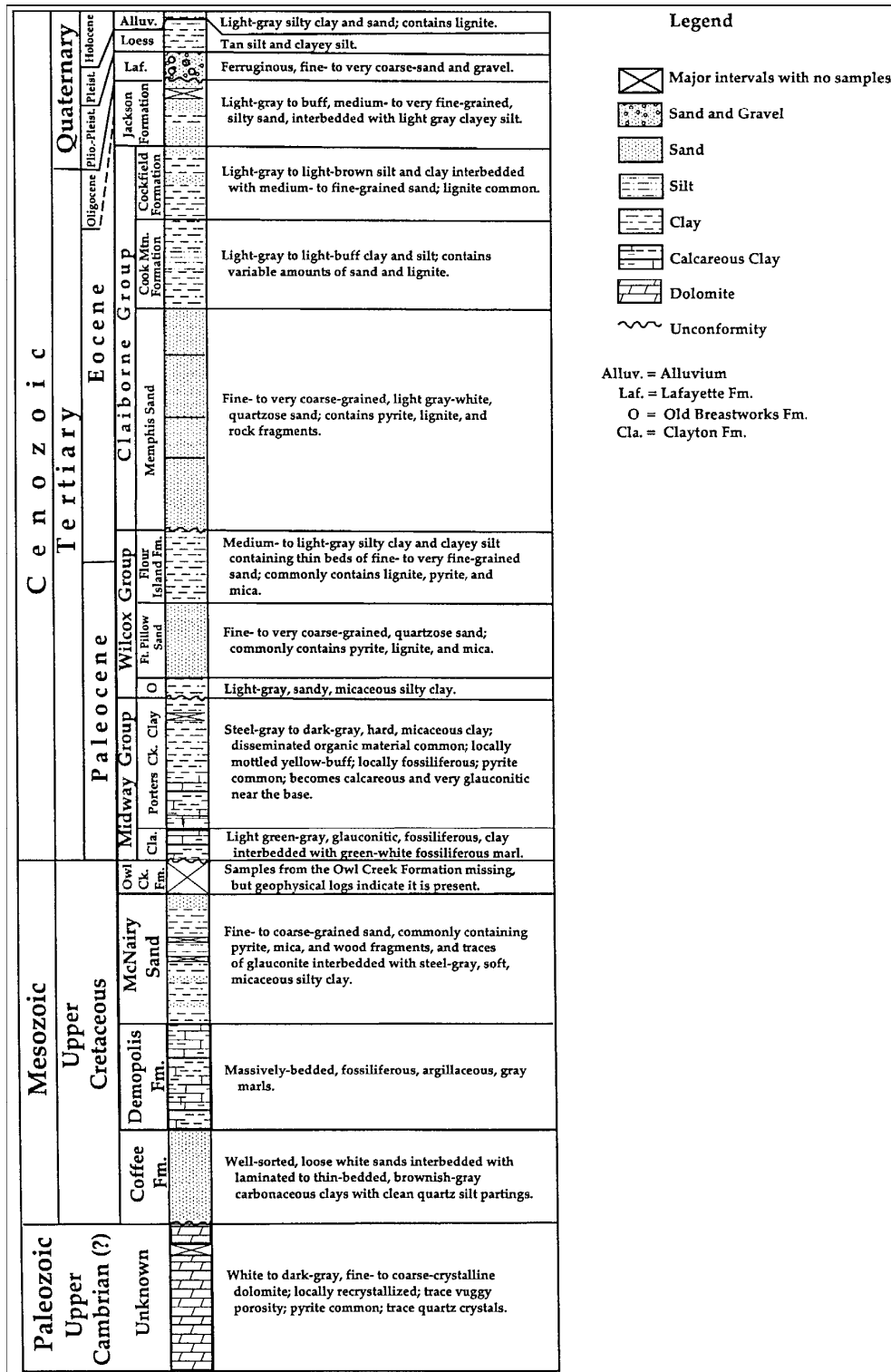


Figure 3.1 Plan view of the upper Mississippi Embayment (Van Arsdale and TenBrink, 2000).



Legend

- Major intervals with no samples
- Sand and Gravel
- Sand
- Silt
- Clay
- Calcareous Clay
- Dolomite
- Unconformity

Alluv. = Alluvium
Laf. = Lafayette Fm.
O = Old Breastworks Fm.
Cl. = Clayton Fm.

Figure 3.2 Stratigraphic column of sediments in the Mississippi Embayment (Van Arsdale and TenBrink, 2000).

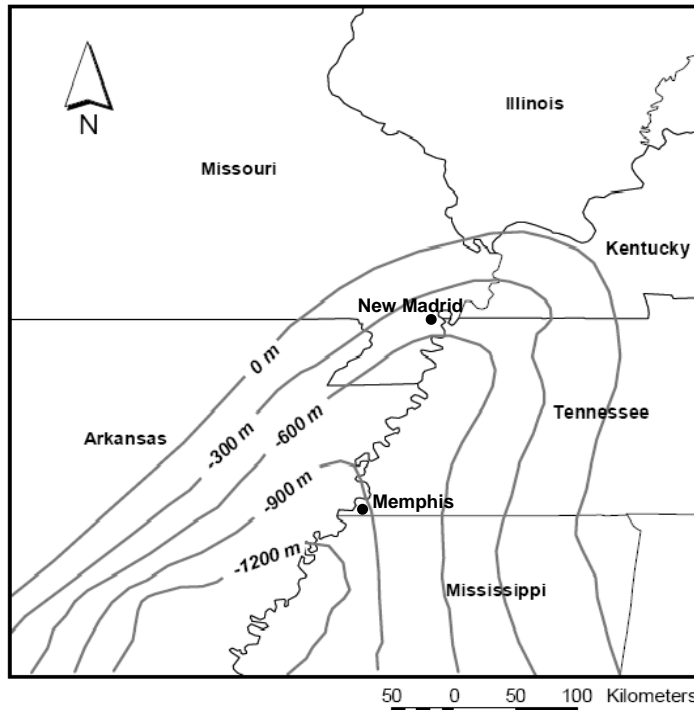


Figure 3.3 Elevation of Paleozoic bedrock relative to mean sea level in the Mississippi Embayment (Romero and Rix, 2001).

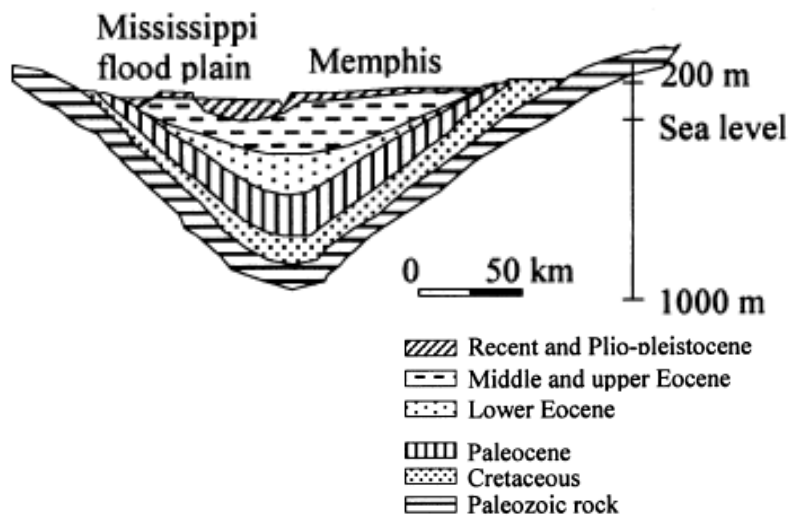


Figure 3.4 East-West cross-section through Memphis, Tennessee in the Mississippi Embayment (Hashash and Park, 2001).

amplitude of the earthquake motions. Therefore, the effect of very deep soft sediments on the propagation of seismic waves has been drawing the attention of researchers for many years.

3.2 Site Descriptions

Field measurements were performed at 11 site locations, designated as Sites 1 to Site 11 in Figure 3.5. Measurements at the first five sites (Site 1 to Site 5) were performed in May, 2006 while measurements at the other six sites (Site 6 to Site 11) were performed in May, 2007. These 11 sites were chosen based on several criteria including: (1) a large spatial distribution to cover different subsurface conditions, (2) variable sediment depth to the Paleozoic bedrock, (3) proximity to seismic station,

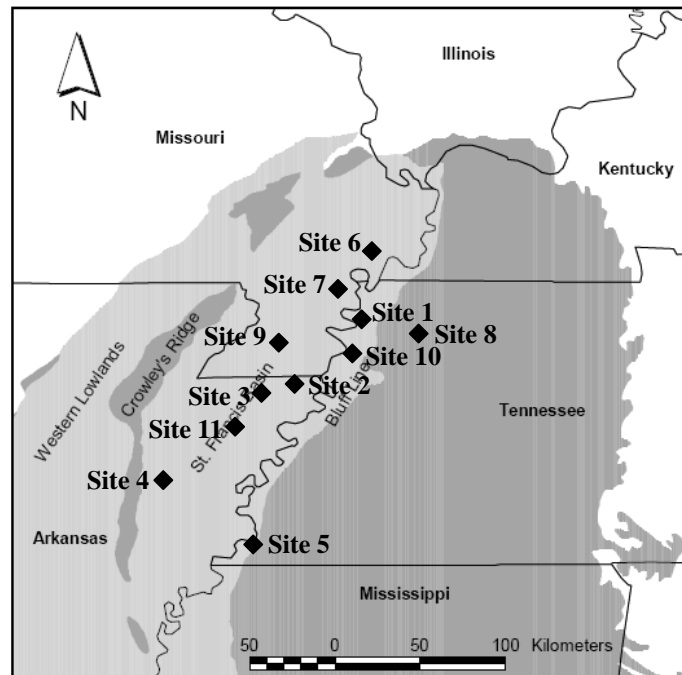


Figure 3.5 Eleven site locations in the Mississippi Embayment (map modified from Romero and Rix, 2001).

(4) accessibility for the large hydraulic vibrator, and (5) proximity to locations of past field studies or sites of interest for earthquake engineering studies. The coordinates of each measurement location are presented in Table 3.1 and brief descriptions of each site are presented in the following sections.

Table 3.1 Coordinates of site locations

Name	Site Location	Coordinates	
Site 1	Mooring, TN	36.324N	89.566W
Site 2	Yarbro, AR	35.981N	89.915W
Site 3	Gosnell, AR	35.960N	90.016W
Site 4	Lepanto, AR	35.614N	90.413W
Site 5	Memphis, TN	35.136N	89.846W
Site 6	East Prairie, MO	36.717N	89.358W
Site 7	Portageville, MO	36.450N	89.628W
Site 8	Glass, TN	36.269N	89.288W
Site 9	Braggadocio, MO	36.205N	89.859W
Site 10	Tennemo, TN	36.166N	89.579W
Site 11	Manila South, AR	35.784N	90.147W

3.2.1 Site 1: Mooring, Tennessee

Site 1 is located on Holocene-age, near-surface alluvial deposits on private farmland in the town of Mooring, Tennessee. Site 1 is located about 1 km from the Mississippi River and approximately 50 m from the MORT seismic station operated by the Center for Earthquake Research and Information (CERI) at the University of Memphis. In addition, this site is located approximately 10 km south of the New Madrid Test Well 1-X which provides general soil stratigraphy information for this region (Crone, 1981). The depth to bedrock at Site 1 is estimated to be approximately 700 meters. Figure 3.6 presents a Google Earth image of Site 1 showing the locations of surrounding major roadways. Figure 3.7 presents a zoomed-in Google Earth image of

Site 1 with the location and orientation of the linear array and the circular array shown with a black line and a black circle. The location of the seismic source and seismic station, MORT, are also indicated in Figure 3.7.

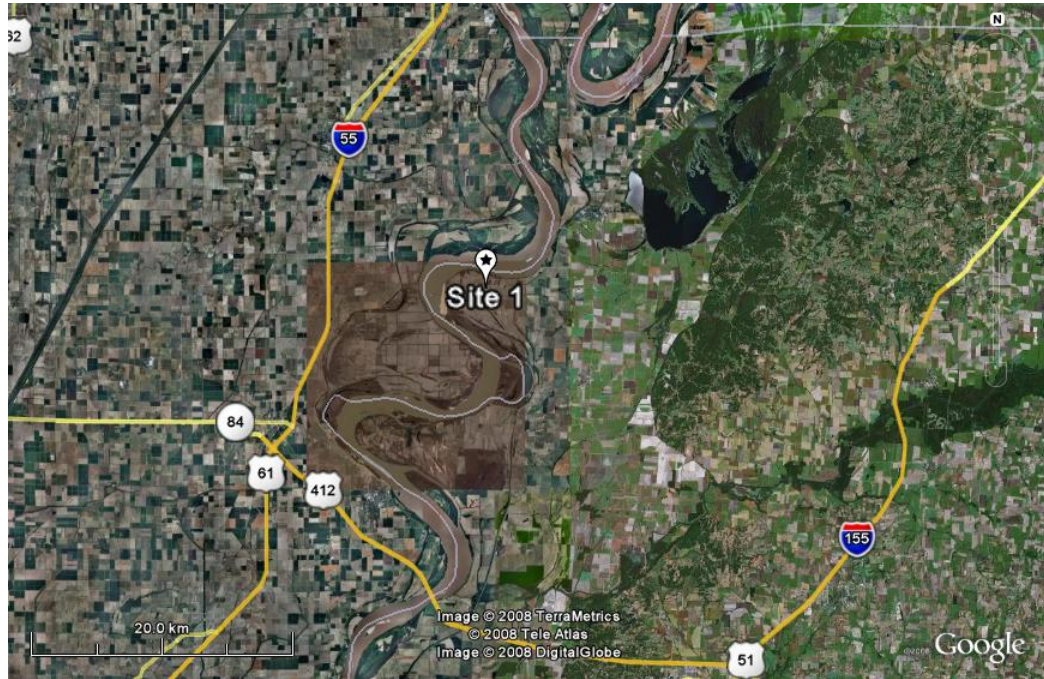


Figure 3.6 Google Earth image of Site 1 and surrounding major roadways.



Figure 3.7 Google earth image of Site 1 showing array location and orientation (from Bailey, 2008).

3.2.2 Site 2: Yarbro, Arkansas

Site 2 is located on private land in the town of Yarbro, Arkansas, and is on Holocene-age, near-surface alluvial deposits. Previous studies near this site include shallow CPT measurements and paleo-liquefaction studies (Schneider et al. 2001; Tuttle et al., 2002; Schneider and Mayne, 1999). The estimated depth to bedrock at this site is 820 m. Figure 3.8 presents a Google Earth image of Site 2 showing the locations of surrounding major roadways. Figure 3.9 presents a zoomed-in Google Earth image of Site 2 with the extent and orientation of the linear array shown with a black line. The location of the energy source is also indicated in Figure 3.9.

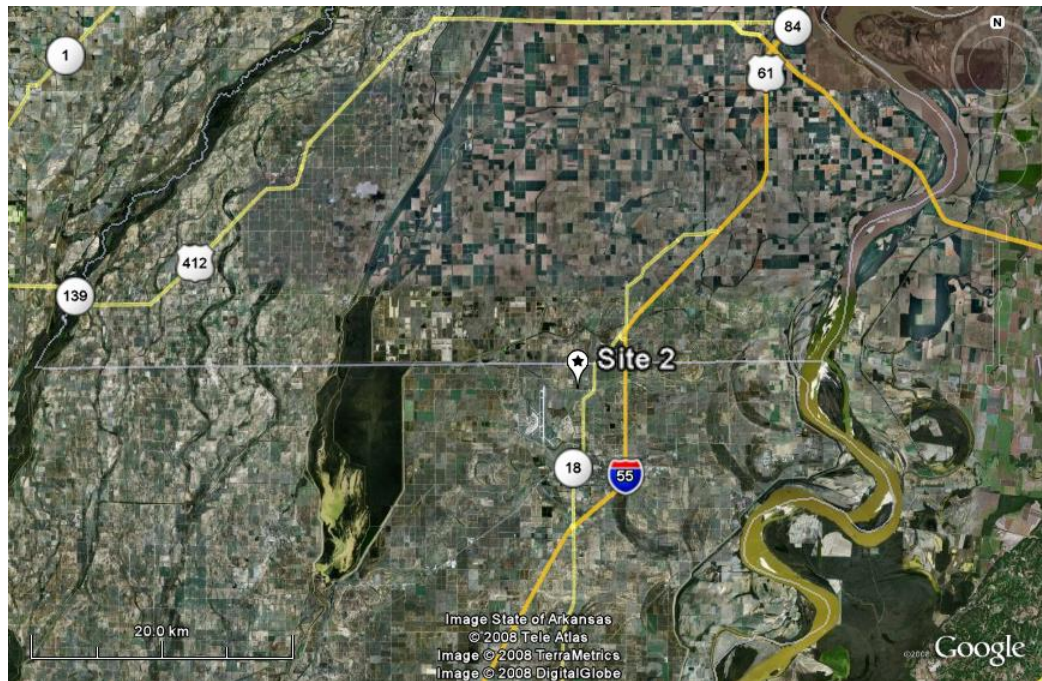


Figure 3.8 Google earth image of Site 2 and surrounding major roadways.



Figure 3.9 Google Earth image of Site 2 showing array location and orientation (from Bailey, 2008).

3.2.3 Site 3: Gosnell, Arkansas

Site 3 is located on private farmland in Gosnell, Arkansas, approximately 9 km southwest from Site 2. This site is located within approximately 100 m of the GNAR seismic station operated by CERI and is located on Holocene-age, near-surface alluvial deposits. The estimated depth to bedrock at this site is 780 m. Figure 3.10 presents a Google Earth image of Site 3 showing the locations of surrounding major roadways. Figure 3.11 presents a zoomed-in Google Earth image of Site 3, with the location of the linear array and the circular array shown with a black line and a black circle, respectively. The location of the energy source and seismic station, GNAR, are also indicated in Figure 3.11.

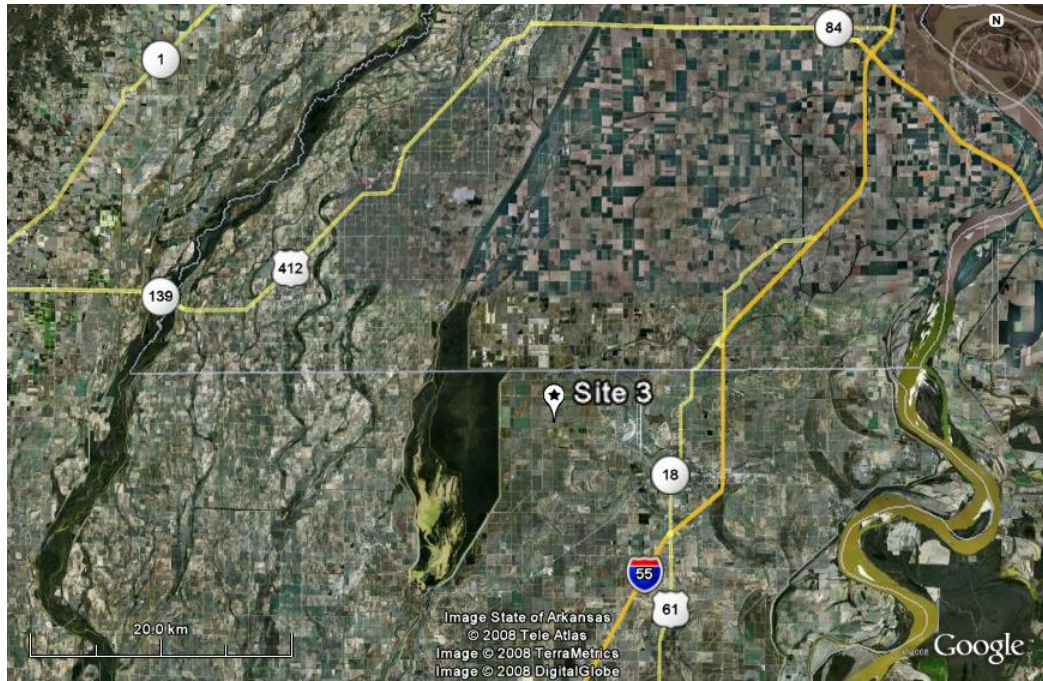


Figure 3.10 Google Earth image of Site 3 and surrounding major roadways.



Figure 3.11 Google Earth image of Site 3 showing array location and orientation (from Bailey, 2008).

3.2.4 Site 4: Lepanto, Arkansas

Site 4 is located west of Interstate 55 in Lepanto, Arkansas. This site is near the location of a seismic reflection survey conducted by the United States Geological Survey (USGS) in Lepanto about one week prior to the surface wave measurements in May, 2006. Site 4 is located on Holocene-age, near-surface alluvial deposits and the estimated depth to bedrock at Site 4 is approximately 790 m. Figure 3.12 presents a Google Earth image of Site 4 showing the locations of surrounding major roadways. Figure 3.13 presents a zoomed-in Google Earth image of Site 4, with the location and orientation of the linear array shown with a black line. The location of the seismic source is also indicated in Figure 3.13.

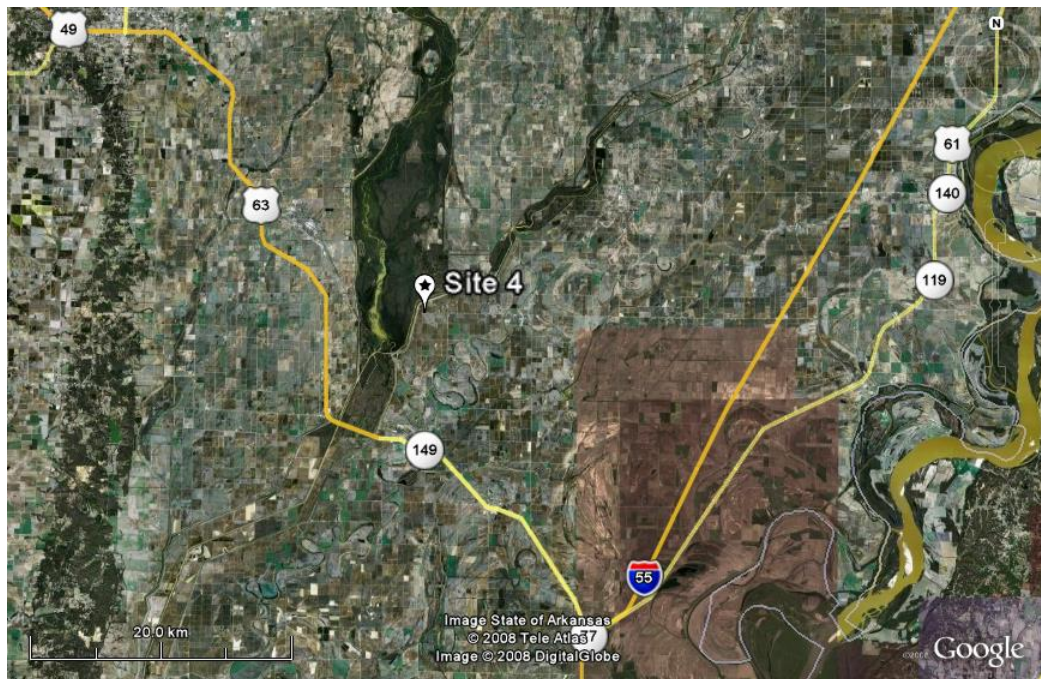


Figure 3.12 Google Earth image of Site 4 and surrounding major roadways.



Figure 3.13 Google Earth image of Site 4 showing array location and orientation (from Bailey, 2008).

3.2.5 Site 5: Shelby Farms, Memphis, Tennessee

Site 5 is the furthest site to the south, and is located at the Shelby Farms public park in Memphis, Tennessee. Site 5 is the only site located in an urban environment. Shallow shear wave velocity measurements and cone penetration tests in the top 30 m have been conducted near this site location (Mayne, 2000; Romero and Rix, 2001; Rix et al., 2002; Schneider et al., 2001). Williams et al. (1999) conducted S-wave refraction measurement to a depth of about 120 m at one site about 1 km south of Site 5. In addition, soil lithology near this site could be established from a detailed lithologic model that has been developed for Memphis and Shelby County (Gomberg et al., 2003). Site 5 is located on Holocene-age, near-surface alluvial deposits in the floodplain of the Wolf River. The estimated depth to bedrock at this site is approximately 840 m. Figure 3.14 presents a Google Earth image of Site 5 showing the locations of surrounding major roadways. Figure 3.15 presents a zoomed-in

Google Earth image of Site 4, with the location of the linear array and the circular array shown with a black line and a black circle, respectively. The location of the energy source is also indicated in Figure 3.15.

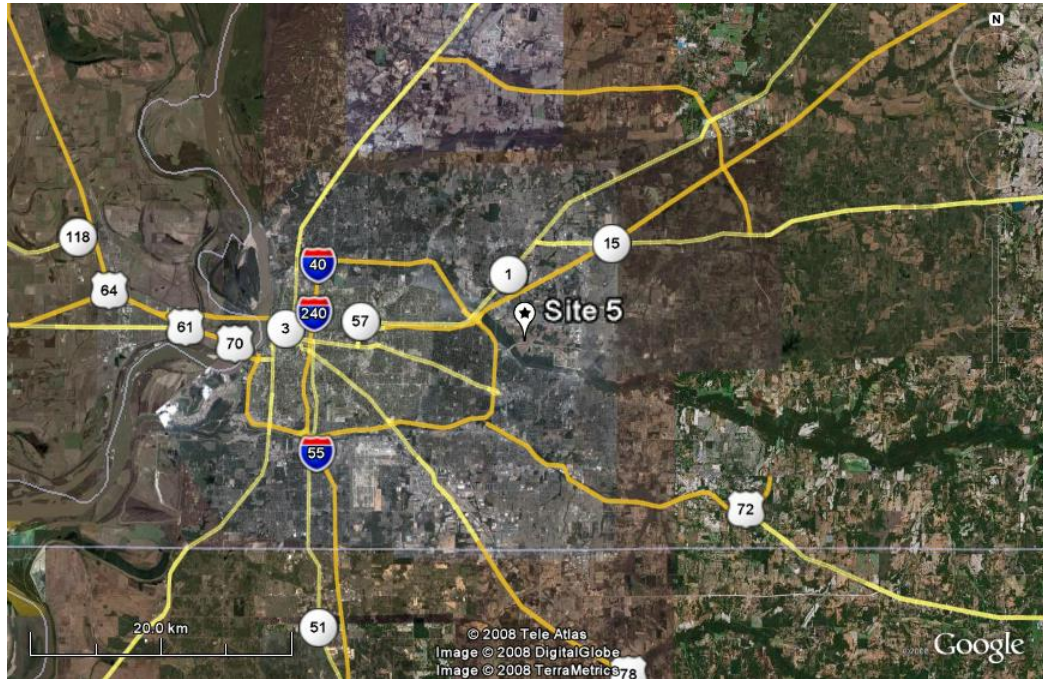


Figure 3.14 Google Earth image of Site 5 and surrounding major roadways.



Figure 3.15 Google earth image of Site 5 showing array location and orientation (from Bailey, 2008).

3.2.6 Site 6: East Prairie, Missouri

Site 6, the furthest site to the north, is located on private farmland in the town of East Prairie, Missouri. This site is located approximately 300 m from the EPRM seismic station operated by CERL. Site 6 is located on Holocene-age, near-surface alluvial deposits, and the estimated depth to bedrock at this site is approximately 450 m. Street and Woolery (2003) conducted P- and SH- wave seismic reflection and refraction measurements near this location, and profiled V_s structure down to 140 m. Figure 3.16 presents a Google Earth image of Site 6 showing the locations of surrounding major roadways. Figure 3.17 presents a zoom-in Google Earth image of Site 6, with the location of the linear array shown with a black line. The location of the seismic source is also indicated in Figure 3.17.

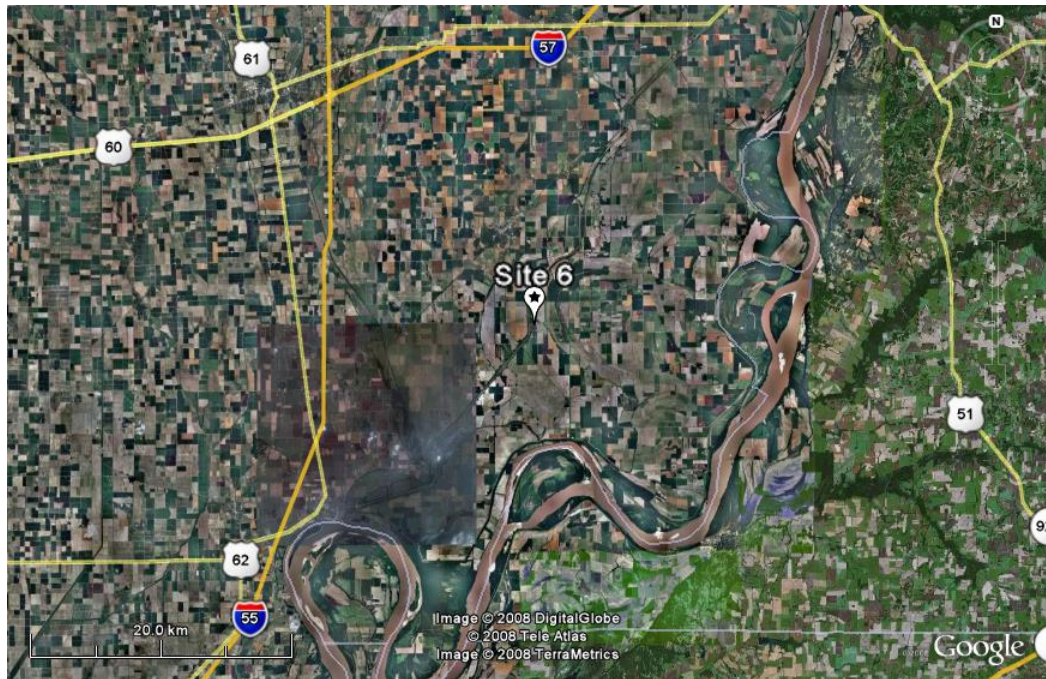


Figure 3.16 Google earth image of Site 6 and surrounding major roadways.

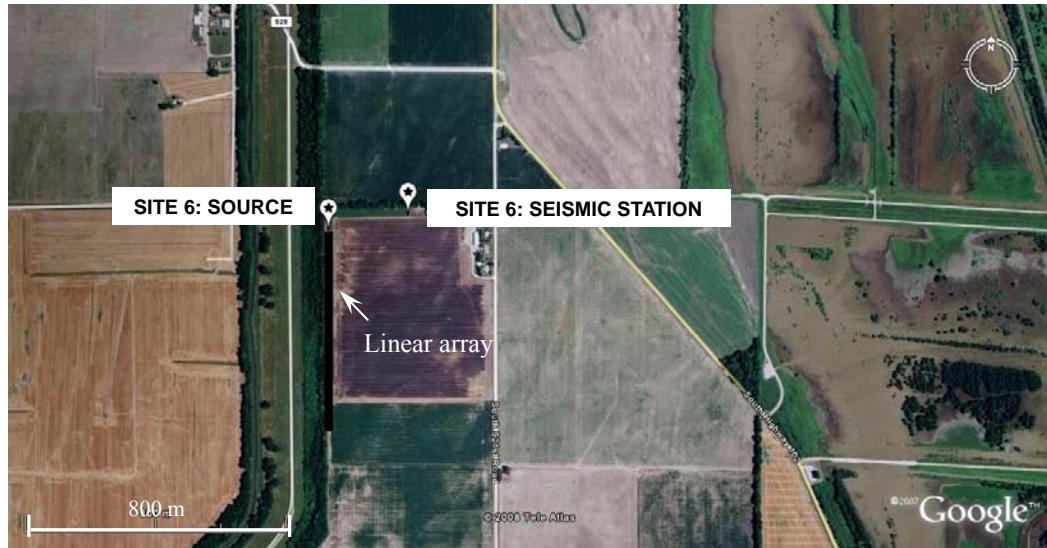


Figure 3.17 Google Earth image of Site 6 showing array location and orientation (from Bailey, 2008).

3.2.7 Site 7: Portageville, Missouri

Site 7 is located on private farmland in the town of Portageville, Missouri, about 2.5 km southeast of interstate I-55. This site is located near the PENM seismic station operated by CERl and is underlain by Holocene-age, near-surface alluvial deposits. The estimated depth to bedrock at this site is about 590 m. Figure 3.18 presents a Google Earth image of Site 7 showing the locations of surrounding major roadways. Figure 3.19 presents a zoomed-in Google Earth image of Site 7, with the location of the linear array shown with a black line. The location of the seismic source is also indicated in Figure 3.19.

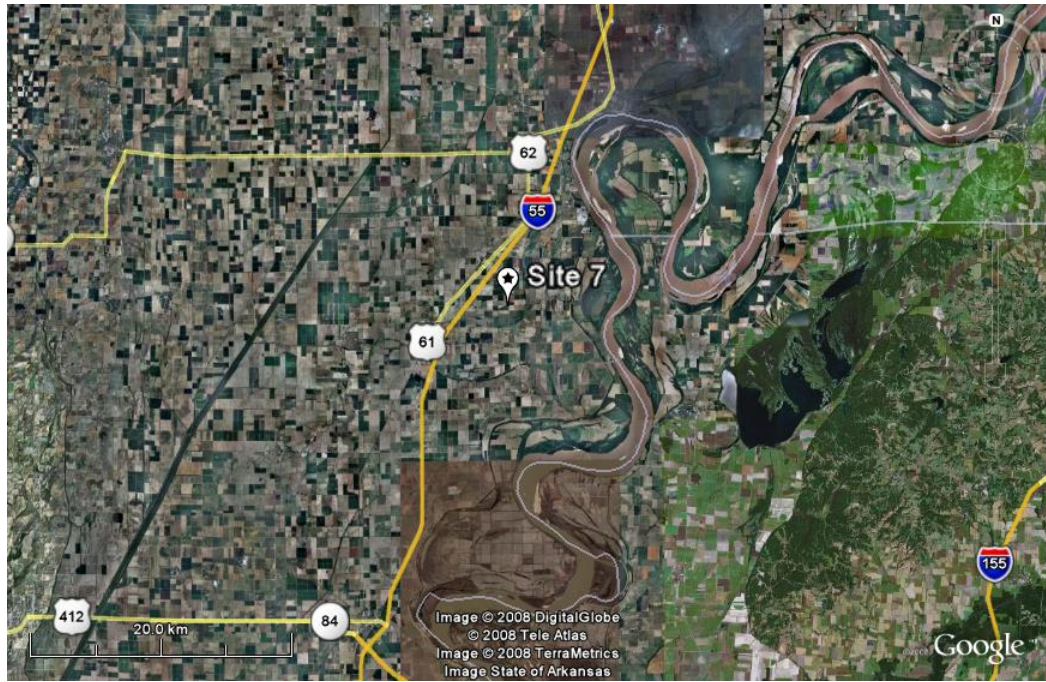


Figure 3.18 Google Earth image of Site 7 and surrounding major roadways.



Figure 3.19 Google Earth image of Site 7 showing array location and orientation (from Bailey, 2008).

3.2.8 Site 8: Glass, Tennessee

Site 8 is located on private farmland in the town of Glass, Tennessee. This site is located adjacent to the GLAT seismic station operated by CERI. Site 8 is the only one of the sites located in the upland region on Pleistocene-age deposits. More sites were not measured in the upland region due to rougher terrain and limited space to deploy long arrays. The site has a south-north incline with a slope of over 3%. The estimated depth to bedrock at this site is about 750 m. Figure 3.20 presents a Google Earth image of Site 8 showing the locations of surrounding major roadways. Figure 3.21 presents a zoomed-in Google Earth image of Site 8, with the location of the linear array shown with a black line. The location of the energy source is also indicated in Figure 3.21.

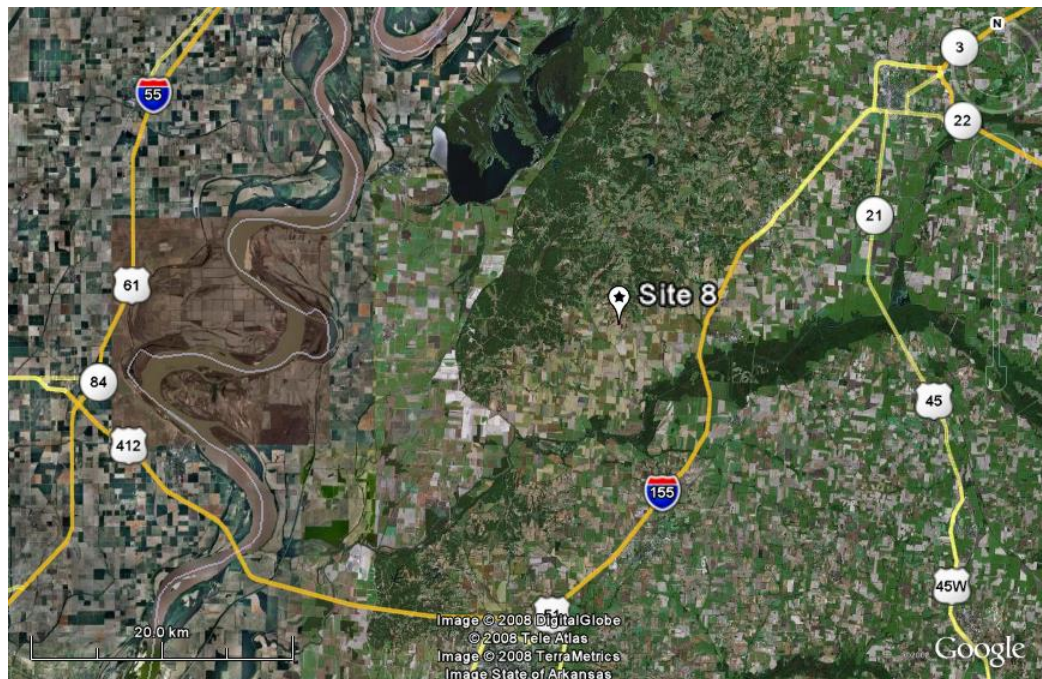


Figure 3.20 Google Earth image of Site 8 and surrounding major roadways.

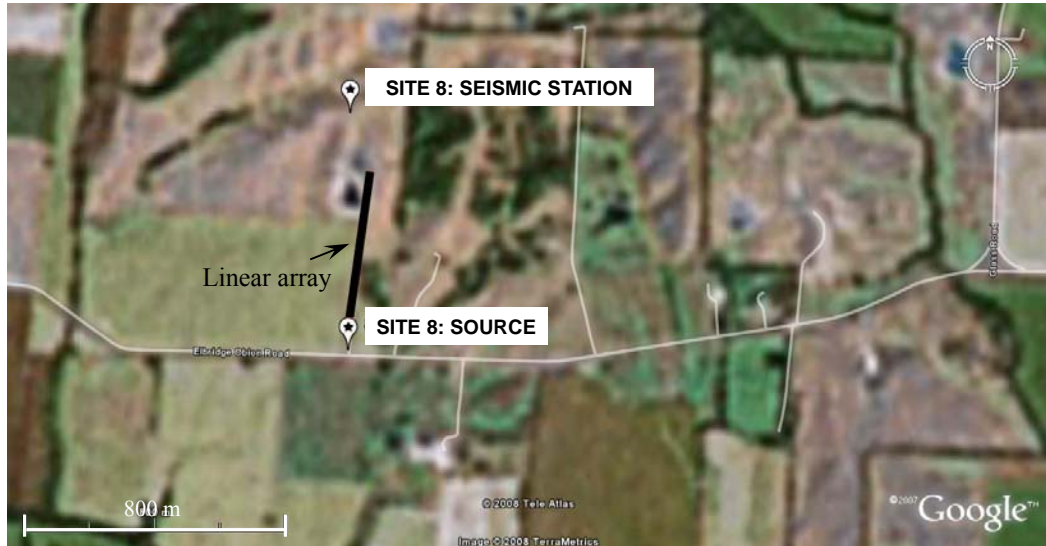


Figure 3.21 Google Earth image of Site 8 showing array location and orientation (from Bailey, 2008).

3.2.9 Site 9: Braggadocio, Missouri

Site 9 is located on private farmland in the town of Braggadocio, Missouri, about 30 km southeast of Site 1. This site is located approximately 200 m from the BRGM seismic station operated by the CERI. Site 9 is located on Holocene-age, near-surface alluvial deposits and the estimated depth to bedrock at this site is approximately 715 m. Figure 3.22 presents a Google Earth image of Site 9 showing the locations of the surrounding major roadways. Figure 3.23 presents a zoom-in Google Earth image of Site 9, with the location of the linear array and the circular array shown with a black line and a black circle, respectively. The locations of the seismic source and the seismic station, BRGM, are also indicated in Figure 3.23.

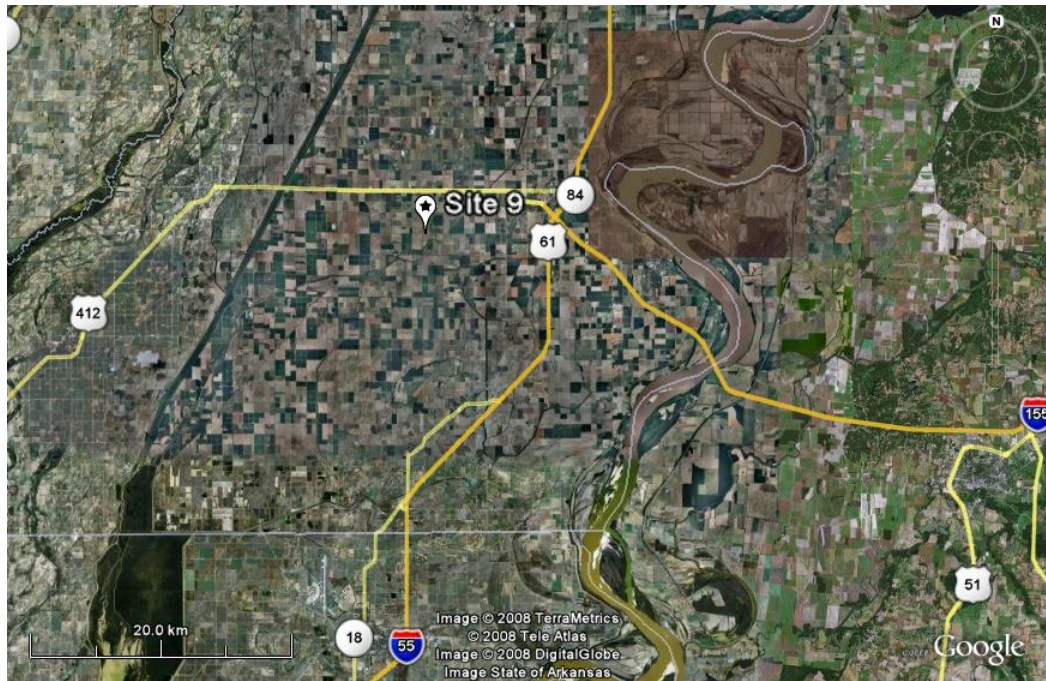


Figure 3.22 Google Earth image of Site 9 and surrounding major roadways.

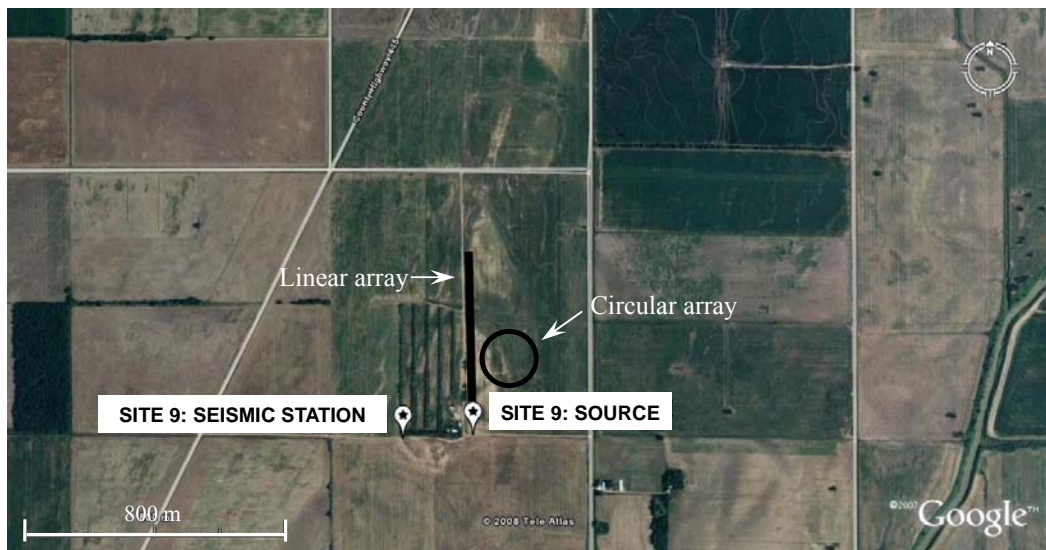


Figure 3.23 Google Earth image of Site 9 showing array location and orientation (from Bailey, 2008).

3.2.10 Site 10: Tennemo, Tennessee

Site 10 is located on private farmland in the town of Tennemo, Tennessee, about 18 km south of Site 1. This site is located near the TNMT seismic station operated by CERI. This site is only about 650 m south of the Mississippi river at its closest point and is underlain by Holocene-age, near-surface alluvial deposits. The depth to bedrock at Site 6 is estimated to be approximately 780 m. Figure 3.24 presents a Google Earth image of Site 10 showing the locations of surrounding major roadways. Figure 3.25 presents a zoomed-in Google Earth image of Site 10, with the location of the linear array and the circular array shown with a black line and a black circle, respectively. The locations of the seismic source and the seismic station, TNMT, are also indicated in Figure 3.25.

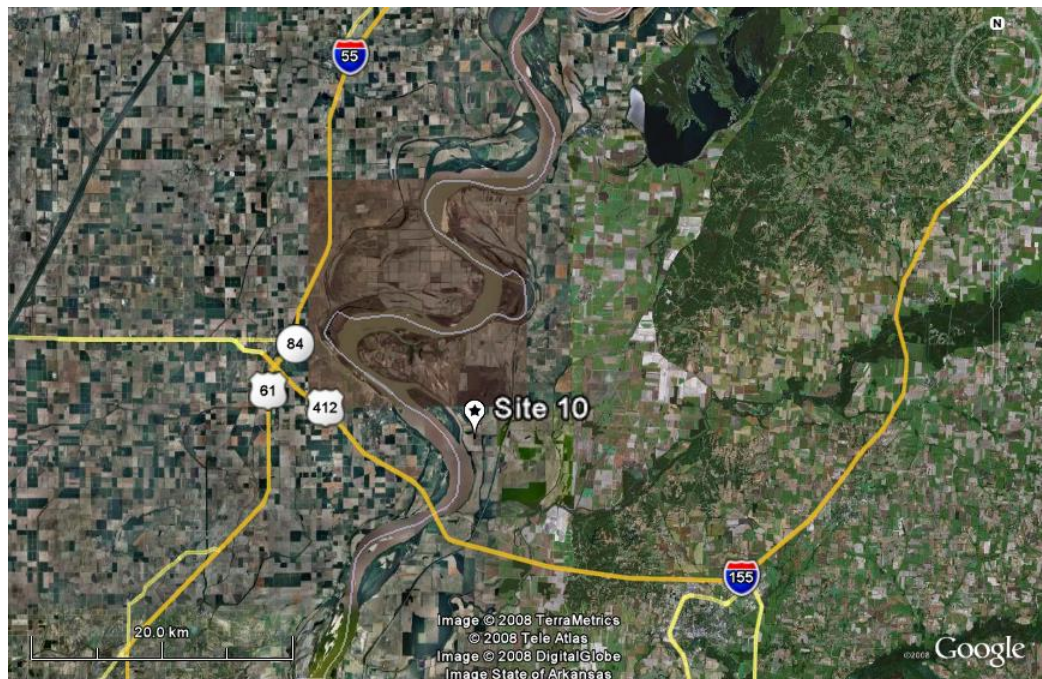


Figure 3.24 Google Earth image of Site 10 and surrounding major roadways.

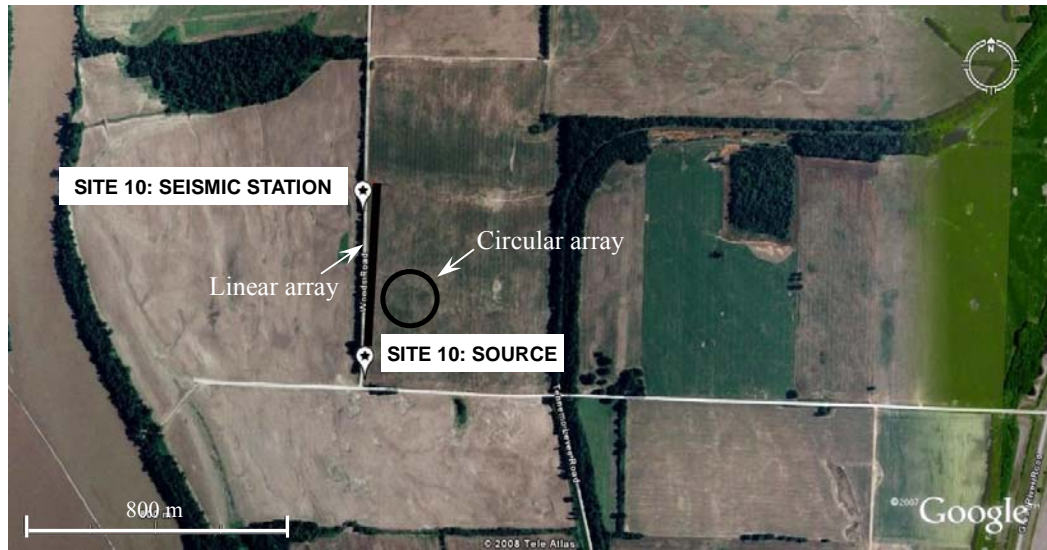


Figure 3.25 Google earth image of Site 10 showing array location and orientation (from Bailey, 2008).

3.2.11 Site 11: Manila, Arkansas

Site 11 is located on private farmland in the town of Manila, Arkansas, about approximately 22 km southwest of Site 3. This site is located near the MSAR seismic station operated by CERL. Site 11 is located on Holocene-age, near-surface alluvial deposits and the estimated depth to bedrock at this site is approximately 850 m. According to Street et al. (2001), the average SH-wave velocity of the top 30 m of the soils around this site is 181-240 m/sec. Figure 3.26 presents a Google Earth image of Site 11 along with the surrounding major roadways. Figure 3.27 presents a zoomed-in Google Earth image of Site 11, with the location of the linear array shown with a black line. The locations of the seismic source and the seismic station, MSAR, are also indicated in Figure 3.27.

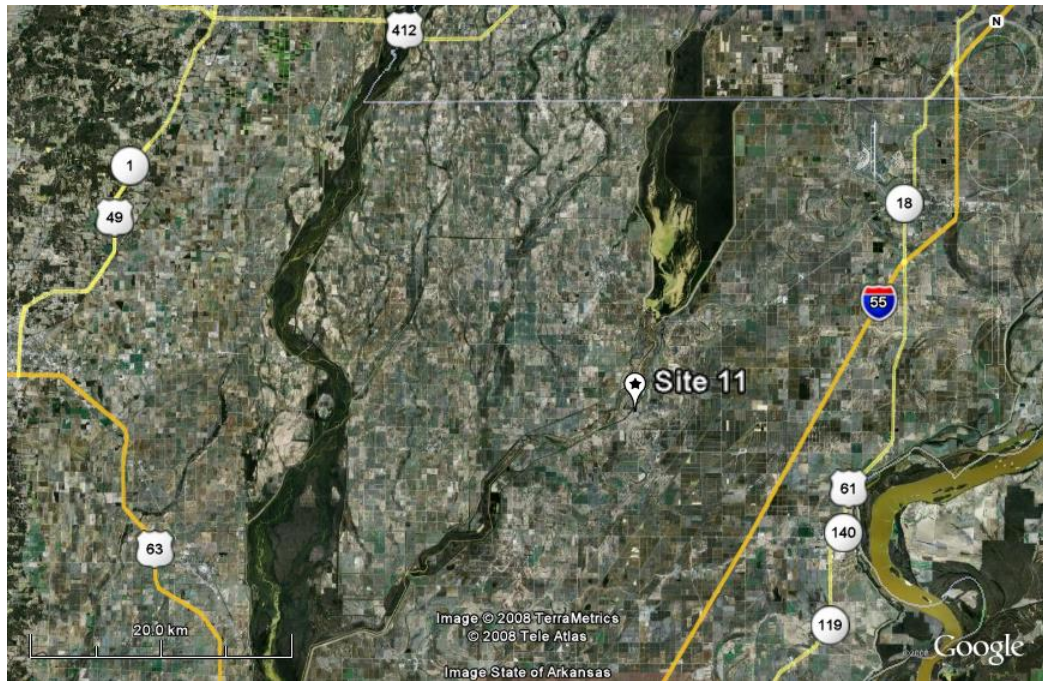


Figure 3.26 Google earth image of Site 11 and surrounding major roadways.

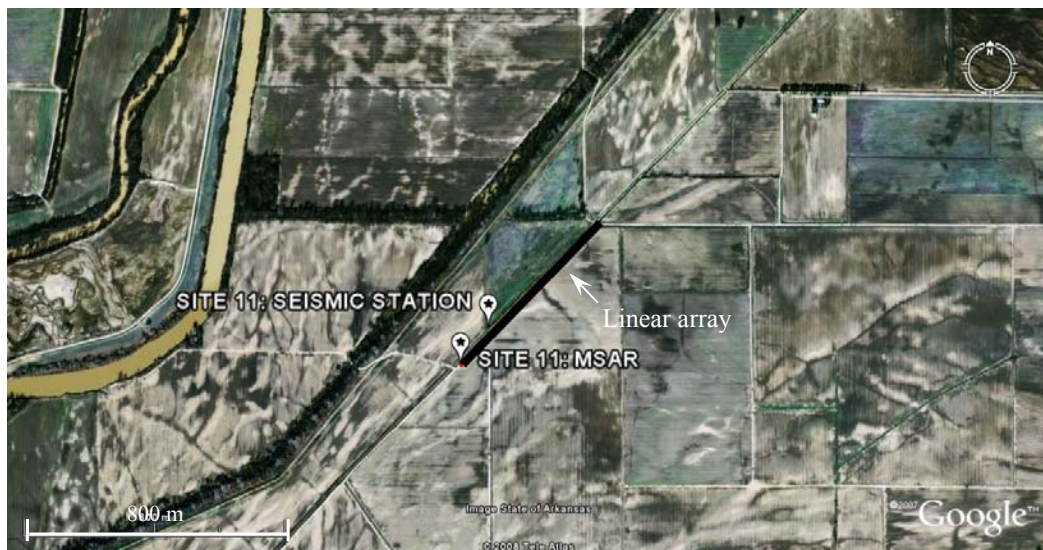


Figure 3.27 Google Earth image of Site 11 showing array location and orientation (from Bailey, 2008).

3.3 Estimated Lithology at Site Locations

At these eleven soil sites, field measurements were designed to develop experimental dispersion curves out to a maximum wavelength of about 600 m, and thus shear wave velocity (V_s) profiles to depths of about 200 to 300 m, considering the maximum exploration depth is typically 1/3 to 1/2 of maximum wavelength. This wavelength range was based on a study by Cramer et al. (2004) and the limitations of equipment and space. According to Cramer et al. (2004), the site amplification analyzed for Memphis is sensitive to uncertainties in V_s for the layers up to depths of 300 m, and most sensitive to depths of 80 m. In this sense, the V_s structures to depths of 200 to 300 m are sufficient for site response studies.

The general soil stratigraphy in the Mississippi Embayment over the depth range of this study is summarized in Table 3.2. The near-surface Quaternary deposits consist of Holocene alluvium in the lowland region (west of the Mississippi River), but Pleistocene loess and the Lafayette formation in the upland region (east of the Mississippi River). Below the surface deposits is the Jackson Formation, which is fluvial/deltaic silty sand interbedded with clayey silt and lignite. The underlying Eocene Claiborne Group is subdivided in descending order into Cockfield formation, Cook Mountain formation, and the Memphis Sand formation. The first two formations consist primarily of silts and clays. The Memphis Sand formation is composed of fluvial/deltaic sand and is part of the middle Claiborne aquifer as well as the lower Claiborne-upper Wilcox aquifer system (Parks and Carmichael, 1990). Additional soil formations are not presented in Table 3.2 because they are below the

Table 3.2 Lithology of the Mississippi Embayment sediments in the depth range of this study (modified from Van Arsdale & TenBrink, 2000 and Romero & Rix, 2001).

Unit Name	Thickness (m)	Description
Alluvium	0-57	Silty clay and sand
Loess	0-21	Silt and clayey silt
Lafayette Formation	0-33	Fine to very coarse-sand and gravel
Jackson Formation	0-121	Very Fine grained silty-sand with light gray clayey silt
Cockfield Formation		Silt and clay interbedded with medium to fine-grained sand
Cook Mtn Formation		Clay and silt
Memphis Sand	164-292	Fine to very coarse-grained sand

profiling depths of this study. However, the complete soil stratigraphy is presented in Figure 3.2. More specific soil profile information for each of the sites was provided by Prof. Roy Van Arsdale from the University of Memphis, as shown in Figure 3.28 for each of the eleven sites. The depth to the alluvial deposits and top of the upper Claiborne deposits at the eleven sites were based on geologic and geotechnical logs. In most cases, the nearest well site was within 0.5 to 1.5 km of the site location. The depth to the top of the mid-Claiborne and lower Claiborne was based on more sparsely sampled well data typically located 4 to 8 km from our sites. Therefore, the depths to the formation tops presented in this study are interpolated values for our locations. For Site 5, profile information from Gomberg et al. (2003) was used. From these profiles, it can be observed that the same formations are present at each site, but the depths and thicknesses are variable from site to site.

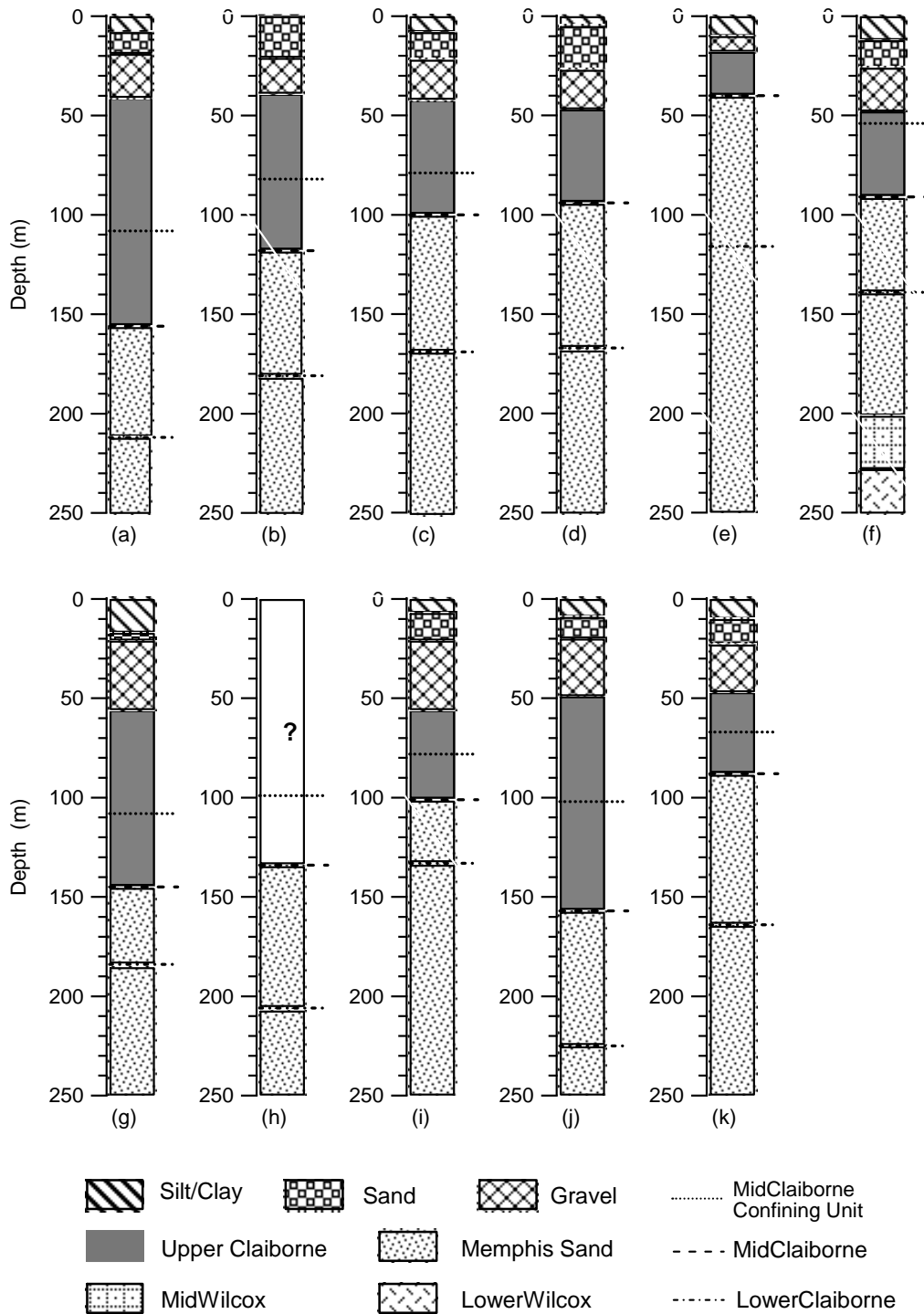


Figure 3.28 Estimated soil stratigraphy at Sites 1 through 11, presented in (a) through (k), respectively.

3.4 Field Equipment

3.4.1 Active Energy Sources

To profile to the desired depth range of this study, a unique field vibrator, designed to generate low-frequency energy, was used as the active source. This vibrator, shown in Figure 3.29a, was developed at the University of Texas at Austin as part of the NSF-funded Network for Earthquake Engineering Simulation (NEES) program (Stokoe et al., 2004a). The servo-hydraulic vibrator is capable of generating a peak force of 89 kN down to a frequency of about 1.3 Hz as shown in Figure 3.29 (b), and can operate down to frequencies of about 0.6 Hz. As compared to conventional Vibroseis equipment used in the exploration industry, this vibrator provides a much improved output at low frequencies (< 5 Hz). The improved performance at low frequencies was achieved by dramatically increasing both the weight and stroke of the reaction mass. Operating the vibrator to such low frequencies also required a redesign of the baseplate isolation system. Table 3.3 compares the characteristics of the NEES vibrator to those of a conventional Vibroseis. The vibrator has a length of 9.8 m, a width of 2.4 m, and a total weight of approximately 32,000 kg. It is transported to field sites on a tractor-trailer with a total loaded weight of over 54,000 kg.

Table 3.3 Comparison of characteristics of NEES vibrator and a conventional Vibroseis.

	NEES vibrator	Vibroseis
Reaction mass (kg)	5900	1680
Stroke (cm)	40	10
Peak force (kN)	89	155
Force at 1Hz (kN)	48	3.3
Isolation resonance (Hz)	0.3	1.5

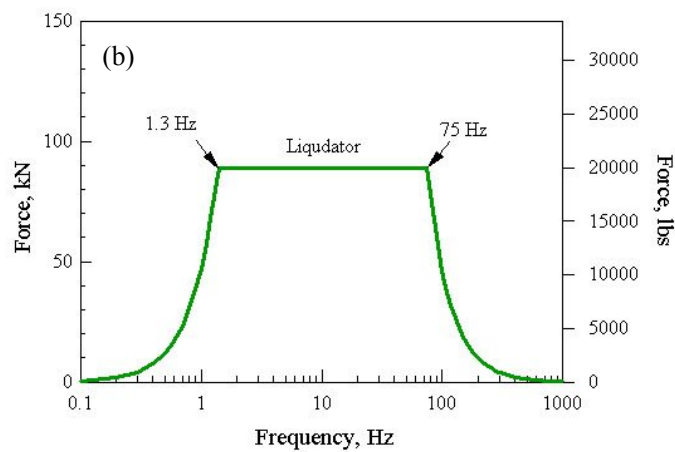


Figure 3.29 Low-frequency NEES vibrator and its theoretical force output (from: <http://nees.utexas.edu/Equipment-Liquidator.shtml>) as presented in (a) and (b).

Short arrays of about 20 m in length were used to obtain detailed V_s information in very near surface soils. For these measurements, an instrumented impact hammer (PCB Piezotronics, Inc. Model 086D50) served as the active energy source, as shown in Figure 3.30a. The hammer weighs 5.5 kg and has a sensitivity of 0.23 mV/N. From Figure 3.30b, it has been seen that this sledge is an effective source for generating relatively high-frequency Rayleigh waves (> 15 Hz).

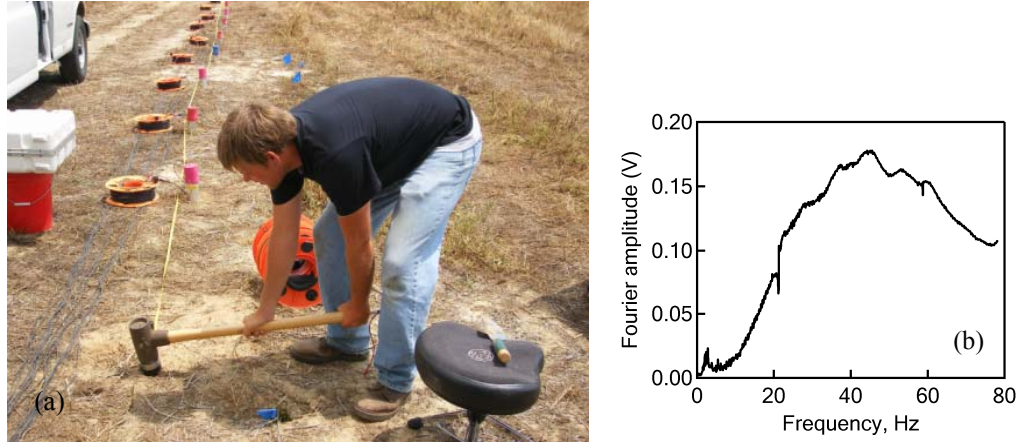


Figure 3.30 Instrumented impact hammer and its frequency content as presented in (a) and (b).

3.4.2 Data Acquisition Systems

The data acquisition system used in these measurements includes a digital signal analyzer (DSA), a laptop computer, and multiple low-frequency geophones (seismometers) as signal receivers. Different DSA were used in the 2006 and 2007 field measurements. As shown in Figure 3.31a, a DSA developed by VXI Technology, Inc., was used in 2006. This analyzer consists of a VXI CT 100C main frame with four 16-channel cards with maximum sampling rate of 50 ksamples/sec, and one 8-channel card with a sampling rate of up to 100 ksamples/sec. A Panasonic notebook (Toughbook) computer (Model: CF- 29CTPGZKM) was used to control the DSA and record the data. In 2007, a 32-channel Data Physics DSA (Figure 3.31b) with a maximum sampling rate of 100 ksamples/sec per channel was used. The same Toughbook computer was used to control the DSA and record the data.

All measurements were performed using Mark Product L-4 high-sensitivity

geophones, with a natural frequency of 1.0 Hz, a nominal sensitivity of 2.77 Volt/cm/sec, and a coil resistance of 5500 Ohms. As shown in Figure 3.32, the geophones were buried to a depth of around 15 cm and leveled with a hand level. Geophone locations were surveyed using a Nikon Model NPL-821 total station to form the receiver array in the field.

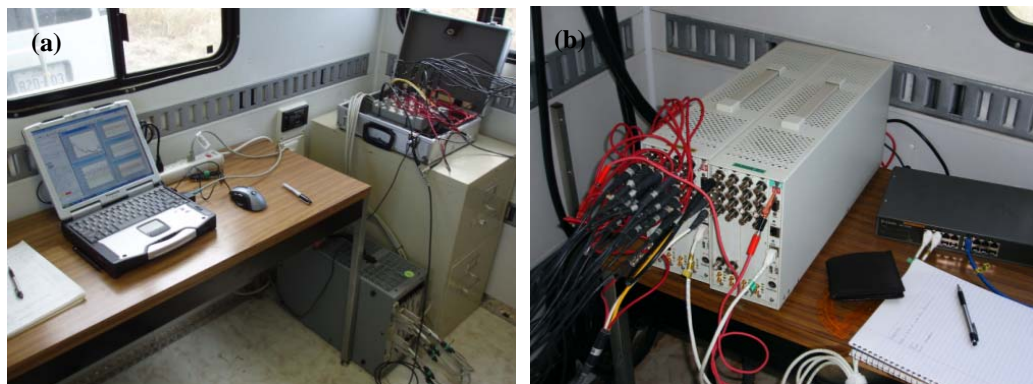


Figure 3.31 Digital signal analyzers used for field measurements: (a) VXI analyzer and (b) Data Physics analyzer.



Figure 3.32 Mark Product L-4 high-sensitivity geophone (1 Hz).

3.5 Field Testing Procedures

Field testing procedures were designed to allow for flexibility in applying different surface wave processing methods. For SASW, active $f-k$ and ReMi methods, linear arrays were used. At 8 of the 11 sites, two equally-spacing linear array configurations were used. The first array (Array 1) had a total length of about 120 to 150 m. The second array (Array 2) had a length from 280 to 450 m. At three of the sites, a single array with unequal receiver spacings was used. For passive $f-k$ measurements, three circular array configurations were used, each having a maximum diameter of 200 m. Details of the array configurations and field testing operations are summarized below.

3.5.1 SASW Testing

As described in Chapter 2, the SASW measurement typically uses a single receiver pair, which is placed with several different spacings from small to large to develop a dispersion curve. For this study, the SASW measurements were performed using selected receivers pairs from the multi-channel linear arrays. This allowed for receiver spacings of 10 to 300 m to be interpreted. Information on the configuration of the multi-channel linear arrays at each site is provided in the next section. At one site, Site 1, the traditional two-channel data collection approach was used to create the dispersion curve. During SASW measurements at Site 1, the NEES vibrator produced continuous harmonic surface waves of specific frequencies using a stepped-sine excitation. Surface waves were linearly swept through a suite of frequencies. The

array receiver spacing pairs, frequency range, and number of frequency points used at Site 1 are summarized in Table 3.4. In this table, d_1 and d_2 are near-offset and the receiver spacing, as shown in Figure 2.1.

Data were recorded in terms of frequency domain functions, such as cross-power spectra, transfer function, and coherence spectra between each receiver and the reference receiver.

Table 3.4 Summary of the measurements performed using traditional SASW testing procedures.

Site name	Test No.	Active source	d_1 (m)	d_2 (m)	Freq. range (Hz)	Number of freq.
Site 1	1	Vibrator	40	60	4-20	100
	2	Vibrator	60	100	2-15	100
	3	Vibrator	100	180	1-10	100
	4	Vibrator	180	340	0.7-5	100
	5	Vibrator	340	640	0.7-3	80
	6	Vibrator	500	1000	0.5-1.5	20

3.5.2 Active $f-k$ and ReMi Testing

The same array configurations were used for the data collection of active $f-k$ and ReMi measurements. Details on the array configurations used for the field measurements at each site are summarized in Table 3.5. At eight sites (except Site 2, Site 3 and Site 4), two arrays, with 16 receivers (at almost all sites) spaced equally, were used. The short array (denoted as Array 1) had close near-source offsets, d_1 , of 30 to 60 m and receiver spacing, d_2 , of 8 to 10 m. The long array (denoted as Array 2) generally had d_1 of 150 to 200 m and d_2 of 20 to 30 m. Two arrays with different lengths were used to cover the desired range of wavelengths with 16 receivers. Array

1 provides good measurements of wavelengths of 20 m to about 200 m, but is limited at longer wavelengths due to contamination by near-field effects. Array 2 has a larger near-source offset to reduce the near-field effects and provides good information to wavelengths up to 600 m, but can not provide data at shorter wavelengths due to spatial aliasing at wavelengths smaller than two times the minimum receiver spacing. For each site, the d_1 and d_2 values of Array 1 and Array 2 were adjusted, considering space limitations and limiting the distance from the source to the farthest

Table 3.5 Summary of linear arrays used

Site name	Array No.	Array type	d_1 (m)	d_2 (m)	Number of receivers	Array length (m)
Site 1	1	Equal- spacing	30	10	16	150
	2		180	20	16	300
Site 2	1	Unequal-spacing	35	10 for R1-R5; 30 for R5-R6; 20 for R6-R7; 40 for R7-R15; 70 for R15-R16	16	480
Site 3 Site 4	1	Unequal-spacing	30	10 for R1-R4; 20 for R4-R8; 40 for R8-R11; 80 for R11-R16;	16	630
Site 5	1	Equal- spacing	50	10	16	150
	2		200	20	15	280
	3		2	2	16	30
Site 6	1	Equal- spacing	60	8	16	120
Site 7	2		200	25	16	375
Site 11	3		5.49	1.83	12	20.13
Site 8 Site 9	1	Equal- spacing	40	8	16	120
	2		160	24	17	384
	3		5.49	1.83	12	20.13
Site 10	1	Equal- spacing	30	10	16	150
	2		150	30	16	450
	3		3.05	0.91	12	10.06

receiver of array to be around 600 m. At Site 2, Site 3 and Site 4, a single array, with 16 receivers spaced unequally, was used. The purpose of using this “unequal-spacing” array was to study its effectiveness on dispersion curve estimates. As shown in Table 3.5, the expression “10 for R1-R5” in d_2 column for Site 2 means that d_2 equals 10 m for receiver 1 to receiver 5. The d_1 and d_2 of each “unequal-spacing” array were adjusted, considering the space limitation at each site. Because of obstructions at Site 2, the linear array portion from receiver 1 to receiver 6 was rotated about 6 degrees off the array portion from receiver 6 to receiver 16. The resulting small changes in the effective receiver spacings were accounted for in the data analysis. For Site 5 to Site 11, a third array (Array 3) was used. The short array used the sledge hammer as the energy source, as shown in Table 3.5, and provide near surface (short wavelength) data.

For the active-source $f-k$ measurements, the operational procedures for the NEES vibrator were the same as mentioned in the previous section, except that it was swept over a broader range of frequencies (typically, 20 Hz to 0.7 Hz). The number of cycles (or integration time) and number of averages taken at each frequency were adjusted with typically 10 to 20 cycles and 5 to 10 averages. Data were recorded in the frequency domain for the active $f-k$ measurements. The quality of the measurement was evaluated based on the coherence value (indicative of signal-to-noise ratio). Coherence values of about 0.95 to 1.0 were measured at frequencies down to about 1 Hz at all sites.

For ReMi measurements, microtremors (ambient noise) were recorded in the

time domain at each receiver for about 20 to 30 minutes. More details on the active $f-k$ and ReMi measurements procedures are presented in Table 3.6.

Table 3.6 Summary of the measurements performed using active $f-k$ and ReMi procedures.

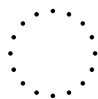
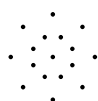
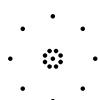
Site name	Array No.	Active $f-k$ method			ReMi	
		Active source	Freq. range (Hz)	Number of freq.	Sampling freq. (Hz)	Duration (min)
Site 1	1	Vibrator	2-50	200	320	15
		Vibrator	0.7-5	40		
	2	Vibrator	2-50	200	320	10
		Vibrator	0.7-5	40		
Site 2	1	Vibrator	0.7-40	100	320	30
Site 3	1	Vibrator	0.8-25	120	320	30
Site 4	1	Vibrator	0.7-25	120	320	30
Site 5	1	Vibrator	0.7-25	120	320	40
	2	Vibrator	0.7-25	120	320	20
	3	Hammer	0-78.125	801	--	--
Site 6	1	Vibrator	0.7-15	50	160	20
	2	Vibrator	0.65-8	40	160	25
	3	Hammer	0-100	801	--	--
Site 7	1	Vibrator	1-20	70	160	20
	2	Vibrator	0.65-8	40	160	30
	3	Hammer	0-100	801	--	--
Site 8/ Site 9	1	Vibrator	0.7-20	75	160	20
	2	Vibrator	0.7-20	75	160	25/20
	3	Hammer	0-100	801	--	--
Site 10	1	Vibrator	0.6-20	100	160	20
	2	Vibrator	0.6-20	100	160	25
	3	Hammer	0-100	801	--	--
Site 11	1	Vibrator	1-15	50	160	20
	2	Vibrator	0.65-8	40	160	30
	3	Hammer	0-100	801	--	--

3.5.3 Passive $f-k$ Testing

Passive $f-k$ measurements were performed using a circular receiver array at five of the eleven sites. The other sites did not have sufficient space or access to

deploy the large circular array. At 3 of the 5 sites, a 16-receiver circular array with a diameter of 200 m was used. The 16 receivers were placed at equal intervals around the perimeter of the circle. For the other sites, an array configuration consisting of two 8-sensor circular arrays and one receiver at the center, was used. The diameter of the outer array was also 200 m, and the diameter of the inner array was 50 m or 20 m. The details of the circular array configurations are presented in Table 3.7. Only circular arrays were used because they have been shown to provide the good results under most circumstances, and they have equal spatial resolution in all directions, which is favorable for detecting multiple passive energy sources (Zywicki, 1999). According to Tokimatsu (1997), the longest wavelength that can be resolved in passive $f-k$ measurements is three times the maximum array aperture. Therefore, a maximum diameter of 200 m was selected to obtain the desired objective of a maximum wavelength of 600 m. The circular arrays were located adjacent to or overlapping with the linear arrays, as show in Figures 3.7, 3.11, 3.15, 3.23 and 3.25.

Table 3.7 Description of the three circular arrays.

Array name	Array Shape	Number of receivers	Array geometry
A		16	16-sensor circular array with a radius of 100m
B		17	Consists of two 8-sensor circular arrays and one sensor at the center. The radii of outer and inner circular arrays are 100m and 50m.
C		17	Consists of two 8-sensor circular arrays and one sensor at the center. The radii of outer and inner circular arrays are 100m and 20m.

Ambient noise was recorded in the time domain for 30 to 45 minutes at each receiver.

Details of the passive f - k data collection procedures are presented in Table 3.8.

Table 3.8 Summary of data collection using passive f - k procedure.

Site name	Array used	Sampling freq. (Hz)	Duration (min)
Site 1	A	320	30
Site 3	A	320	60
Site 5	A	320	40
Site 9	B	81.92	45
	C	81.92	45
Site 10	B	81.92	40

CHAPTER 4

DATA PROCESSING PROCEDURES

4.1 Introduction

One of the critical aspects of surface wave measurements is the development of a reliable dispersion curve from the data collected in the field. In this chapter, data processing procedures for the four surface wave methods used in this study are presented in detail. These four methods are: (1) the SASW method, (2) the active f - k method, (3) the passive f - k method, and (4) the ReMi method. These methods differ with regard to array configurations, energy sources, data collection approaches as well as data processing steps.

4.2 Data Processing of SASW Measurements

SASW data were collected in the form of cross-power spectra and coherence functions in the field, as discussed in Section 3.5.1. Development of the experimental dispersion curves was performed using the program WinSASW2, developed at the University of Texas at Austin (Joh, 1996). An example of a wrapped phase spectrum and coherence function recorded between two receivers with a receiver spacing of 300 m at Site 1 is presented in Figure 4.1. In the phase plot a typical “sawtooth” pattern is observed. The coherence function shows coherence values of near one at frequencies down to less than 1 Hz, indicating high signal-to-noise ratios at low frequencies. Data with low coherence and data in the near-field (shaded portion in Figure 4.1) are not

included in the phase analysis. The wrapped phase angle represents the relative lead or lag (± 180 degrees) between the two receivers, with each jump in the “sawtooth” pattern representing 360 degrees of phase. The cumulative phase shift between two receivers is determined by manually unwrapping the phase plot by identifying 360 degrees jumps in phase, as shown in Figure 4.2.

For each frequency f , the phase velocity V_R is calculated from the unwrapped phase shift, ϕ , and receiver spacing, d , using:

$$V_R = f \cdot \lambda_R = f \cdot \frac{360}{\phi} \cdot d, \quad (4.1)$$

in which, λ_R , denotes the wavelength. To minimize near-field effects, the following criterion is imposed on the dispersion data:

$$\lambda_R < 2 \cdot d. \quad (4.2)$$

All lower-frequency (long wavelength) data not meeting this criterion are eliminated from the dispersion curve (Stokoe et al, 1994).

This process was repeated for all receiver pairs at each site, yielding a composite experimental dispersion curve for this study that covers a wavelength range from less than 1 m to 600 m for this study, as shown in Figure 4.3. Receiver pairs used at each site for developing the SASW dispersion curves are listed in Table 4.1. In the table, d_1 and d_2 are the distance from source to the closest receiver and the spacing between two receivers, respectively. It should be noted that the phase velocity obtained from this procedure does not necessarily represent the fundamental mode of propagation but is instead an “effective” velocity with contribution (potentially) from higher surface wave modes, and body waves.

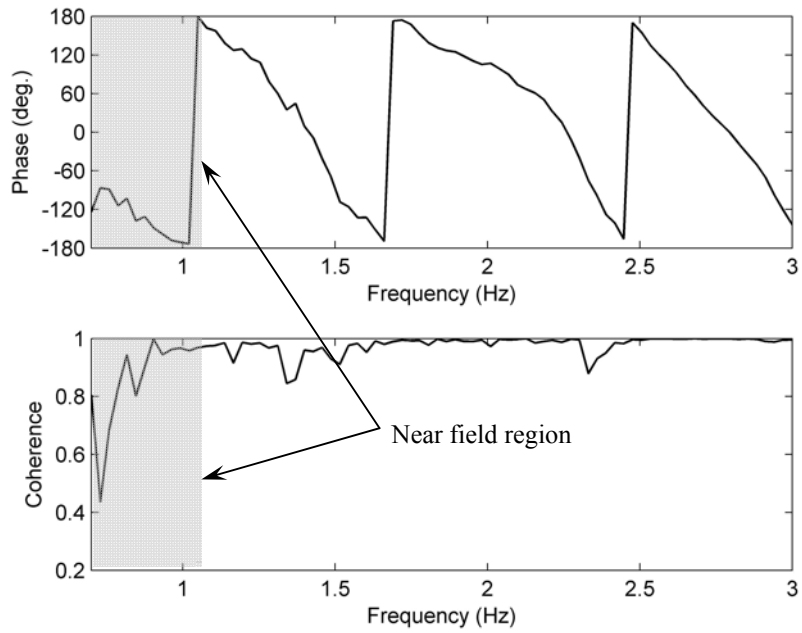


Figure 4.1 Cross-power spectrum and coherence function from 300-m spacing at Site 1 with masking (shaded) of near-field region shown.

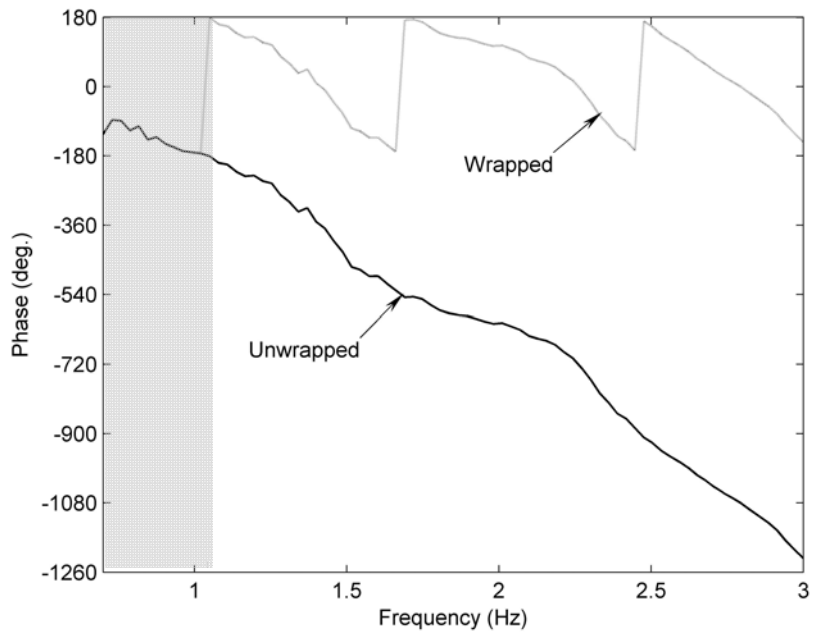


Figure 4.2 Unwrapping of cross-power spectrum shown in Figure 4.1.

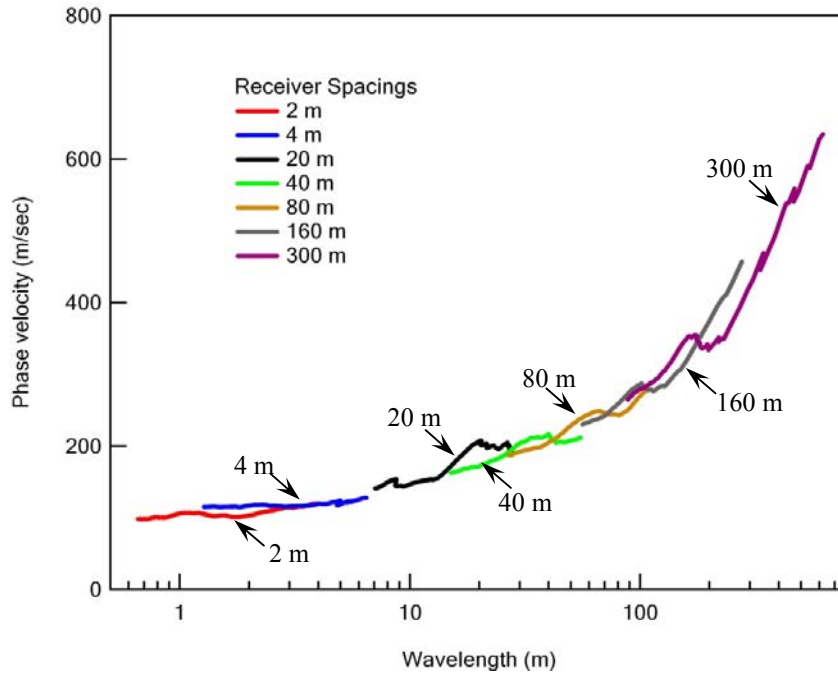


Figure 4.3 Composite dispersion curve for Site 1 presented in terms of phase velocity versus wavelength.

Table 4.1 Receiver pair spacings used for SASW analyses at 11 testing sites.

Site 1		Site 2		Site 3		Site 4		Site 5	
d_1 (m)	d_2 (m)	d_1 (m)	d_2 (m)	d_1 (m)	d_2 (m)	d_1 (m)	d_2 (m)	d_1 (m)	d_2 (m)
2	2	55	20	3	3	3	3	8	8
4	4	105	60	40	10	40	40	50	40
40	20	205	80	40	20	100	80	100	50
60	40	105	100	40	40	220	200	100	80
100	80	105	140	220	200	340	320	50	120
180	160	285	160	340	320			340	310
340	300	285	230						

Site 6		Site 7		Site 8		Site 9		Site 10		Site 11	
d_1 (m)	d_2 (m)	d_1 (m)	d_2 (m)	d_1 (m)	d_2 (m)	d_1 (m)	d_2 (m)	d_1 (m)	d_2 (m)	d_1 (m)	d_2 (m)
5.49	3.65	5.49	1.83	5.49	1.83	5.49	1.83	3.048	3.352	5.49	3.65
10.98	10.97	10.98	10.97	5.49	3.65	5.49	3.65	6.44	6.44	16.46	9.2
60	56	60	56	16.46	9.2	10.98	10.97	30	30	60	56
76	72	76	72	40	40	40	40	60	60	76	72
100	80	100	80	80	80	64	64	150	150	100	80
200	200	200	200	160	144	80	80	300	300	200	200
250	250	250	250	208	192	208	192	3.048	3.352	250	250
300	300	300	300	280	264	280	264			300	300

4.3 Data Processing of Active f - k Measurements

Field measurement procedures and array information for the active-source f - k measurements are described in Section 3.5.2. MATLAB algorithms were developed to perform the f - k analysis of the active-source measurements based on procedures described in Zywicki (1999). Step-by-step procedures included in the analyses are specified in the following sections.

4.3.1 Spatospectral Correlation Matrix

4.3.1.1 Computation of Spatospectral Correlation Matrix

The first step in the f - k analysis is to compute the spatospectral correlation matrix $\mathbf{R}(f)$ over the range of interested frequencies. In this matrix, the main diagonal elements are the auto-power spectral densities for each sensor in the array and the off-diagonal elements are the cross-power-spectra (CPS) between every combination of receiver pairs. As mentioned in Section 3.5.2, the data were recorded in the frequency domain for the active f - k measurements. Namely, the averaged auto-power spectrum at each receiver, and the cross-power spectrum between each receiver and the reference source signal were directly collected at each frequency. The auto- and cross-power spectrum are related by:

$$\frac{R_{i,j}(f)}{R_{i,i}(f)} = \frac{S_i^*(f) \cdot S_j(f)}{S_i^*(f) \cdot S_i(f)} = \frac{S_j(f)}{S_i(f)} = \frac{S_r^*(f) \cdot S_j(f)}{S_r^*(f) \cdot S_i(f)} = \frac{R_{r,j}(f)}{R_{r,i}(f)}, \quad (4.3)$$

where, the subscripts r, i, j denotes the reference, i th and j th sensor; $R_{i,i}(f)$ denotes the auto-power spectrum at i th sensor; $R_{i,j}(f)$ denotes the cross-power spectrum between the i th and j th sensor; $S_i(f), S_j(f), S_r(f)$ are the Fourier

spectrum of i th, j th and reference sensors, respectively. From Equation 4.3, $R_{i,j}(f)$ can be determined from:

$$R_{i,j}(f) = \frac{R_{r,j}(f)}{R_{r,i}(f)} \cdot R_{i,i}(f), \quad (4.4)$$

where, as mentioned above, $R_{r,i}(f)$, $R_{r,j}(f)$ and $R_{i,i}(f)$ are recorded data.

4.3.1.2 Modification of Spatospectral Correlation Matrix due to Geophone Calibration

In the field measurements, the geophones deployed in the array will exhibit variability in their amplitude and phase response, particularly near their resonant frequency. To account for the variable receiver response, all geophones used in the field measurements were calibrated in the laboratory at the University of Texas at Austin. This calibration showed that two older geophones used in the 2006 study had obvious and significant phase difference relative to the other geophones, especially at low frequencies. During the f - k analysis, this receiver response was accounted for by modifying the spatospectral correlation matrix, $\mathbf{R}(f)$, as:

$$[\mathbf{R}(f)]_{\text{after calibration}} = \mathbf{W}[\mathbf{R}(f)]_{\text{before calibration}} \mathbf{W}^H, \quad (4.5)$$

and

$$\mathbf{W} = \text{diag}[\exp(-j\phi_{R1}), \exp(-j\phi_{R2}) \cdots \exp(-j\phi_{Ri})], \quad i = 1, 2 \cdots N, \quad (4.6)$$

where, $[\mathbf{R}(f)]_{\text{before calibration}}$, can be calculated as above, ϕ_{Ri} denotes the phase difference from a chosen reference geophone and i th geophone, N is the total number geophones used, and H indicates Hermitian transpose. As an example, Figure 4.4 compares the steered responses from calibrated and un-calibrated data at a frequency of 1.35 Hz using Array 2 at Site 1. This array had two older geophones as the first two

receivers in the array during the field testing. From this figure, it can be seen that a large shift in the peak wavenumber is observed when geophone calibration is applied. This was primarily due to the effect of two older geophones. In the 2007, these older geophones were replaced with geophones with better phase matching the other geophones. The differences in the 2007 study were much smaller, but corrections to account for geophone response were still applied in the analyses.

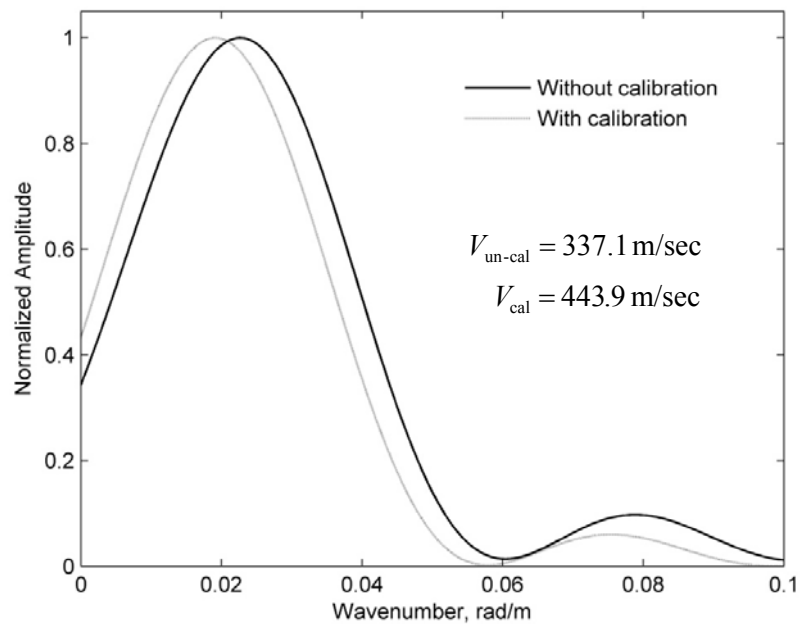


Figure 4.4 Steered response power estimated with and without geophone calibration at a frequency of 1.35 Hz for Site 1, Array 2.

4.3.1.3 Normalization of Spatospectral Correlation Matrix

Due to the effect of geometric spreading, the contribution of sensors at larger offsets will be weighted less than sensors near the source if the spatospectral correlation matrix, $\mathbf{R}(f)$, is not normalized. As discussed by Zywicki (1999), two normalization techniques can be used: 1) dividing each element in $\mathbf{R}(f)$ by its magnitude so that all the elements have a magnitude of one such that each will be

weighted equally, or 2) multiplying the amplitude of recorded wave at each sensor by the square root of the distance of the sensor from the source to account for geometric spreading. In Figure 4.5, the effects of two normalization techniques on the steered power estimates are compared. It can be seen that the peak locations are nearly the same using these two techniques. Compared to the second technique, however, the first one tends to yield peaks with narrower width and smaller sidelobes. Therefore, The first normalization technique has been used in this study.

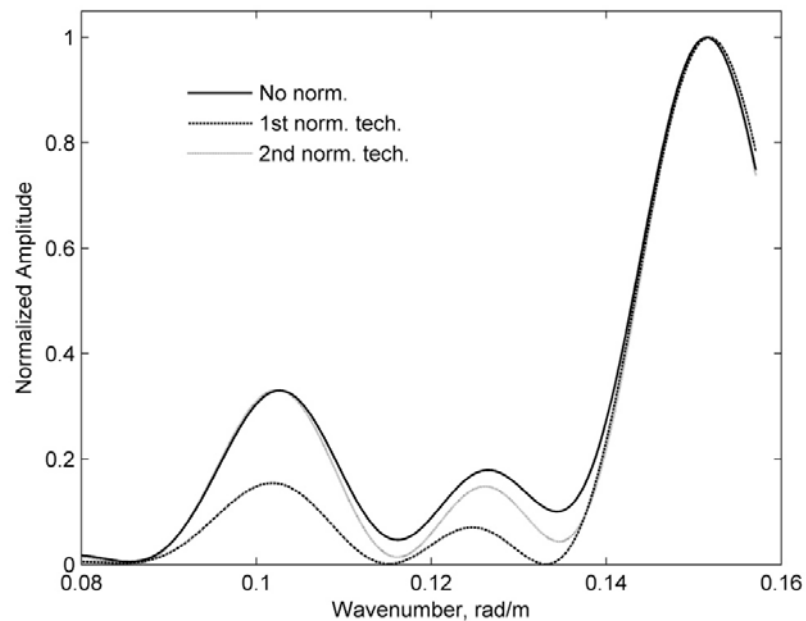


Figure 4.5 Steered response powers estimated with different normalization techniques at 5.03Hz for Site 1, Array 2.

4.3.2 Formation of Steering Vector

Obtaining the array output power in the frequency-wavenumber domain requires the development of an algorithm to steer the array toward many directions with a steering vector containing the phase shift information. With an active energy

source, the direction of wave propagation is known, so the f - k analysis here is one dimensional. The corresponding steering vector can be expressed as:

$$\mathbf{e}(k) = [\exp(-jk \cdot x_1), \exp(-jk \cdot x_2), \dots, \exp(-jk \cdot x_N)]^T, \quad (4.7)$$

where, $\mathbf{e}(k)$, is the steering vector associated with a trial wavenumber, k , and x_i is the distance of the i th receiver from the energy source.

In order to reduce near-field effects due to non-planar wavefronts, Zywicki (1999) proposed the use a cylindrical steering vector as:

$$\mathbf{h}(k) = \exp\{-j[\phi(H_0(k \cdot x_1)) \phi(H_0(k \cdot x_2)) \dots \phi(H_0(k \cdot x_N))]\}^T, \quad (4.8)$$

where, ϕ denotes the phase angle of the argument in parentheses, H_0 denotes the Hankel function, and $\mathbf{h}(k)$ denotes the Hankel function steering vector of a function of k . The effectiveness of cylindrical beamforming on mitigation of near-field effects will be discussed in Section 5.5 of Chapter 5.

During the analysis, a vector of trial wavenumbers is searched, with each wavenumber in this vector representing an assumed velocity of wave propagation. Each trial wavenumber is used in Equation 4.7 to form a steering vector to calculate the array output power, as discussed in the next section. In basic terms, this procedure is simply shifting and summing the power output for different assumed velocities (k for a given frequency). For this study the vector of trial wavenumbers was:

$$\left[\overbrace{0, 0.02}^{N_1} \overbrace{0.02, k_{alias}}^{N_2} \right], \quad (4.9)$$

where, N_1 , N_2 are the numbers of trial wavenumbers (64 and 1048, respectively).

The range $[0, 0.02]$ corresponds to wavelengths longer than 314 m. This range is

subdivided into N_1 points in order to reach sufficient precision for distinguishing wave propagation with low wavenumbers. The k_{alias} is the array aliasing limit, which is related to the minimum receiver spacing, D_{min} , as:

$$k_{alias} = \frac{2\pi}{\lambda_{min}} = \frac{\pi}{D_{min}}. \quad (4.10)$$

As seen from Equation 4.10, the smallest wavelength that can be detected by one array equals twice the minimum receiver spacing.

4.3.3 Beamforming

Beamforming is the name given to a wide variety of array processing algorithms that determine the array's signal-capturing abilities in a particular signal transmission direction (Johnson and Dudgeon, 1993). The outcome of beamforming is the steered response power of the array. The widely-used conventional frequency domain beamformer (FDBF) calculates the power as:

$$\mathbf{P}_{FDBF}(k, f) = \mathbf{e}^H(k) \mathbf{R}(f) \mathbf{e}(k). \quad (4.11)$$

The $\mathbf{e}(k)$ term can be replaced by $\mathbf{h}(k)$ in Equation 4.9 to perform the cylindrical beamformer analysis (Zywicki, 1999).

The beamforming procedure results in a steered power spectrum for each $f-k$ pair. Figure 4.6 presents a contour plot of array power for $f-k$ pairs determined using Array 1 at Site 7. At each frequency, the empty circle denotes the location of the peak in the power plot. Cross-sections of this power plot at frequencies equal to 4.01 Hz and 6.19 Hz are displayed in Figure 4.7. In each $f-k$ spectrum plot, the dominant peak corresponds to the wavenumber of the propagating wave for each

frequency. Secondary peaks may represent other Rayleigh modes, sidelobes from the array pattern, or superposition of sidelobes.

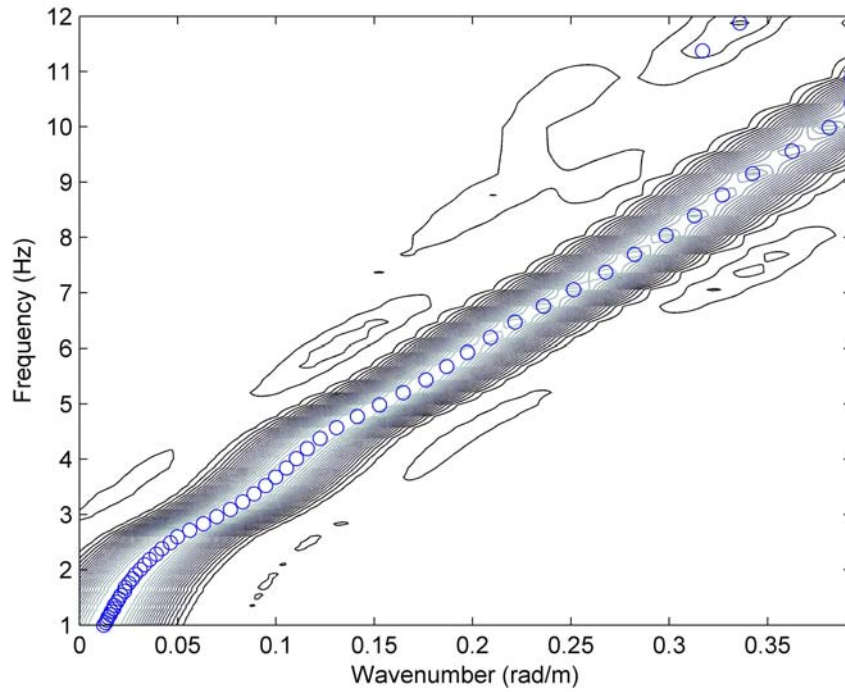


Figure 4.6 Contour plot of steered power spectrum in terms of frequency and wavenumber for Array 1, Site 7.

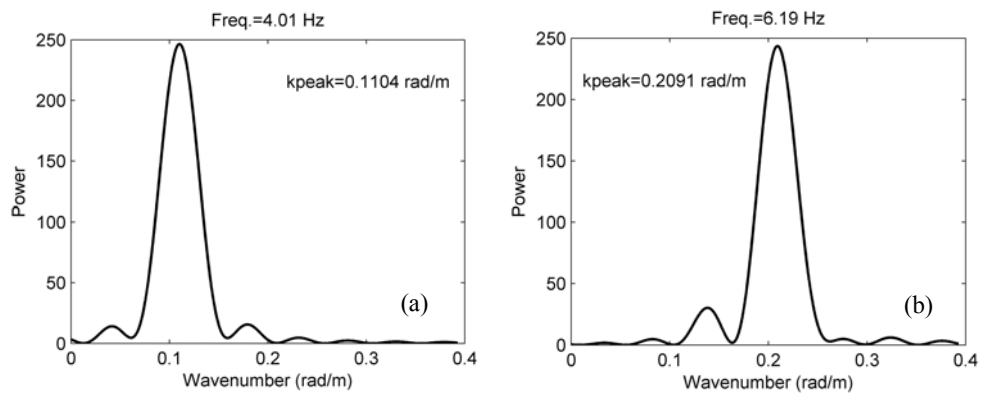


Figure 4.7 Spectral power spectrum estimates at (a) 4.01 Hz and (b) 6.19 Hz.

4.3.4 Interpretation of Dispersion Curves from Active f - k Measurements

The wavenumber, k , of the dominant propagating wave energy with frequency, f , is indicated by the peak in the power plot. The phase velocity, V_R , can be calculated from:

$$V_R = \lambda_R \cdot f = \frac{2\pi f}{k}. \quad (4.12)$$

The resulting dispersion curve, using the data shown in Figure 4.6 and calculated from Equation 4.12, is shown in Figure 4.8. Final dispersion curves used in the inversion analysis are developed by excluding the dispersion curve points influenced by near-field effects at low frequencies and the aliased points at high frequencies.

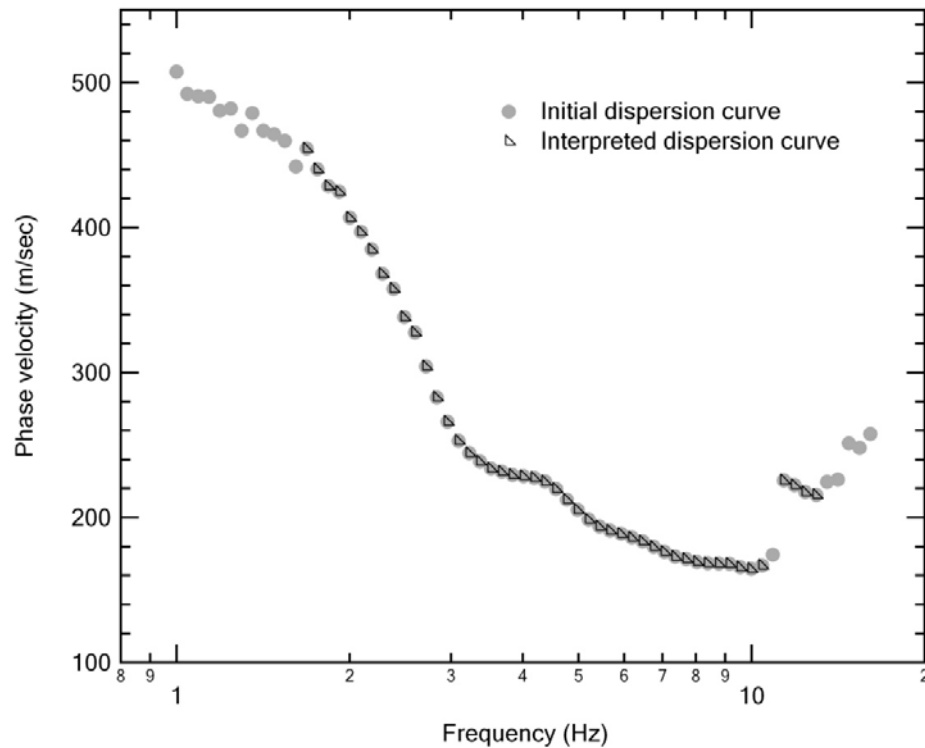


Figure 4.8 Dispersion curve estimated from f - k analysis for Array 1, Site 7

In this study, all comparisons are made out to a longest wavelength of 600 m. Although it may be possible to attain reliable dispersion velocities at larger wavelengths, this was considered a reasonable limit based on the source offset and array configuration used.

4.4 Data Processing of Passive f - k Measurements

Field procedures and array information for passive f - k measurements are described in Section 3.5.3. MATLAB algorithms were developed to process the ambient data collected at the five sites where sufficient space was available to deploy the circular array. Step-by-step procedures performed in the passive f - k analysis are described in the following sections.

4.4.1 Spatospectral Correlation Matrix

As mentioned in Section 3.5.3, data were recorded in the time domain for the passive f - k measurements. Each receiver recorded the signal as a time history, $x(n)$, with M sampling points ($n=0$ to $M-1$). In this case, the spatospectral correlation matrix, $\mathbf{R}(f)$, is estimated using the method of Barlett power spectral estimation as (Zywicki, 1999):

$$R_{i,j}(f) = \frac{1}{B} \sum_{n=1}^B S_{i,n}(f) S_{j,n}^H(f), \quad (4.13)$$

where, B is the number of blocks that $x(n)$ is divided into (with each block having L sampling points), $R_{i,j}(f)$ is cross-power spectrum between the i th and j th sensor,

$S_{i,n}(f)$ denotes Fourier spectra of the i th sensor's data in the n th block, and H indicates complex conjugation. The averaging of the cross-power spectra of all blocks is performed to reduce the variance of $\mathbf{R}(f)$ estimate.

The original field measurements which were sampled as shown in Table 3.7 were re-sampled using a lower sampling frequency, as shown in Table 4.2. The block length (in terms of sampling points) is set to a power of 2, which is favorable for FFT computations. Different block lengths of 1024, 2048 and 4096 were applied in the f - k analyses with results showing consistent dispersion curve estimates. Considering the computation time and the need for a sufficient number of dispersion curve points, a block length of 2048 was selected for the analyses presented in this study. With a block length of 2048 points, the block duration is 64.0 sec for Site 1, Site 3 and Site 5, and 75.0 sec for Site 9 and Site 10. These values are consistent with the duration ranges suggested and used by other researchers for ambient vibration processing (Tokimastu, 1995; Liu et al., 2000).

Table 4.2 Parameters for calculation of $\mathbf{R}(f)$ at five sites.

Site Name	Re-sampling frequency	Duration after re-sampling	Block length L	Block number B
Site 1	32 (Hz) 0.03125 (sec)	1784 (sec)	2048 (points) 64.0 (sec)	27
Site 3	32 (Hz) 0.03125 (sec)	3584 (sec)	2048 (points) 64.0 (sec)	56
Site 5	32 (Hz) 0.03125 (sec)	2392 (sec)	2048 (points) 64.0 (sec)	37
Site 9	27.30 (Hz) 0.03662 (sec)	2700 (sec)	2048 (points) 75.0 (sec)	36
Site 10	27.30 (Hz) 0.03662 (sec)	2700 (sec)	2048 (points) 75.0 (sec)	36

4.4.2 Formation of Steering Vector

Since the location of the surface wave energy source remains unknown in passive measurements, the wavenumber search procedure is performed using wavenumber pairs $\mathbf{k} = (k_x, k_y)$, where k_x, k_y are trial wavenumber in the x and y directions. The corresponding steering vector can be expressed as:

$$\mathbf{e}(\mathbf{k}) = [\exp(-j\mathbf{k} \cdot \mathbf{x}_1), \exp(-j\mathbf{k} \cdot \mathbf{x}_2), \dots, \exp(-j\mathbf{k} \cdot \mathbf{x}_N)]^T, \quad (4.14)$$

where, \mathbf{x}_n is receiver location vector for $n=1, 2, \dots, N$. The \mathbf{k} and \mathbf{x}_n vectors are defined relative to a specified $x-y$ coordinate system. In this study, the center of the circular array is chosen as the origin of this coordinate system. The y -axis points from the origin to the first receiver recorded in the field measurements. The coordinate system used for Array A (described in Table 3.7) is plotted along with the NS-EW directions in Figure 4.9.

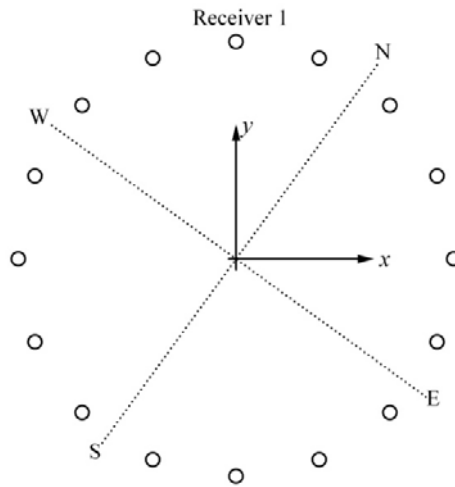


Figure 4.9 Coordinate system used for Array A along with NS-EW directions.

Two vectors of trial wavenumbers are needed for passive $f-k$ analysis, one for each direction (x and y direction). Each (k_x, k_y) pair represents an assumed velocity

and direction of energy propagation. In this study, the trial wavenumber vectors are given as below:

$$\left[\overbrace{-k_{alias}, -0.02}^{N_1} \overbrace{-0.02, 0.02}^{N_2} \overbrace{0.02, k_{alias}}^{N_1} \right], \quad (4.15)$$

where, N_1 , N_2 are 128 and 100 and denote the numbers of trial wavenumbers in the interval. The range $[-0.02, 0.02]$ corresponds to wavelengths longer than 314 m. This range is subdivided by N_2 in order to obtain sufficient precision on distinguishing wave propagation with low wavenumbers. The aliasing limit of the array, k_{alias} , is computed using Equation 4.10. For circular arrays used in this study, the aliasing limits, k_{alias} , are listed in Table 4.3.

Table 4.3 Aliasing limits of circular arrays used for ambient noise measurements

Array name	Minimum spacing, D_{\min} (m)	Aliasing limit, k_{alias} (rad/m)
Array A	7.61	0.4125
Array B	14.64	0.2145
Array C	5.85	0.5360

4.4.3 Beamforming

Passive f - k measurements have the additional complication of the possibility of a wavefield with multiple sources. This is not a problem for active-source measurements where the wavefield is dominated by a single source with a known location. In passive measurements, the presence of multiple sources can be problematic for dispersion curve determination in some cases. Therefore, besides the conventional FDBF beamforming approach used in the active-source analyses, two

high-resolution beamforming approaches, the Minimum Variance Beamforming (MVBF) method and Multiple Signal Classification (MUSIC) method, were also applied for the passive measurements to provide better wavenumber resolution for identifying multiple energy sources. These methods are described below.

4.4.3.1 Conventional FDBF Method

For passive f - k analysis, the conventional FDBF gives a similar equation to the linear-array active-source case (Equation 4.11) for output power estimates, except that the single wavenumber, k , is replaced by a wavenumber pair $\mathbf{k} = (k_x, k_y)$. The resulting equation is:

$$\mathbf{P}_{\text{FDBF}}(\mathbf{k}, f) = \mathbf{e}^H(\mathbf{k})\mathbf{R}(f)\mathbf{e}(\mathbf{k}). \quad (4.16)$$

An example of the FDBF f - k power spectrum estimate at a frequency of 1.5 Hz for Site 1 is presented in Figure 4.10. A single dominant peak is located at $(k_x = -0.018 \text{ rad/m}, k_y = -0.010 \text{ rad/m})$ with a wavenumber magnitude of 0.0206 rad/m. This magnitude along with the frequency is used to calculate the wave velocity, which is discussed in the next section. Smaller peaks around the main peak in Figure 4.10 are sidelobes resulting from the finite dimensions of the array.

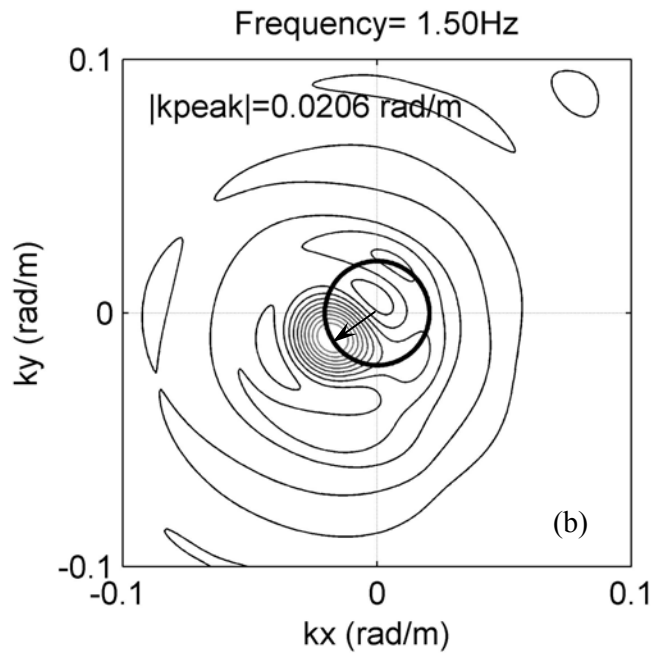
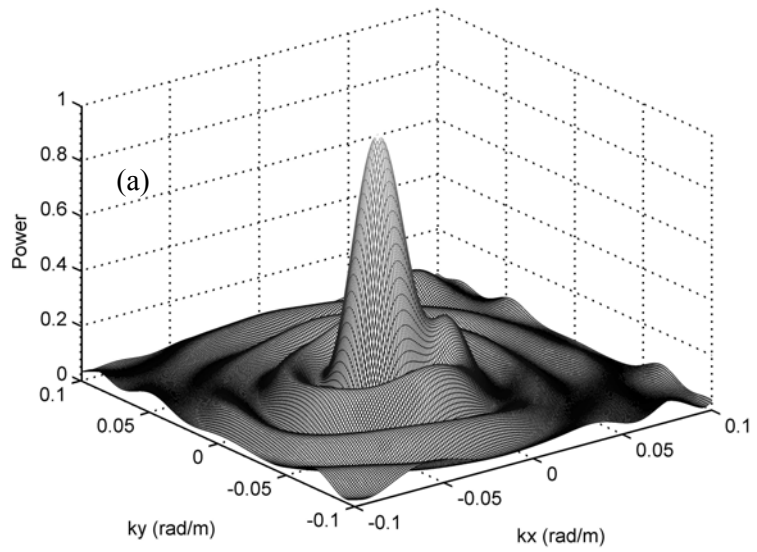


Figure 4.10 FDBF power spectrum estimate at 1.5 Hz for Site 1 shown in (a) 3-D mesh plot and (b) 2-D contour plot.

4.4.3.2 Multiple Signal Classification (MUSIC) Method

MUSIC is a high-resolution f - k method introduced by Schmidt (1986) based

on a truncated decomposition of the inverse spatio-spectral correlation matrix $\mathbf{R}^{-1}(f)$. $\mathbf{R}^{-1}(f)$ can be decomposed in terms of eigenvectors and eigenvalues as:

$$\mathbf{R}^{-1}(f) = \sum_{i=1}^N \lambda_i^{-1}(f) \mathbf{v}_i(f) \mathbf{v}_i^H(f), \quad (4.17)$$

where, $\lambda_i(f)$ and $\mathbf{v}_i(f)$ are the i th eigenvalue and eigenvector of $\mathbf{R}(f)$.

Grouping the eigenvectors into signal and noise subspaces, Equation 4.17 can be rewritten as:

$$\mathbf{R}^{-1}(f) = \sum_{i=1}^{N_s} \lambda_i^{-1}(f) \mathbf{v}_i(f) \mathbf{v}_i^H(f) + \sum_{i=N_s+1}^N \lambda_i^{-1}(f) \mathbf{v}_i(f) \mathbf{v}_i^H(f), \quad (4.18)$$

in which N_s is the number of eigenvectors related to the signal subspace. The largest N_s eigenvalues define a signal subspace. MUSIC is an approach using only the noise subspace truncated eigen-expansion in Equation 4.18 with all eigenvectors weighted equally instead of by their corresponding eigenvalues, namely:

$$\mathbf{R}_{\text{MUSIC}}^{-1}(f) = \sum_{i=N_s+1}^N \mathbf{v}_i(f) \mathbf{v}_i^H(f). \quad (4.19)$$

The output power can then be estimated from:

$$\mathbf{P}_{\text{MUSIC}}(\mathbf{k}, f) = \frac{1}{\mathbf{e}^H(\mathbf{k}) \mathbf{R}_{\text{MUSIC}}^{-1}(f) \mathbf{e}(\mathbf{k})}. \quad (4.20)$$

In Figure 4.11, the MUSIC f - k power spectrum estimate at a frequency of 1.5 Hz for Site 1 and noise subspace dimension set as 15 ($N_s = 1$) is presented. From this figure, it can be seen that the signal peak estimated from MUSIC is at nearly the same wavenumbers but is much narrower than that obtained using from FDBF, and the background level is much smoother. This demonstrates the much improved resolution and sidelobe control achieved with the MUSIC method. With one signal

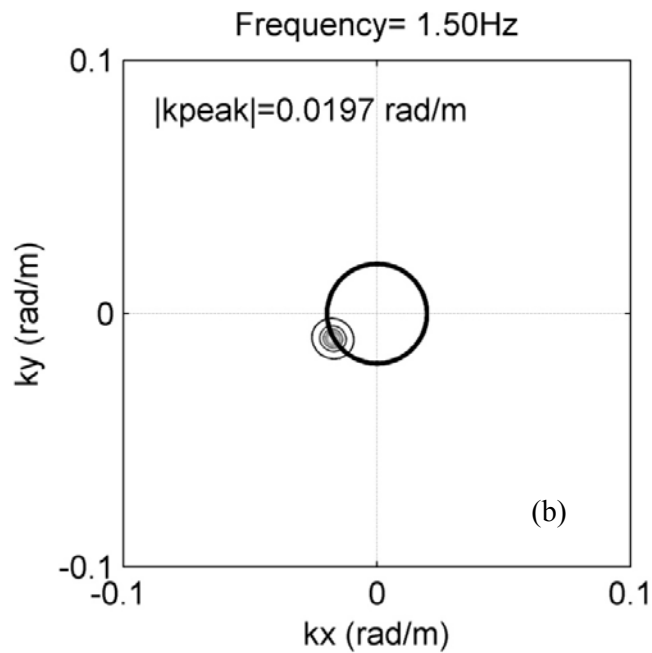
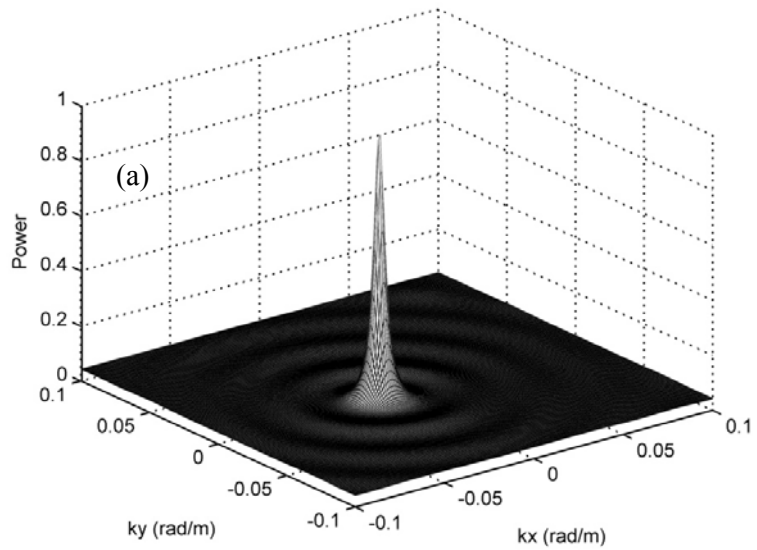


Figure 4.11 MUSIC power spectrum estimate at 1.5 Hz for Site 1 with a noise subspace dimension of 15, shown in (a) 3-D mesh plot and (b) 2-D contour plot.

assumed here, the peaks related to other signals are suppressed. Using noise subspace dimension equal to 12 ($N_s = 4$), the MUSIC estimate was repeated, as shown in Figure 4.12. Besides the peak related to the dominant energy signal, a

second peak with lower energy is also detected.

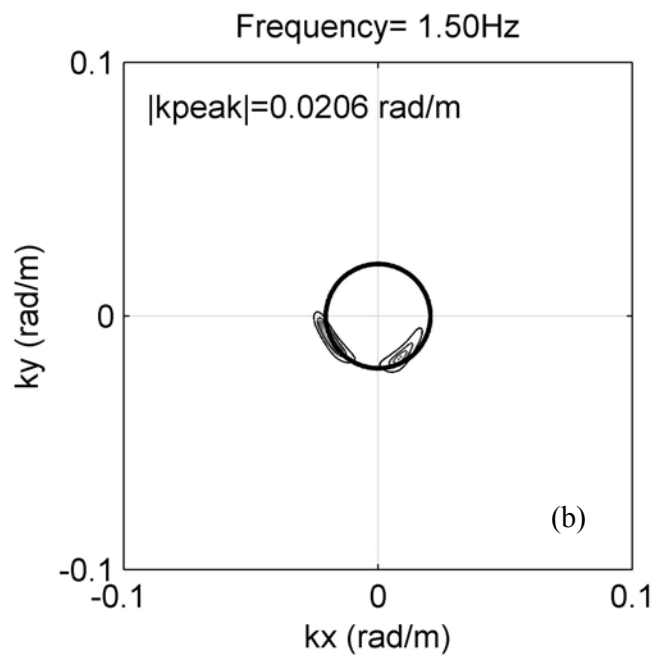
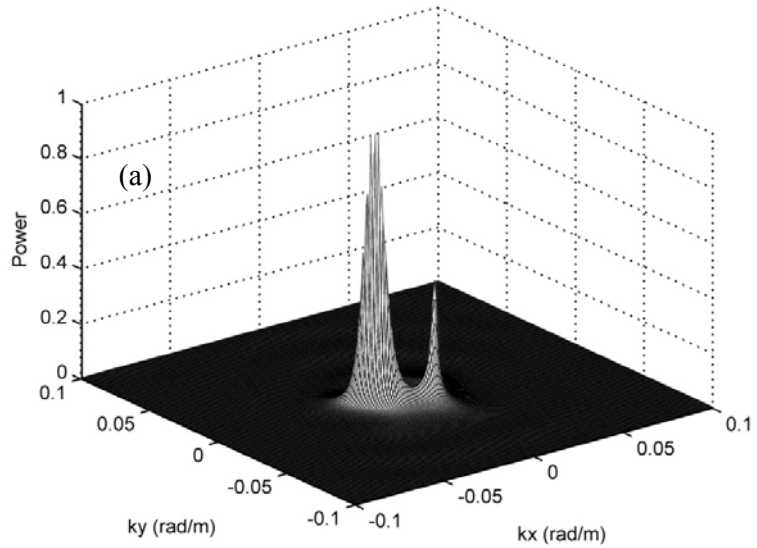


Figure 4.12 MUSIC power spectrum estimate at 1.5 Hz for Site 1 with a noise subspace dimension of 12, shown in (a) 3-D mesh plot and (b) 2-D contour plot.

4.4.3.3 Minimum Variance Beamforming (MVBF) Method

The MVBF method, often referred to as Capon's method, is a high-resolution f - k method introduced by Capon (1969). The output power of Capon's method is:

$$\mathbf{P}_{\text{Capon}}(k, f) = \frac{1}{\mathbf{e}^H(k) \mathbf{R}(f)^{-1} \mathbf{e}(k)}. \quad (4.21)$$

Capon's method is an optimization approach constructed to determine the optimal weights applied to each sensor such that the output power is estimated along a specific direction (e.g. for a specific $f - \mathbf{k}$ pair) while power contributions from all other directions are minimized (Pillai, 1989). From Equation 4.21, it can be seen that Capon's method is based on the inverse of the estimated spectral matrix, $\mathbf{R}(f)$.

The f - k power spectrum estimated from Capon's method at a frequency of 1.5 Hz for Site 1 is shown in Figure 4.13. Compared to the FDBF method, Capon's method results in a slightly lower wavenumber estimate at the peak, and a much narrower power peak along with much smoother background power, as seen in Figure 4.13a. Three possible energy sources are detected by Capon's method.

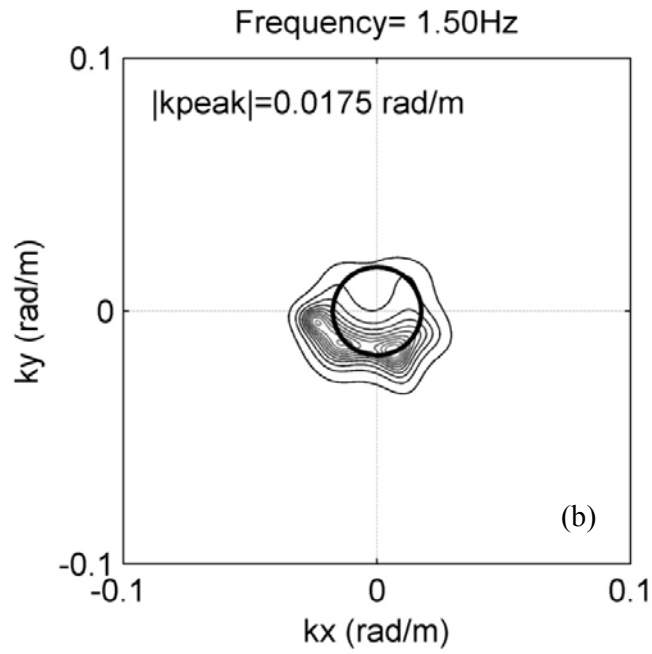
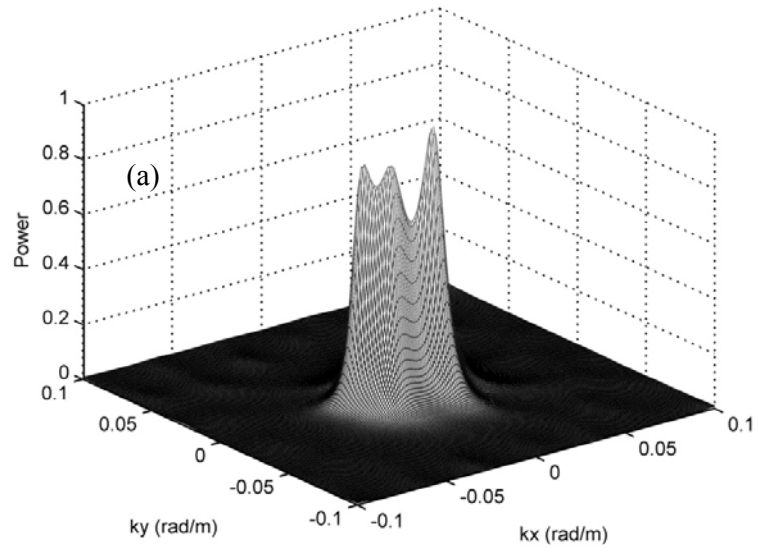


Figure 4.13 Power spectrum estimate using Capon's method at 1.5 Hz for Site 1 shown in (a) 3-D mesh plot and (b) 2-D contour plot.

4.4.4 Interpretation of Dispersion Curves from Passive f - k Measurements

For a given frequency, f , the wavenumber pair $\mathbf{k} = (k_x, k_y)$ that provides the peak power can be used to calculate the direction of the propagating wave, θ , and the phase velocity, V_R . The direction of the propagating wave, θ , can be given by:

$$\theta = \tan^{-1} \left(\frac{k_x}{k_y} \right). \quad (4.22)$$

It should be noted that, θ , is an azimuth angle measured clockwise from the y axis in the x - y coordinate system defined in Section 4.4.2. The direction in the NS-EW coordinate system can be determined based on the relationship of the x - y coordinate system to the NS-EW system. More details on wave propagation directions will be discussed in the next chapter. The phase velocity, V_R , is calculated using:

$$V_R = \frac{2\pi f}{|\mathbf{k}|}, \quad (4.23)$$

where, $|\mathbf{k}| = \sqrt{k_x^2 + k_y^2}$. These calculations are performed for each frequency of interest to construct the experimental dispersion curve.

The dispersion curve estimated by the conventional FDBF method for Site 1 is presented in Figure 4.14. The dashed line in this figure denotes the maximum wavelength resolution limit. The resolution limit determines the lowest wavenumber (or longest wavelength) that can be reliably resolved. The empirical criterion by Tokimatsu (1997) is applied in this study. It defines the longest wavelength that can be resolved to be 3 times the array size or maximum array aperture. That is,

$$\lambda_{\max} < 3D_{\max} \quad \text{or} \quad k_{\min} > \frac{2\pi}{3D_{\max}}, \quad (4.24)$$

where, k_{\min} is the lowest wavenumber, and D_{\max} is the maximum aperture of the

array. All of the circular arrays used in this study have D_{\max} of 200 m, hence a largest resolvable wavelength is 600 m. The final dispersion curve used for inversion is developed by removing artifact dispersion points due to aliasing and points out of the resolution limit, as shown in Figure 4.14.

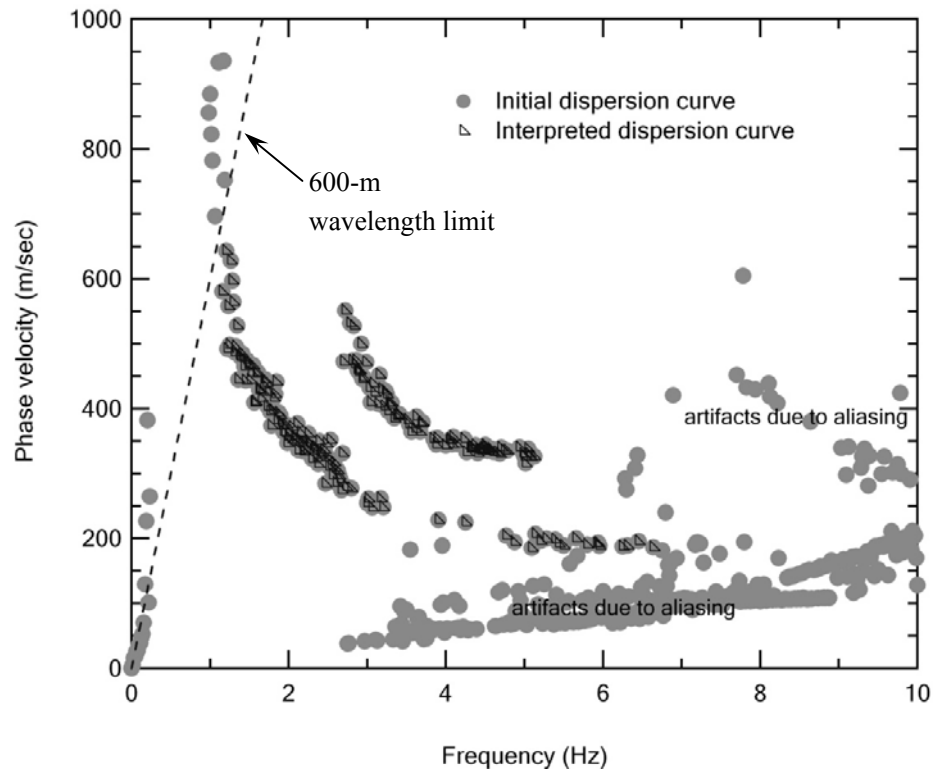


Figure 4.14 Dispersion curve estimated by conventional FDBF method for Site 1.

4.5 Data Processing of ReMi Measurements

Field measurement procedures and array information for ReMi measurements are described in Section 3.5.2. Algorithms were developed in MATLAB to perform ReMi analysis and pick dispersion curves. The ReMi analysis was performed for 8 sites, where equally-spacing linear arrays were used. The procedures included in the ReMi analysis are described in the following sections. These methods are consistent

with those presented in the original ReMi publication by Louie (2001).

4.5.1 Slowness-Time Intercept ($p - \tau$) Transformation (Thorson and Claerbout, 1985)

The $p - \tau$ transformation (sometimes called a slantstack transformation) is a method to convert the records of multiple seismograms, in the distance and time ($x - t$) domain to the slowness (the inverse of apparent velocity), p , and an intercept time, τ , domain. It can also be considered as time-domain beamforming. The discrete $p - \tau$ transformation can be described as:

$$A(p, \tau) = \sum_{i=1}^N A(x_i, t = kdt = \tau + px_i), \quad (4.25)$$

where, N denotes the number of receivers, x_i denotes the offset of the i th receiver to one end of the linear array, t denotes time, which is discretized as kdt with dt usually 0.001-0.01 sec, and p denote the slowness. The parameter, p_{\max} , defines the inverse of the minimum velocity that will be determined. The dp value typically ranges from 0.0001 to 0.0005 sec/m and is set to cover the interval from $-p_{\max}$ to p_{\max} in $2np$ slowness steps, the τ term denotes the intercept times, which equal the arrival times of the recorded ambient noise. In this study, a MATLAB script written by Prof. M.D. Sacchi (used with permission), from the University of Alberta was used to perform the $p - \tau$ transformation.

For the analysis used in this study, the slowness, p , has a range $[-0.01, 0.01]$ with a dp value of 0.0001. The dt value is equal to the sampling interval (the inverse of sampling frequency), e.g. 0.003125 sec for Sites 1 and 5, and 0.00625 sec

for Sites 6 to 11, as shown in Table 3.6. The ReMi data were collected continuously in the time domain during a period of time of typically 20 to 30 min at most sites. The continuous, long noise records were discretized into segments. The duration of each segment is 2^{14} in terms of sampling points, e.g. 51.2 sec for Sites 1-5, and 102.4 sec for Site 6 through Site 11. The number of segments varies at each site depending on the duration of recorded data.

Before performing the $p-\tau$ transformation, the noise records were pre-processed to improve the final ReMi results based on the typical procedures used in ReMi data processing. First, the noise amplitude of each sensor was clipped at 3 times the root mean square (RMS) amplitude. This procedure is recommended by the originator of ReMi method because it removes many high-amplitude artifacts from the sensor data while preserving useful microtremor data. Secondly, the data from each sensor was normalized by its maximum amplitude and any offset was removed. This normalization process provides a more coherent velocity spectrum by weighting all sensor traces equally.

4.5.2 Slowness-Frequency ($p-f$) Transformation (McMechan and Yedlin, 1981)

Through the $p-\tau$ transformation (Equation 4.25), $2np$ $p-\tau$ traces are produced. Each of these traces contains the linear sum across a record at all intercept times for a single slowness value. The complex Fourier transform is then performed on each $p-\tau$ trace in the intercept time (τ) direction as:

$$F_A(p, f) = \sum_{k=0}^{n-1} A(p, \tau = kdt) \exp(-i2\pi f kdt). \quad (4.26)$$

The power spectrum, $S_A(p, f)$, is calculated as the magnitude squared of the complex Fourier transform:

$$S_A(p, f) = F_A^*(p, f) \cdot F_A(p, f), \quad (4.27)$$

in which, $*$, denotes the complex conjugate. Energy from the forward and reverse directions along the receiver array is summed into one slowness axis that represents the absolute value of p , $|p|$. The slowness axis is folded and summed about $p = 0$ with:

$$S_A(|p|, f) = [S_A(p, f)]_{p \geq 0} + [S_A(-p, f)]_{p < 0}. \quad (4.28)$$

If the analysis involves more than one noise record (as was the case for this study), the individual $p - f$ images from each record are added point-by-point into an image of summed power as:

$$S_{\text{total}}(|p|, f) = \sum_n S_{A_n}(|p|, f). \quad (4.29)$$

4.5.3 Normalization of $p - f$ Images (Louie, 2001)

The average power over all the slowness values calculated from Equation 4.28 (or Equation 4.29) may be orders of magnitude different from one frequency to another. In order to show power peaks more clearly at each frequency, the ReMi method takes the spectral ratio $R(|p|, f)$ of the power at each slowness-frequency combination over the average power across all slownesses at that frequency in individual $p - f$ images $S_A(|p|, f)$, or in a summed image $S_{\text{total}}(|p|, f)$. Thus,

$$R(|p|, f) = S(|p|, f) n_p / \left[\sum_{l=0}^{n_p-1} S(|p| = ldp, f) \right], \quad (4.30)$$

where, np is half of the original number of slowness steps, $2np$.

The $p-f$ spectral ratio images were first calculated from individual segments of noise records according to the procedures described above. These individual images were then examined and selected to include in the cumulative $p-f$ image. Figure 4.15 presents four individual $p-f$ images calculated for Array 2, Site 9. The $p-f$ image in Figure 4.15a is an example of the data that was included in the cumulative $p-f$ image. It can be seen that this image has coherent and continuous dispersive energy across frequencies from about 1.5 Hz to 8 Hz. The $p-f$ image in Figure 4.15b wasn't included because it has a large gap in the spectral energy over the 3 Hz to 5 Hz range. The individual $p-f$ images in Figures 4.15c and 4.15d weren't included because they exhibit poor energy at high

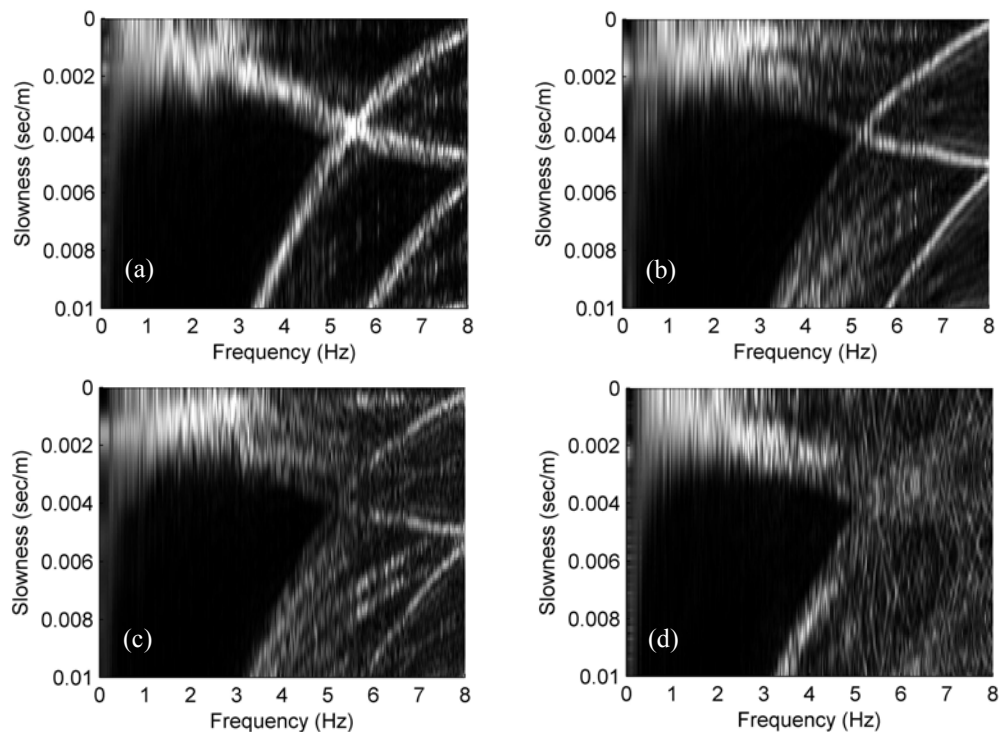


Figure 4.15 $p-f$ spectral ratio images of 4 individual noise records for Array 2, Site 9.

frequencies. The results, obtained using the MATLAB program developed for this study, were compared to results from commercial software (SeisOpt ReMi developed by Optim). Figure 4.16 shows this comparison for data collected using Array 1 at Site 9. It can be seen that the MATLAB program effectively reproduces the dispersion image obtained with the commercial software.

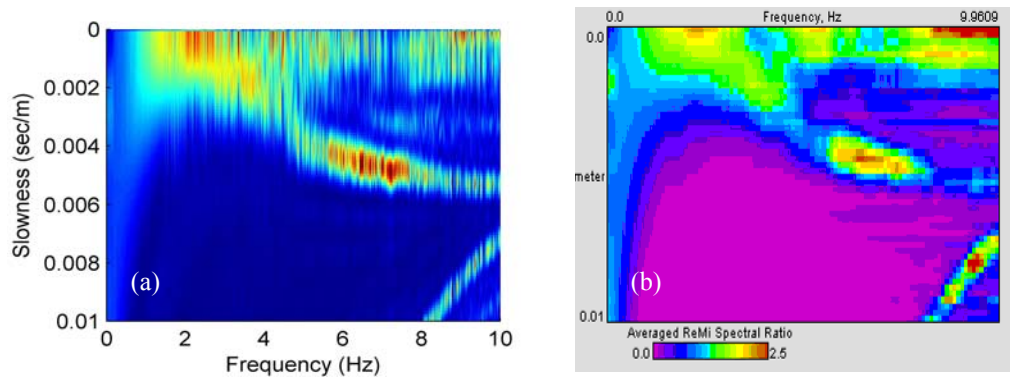


Figure 4.16 Comparison of p-f images estimated for Array 1, Site 9 from (a) MATLAB program developed for this study and (b) the commercial SeisOpt ReMi software

4.5.4 Dispersion Curve Picking

The determination of the phase velocity using the ReMi method is a more ambiguous and subjective procedure as compared to the SASW and $f-k$ methods. The ReMi approach relies on an assumption that energy is impinging equally on the receiver array from all directions, and therefore, the lower bound of the dispersion image represents the fundamental-mode surface wave propagating along the length of array. Identifying the lower bound is not as straightforward as identifying the peak power in the $f-k$ method. Louie (2001) recommends making three possible dispersion curve picks: (1) a low phase velocity where the spectral ratio just rises above the low

values of incoherent noise, (2) a high-velocity value at a spectral-ratio peak near the drop-off in spectral ratio, and (3) a “best guess” (Louie, 2001) value where the ratio is at the steepest gradient. There is apparently no theoretical basis for any of these picks, but instead they are meant to bracket the “true” velocity value. However, Zywicki (2007) has pointed out that the low-velocity pick will depend on the noise properties of the equipment utilized and the array mainlobe properties and thus is not meaningful. Therefore, for this study dispersion picks are presented only at the steepest slope and at the peak.

A MATLAB algorithm was developed to expedite the dispersion curve picking procedure from the $p-f$ image. Three basic steps were followed. As shown in Figure 4.17a, Step 1 was to select the frequencies at which the picks will be made. In order to directly compare the ReMi dispersion curve with active $f-k$ dispersion curves, the frequencies for dispersion picking were chosen to be the same as those used for the active-source measurements. The next step was to plot the power-slowness profile at the selected frequency, as shown in Figure 4.17b. The peak and the lowest velocities are picked manually, and then the pick at the steepest slope between the upper and lower picks was determined by the program. Initial dispersion curves were generated by repeating the first two steps for all the selected frequencies. The third step was to eliminate the picks that clearly didn't follow the lower bound dispersion trend. These slowness picks were then used to calculate a final dispersion curve, as shown in Figure 4.17c. During this procedure, picks were only made at frequencies where the power-slowness profile had a clear peak, as shown in Figure 4.17b. Picks

were not made for power-slowness plots like Figure 4.18a where no clear peak was identified. For power-slowness plots having multiple peaks, like Figure 4.18b, the picks were made at the peak with the largest slowness value (lowest velocity) which represents ambient energy propagating more parallel to the geophone array.

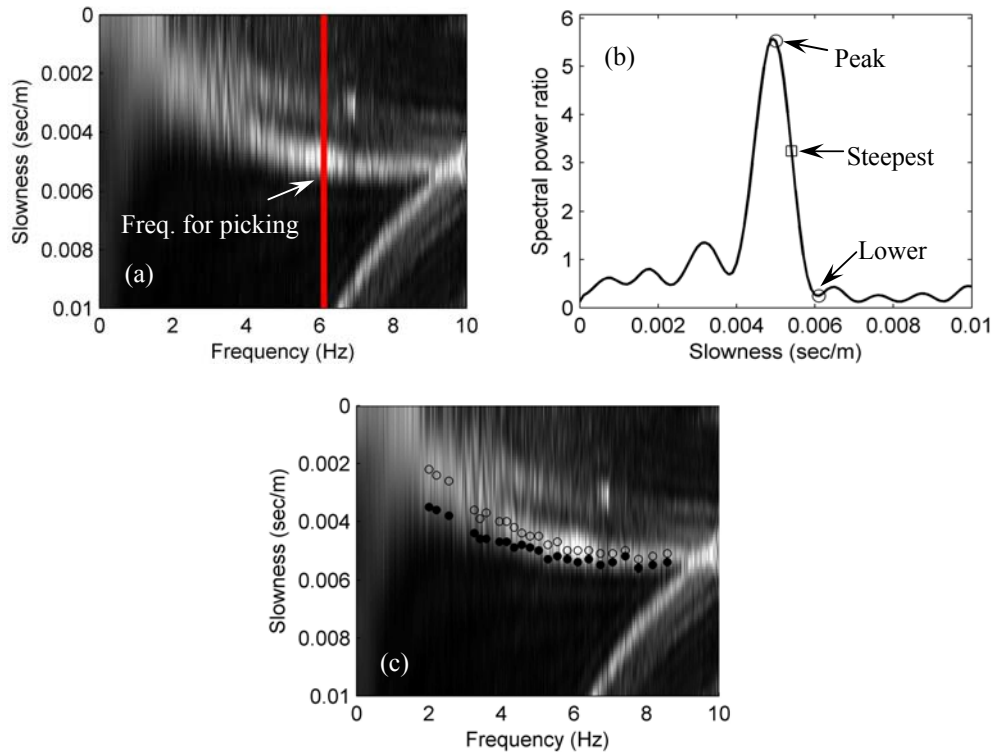


Figure 4.17 Procedures of picking dispersion curves from p-f image.

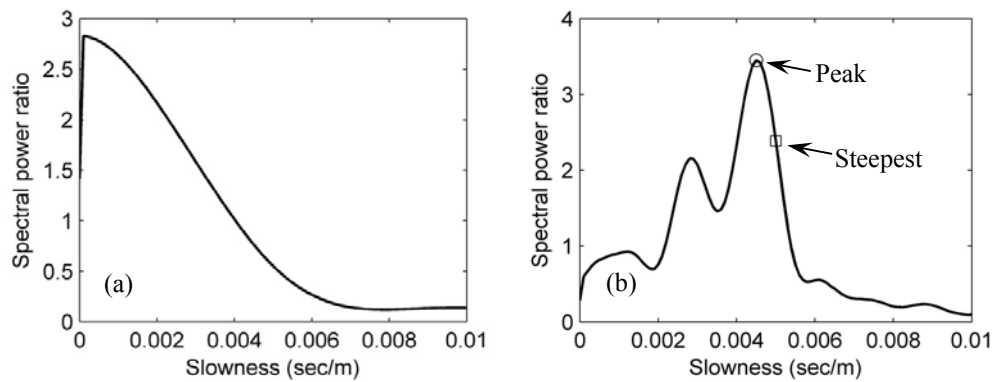


Figure 4.18 Examples of data quality of power-slowness profiles used for dispersion picking from ReMi.

CHAPTER 5

DISPERSION CURVE COMPARISON BETWEEN SASW AND ACTIVE $f-k$ METHODS

5.1 Introduction

The SASW and $f-k$ methods are common active-source approaches for developing surface wave dispersion curves. However, due to the lack of a low frequency source, these methods have not been used to develop low frequency dispersion curves. This study is the first application of the NEES equipment to develop long-wavelength dispersion curves of deep soil sites. In this chapter, dispersion curves developed from SASW and active $f-k$ methods are compared for the 11 test sites. The purpose of these comparisons is to identify inconsistencies and find the cause. Also, the performance of the NEES vibrator and the impact of near-field effects on the active-source $f-k$ analysis are discussed.

5.2 Field Performance of NEES Vibrator

The NEES vibrator is a one-of-a-kind truck that has been used in only a few studies prior to this work (Stokoe et al., 2004a). This study is the first application of the NEES equipment for deep V_s profiling at soil sites. This equipment was built with the objective of improving force output at low frequencies, as shown in Figure 3.29b of Chapter 3. In the field measurements, the force output of the vibrator was not directly measured. However, output levels recorded by the receivers in the arrays

showed high-levels down to frequencies of about 1 Hz at most sites. As an example, the recorded power spectrum at the farthest receiver (544 m from source) of Array 2 for Site 8 is presented in Figure 5.1a. It can be seen from this figure that the recorded output remained at high levels over the frequency range of 1 to 4 Hz. The recorded output begins to drop off at about 1.3 Hz, which is consistent with the theoretical performance of NEES vibrator, as show in Figure 3.29b. Figure 5.1b presents an example of the recorded coherence function, indicative of signal-to-noise ratio, recorded at a distance of 544 m from the source at the same site. Coherence values of near 1.0 were observed over the low-frequency (1 to 4 Hz) portion of the frequency range. Similar coherence values were recorded at low frequencies at all 11 sites, indicating that high signal-to-noise ratios were obtained at frequencies down to less than 1 Hz.

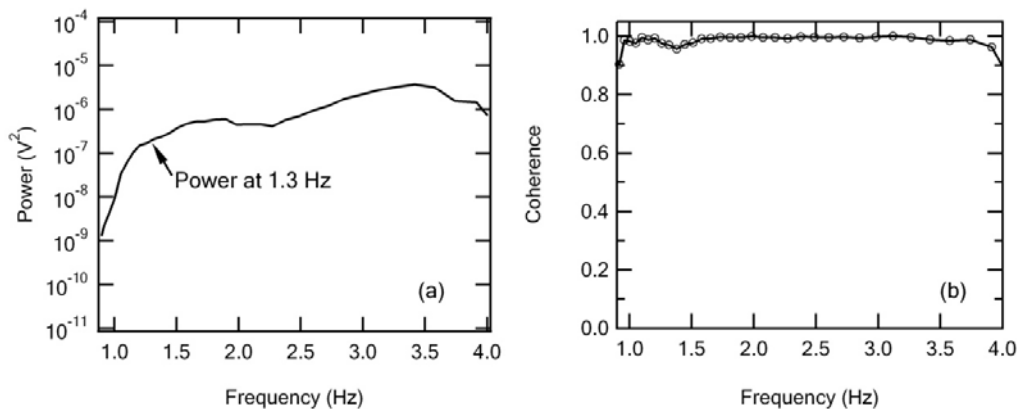


Figure 5.1 Recording at last receiver of Array 2 at Site 8 showing (a) power spectra with NEES vibrator operating and (b) coherence function between source signal and measured signal.

With above discussion, it can be concluded that the NEES vibrator performed as expected by successfully generating high-quality surface wave energy down to frequencies of less than 1 Hz.

5.3 Comparison of Dispersion Curves Developed from SASW and Active $f-k$ Methods

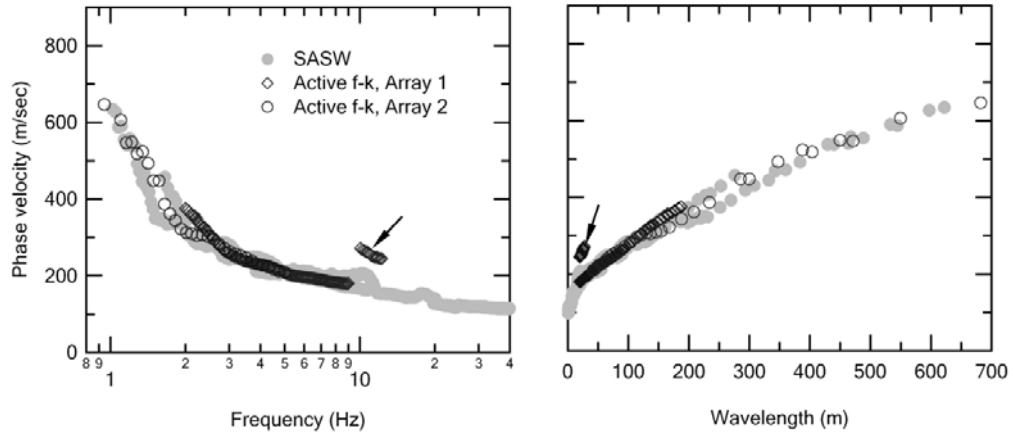
Surface wave dispersion curves were developed for all 11 sites using the SASW and active $f-k$ methods, as described in Chapter 4. The dispersion curves are presented for Site 1 through Site 11 in Figures 5.2a to 5.2k, respectively. It can be observed from Figure 5.2 that the dispersion curves from these two methods generally show the same dispersion trend at each site. It should be noted that it was not expected that the dispersion curves from these two methods would be identical. The reason is that the SASW method uses a two-point measurement, and does not separate the contributions from body wave energy and surface wave energy. Therefore, the SASW method often shows a more undulated dispersion curve than the active $f-k$ method.

There are two cases where the dispersion curves are clearly not in agreement. First, for Sites 2, 3 and 4, the active-source $f-k$ method yielded lower velocity estimates at long wavelengths (low frequencies) as compared to the SASW results (see boxes in Figure 5.2b, 5.2c and 5.2d). These three sites are where measurements were performed using a single linear array with unequal receiver spacing. For the unequally-spaced array, the first several receivers have short offsets to the source. The lower $f-k$ dispersion estimates are likely due to the near-field effects caused by these close-to-source receiver spacings. Mitigation of these near-field effects at these three sites is discussed in Section 5.5.1.

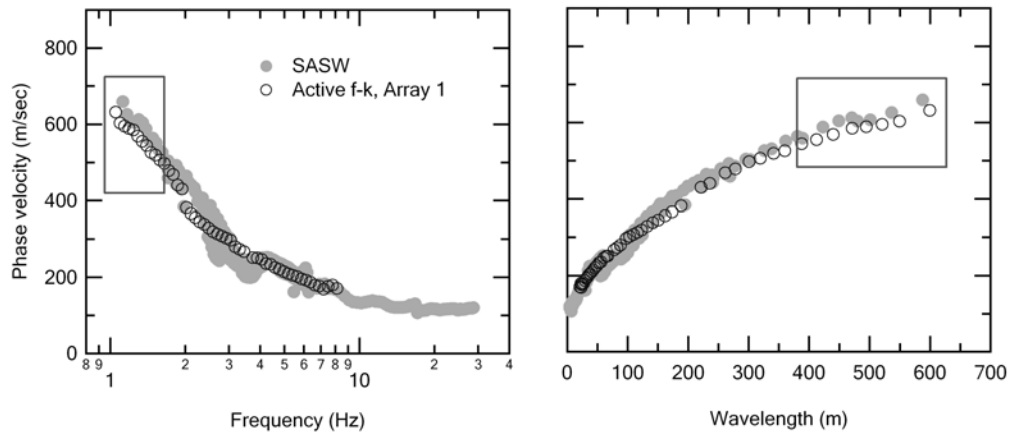
The second case where the dispersion curves differ was observed at Sites 3, 6 and 9. As shown in Figures 5.2c, 5.2f and 5.2i, significant differences in the

dispersion curve comparison are observed over a portion of the frequency range at these sites (see circles in Figures 5.2c, 5.2f and 5.2i). For Sites 6 and 8, these differences are as high as 80% at some frequencies. These differences are associated with sites with abrupt mode transitions, as discussed in detail in the next section.

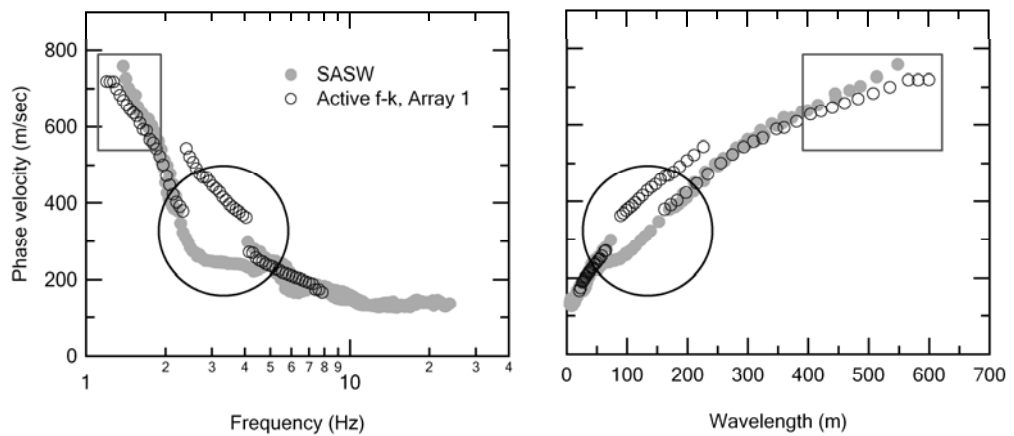
Lastly, it should be noted that higher mode transitions observed at some sites at high frequencies (indicated with an arrow in Figures 5.2a, 5.2f, 5.2g to 5.2k) are artifacts of the anti-aliasing cut-off frequency used in the analysis. The fundamental mode is not identified past the minimum wavelength limit (twice the minimum receiver spacing in Equation 4.10). However, higher mode energy (travelling at a higher velocity) has a wavelength smaller the aliasing limit, and, hence, appears to become the dominant energy. These modes are real, but are not necessarily the dominant modes.



(a) Site 1

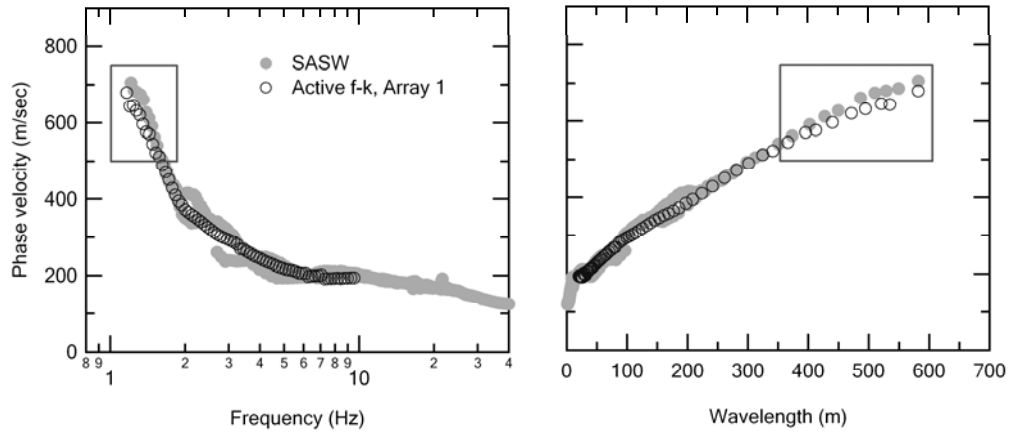


(b) Site 2

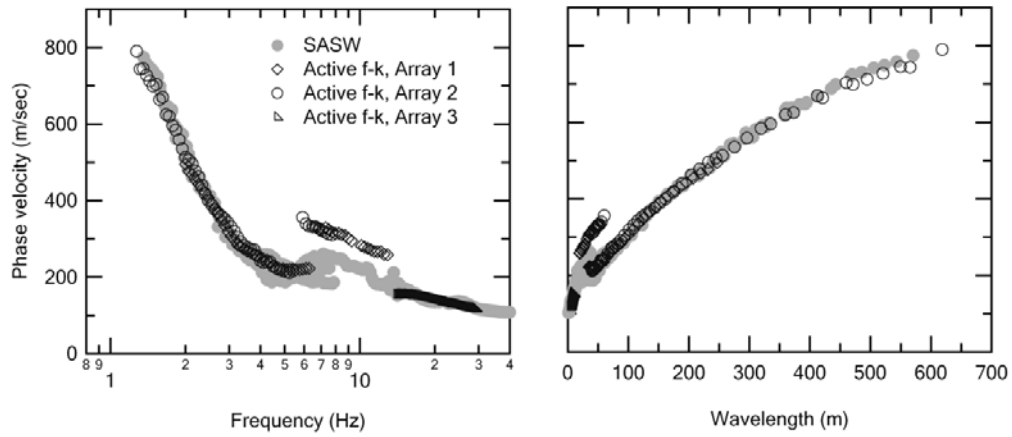


(c) Site 3

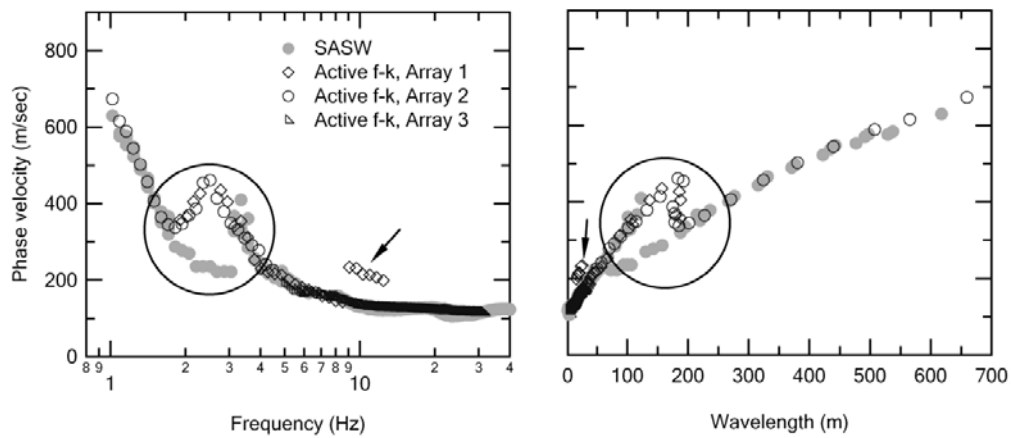
Figure 5.2 Comparison of dispersion curves developed from SASW and active f - k methods presented in terms of frequency (left column) and wavelength (right column) for Site 1 to Site 11 as (a) to (k).



(d) Site 4

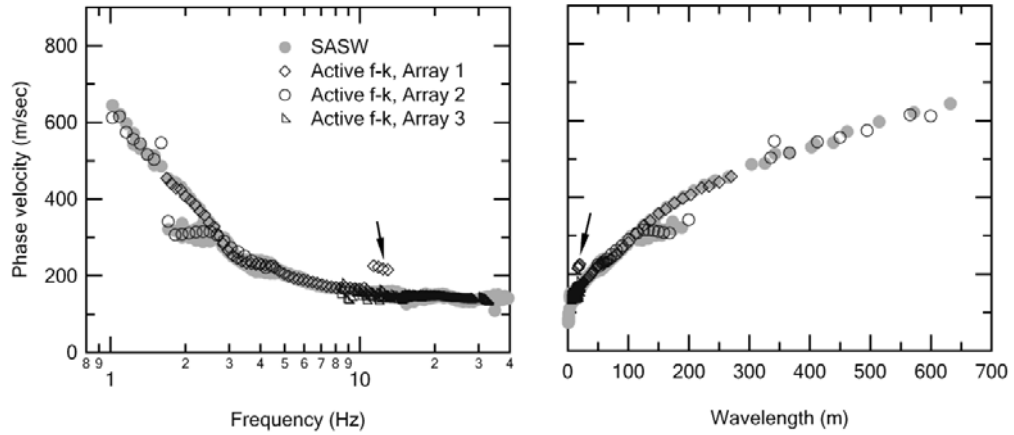


(e) Site 5

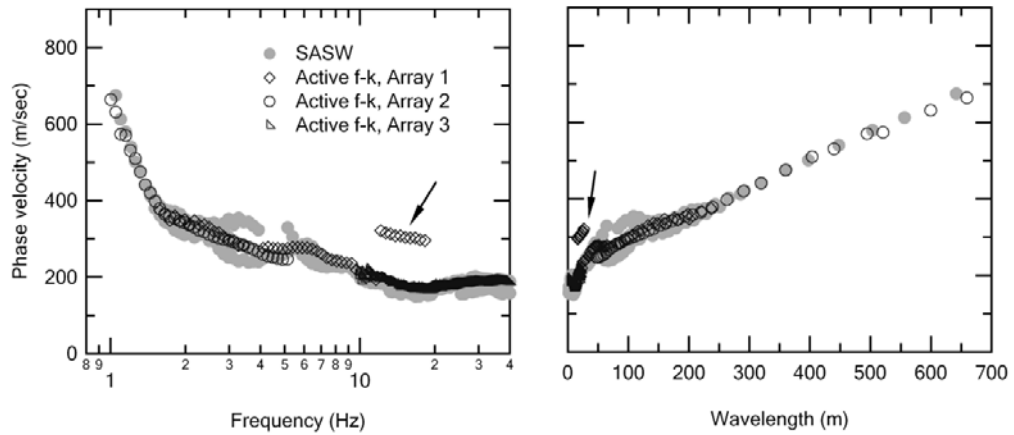


(f) Site 6

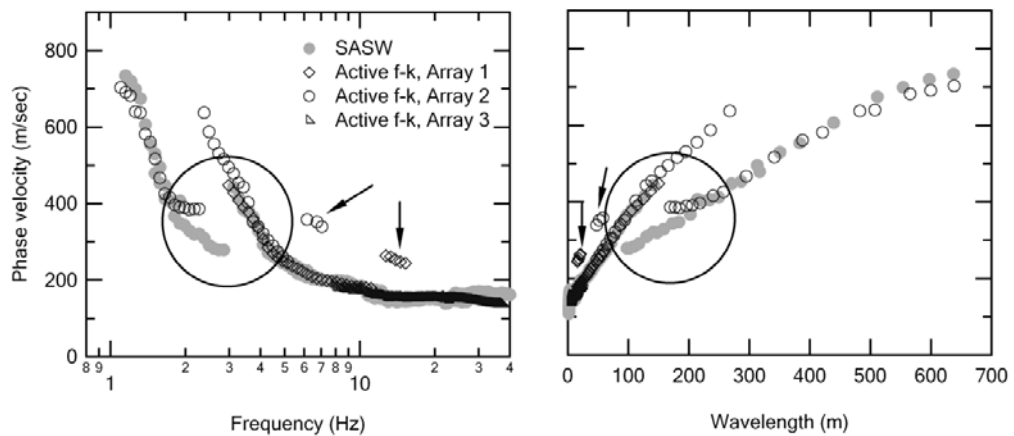
Figure 5.2 (Cont.) Comparison of dispersion curves developed from SASW and active $f-k$ methods presented in terms of frequency (left column) and wavelength (right column) for Site 1 to Site 11 as (a) to (k).



(g) Site 7

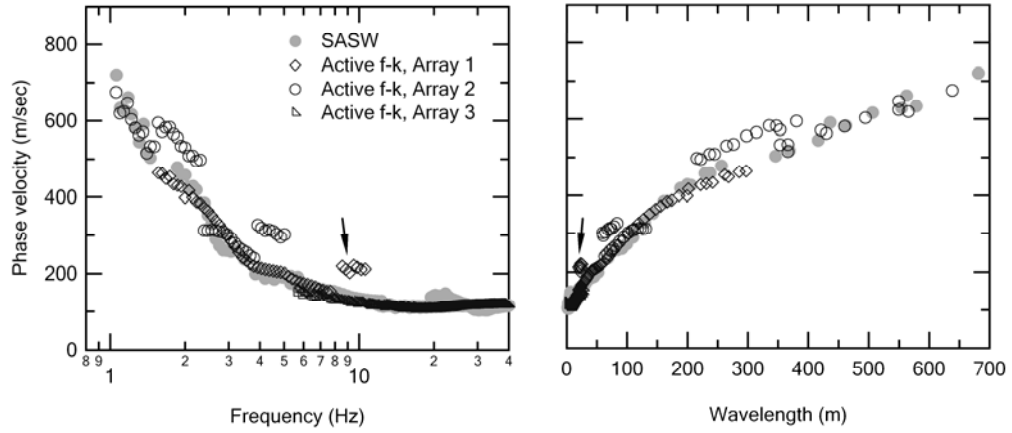


(h) Site 8

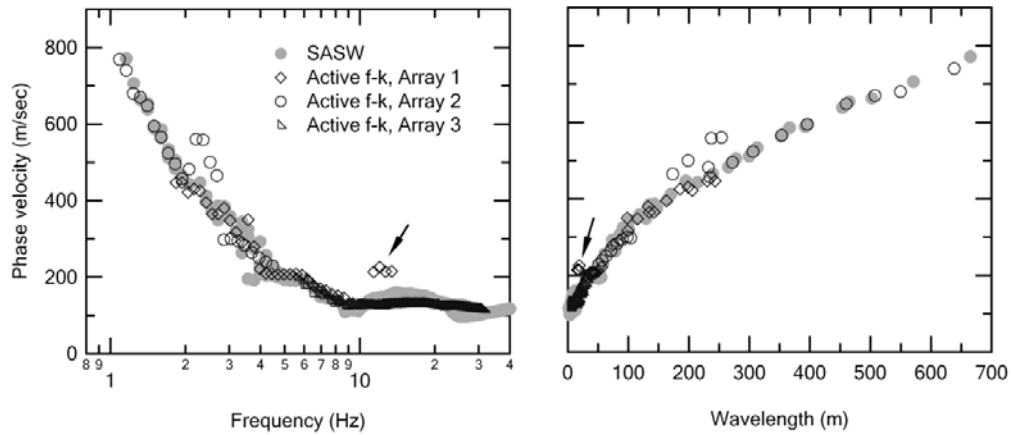


(i) Site 9

Figure 5.2 (Cont.) Comparison of dispersion curves developed from SASW and active f - k methods presented in terms of frequency (left column) and wavelength (right column) for Site 1 to Site 11 as (a) to (k).



(j) Site 10



(k) Site 11

Figure 5.2 (Cont.) Comparison of dispersion curves developed from SASW and active $f-k$ methods presented in terms of frequency (left column) and wavelength (right column) for Site 1 to Site 11 as (a) to (k).

5.4 Phase Unwrapping Errors

As shown in Figures 5.2c, 5.2f and 5.2i for Sites 3, 6 and 9, respectively, significant differences in the SASW and active $f-k$ dispersion curves are observed over a portion of the frequency range. For these sites, the $f-k$ dispersion curves have in common a transition or jump from a lower mode to a higher mode around 4 Hz, followed by an abrupt return to the lower mode at a frequency of around 2 Hz.

Bertel (2006) performed numerical simulations to compare simulated SASW experimental and theoretical dispersion curves using various soil profile conditions, and identified similar features as observed in this study that were associated with a strong V_s contrast at shallow depth. For example, Figure 5.3a presents one V_s profile simulated by Bertel (2006). This is a soft-over-stiff profile with layer velocities of 103 m/sec to 180 m/sec in the top 10 m, underlain by a high-velocity (457 m/sec) half-space. The ratio of the V_s of the stiff layer to the average V_s of the soft layer is 3.1. As shown in Figure 5.3b, the simulated SASW and theoretical dispersion curves do not match over a portion of the frequency range. The theoretical dispersion curve transitions to a higher mode, which is similar to what was observed at Sites 3, 6 and 9 in this study (although at higher frequencies in Bertel (2006) due to the shallower depths of the stiff layer).

According to Bertel (2006), this difference can be attributed to a phase unwrapping error when developing the simulated SASW experimental dispersion curve. This phase unwrapping error is associated with the abrupt mode transition. For the example shown in Figure 5.3, the problematic unwrapping occurred with the

phase plot taken from the 61.0-m receiver pair. Figure 5.4a shows the initial interpretation of this phase data based on a single unwrapping over frequencies of 4.7 to 7.6 Hz. The unwrapping interpretation applied to this data is indicated by the number of phase “jumps” in this figure. Although this phase plot shows a seemingly classic “sawtooth” pattern, continuous unwrapping of the phase produces an artificially low estimate of the phase velocity, as observed in Figure 5.3. Because of the abrupt mode transition occurring at 4.6 Hz, it is not valid to interpret the unwrapped phase at frequencies above 4.6 Hz based on this single phase unwrapping. Instead, the correct interpretation requires considering two portions of the phase plot separately, as shown in Figure 5.4b and 5.4c. The first portion is related to the lower mode at frequencies lower than 4.6 Hz (Figure 5.4b). The second portion is related to the higher mode at frequencies between 4.6 Hz and 7.6 Hz (Figure 5.4c). When this separate unwrapping of the phase plot is applied, the simulated and theoretical

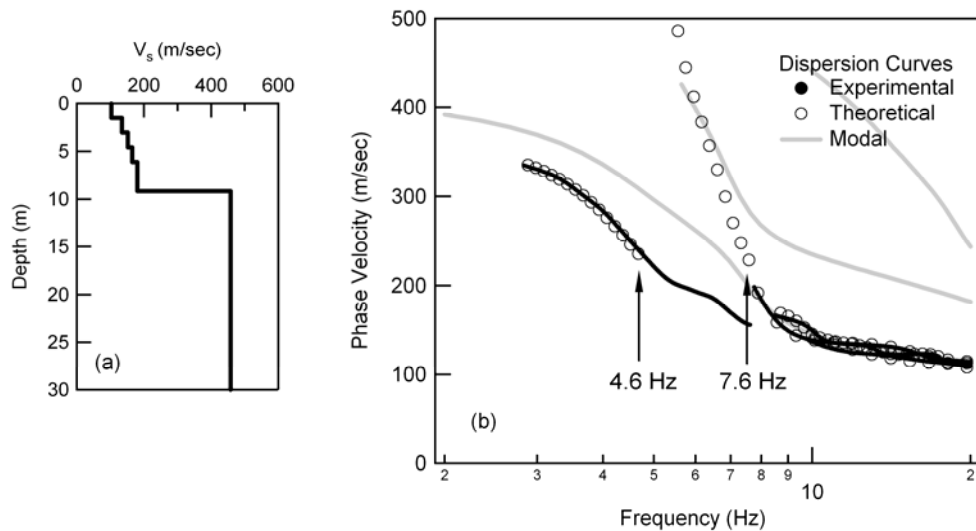


Figure 5.3 Results from Bertel (2006) showing (a) example V_s profile, and (b) comparison of simulated experimental dispersion curve with theoretical and modal dispersion curves from profile shown in (a).

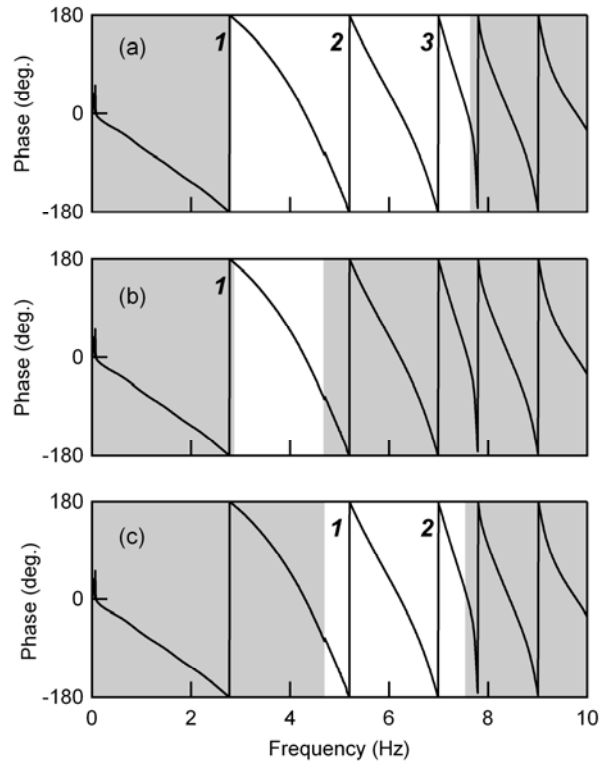


Figure 5.4 Interpretation of the 61-m pair phase data for example V_s profile (in Figure 5.3) showing (a) continuous phase unwrapping over frequencies 4.6 Hz to 7.6 Hz, (b) phase unwrapping of the lower mode at frequencies less than 4.6 Hz and (c) phase unwrapping of the higher mode at frequencies between 4.6 and 7.6 Hz (Bertel, 2006).

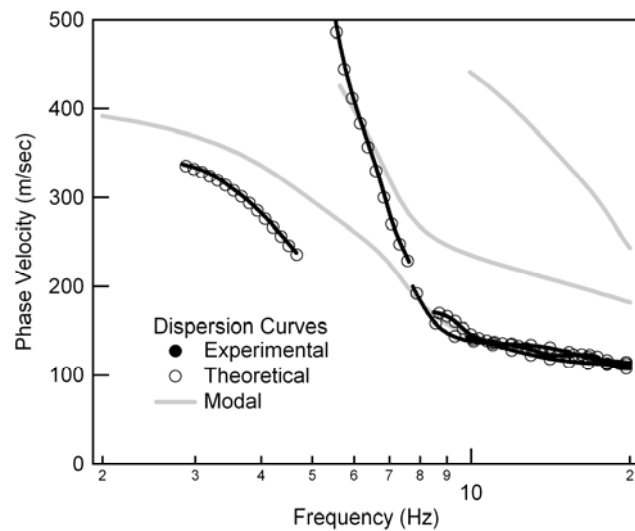


Figure 5.5 Comparison of simulated experimental and theoretical dispersion curves for example profile (in Figure 5.3a) after the application of correct phase unwrapping shown in Figure 5.4b and 5.4c (Bertel, 2006).

dispersion curves come into good agreement, as shown in Figure 5.5.

Bertel (2006) did not show field measurements to support his observations from his simulated data. However, these observations can be demonstrated by actual measurements from Sites 3, 6 and 9 in this study. As an example, the data from Site 3 is used. For Site 3, the SASW method yields lower velocities than the active $f-k$ method over the frequency range of 2.4 Hz to 4.0 Hz, as shown in Figure 5.2c. This problematic dispersion portion is produced by the 200-m receiver pair when a single unwrapping of the phase plot from the 200-m pair is performed, as shown in Figure 5.6a. This erroneous dispersion interpretation can lead to significant errors in the final

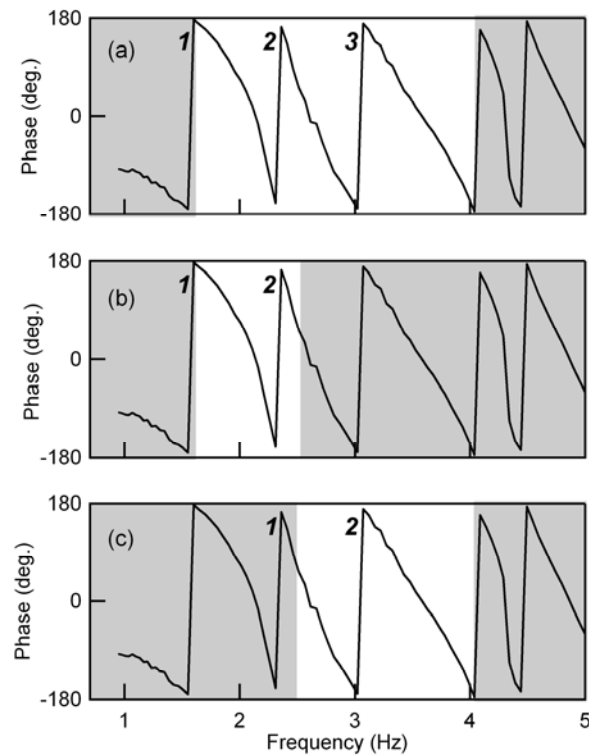
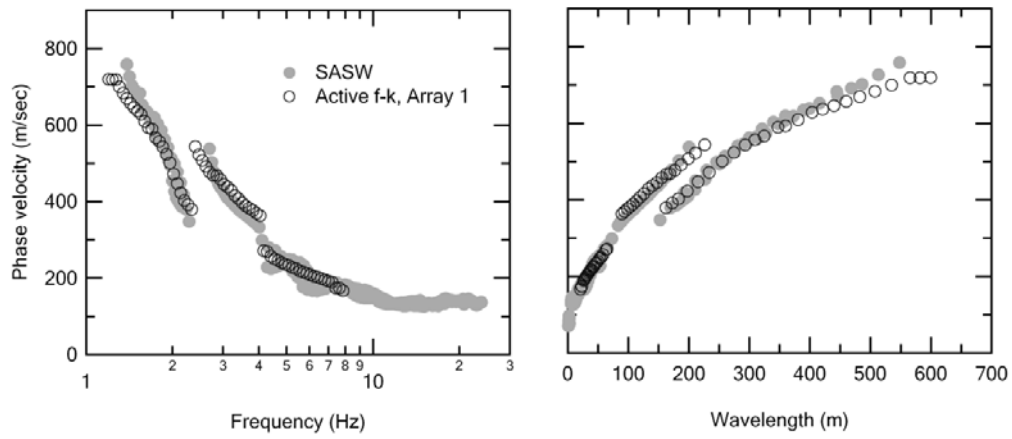
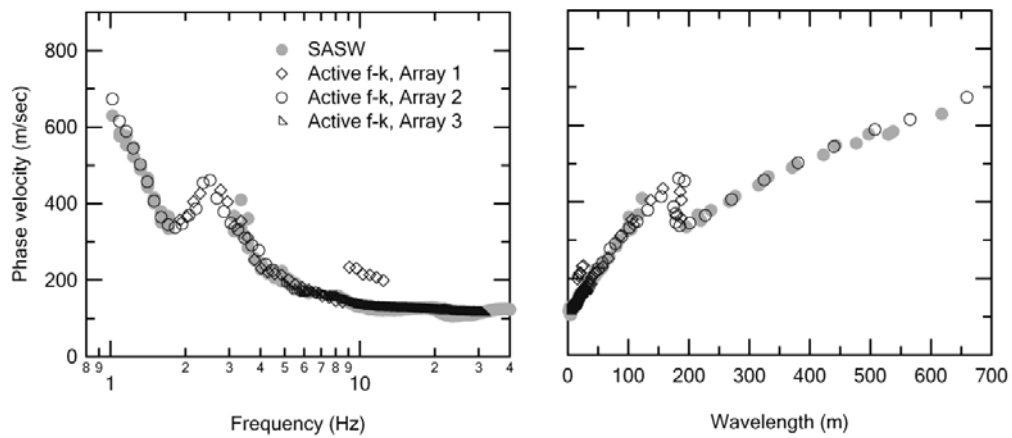


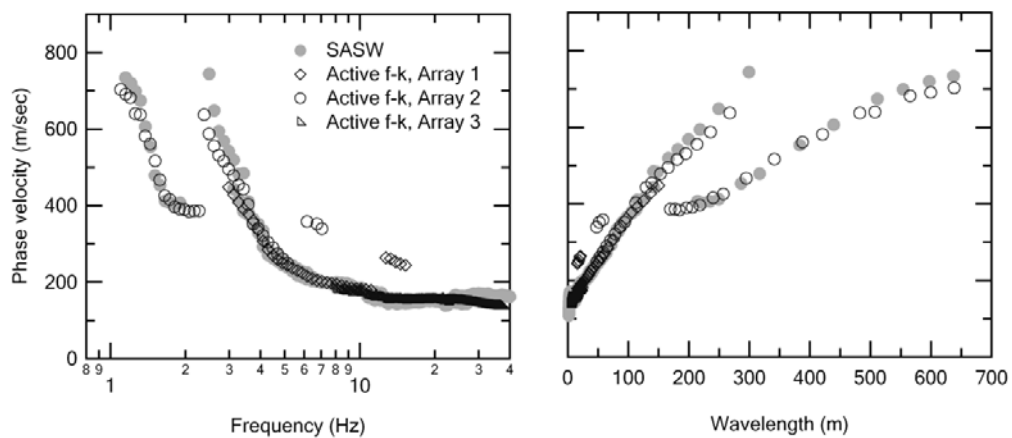
Figure 5.6 Interpretation of the 200-m pair phase data for Site 3 showing (a) continuous phase unwrapping over frequencies from 1.6 Hz to 4.0 Hz, (b) phase unwrapping of the lower mode at frequencies between 1.6 and 2.4 Hz and (c) phase unwrapping of the higher mode at frequencies between 2.4 and 4.0 Hz.



(a) Site 3



(b) Site 6



(c) Site 9

Figure 5.7 Comparison of dispersion curves developed from SASW and active $f-k$ methods for (a) Site 3, (b) Site 6 and (c) Site 9 after correct interpretation of phase unwrapping.

V_s profile, as discussed by Bertel (2006). The correct unwrapping procedures, as previously described, are also applied to this phase plot, as shown in Figure 5.6b and 5.6c. The SASW dispersion curve, after the application of correct phase interpretation, is shown in Figure 5.7a. It can be observed that when the correct phase unwrapping is applied, the SASW and active $f-k$ results come into agreement. Similar re-interpretation procedures were also applied to data at Sites 6 and 9. The corrected SASW dispersion curves are exhibited in Figure 5.7b and 5.7c, and also show good agreement.

Shear wave velocity profiles for Sites 3, 6 and 9 were developed by Bailey (2008) using the correct SASW dispersion curves. These profiles and the estimated soil stratigraphy are presented in Figures 5.8, 5.9 and 5.10. It can be observed that all of these sites show a strong soft-over-stiff condition at a depth of about 20 to 30 m (marked by arrow), as expected based on Bertel's observations. This stiff layer appears to be at the top of the gravel layer, based on the profiles supplied by Prof. Roy Van Arsdale from the University of Memphis. Bertel (2006) also observed that the lower transition frequency is close to the shear wave resonant frequency of the shallow softer layer. The resonant frequency, f_r , can be estimated from (Kramer, 2005):

$$f_r = \frac{\bar{V}_s}{4H}, \quad (5.1)$$

where, \bar{V}_s is the average shear wave velocity of the softer soil, and H is the combined thickness of the soft layers. The, \bar{V}_s , can be computed from:

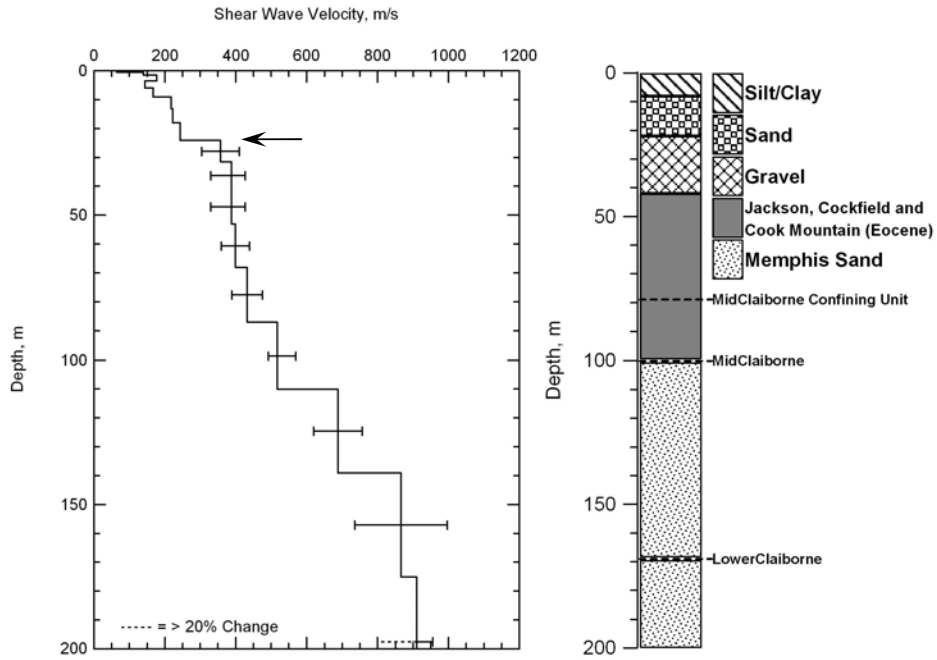


Figure 5.8 V_s profile inverted from SASW measurements and estimated soil profile for Site 3 (Bailey, 2008).

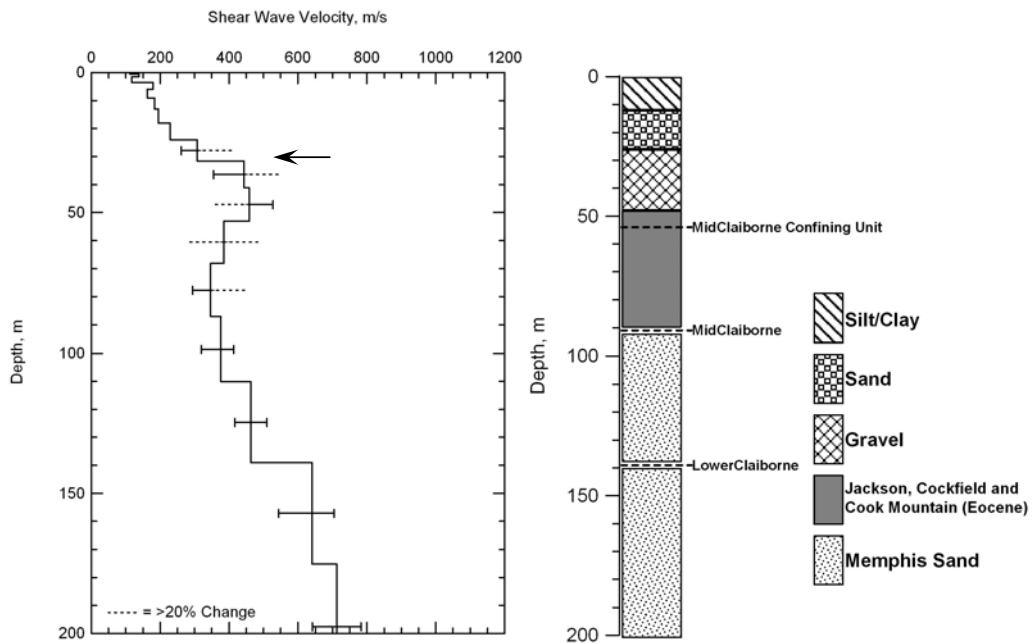


Figure 5.9 V_s profile inverted from SASW measurements and estimated soil profile for Site 6 (Bailey, 2008).

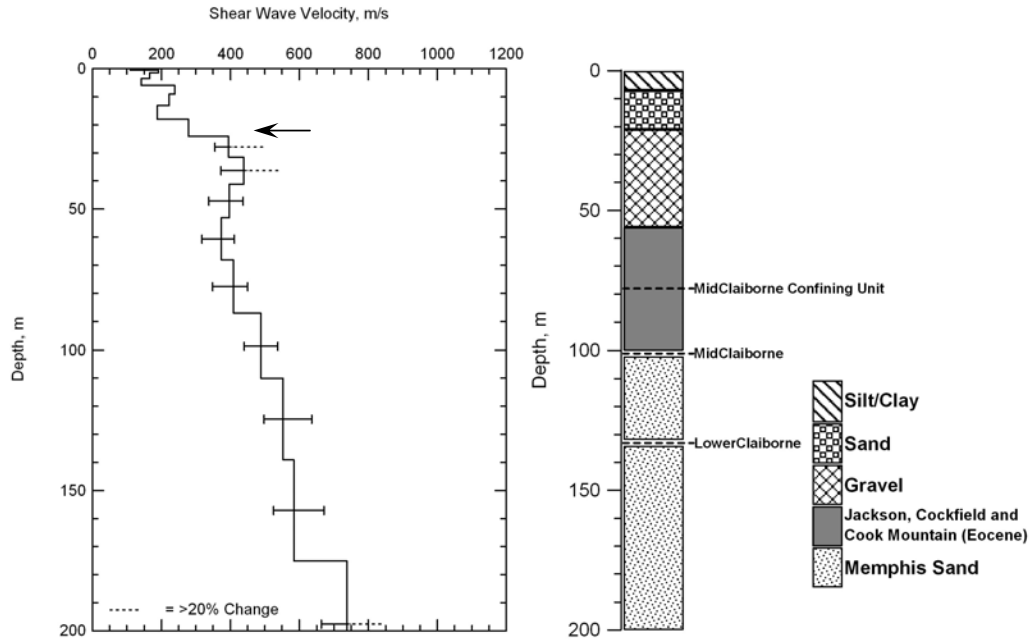


Figure 5.10 V_s profile inverted from SASW measurements and estimated soil profile for Site 9 (Bailey, 2008).

$$\bar{V}_s = \sum_1^n d_i / \sum_1^n \frac{d_i}{(V_s)_i}, \quad (5.2)$$

where, d_i is the thickness of layer i and $(V_s)_i$ is the shear wave velocity of layer i .

Table 5.1 presents a comparison of the estimated resonant frequencies to the observed lower transition frequencies for Sites 3, 6 and 9. The Good agreement between these results supports the observations from Bertel (2006).

Table 5.1 Comparison of layer resonant frequencies with mode-transition frequencies for Site 3, 6, and 9.

Site Name	Resonant frequency (Hz)	Transition frequency (Hz)
Site 3	2.0	2.4
Site 6	1.6	1.8
Site 9	2.1	2.3

5.5 Near-Field Effects on Active f - k Analysis

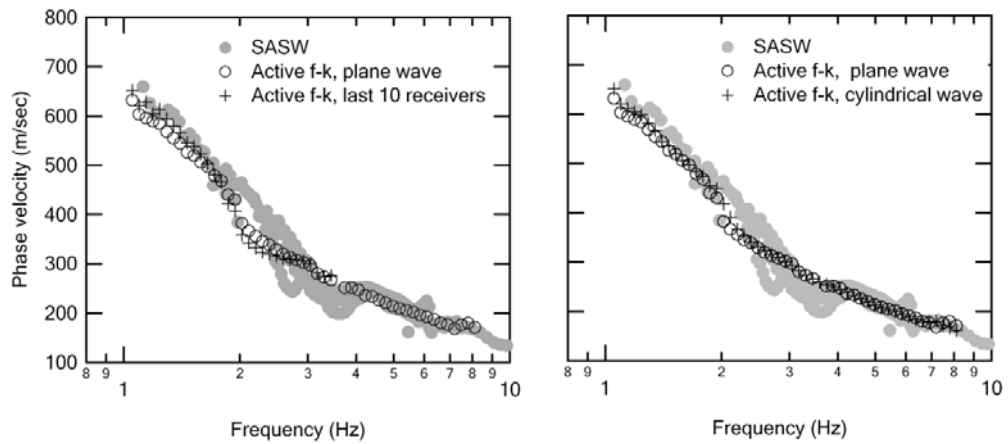
Surface wave measurements require a sufficient offset between the source and the first receiver to allow the surface waves to fully develop and to allow the planar surface wavefield to develop from the cylindrical wavefield. Near-field effects arise when these conditions are not satisfied during the measurements, resulting in lower phase velocity estimates at low frequencies (Sanchez-Salinero, 1987). In the SASW method, the criterion of a near-source offset equal to at least twice the maximum desired wavelength is used to minimize near-field effects (Stokoe et al., 1994). A similar criterion for multi-channel methods like the active-source f - k approach has not been developed. Mitigation of near-field effects on velocity estimates at Sites 2, 3 and 4 is discussed in the next section. An acceptable-source offset criterion based on the observation from this study is also presented in Section 5.5.2.

5.5.1 Mitigation of Near-Field Effects

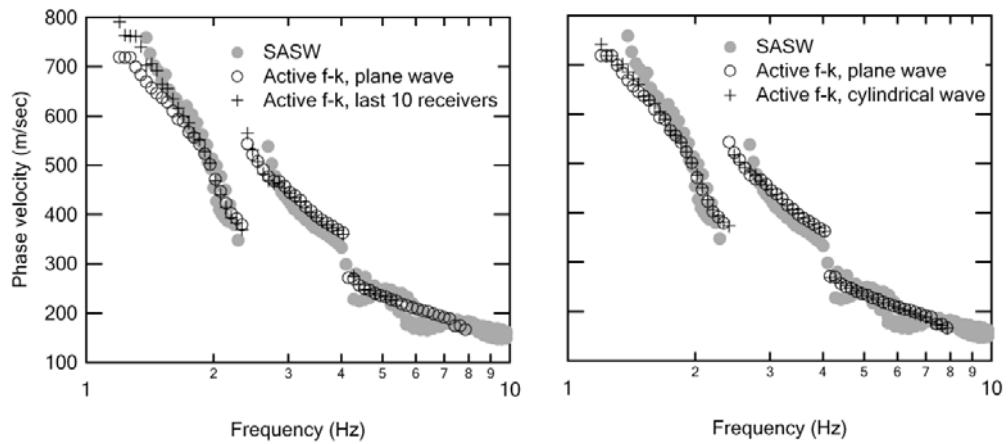
At Sites 2, 3 and 4, active f - k measurements were performed using a single long array with unequal receiver spacing. The source to near receiver offsets were in the range of 30 to 50 m. As shown in Figure 5.2b, 5.2c and 5.2d, the phase velocities estimated for these sites show lower values at long wavelengths, which is likely due to near-field effects.

In order to mitigate the near-field effects, two approaches were examined. The first approach was to increase the near-receiver offset by removing the first 6

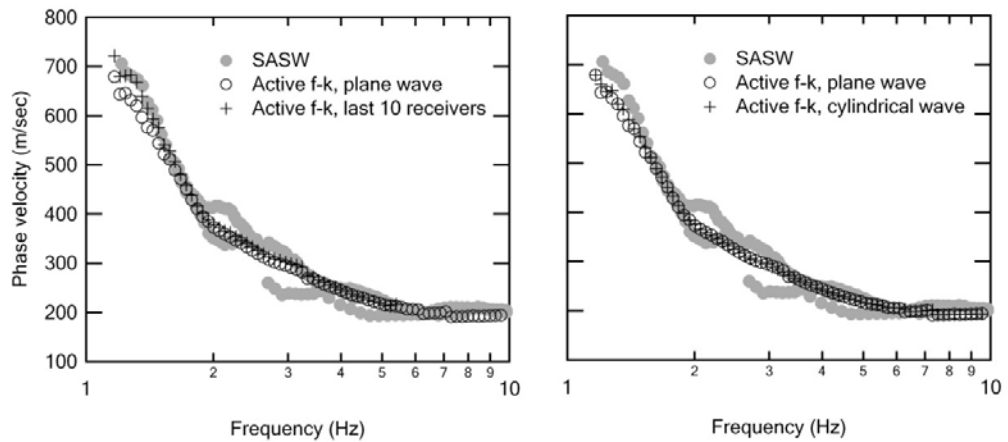
receivers and using only last 10 receivers of the array, while still using the same conventional beamformer based on a planar wavefront assumption. The second approach was to use the same array but perform the cylindrical beamformer analysis based on the cylindrical wavefield model, as proposed by Zywicki (1999). The cylindrical wave beamformer is described in detail in Section 4.3.2 of Chapter 4. Figures 5.11a to 5.11c present the dispersion curves developed at Sites 2, 3 and 4 by using these two approaches. For each site, the percent differences between the modified and initial dispersion curves are compared in Figure 5.12. It can be observed that the percent differences in the velocity values when using the cylindrical beamformer are generally well below 3%, while when using the last 10 receivers the differences range from 4% to 10%. The use of an increased receiver offset brings the dispersion curves into good agreement with the SASW results, while the use of the cylindrical beamformer has a minimal effect. This result suggests that application of the cylindrical beamformer does not account for all effects influencing the velocity estimate.



(a) Site 2



(b) Site 3



(c) Site 4

Figure 5.11 Mitigation of near-field effects by using measurements of last 10 receivers (offset of 100 m) (left column) and using cylindrical wave beamformer (right column) for Sites 2, 3 and 4 in (a), (b) and (c), respectively.

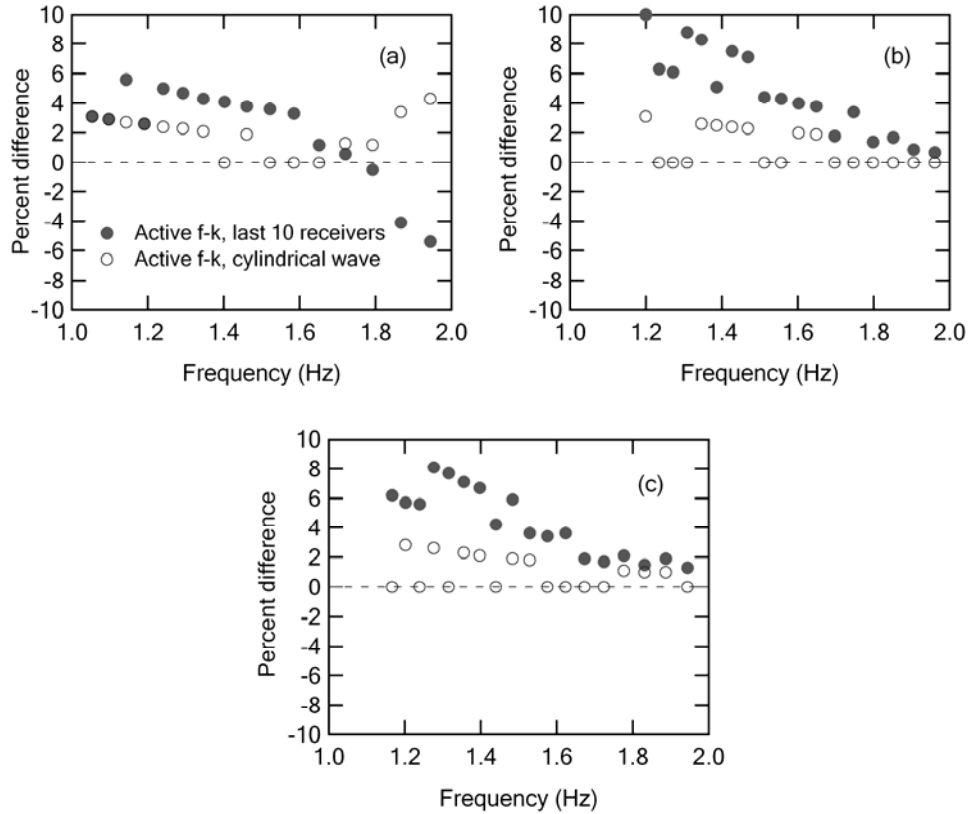


Figure 5.12 Comparison of percent differences corresponding to the two approaches of mitigating near-field effects for Sites 2, 3 and 4 in (a), (b) and (c), respectively.

5.5.2 Near-Field Effect Criterion Based on Observations

In SASW measurements, the near-field criterion is that the measured wavelengths λ_R should not be greater than two times the near-offset d_1 , e.g. $\lambda_R \leq 2d_1$ (Stokoe et al., 1994). For multi-channel linear array methods, no firm criterion has been established, however it seems that the SASW criterion is too restrictive. For example, Miller et al. (1999) presented wavelengths up to 61 m at 6 sites by utilizing a single 48-channel linear array with a 7.3 m near offset and 0.61-m receiver spacing. Park et al. (2002) observed that a source-to-closest receiver distance of 10 m is sufficient to assure plane wave propagation for wavelengths up to

60 m. Yoon (2005) defined the range of the near-field effects in terms of the offset of the array center to the source, d_{AC} , and presented that the longest wavelength is about 1-2 times d_{AC} (dependent on different soil profiles).

As previously mentioned, 2 or 3 arrays of different lengths with equally-spaced receivers were applied at 8 sites. The longest wavelengths that can be interpreted without near-field effects from the shorter array can be estimated by comparing the dispersion curves over the same wavelength range developed from the shorter arrays with those from longer arrays with greater source offsets. For this study, a deviation of 5% was the criterion to establish the point at which near-field effect were important. This procedure is illustrated in Figure 5.13 for Site 8 as an example. As observed from this figure, the dispersion curve obtained using Array 3 (with

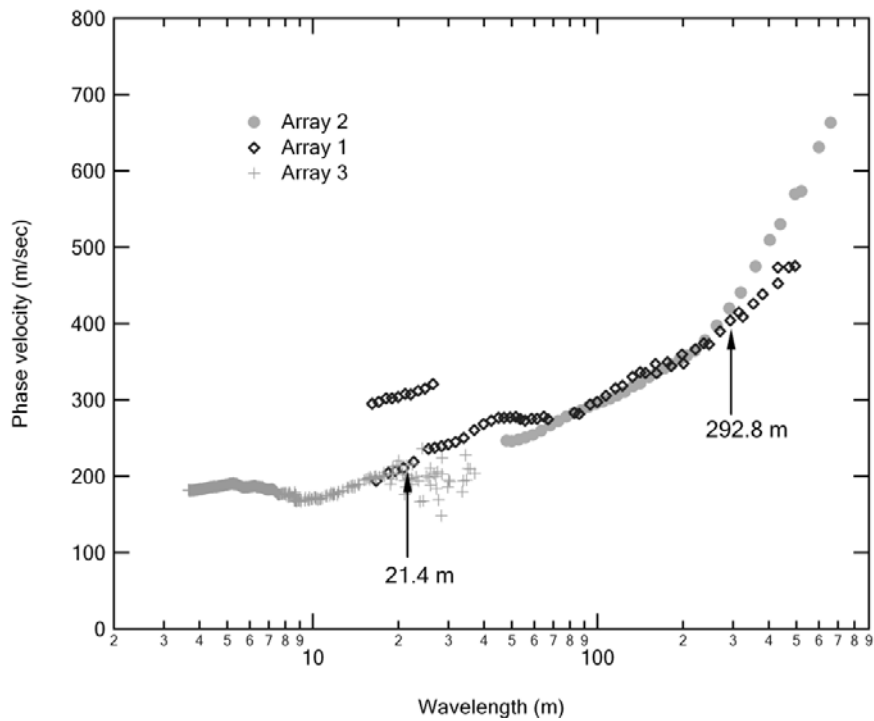


Figure 5.13 Determination of longest wavelength without near-field effects by comparing dispersion curves from shorter array with those from longer array at Site 8.

near-source offset of 5.49 m) shows a good agreement with the dispersion curve obtained using Array 2 (with near-source offset of 40 m) out to a wavelength of 21.4 m. Similarly, the dispersion curve from Array 2 follows the result from Array 1 (160 m) out to a wavelength of 292.8 m, and then starts to diverge. Therefore, 21.4 m and 292.8 m were interpreted as the maximum wavelengths that Array 3 and Array 2 can detect without near-field effects based on the above criterion. Using this analysis at each of 8 sites, criteria for near-field effects based on d_1 and d_{AC} were developed.

Table 5.2 presents the near-field effect criteria observed by comparing dispersion curves from Array 2 and Array 1. Table 5.3 presents the near-field effect criteria observed from comparing dispersion curves from Array 3 and Array 2. As seen from both tables, the near-field effects vary from site to site. The ratio λ_R/d_1 ranges from 3.7 to 9.1, with an average value of 5.7 while the ratio λ_R/d_{AC} ranges from 1.3 to 3.4, with an average value of 2.1. For this study, a conservative value for λ_R/d_1 of 3 to 4 was used for interpreting the maximum λ_R for Array 2.

Table 5.2 Near-field effect criteria observed from comparing dispersion curves from Array 2 with from Array 1.

Site Name	λ_R (m)	d_1 (m)	d_{AC} (m)	λ_R/d_1	λ_R/d_{AC}
Site 1	187.5	30	105	6.3	1.8
Site 5	285.4	50	125	5.7	2.3
Site 6	287.9	60	120	4.8	2.4
Site 7	269.9	60	120	4.5	2.2
Site 8	292.8	40	100	7.3	2.9
Site 9	150.1	40	100	3.8	1.5
Site 10	261.5	30	105	8.7	2.5
Site 11	243.26	60	120	4.1	2.0

Table 5.3 Near-field effect criteria observed from comparing dispersion curves from Array 3 with from Array 2.

Site Name	λ_R (m)	d_1 (m)	d_{AC} (m)	λ_R/d_1	λ_R/d_{AC}
Site 6	38.6	5.49	15.56	7.0	2.5
Site 7	20.3	5.49	15.56	3.7	1.3
Site 8	21.4	5.49	15.56	3.9	1.4
Site 9	24.0	5.49	15.56	4.4	1.5
Site 10	27.7	3.05	8.08	9.1	3.4
Site 11	35.4	5.49	15.56	6.4	2.3

5.6 Summary

A study of SASW and active $f-k$ methods has been conducted by comparing dispersion curves developed up to wavelengths of 600 m at 11 testing sites. Based on this study, the following findings can be summarized:

1. The NEES vibrator proved capable of generate high-quality surface wave signals down to frequencies of less than 1 Hz. With this vibrator, surface waves with wavelengths up to 600 m were successfully measured using both the SASW and active $f-k$ methods.
2. The dispersion curves from the SASW and active $f-k$ methods generally showed the same dispersion trend at each site. However, there were two cases where the dispersion curves were not in agreement.
3. For Sites 2, 3 and 4 where an unequal-spacing array was applied, near-field effects caused lower velocity estimates from the $f-k$ method at long wavelengths (low frequencies). Mitigation of near-field effects was investigated using two approaches: (1) increasing the near-field offsets by using only the last 10 receivers of the array, and (2) performing the

cylindrical wave beamformer. It was shown that the first approach is more effective than the second one for mitigating near-field effects.

4. For Sites 3, 6 and 9, significant differences in the dispersion curves were found over a portion of the frequency range where an abrupt mode transition to a higher mode is present. These differences were found to be due to phase unwrapping errors associated with the abrupt mode transition and are consistent with simulation studies performed by Bertel (2006). Dispersion curves developed from the SASW and active $f-k$ methods came into good agreement when modified phase unwrapping procedures were used.
5. According to Bertel (2006), the abrupt transition to a higher mode was found to be associated with strong shallow velocity contrasts. This is consistent with V_s profiles developed for Sites 3, 6 and 9 (Bailey, 2008), which show a strong soft-over-stiff condition at a depth of 20 to 30 m.

CHAPTER 6

AMBIENT WAVEFIELD CHARACTERISTICS

6.1 Introduction

Sources of ambient vibrations are usually separated into two main categories: natural or man-made. For ambient noise with low frequencies (less than about 1 Hz), the origin is typically natural, mostly associated with the interaction between ocean waves and coasts. For high frequencies (greater than about 1 Hz), the origin is predominantly related to human activities such as traffic or machinery. For deep V_s profiling, ambient vibrations in the frequency range of 1 to 4 Hz are of particular interest because it is generally difficult to actively excite energy in this frequency range.

The focus of this chapter is on the characteristics of the ambient wavefield measured at the eleven test sites located around the northern Mississippi embayment. Relevant characteristics of the ambient energy are presented, namely: (a) amplitude and frequency content, (b) direction and likely sources of the dominant energy, and (c) the number of energy sources. This study will be followed by an examination of the effects of the ambient wavefield characteristics on passive-source surface wave measurements in later chapters.

6.2 Amplitude and Frequency Content

Measurements of ambient vibrations were performed at each of 11 test sites.

The measurement details are presented in Tables 3.6 and 3.8 in Chapter 3. The duration of the recorded measurements ranged from 20 to 60 min. It should be noted that care was taken to avoid extraneous near-field sources of energy (machinery, walking, etc.). Time records of ambient vibrations recorded at Site 1 to Site 11 are shown on the left column in Figures 6.1a to 6.1k. These time records are presented in terms of voltage (each sensor had a nominal sensitivity of 2.8 Volts/cm/sec). To examine the frequency content, the Fourier spectra of these time records were computed, as presented on the right column in Figures 6.1a to 6.1k. To compute the Fourier spectra, the time records were re-sampled using a sampling frequency of 32 Hz. The re-sampled time records were then segmented into blocks with a duration of 64 sec. The number of blocks used is equal to the ratio of the whole duration to the block duration. Fourier spectra were calculated using the fast Fourier transformation (FFT) on each data block. These individual spectra from each segment were then averaged to generate the average Fourier spectra for the whole record. The final spectra, shown in Figure 6.1, were created by applying sensor calibrations to the average spectra in order to remove the drop-off in response due to the response below the 1-Hz resonant frequency of the sensors.

From Figure 6.1, it can be observed that the amplitudes of the ambient vibrations are highly variable from site to site. Higher ambient vibration levels were recorded at Sites 1, 2, 4, 5 and 7 as compared to Sites 3, 6, 8, 9, 10 and 11. Sites 8 and 9, in particular, exhibited much lower ambient vibration levels than the other sites, with peak values that were about an order of magnitude lower than those measured at

Sites 1 and 7. As mentioned in Chapter 3, Site 5 is the only urban site in this study. As expected, high ambient levels were observed at this site where several major roadways (including Interstates 40 and 240) run within 2 to 3 km (Figure 3.14). It is interesting to note, however, that the highest ambient levels were observed at two sites, Site 1 and 7. Site 1, for example, has no major roadways running closer than 12 km from the array, as shown in Figure 3.6. Likely sources of this energy are discussed in the next section.

Though the amplitudes were variable, the frequency content was generally similar among the eleven sites. It is important to note that all of these sites, which were distributed over a distance of about 180 km and were recorded at different times (2006 and 2007), exhibited high ambient vibration levels at frequencies that are favorable for long-wavelength surface wave dispersion measurements. At each site, similar trends were observed with low amplitude levels above 4 to 5 Hz, peak values in the range of 1 to 4 Hz, and a pronounced decrease in amplitude below a frequency of around 1 Hz. The amplitude decrease below 1 Hz is likely due to source characteristics, although it is possible that it is due to a filter effect from a soft sedimentary layer near its resonant frequency (Scherbaum et al., 2003).

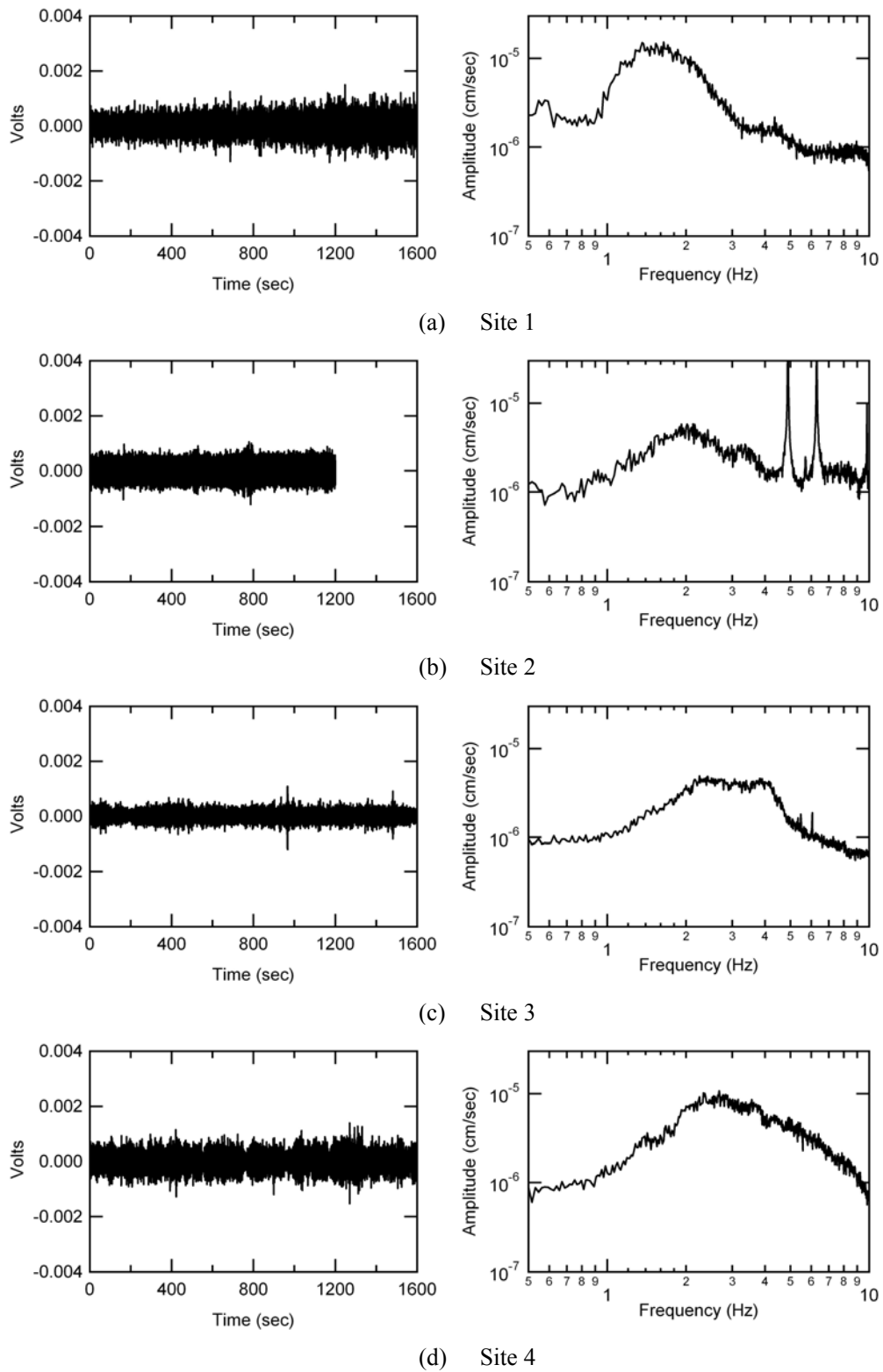
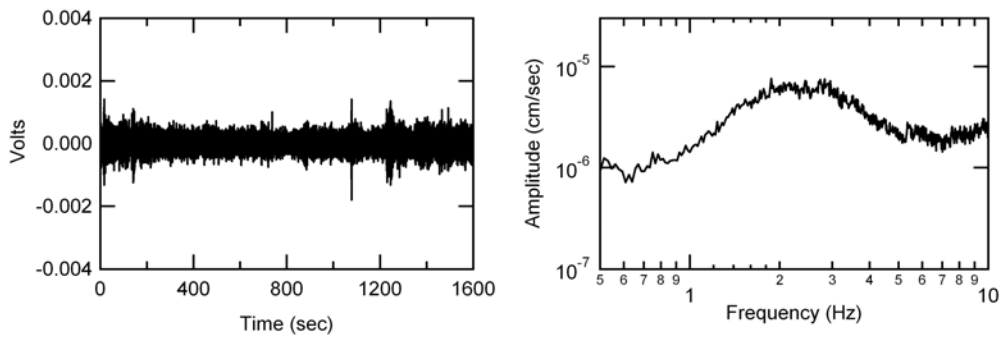
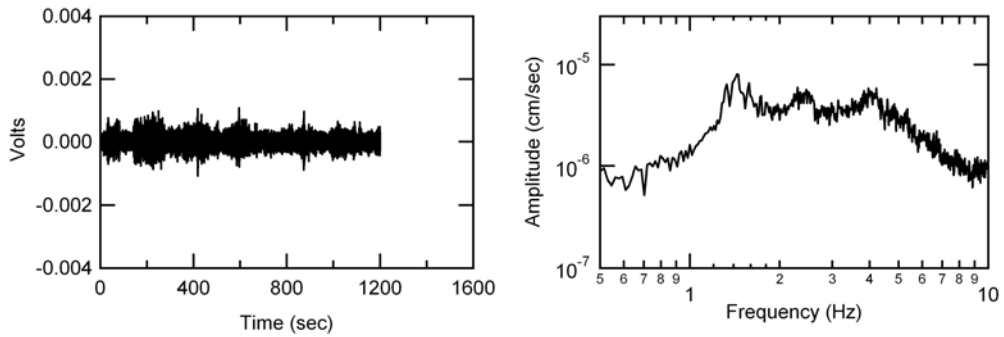


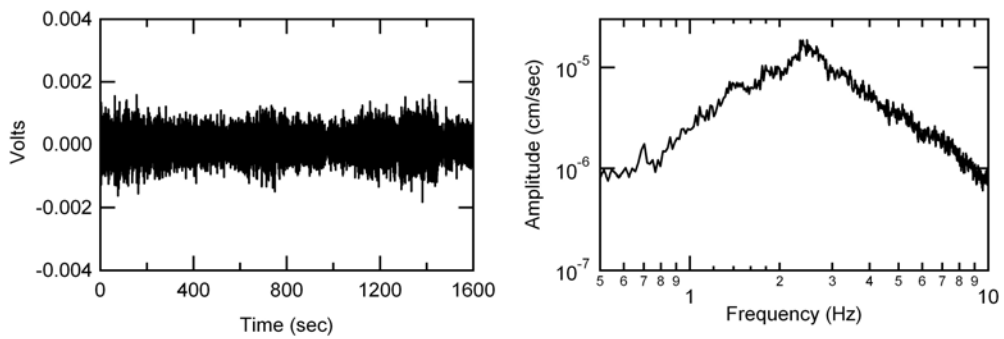
Figure 6.1 Time records (left column) and associated Fourier spectra (right column) at Site 1 through Site 11, in (a) through (k), respectively.



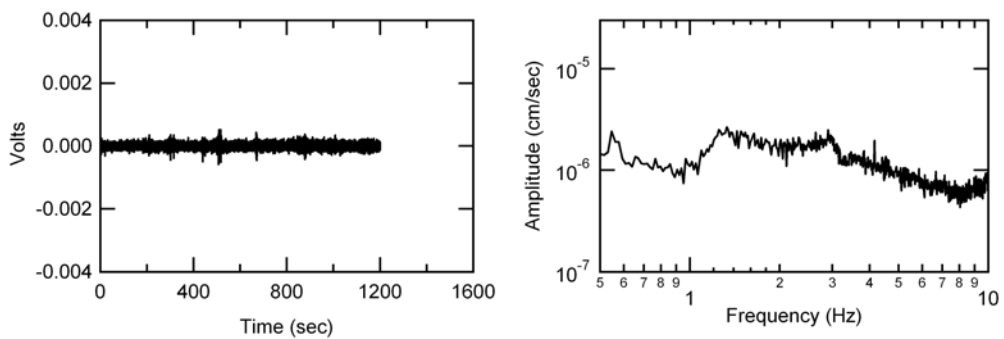
(e) Site 5



(f) Site 6

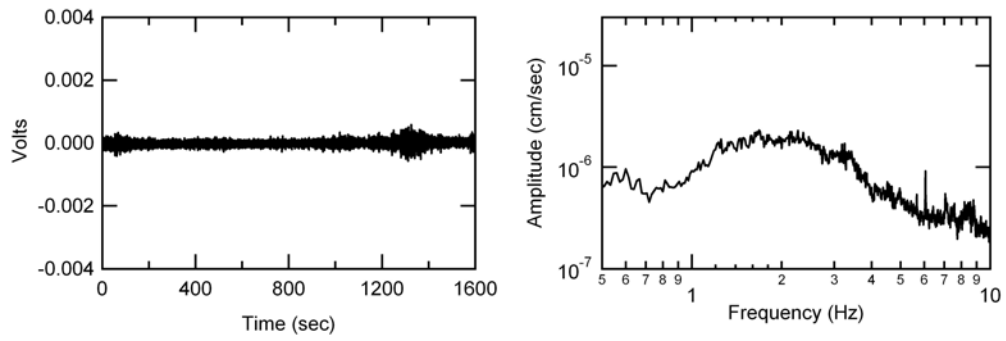


(g) Site 7

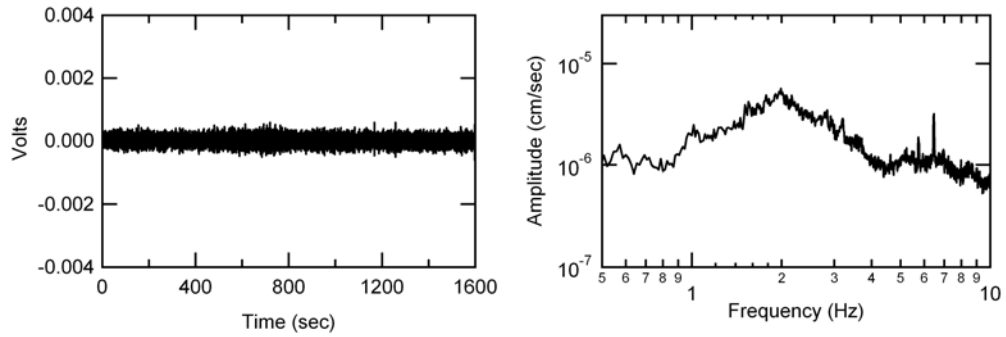


(h) Site 8

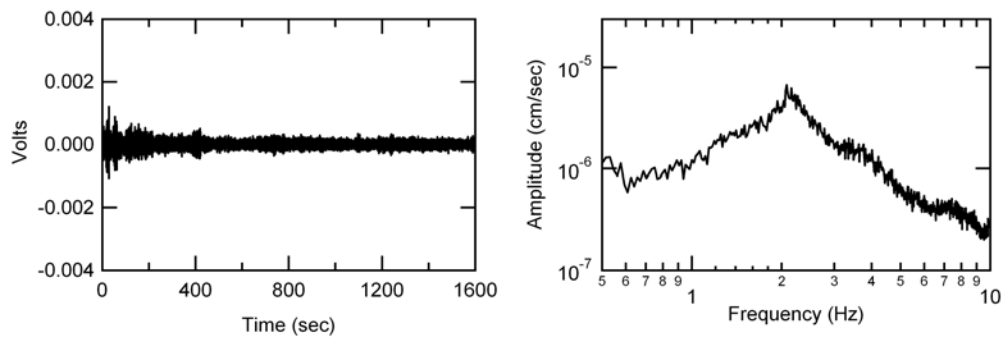
Figure 6.1 (Cont.) Time records (left column) and associated Fourier spectra (right column) at Site 1 through Site 11, in (a) through (k), respectively.



(i) Site 9



(j) Site 10



(k) Site 11

Figure 6.1 (Cont.) Time records (left column) and associated Fourier spectra (right column) at Site 1 through Site 11, in (a) through (k), respectively.

6.3 Direction of the Dominant Energy

At five of the measurement sites (Site 1, Site 3, Site 5, Site 9 and Site 10), ambient vibrations were recorded using large-diameter (200 m) circular arrays. The measurement procedures and array configurations are described in Section 3.5.3 of Chapter 3. Similar measurements were not performed at the other six sites due to space limitations that did not allow for deployment of the large circular arrays.

Ambient vibration records were processed using the conventional FDBF method, MUSIC method (noise subspace dimension equal to 12) and Capon's method, as discussed in Section 4.4.3. These three approaches provided similar results in most cases. However, propagation directions estimated from the MUSIC method are presented here because this method provided higher resolution than the FDBF method, and yielded more consistent results at some sites where Capon's method produced scattered results.

In Figures 6.2a to 6.6a, the propagation direction of the dominant energy is shown in terms of the backazimuth angle versus frequency for Sites 1, 3, 5, 9 and 10, respectively. This backazimuth angle is relative to the NS-EW coordinate system, assuming a positive angle when rotated clockwise from north. As mentioned in Section 4.4.4 of Chapter 4, the arrival direction (azimuth angle) of the dominant signal was first determined by the peak wavenumber (k_x, k_y) using Equation 4.22 in the x - y coordinate system. The azimuth angle was then transformed to the NS-EW coordinate system based on the relationship of the x - y coordinate system to the NS-WE system is shown. This relationship can be seen for each site in Figures 6.7,

6.9, 6.11, 6.13 (6.15), and 6.17 for Sites 1, 3, 5, 9, 10, respectively. The same direction distribution data are presented in the NS-EW coordinate system in Figure 6.2b to 6.6 b. In Figure 6.2c to 6.6c, maps are presented showing the locations of major roadways close to Site 1, 3, 5, 9 and 10.

As can be observed from these figures, the direction of dominant energy varied from site to site. At most sites the direction of dominant signal is relatively consistent at low frequencies (less than 3 to 4 Hz). At higher frequencies, however, the source direction was generally more scattered.

At most of the sites the direction of the dominant energy is generally consistent with the location of major roadways. At Site 3, two distinct source directions were observed, as shown in Figure 6.3a and 6.3b. In the frequency range of 1.5 to 3.0 Hz, sources originate from the S to SE, which is consistent with both Interstate 55 and Highway 18, as shown in Figure 6.3c. In the frequency range of 3.0 to 6.5 Hz, a very stable source direction from the NW is observed. The source of energy in this frequency range is not clear, as the closest roadway (Highway 412) is located over 20 km from the site in this direction. The possible source could be farm equipment operating in the area. As shown in Figure 6.4, at frequencies less than 3 Hz, Site 5 exhibits stable energy sources from the NW which is consistent with Interstate 40/240, located about 2 km to the west of the array. At higher frequencies, more scattered source directions were observed, which is due to many heavily travelled roads in the region, such as Walnut Grove Road which runs about 0.5 km to the south and the Germantown Parkway which runs about 4 km to the east. For Site 10 (Figure 6.6), the propagation direction is consistent with Interstate 55 which runs about 5 km

to the southwest at its closest point. Also, the Mississippi River is a possible energy source because it is located less than 1 km to the southwest at its closest point. At Site 1, the source direction for frequencies in the range of 1.0 Hz to 3.3 Hz clusters about a backazimuth angle of about 15° clockwise from the north, as shown in Figure 6.2a and 6.2b. As shown in Figure 6.2c, there are no major roadways located within 20 km of the site in this direction. However, the Mississippi River is just about 1 km to the northeast and is probably the source of the ambient vibrations.

Site 9 showed different results from the other four sites. As previously mentioned, Site 9 was the only site where measurements were performed at two different times. Slightly different array configurations, Array B and Array C, were used for the two measurements. Configurations of Array B and Array C are presented in Table 3.7 in Chapter 3. Using Array B, very scattered results were obtained showing a broad range of source directions, as shown in Figure 6.5a and 6.5b. The energy coming from the north is consistent with Highway 412 which runs about 3 km to the north of Site 9. However, the source of energy coming from the southwest is not apparent. Interstate 55 runs about 9 km to the east at its closest point, but does not appear to be the dominant source of energy. The measurement was repeated 30 minutes later using Array C. Array C showed more localized results with different directions from those obtained using Array B. For this case, Interstate 55 to the east was the dominant source of energy. The reason for these differences is not known. However, it does suggest that there are several sources of energy with similar amplitude and the dominant energy direction varies considerably with time. The multi-source nature of this site is discussed further in the next section.

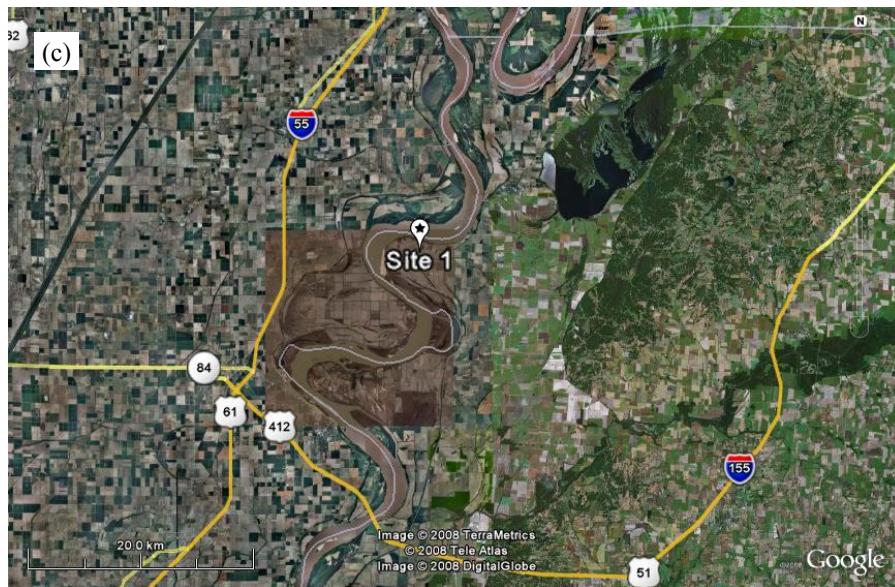
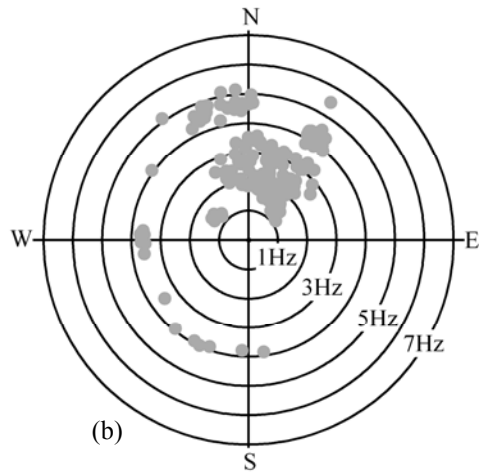
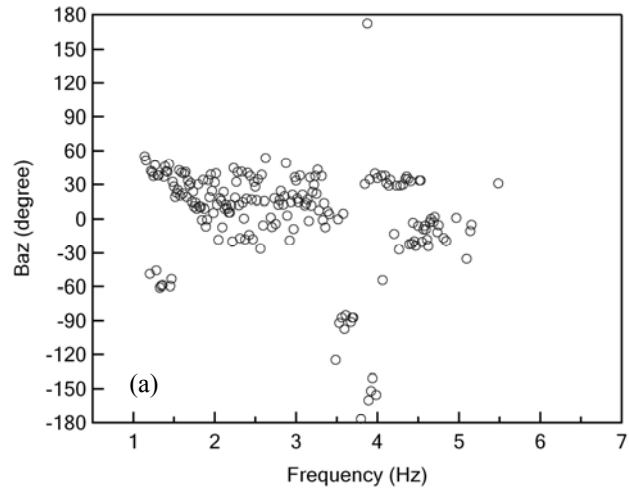


Figure 6.2 Plots showing (a) wave directions at Site 1 in terms of back azimuth versus frequency, (b) wave directions in NS-EW coordinate system, and (c) Google Earth image of major roadways close to Site 1 (same as Figure 3.6).

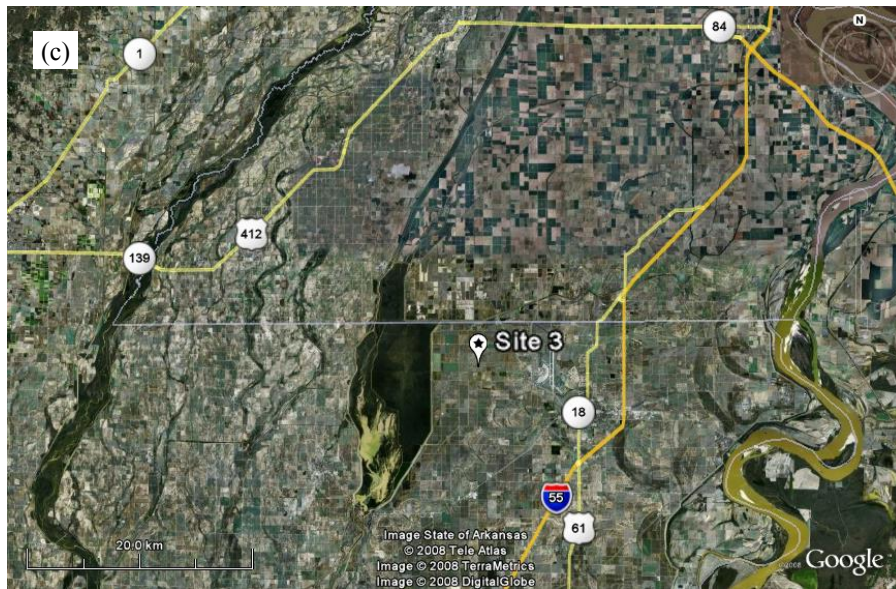
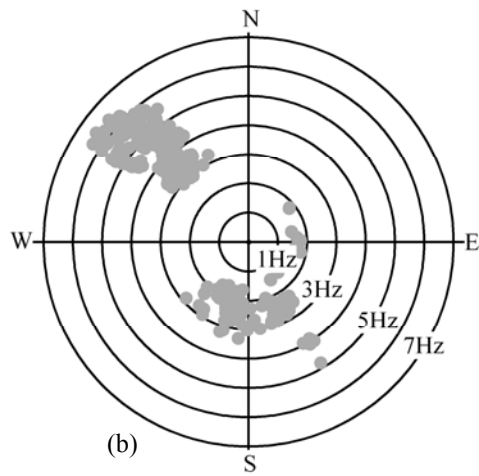
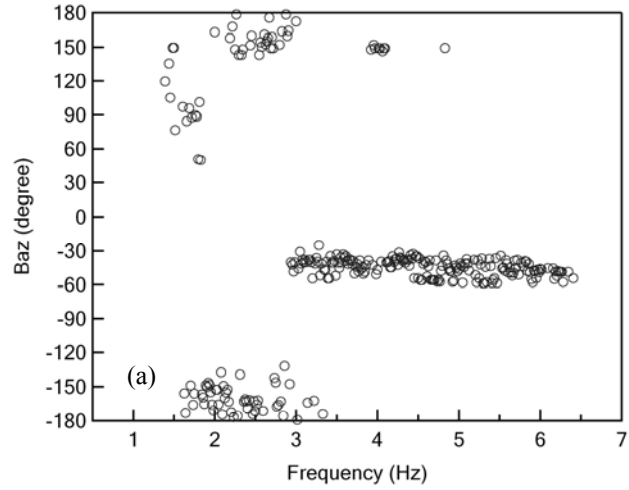


Figure 6.3 Plots showing (a) wave directions at Site 3 in terms of back azimuth versus frequency, (b) wave directions in NS-EW coordinate system, and (c) Google Earth image of major roadways close to Site 3 (same as Figure 3.10).

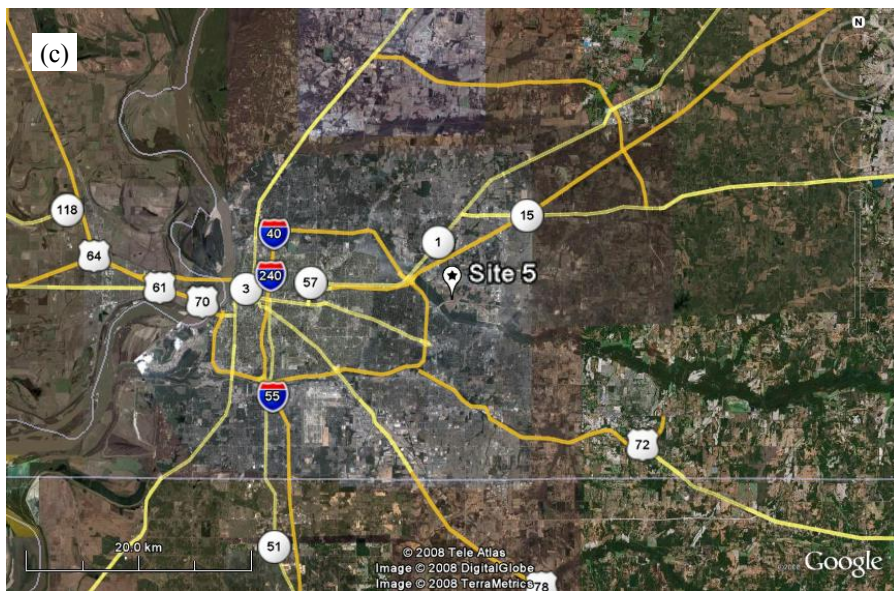
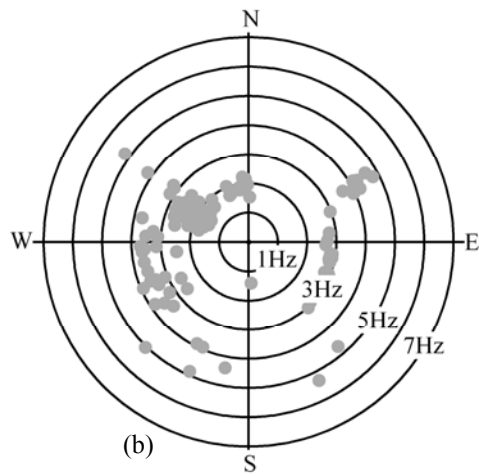
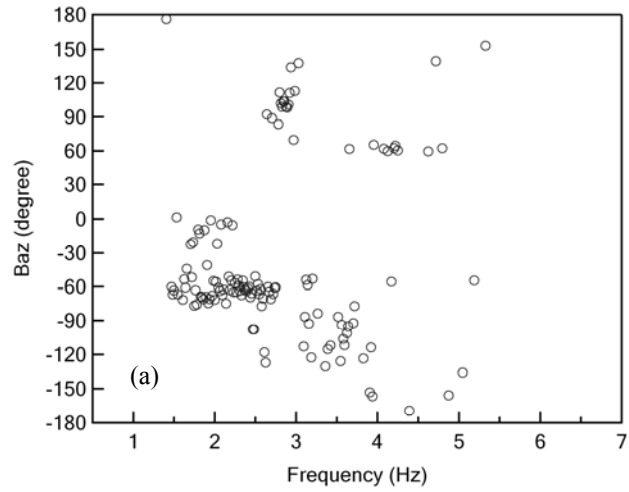


Figure 6.4 Plots showing (a) wave directions at Site 5 in terms of back azimuth versus frequency, (b) wave directions in NS-EW coordinate system, and (c) Google Earth image of major roadways close to Site 5 (same as Figure 3.14).

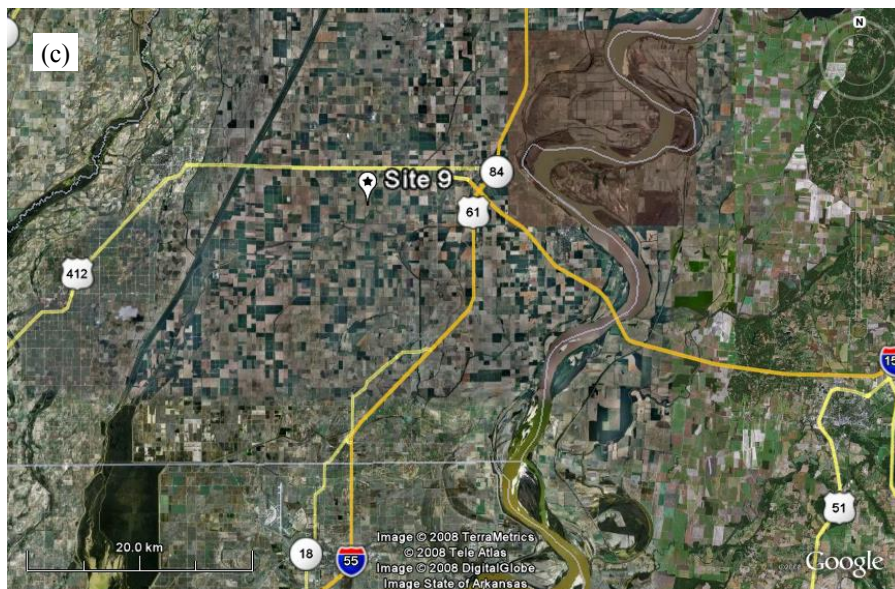
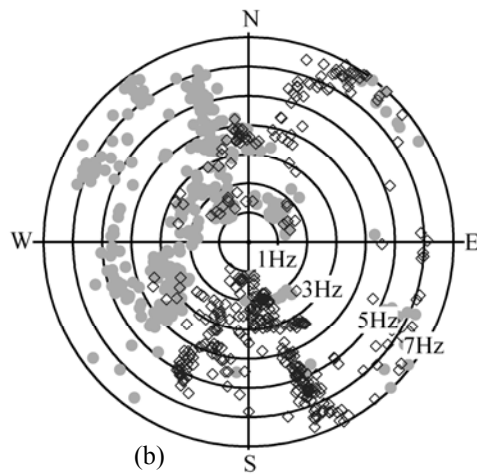
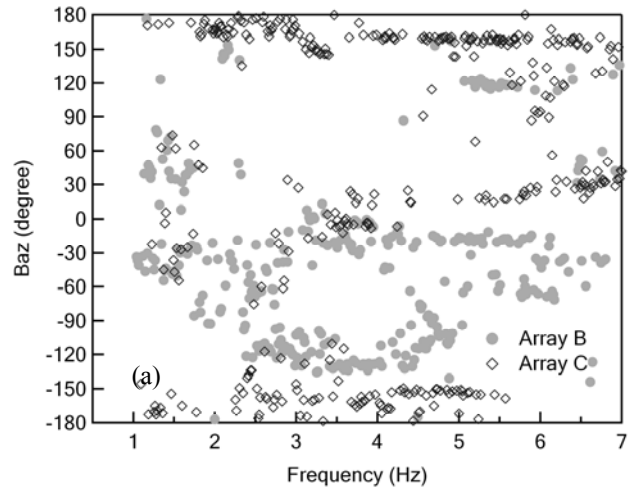


Figure 6.5 Plots showing (a) wave directions at Site 9 in terms of back azimuth versus frequency, (b) wave directions in NS-EW coordinate system, and (c) Google Earth image of major roadways close to Site 9 (same as Figure 3.22).

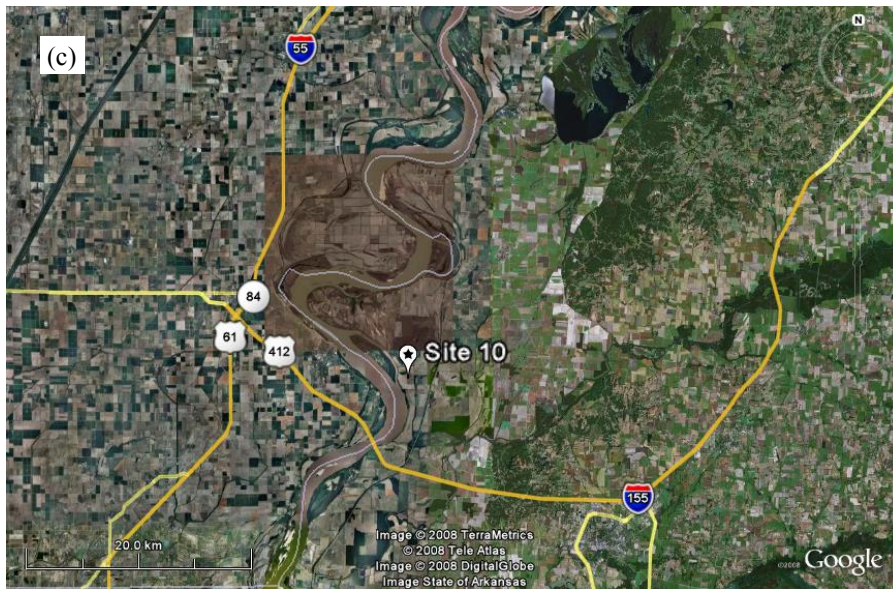
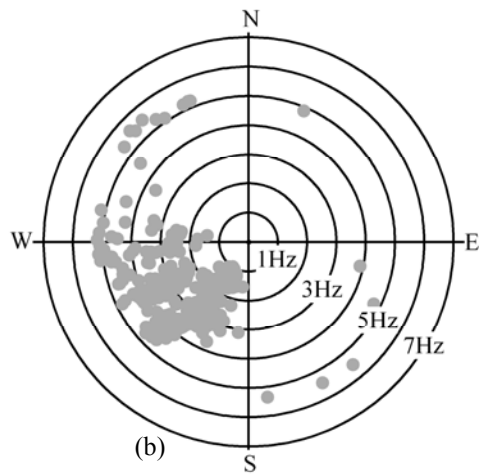
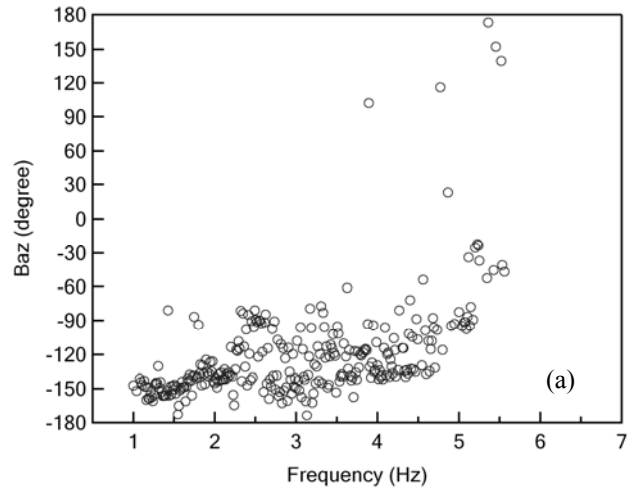


Figure 6.6 Plots showing (a) wave directions at Site 10 in terms of back azimuth versus frequency, (b) wave directions in NS-EW coordinate system, and (c) Google Earth image of major roadways close to Site 10 (same as Figure 3.24).

6.4 Number of Energy Sources

Using the contour power plots developed from passive f - k analysis (Section 4.4.3 of Chapter 4), it is possible to determine if the ambient wavefield is composed of a single source or multiple sources. This will have important implications on the efficacy of the ReMi approach, as discussed in Chapter 8. For each of the five sites, the power plot for each frequency was calculated using the conventional FDBF, MUSIC (noise subspace dimension equal to 12) and Capon's methods. The local x - y coordinate system used for each site is shown in Figure 6.7, 6.9, 6.11, 6.13 (and 6.15), and 6.17 for Sites 1, 3, 5, 9 and 10, respectively. The MUSIC method showed the best ability to localize multiple sources, so only the power plot estimated from MUSIC are presented and discussed in this section. There is no easy way to display the changing characteristics of the power plots with frequency. Therefore, to illustrate wavefield characteristics changing with frequency at each site, four frequencies of near 1.5 Hz, 2.5 Hz, 3.5 Hz and 5.0 Hz have been chosen to be displayed. Contour power plots at four frequencies are presented in Figure 6.8, 6.10, 6.12, 6.14 (and 6.16), and 6.18 for Sites 1, 3, 5, 9 and 10, respectively. In each contour plot, twenty contour levels were used between the maximum and minimum power values.

The ambient wavefield generally showed different characteristics at frequencies above and below 3 Hz. As can be observed from Figures 6.8, 6.10, 6.12, 6.14 (and 6.16), and 6.18, at low frequencies (below 3 Hz) the wavefield is dominated by one or two sources in most cases, with the notable exception of Site 9. The same energy source direction that is present at low frequencies, tends to also be seen at

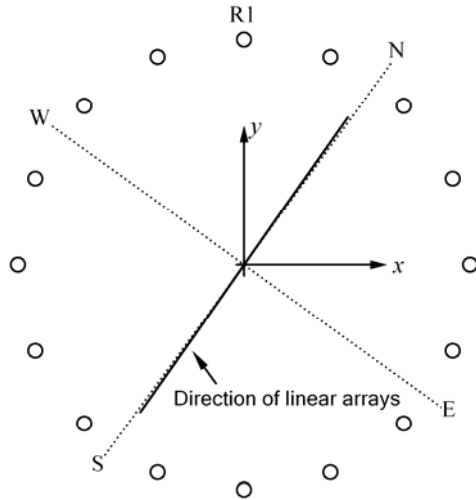


Figure 6.7 Relative location of x - y coordinate of Array A to NS-WE coordinates at Site 1.

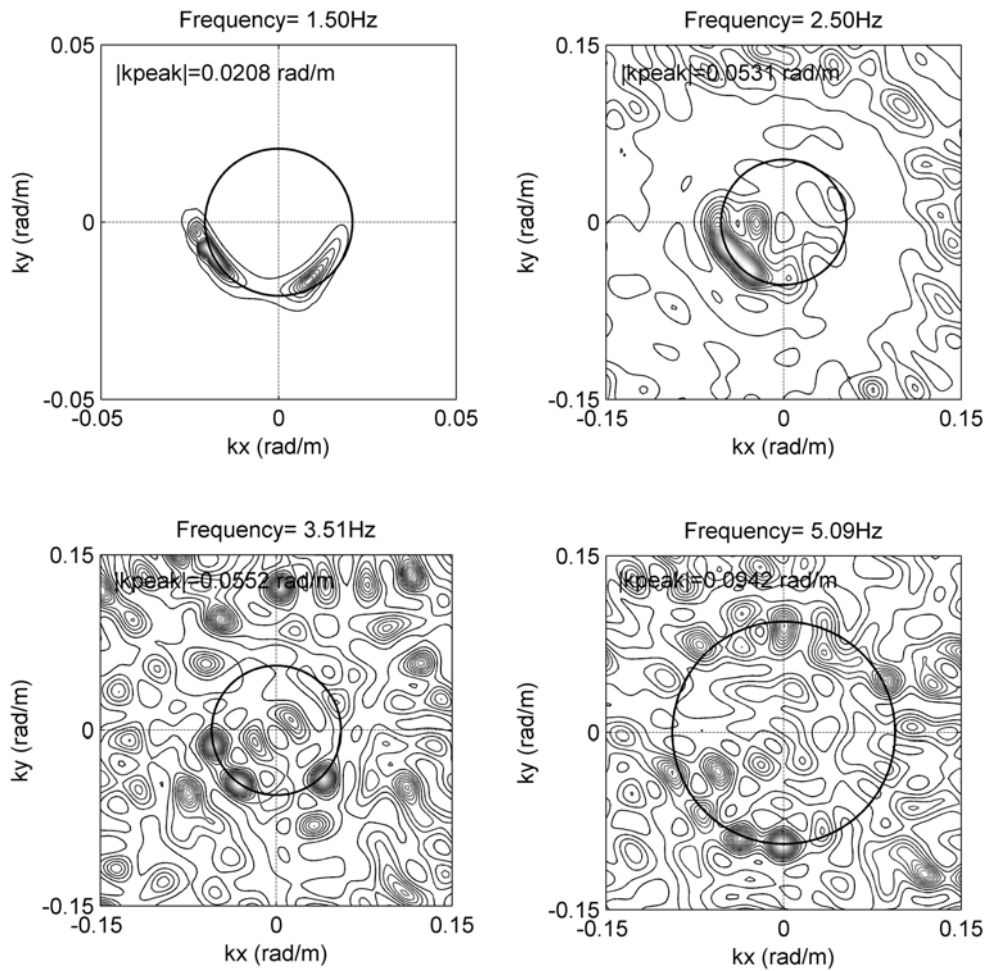


Figure 6.8 Contour plots of power spectra at 1.50 Hz, 2.50 Hz, 3.51 Hz and 5.09 Hz estimated from the MUSIC method at Site 1 using Array A.

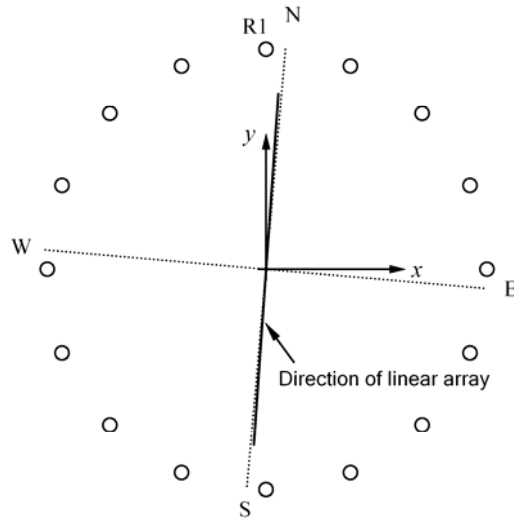


Figure 6.9 Relative location of x-y coordinate of Array A to NS-WE coordinate at Site 3

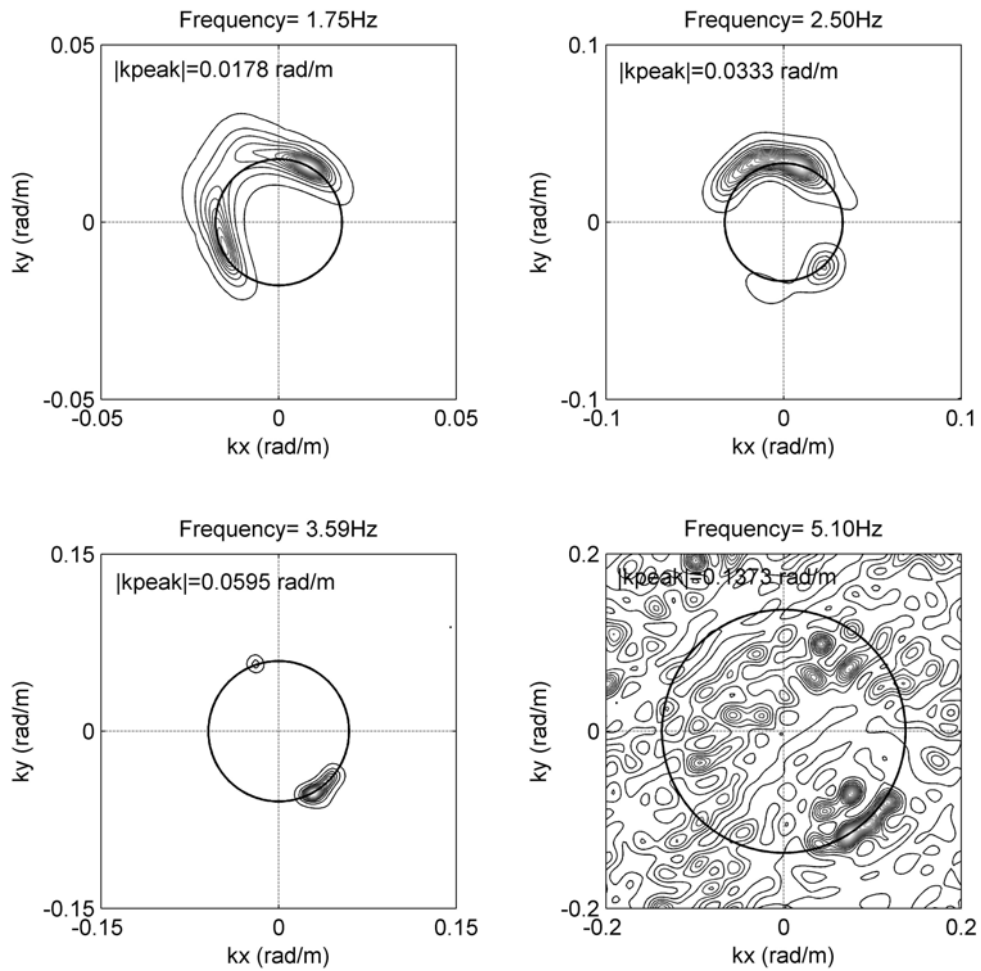


Figure 6.10 Contour plots of power spectra at 1.75 Hz, 2.50 Hz, 3.59 Hz and 5.10 Hz estimated from the MUSIC method at Site 3 using Array A.

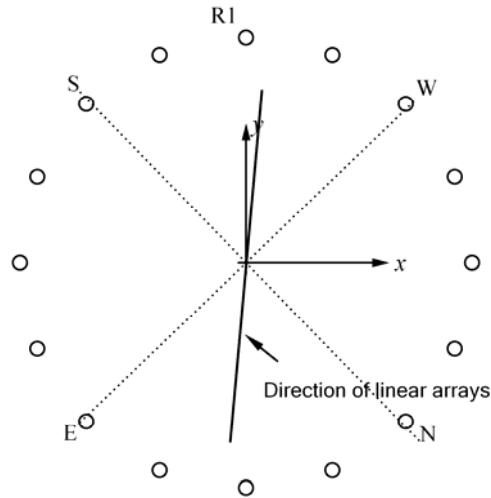


Figure 6.11 Relative location of x - y coordinate of Array A to NS-WE coordinate at Site 5

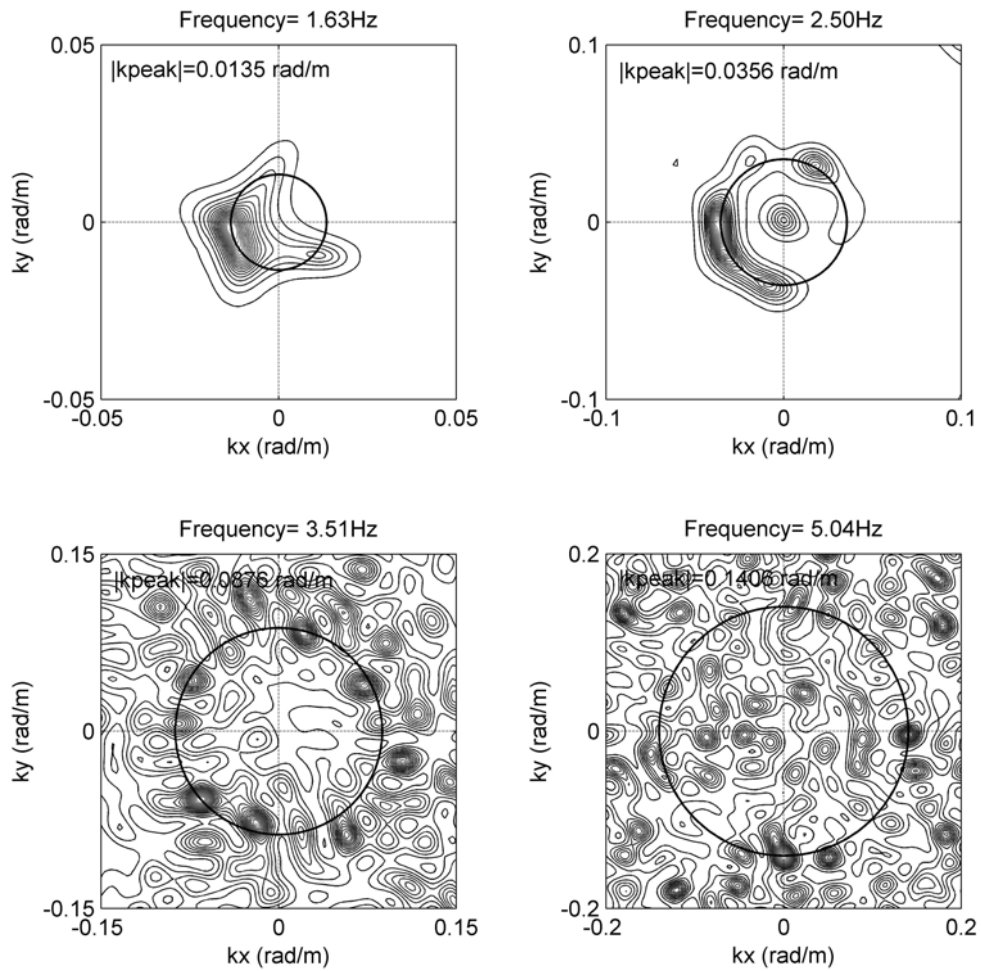


Figure 6.12 Contour plots of power spectra at 1.63 Hz, 2.50 Hz, 3.51 Hz and 5.04 Hz estimated from the MUSIC method at Site 5 using Array A.

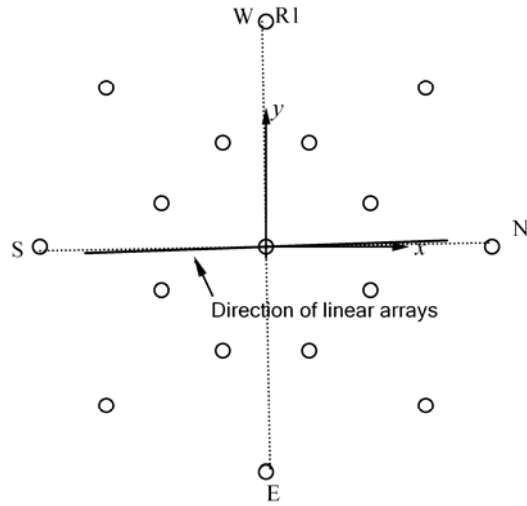


Figure 6.13 Relative location of x - y coordinate of Array B to NS-WE coordinate at Site 9

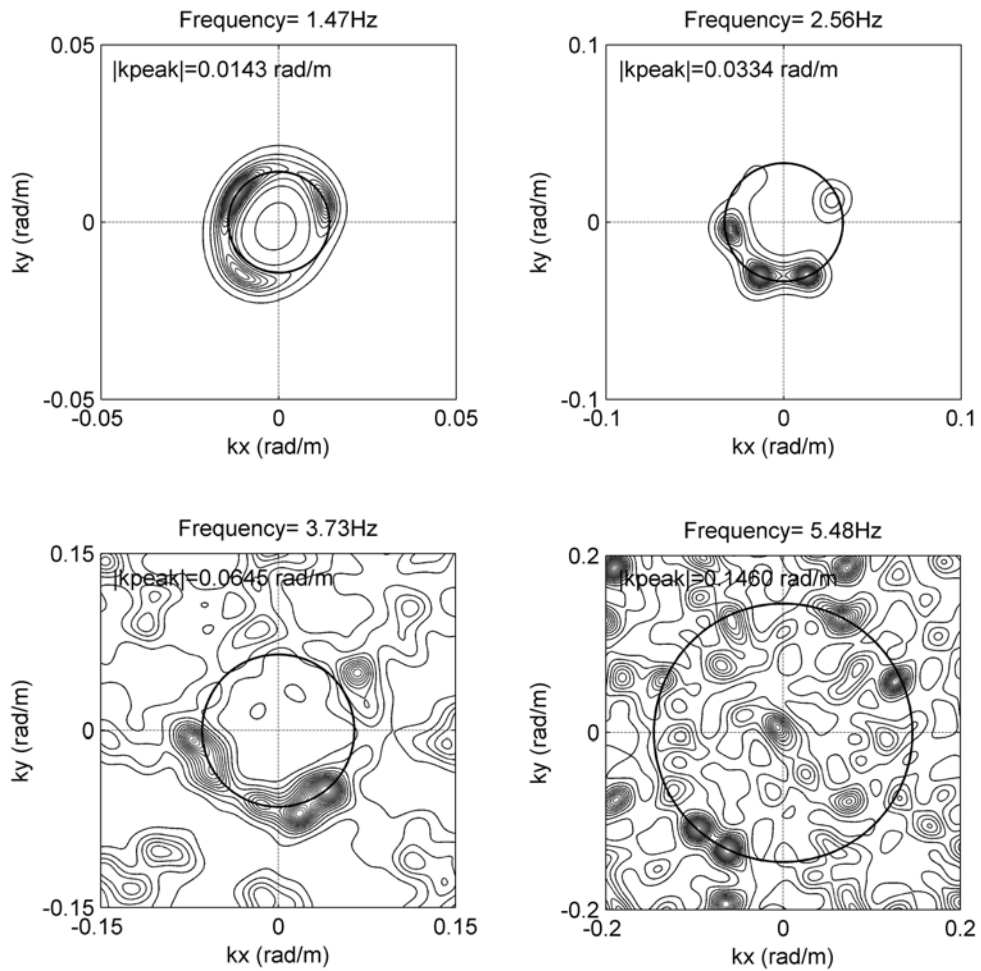


Figure 6.14 Contour plots of power spectra at 1.40 Hz, 2.56 Hz, 3.60 Hz and 5.48 Hz estimated from the MUSIC method at Site 9 using Array B.

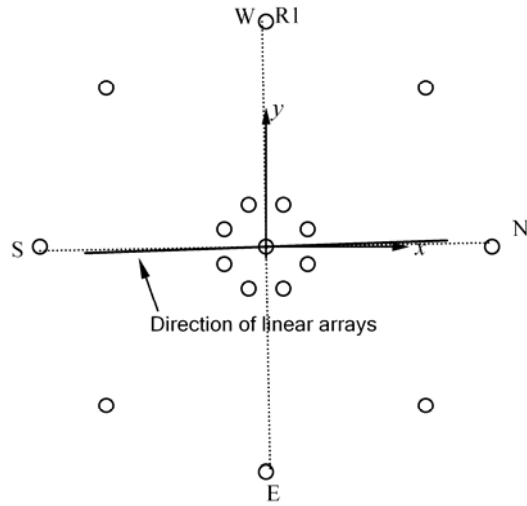


Figure 6.15 Relative location of x - y coordinate of Array C to NS-WE coordinate at Site 9

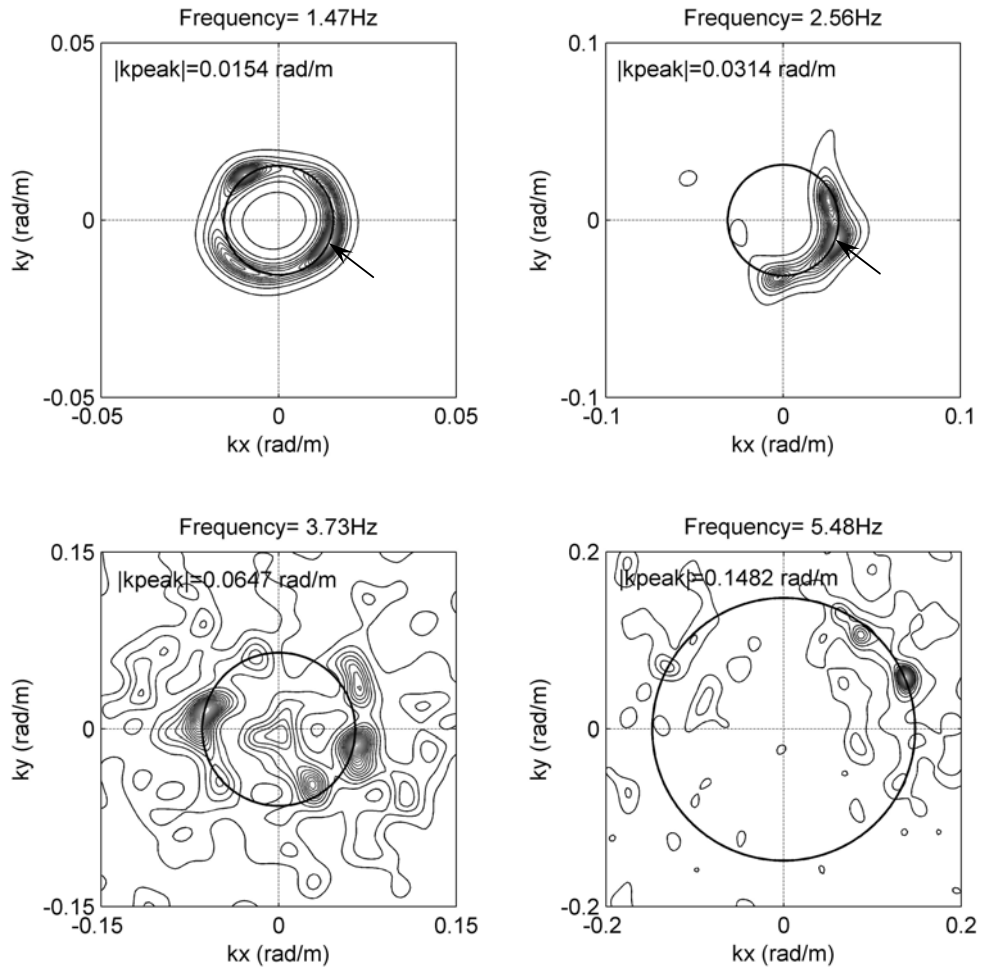


Figure 6.16 Contour plots of power spectra at 1.36 Hz, 2.56 Hz, 3.60 Hz and 5.48 Hz estimated from the MUSIC method at Site 9 using Array C.

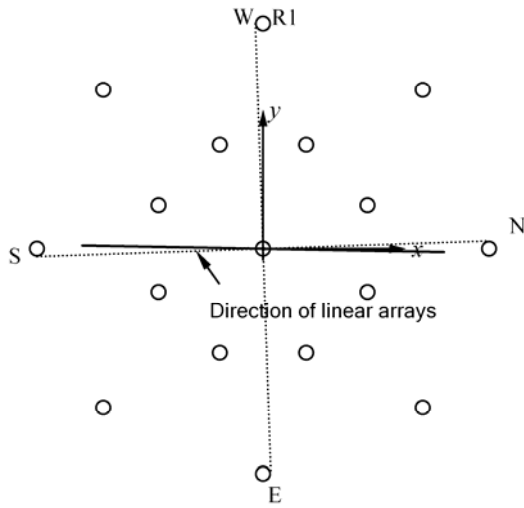


Figure 6.17 Relative location of x-y coordinate of Array B to NS-WE coordinate at Site 10

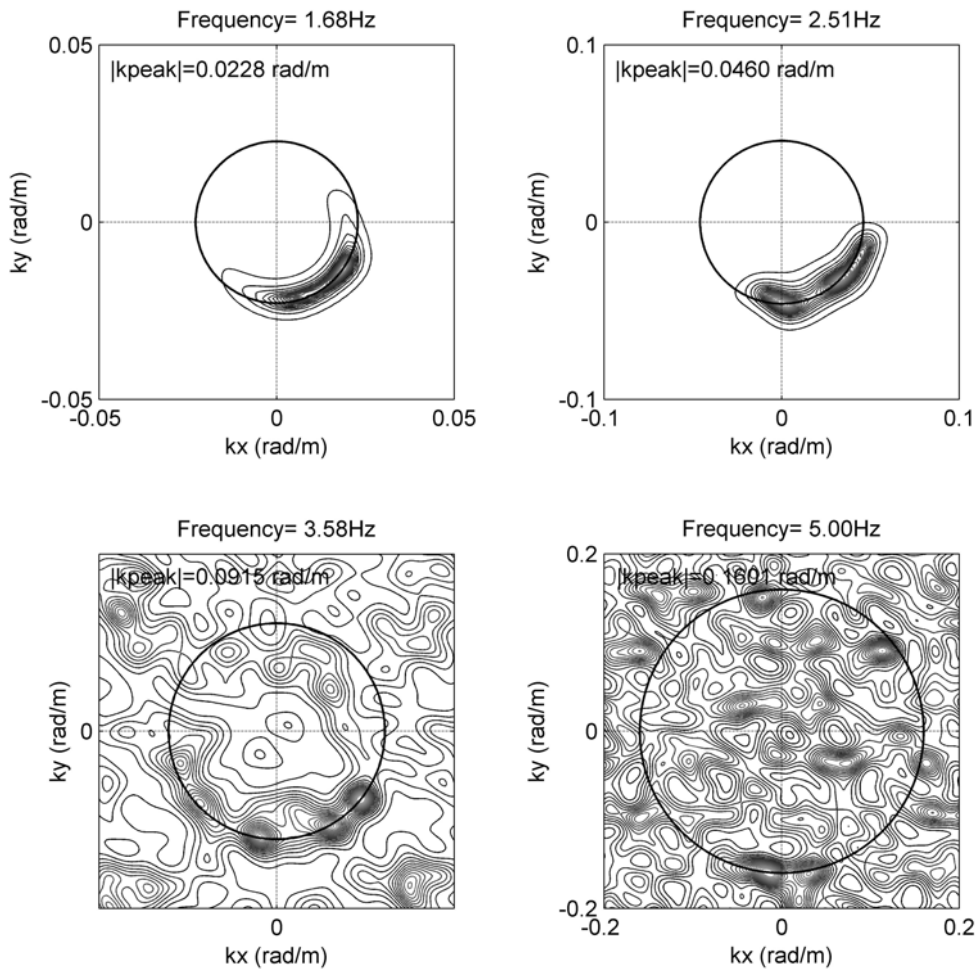


Figure 6.18 Contour plots of power spectra at 1.68 Hz, 2.51 Hz, 3.58 Hz and 5.00 Hz estimated from the MUSIC method at Site 10 using Array B.

higher frequencies (above 3 Hz), but additional sources from different directions are also evident, particularly at Sites 1 and 10, in Figures 6.8 and 6.18, respectively. Site 3 is an exception to this observation. As shown in Figure 6.10, an energy source, appearing at 2.5 Hz but with less dominant power, becomes the single dominant source at frequencies of 3.59 Hz and 5.10 Hz. The difference between the rural and urban wavefield is evident at high frequencies. As shown in Figure 6.12, Site 5 shows multiple energy sources, distributed over many directions at higher frequencies (3.51 Hz and 5.09 Hz). The rural sites also showed multiple sources at high frequencies but were generally distributed over a smaller range of directions and had fewer energy sources as compared to Site 5.

As discussed in the previous section, the two measurements performed at Site 9 using Array B and Array C exhibited very different dominant source directions as shown in Figure 6.5. From Figure 6.14 and 6.16, it can be observed that although the dominant energy sources were different at most frequencies between these two measurements, some of the source directions were observed in both measurements. For example, at a low frequency of 1.47 Hz three source directions are consistent in both measurements. At 5.48 Hz, an energy source from the SE (from the origin to power peak) is common in both measurements. Some source directions are present in the Array C measurement, but not present in the Array B measurement, and vice versa. In Figure 6.16, a source direction from the SW (from the origin to power peak marked by arrow) is dominant at 1.47 Hz and 2.56 Hz using Array C, but it is not apparent in Array B measurement. At 5.48 Hz, two dominant energy sources from the NW (from

the origin to power peaks) are observed with the Array B measurement, but are not evident in the later Array C measurement. These observations demonstrate again that the dominant energy directions are time variable at this site.

6.5 Summary

The ambient wavefield characteristics, including: (a) energy amplitude and frequency content, (b) direction and likely sources of the dominant energy and (c) number of energy sources, have been presented for the eleven test sites located throughout the northern Mississippi embayment. Based on this study, the following findings can be summarized:

1. The energy amplitudes of the ambient vibrations were highly variable from site-to-site, but the frequency content was generally consistent with highest levels in the frequency range of 1 to 4 Hz. Energy levels at some rural sites were higher than that at the urbanized site.
2. At most sites the directions of the dominant signals was relatively consistent at low frequencies (less than 3 to 4 Hz), while at higher frequencies, the source direction was generally more scattered. The direction of dominant energy was generally consistent with the location of major roadways, or in some cases the Mississippi River.
3. The wavefield was generally dominated by one or two sources at low frequencies (below 3 Hz), but exhibited multiple distributed sources at higher frequencies.

4. Site 9 was the only site where measurements were performed at two different times separated by 30 minutes. The two measurements resulted in very different dominant source directions, indicating changing source characteristics with time.

CHAPTER 7

DISPERSION CURVE COMPARISON BETWEEN PASSIVE AND ACTIVE f - k METHODS

7.1 Introduction

Compared to active-source measurements, passive-source measurements which utilize the ambient vibrations in the area have the advantages of: lower cost, simpler equipment deployment, and no environmental issues such as noise and vibration. Passive surface wave measurements have often been used to supplement active-source methods as a means to extend the maximum wavelength measured, and increase the depth of the V_s profile penetration. However, due to the inability to actively excite surface wave energy at low frequencies, there are no direct comparisons of long-wavelength (200 m or greater) dispersion curves from active and passive methods.

Ambient vibration measurements using large-diameter circular receiver arrays were performed at five sites in the northern Mississippi embayment, as discussed in Chapter 3. The data processing procedures used in this study (the conventional FDBF, MUSIC and Capon's passive f - k methods) were described in Chapter 4. This chapter is devoted to comparing the dispersion curves developed from active f - k and passive f - k methods and identifying issues affecting the reliability of the passive dispersion measurements. The effects of a multiple source wavefield on passive f - k estimates are also studied and discussed.

7.2 Comparison of Dispersion Curves Developed from Passive and Active f - k Methods

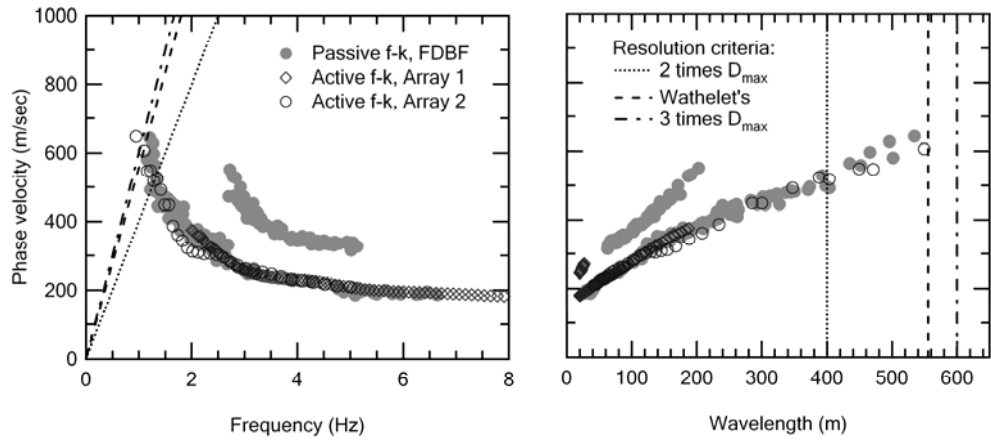
7.2.1 Performance of Conventional FDBF Method

At each of the five sites, the active f - k method and the conventional FDBF passive f - k method were applied independently to develop phase velocity dispersion curves out to wavelengths of about 600 m. Comparison between the results from the active and passive measurements are presented for Sites 1, 3, 5, 9 and 10 in Figures 7.1a, 7.1b, 7.1c, 7.1d (and 7.1e), 7.1f. For Site 3, active-source dispersion curves developed from the last 10 receivers were used in order to reduce the near-field effects. At Site 9, as previously mentioned, the passive-source measurement was first performed using Array B, and then repeated 30 minutes later using Array C. Both measurements were used to develop dispersion curves for Site 9, as presented in Figures 7.1d and 7.1e. Three lines, marked by dot, dash and dot-dash, represent three empirical criteria for resolving the longest wavelength for passive measurements. A detailed discussion of these criteria is presented in Section 7.4.

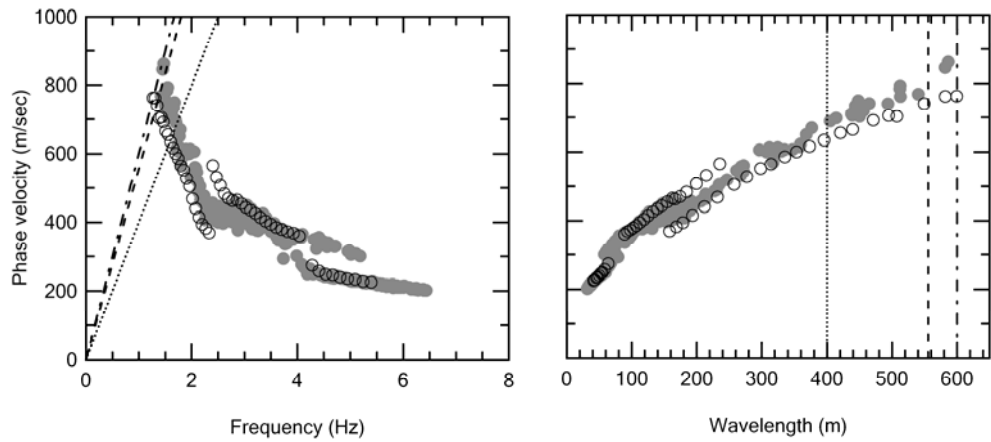
At four of the five sites (Sites 1, 3, 5 and 10), observed from Figures 7.1a, 7.1b, 7.1c and 7.1f, the dispersion curves developed from the active and passive approaches are generally very consistent out to wavelengths of about 500 m. Over this wavelength range, the phase velocities from the passive (ambient vibration) measurements are generally within 5% to 10% of the phase velocities determined from the active measurements. Beyond 500 m, the phase velocities obtained by the conventional FDBF method tend to be overestimated. At Site 3 and 5, at a frequency

of about 1.5 Hz the phase velocities obtained by the passive measurements are overestimated as much as about 24% as compared to those by active measurements.

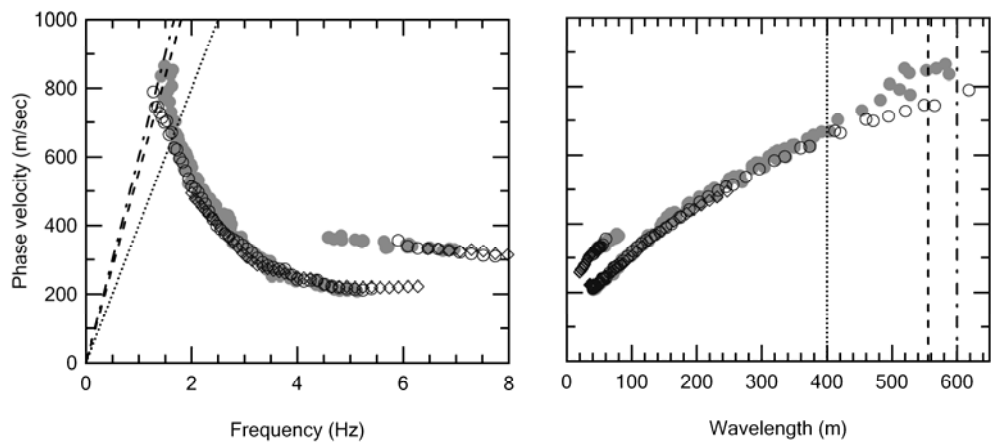
Site 9 was the only site where gross differences in the dispersion estimates were obtained. As mentioned above, data were collected at two different times at this site. From Figures 7.1d and 7.1e, it can be observed that the passive-source dispersion curves, developed from either of the two measurements, are significantly inconsistent with the active-source dispersion curves at this site. For measurements using Array B (Figure 7.1d), both active and passive methods produce consistent dispersion curves down to a frequency of about 2.2 Hz (wavelength of about 200 m). At frequencies below 2.2 Hz, the active-source dispersion curve abruptly transitions to a low velocity while the passive-source dispersion curve continues along an upward trend. At a frequency of 2 Hz, the average phase velocity estimated from the passive measurements is about 60% higher than the velocity from the active-source measurements. The passive-source dispersion curve developed from measurements with Array C exhibits a very similar trend to the dispersion curve developed from Array B measurements, except that the measurements by Array C yield a slightly lower velocity estimates at frequencies below 2.2 Hz, as shown in Figure 7.1e.



(a) Site 1

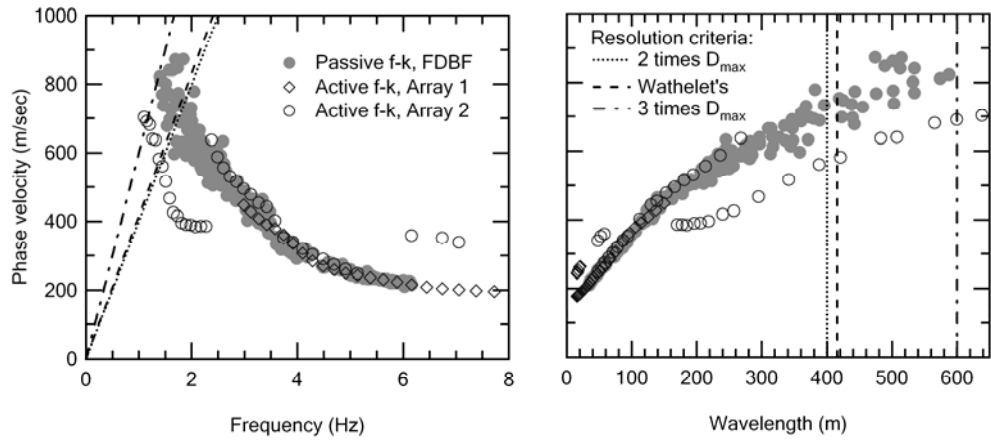


(b) Site 3

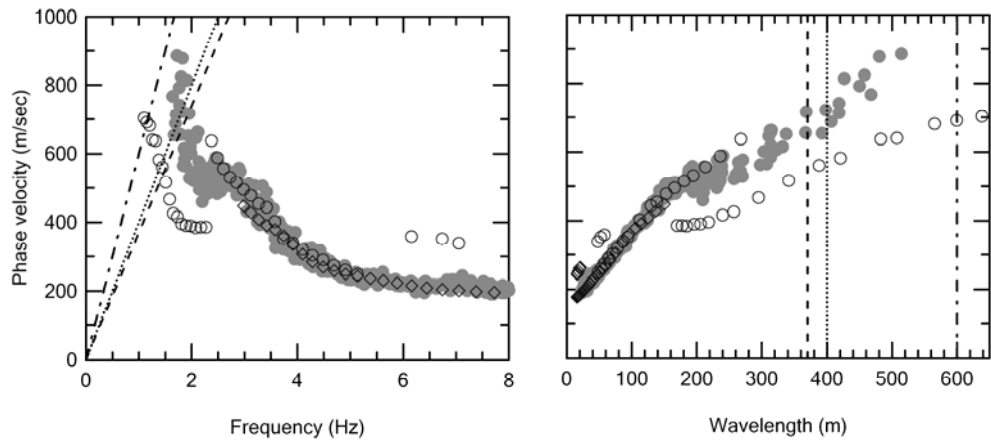


(c) Site 5

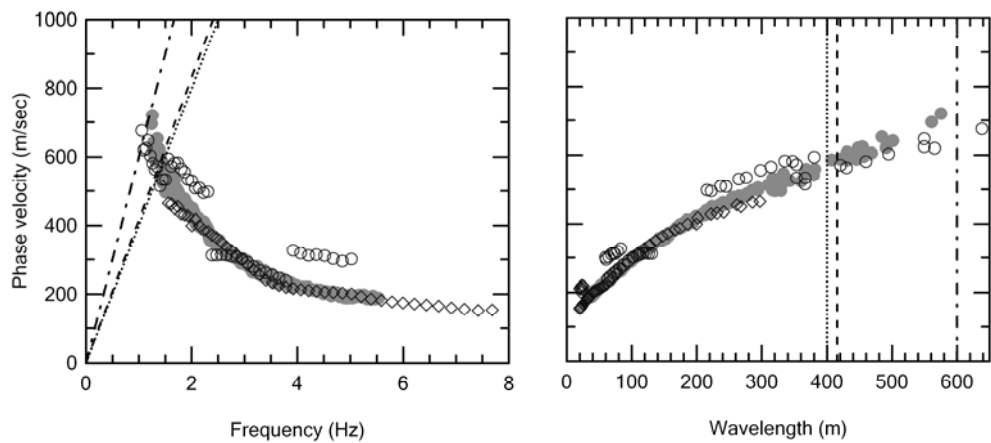
Figure 7.1 Comparison of dispersion curves developed from the active $f-k$ method and the conventional FDBF passive $f-k$ method in terms of frequency (left column) and wavelength (right column) for (a) Site 1, (b) Site 3, (c) Site 5, (d) Site 9 using Array B, (e) Site 9 using Array C and (f) Site 10.



(d) Site 9 using Array B



(e) Site 9 using Array C



(f) Site 10

Figure 7.1 (Cont.) Comparison of dispersion curves developed from the active $f-k$ method and the conventional FDBF passive $f-k$ method in terms of frequency (left column) and wavelength (right column) for (a) Site 1, (b) Site 3, (c) Site 5, (d) Site 9 using Array B, (e) Site 9 using Array C and (f) Site 10.

7.2.2 Performance of High-Resolution Methods

Analysis of the ambient vibration measurements were repeated for these five sites using two high-resolution f - k methods: MUSIC and Capon's method, respectively. Comparisons between the results from the active f - k method and the MUSIC methods are presented in Figure 7.2. Comparisons between the results from the active f - k method and Capon's methods are presented in Figure 7.3.

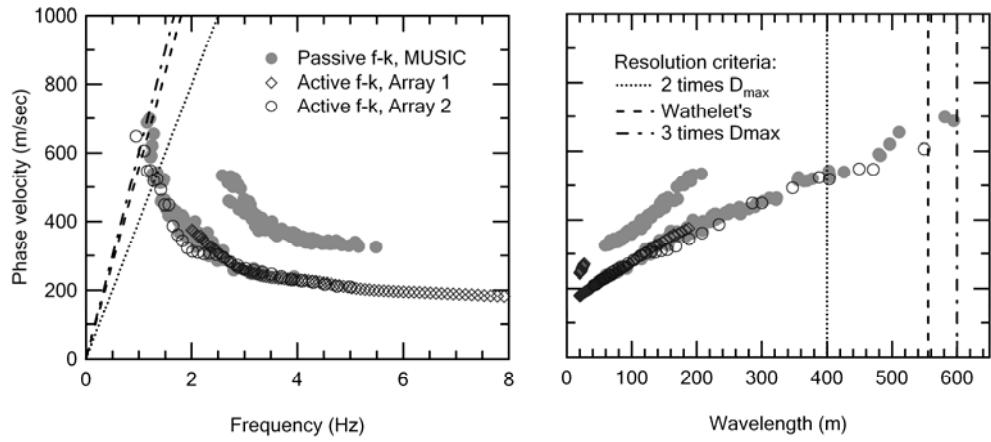
As shown in these figures, the results determined from MUSIC and Capon's methods exhibited mixed results. At Site 1, the dispersion curve obtained from the MUSIC method is similar to the conventional FDBF method but shows a slightly larger deviation at long wavelengths (Figure 7.2a). The dispersion curve estimated from Capon's method is more consistent with the conventional method, although the dispersion curve is more scattered (Figure 7.3a).

At Site 3, both high-resolution methods produced similar dispersion curves as the conventional method but showed a slightly larger deviation at wavelengths longer than 400 m, as shown in Figures 7.2b and 7.3b.

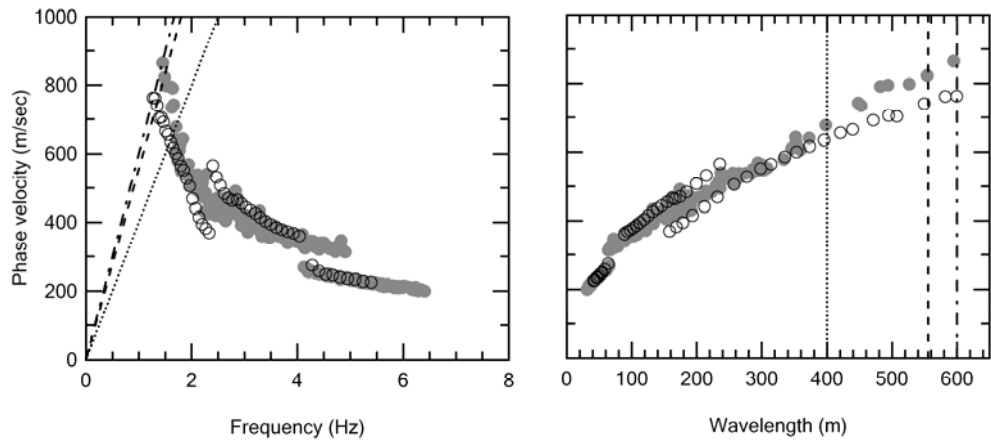
At Site 5, the MUSIC approach yielded very similar phase velocity estimates to the conventional method (Figure 7.2c), but Capon's method performed poorly and produced a much more scattered dispersion curve at wavelengths of 400 m and greater (Figure 7.3c). The greater scatter observed in the dispersion curves developed from Capon's method at this site, as well as at Site 1, is consistent with observations from other studies showing similar performance of Capon's method in some cases (Zywicki, 1999; Bozdag and Kocaoglu, 2005).

At Site 10, both high-resolution approaches produced more consistent dispersion curves with the active-source measurements (as compared to the FDBF approach) at wavelengths over 200 m, as shown in Figure 7.2f and 7.3f.

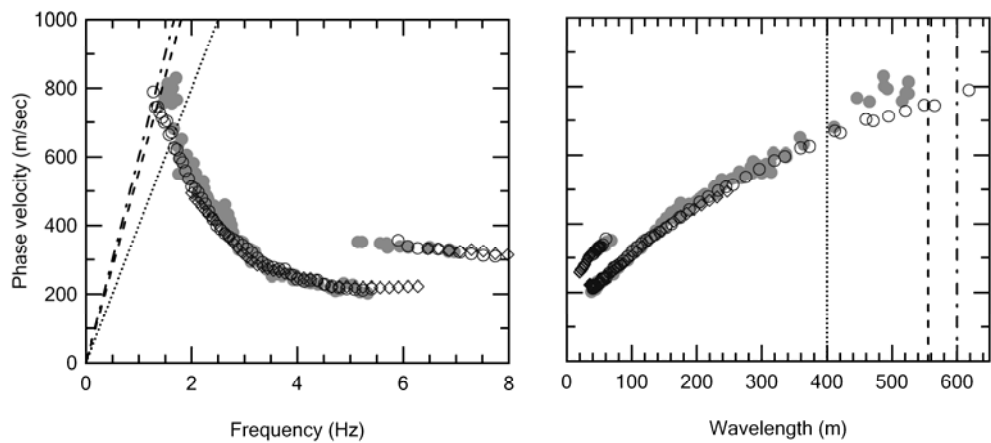
Compared with the conventional FDBF method, both high-resolution approaches did produce much improved dispersion curves at Site 9, as shown in Figures 7.2d, 7.2e and Figures 7.3d, 7.3e. The biggest improvement occurred in the case in which ambient measurements recorded using Array C were analyzed using Capon's method, as shown in Figure 7.3e. In this case, the estimated dispersion curve shows the transition trend from high velocity to low velocity at a frequency of 2.2 Hz. For the other cases, as shown in Figures 7.2d, 7.2e and 7.3d, the dispersion curves did not agree in the frequency range of 1.5 to 2.2 Hz, but the agreement at frequencies below 1.5 Hz was much improved.



(a) Site 1

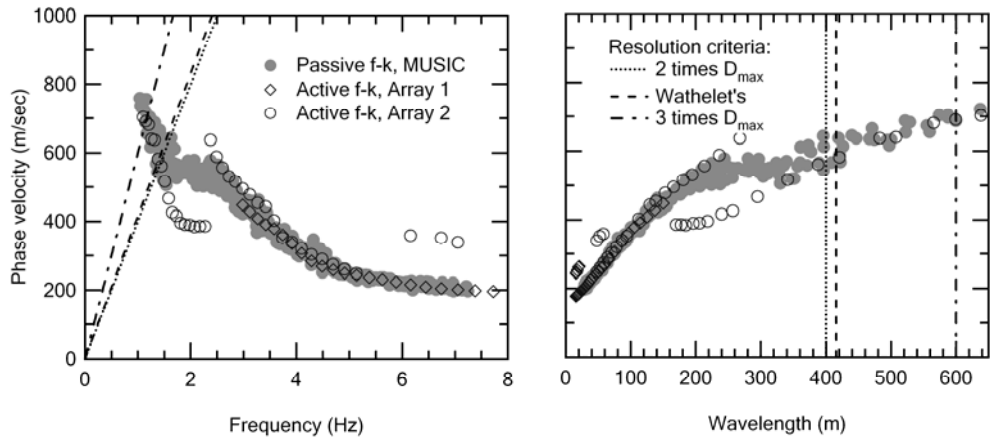


(b) Site 3

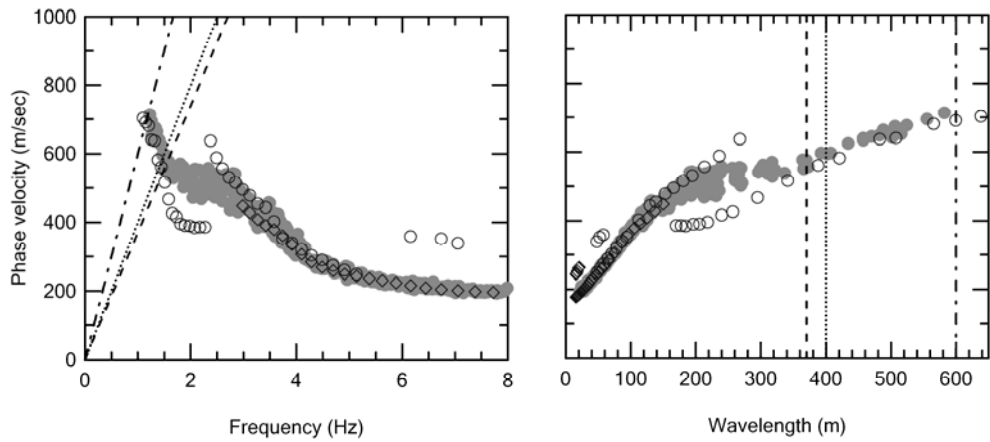


(c) Site 5

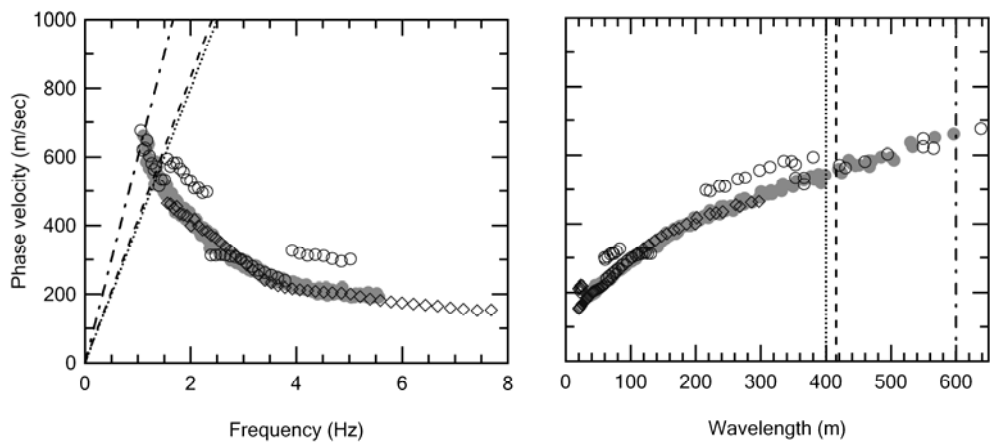
Figure 7.2 Comparison of dispersion curves developed from active $f-k$ method and MUSIC passive $f-k$ method in terms of frequency (left column) and wavelength (right column) for (a) Site 1, (b) Site 3, (c) Site 5, (d) Site 9 using Array B, (e) Site 9 using Array C and (f) Site 10.



(d) Site 9 using Array B

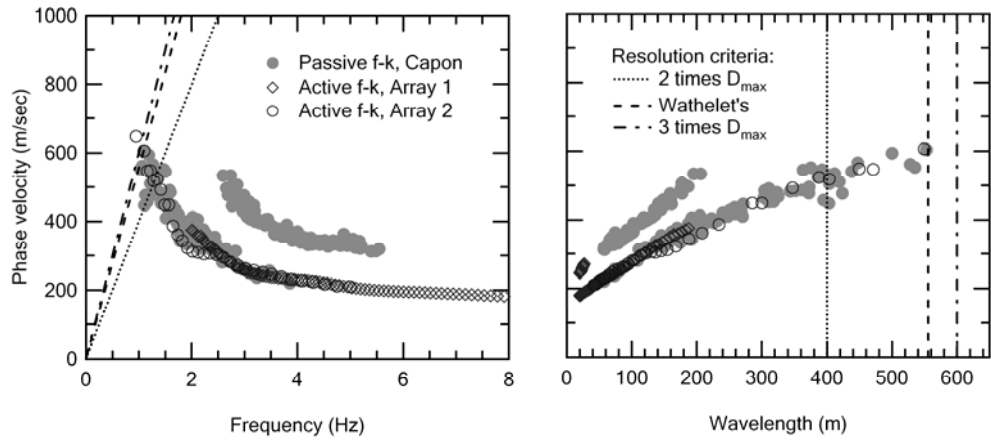


(e) Site 9 using Array C

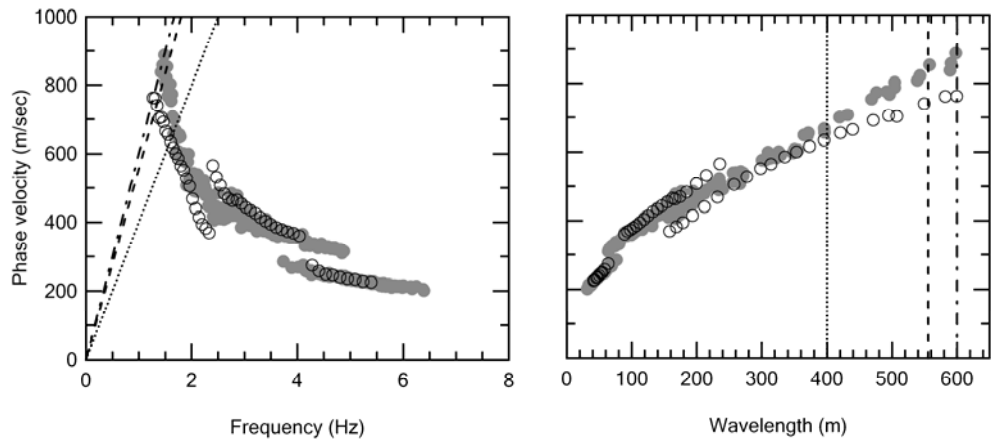


(f) Site 10

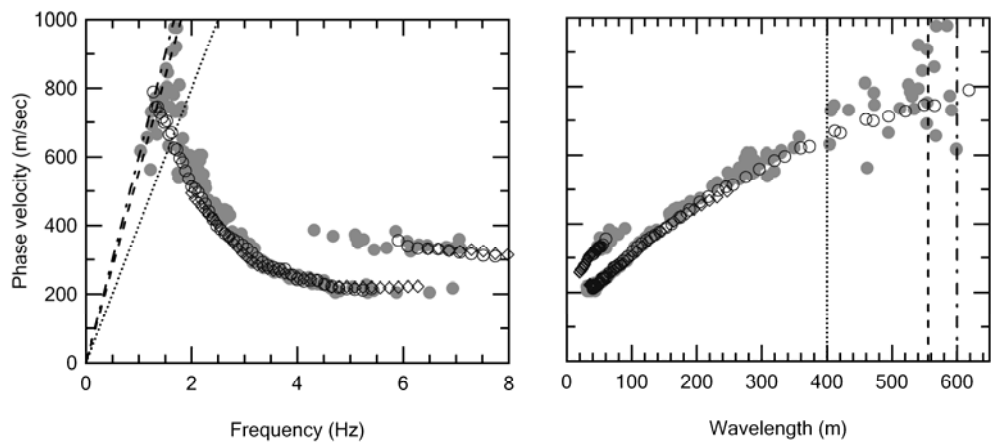
Figure 7.2 (Cont.) Comparison of dispersion curves developed from active $f-k$ method and MUSIC passive $f-k$ method in terms of frequency (left column) and wavelength (right column) for (a) Site 1, (b) Site 3, (c) Site 5, (d) Site 9 using Array B, (e) Site 9 using Array C and (f) Site 10.



(a) Site 1

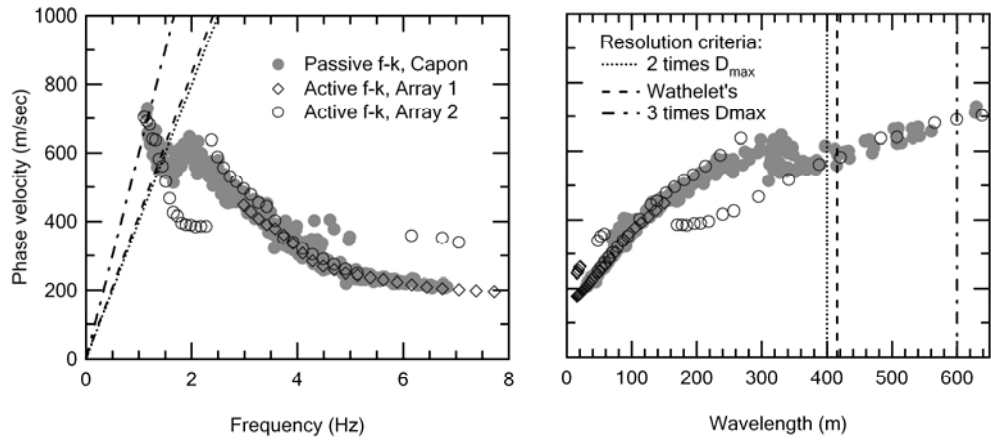


(b) Site 3

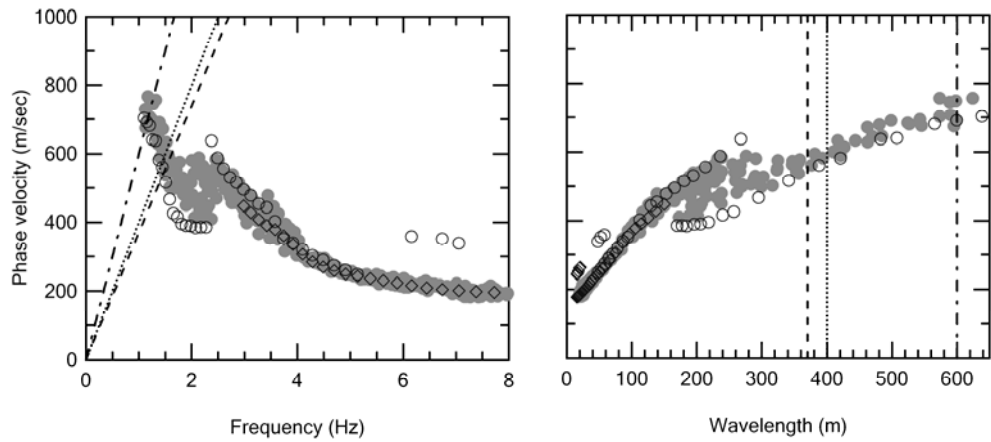


(c) Site 5

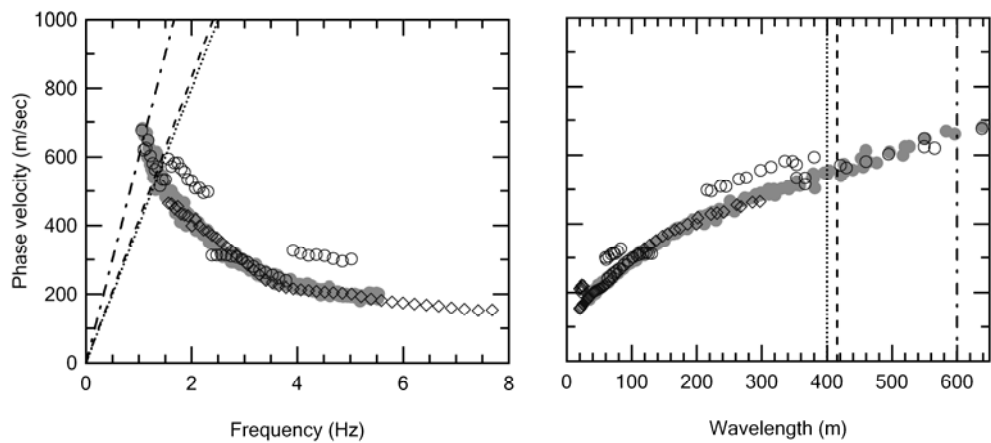
Figure 7.3 Comparison of dispersion curves developed from active $f-k$ method and Capon's passive $f-k$ method in terms of frequency (left column) and wavelength (right column) for (a) Site 1, (b) Site 3, (c) Site 5, (d) Site 9 using Array B, (e) Site 9 using Array C and (f) Site 10.



(d) Site 9 using Array B



(e) Site 9 using Array C



(f) Site 10

Figure 7.3 (Cont.) Comparison of dispersion curves developed from active $f-k$ method and Capon's passive $f-k$ method in terms of frequency (left column) and wavelength (right column) for (a) Site 1, (b) Site 3, (c) Site 5, (d) Site 9 using Array B, (e) Site 9 using Array C and (f) Site 10.

7.2.3 Higher Modes

Detection of higher-mode surface wave energy was not consistent between the active and passive-source methods at Sites 1, 3, 5 and 10, as observed in Figures 7.1a, 7.1b, 7.1c and 7.1d. At Site 1, the ambient measurements show dominant higher mode energy in the frequency range of 2.7 to 5.1 Hz that is not apparent in the active-source measurement. On the other hand, at Site 10 transitions to higher modes are observed over two frequency ranges (4 to 5 Hz and 1.5 to 2.5 Hz) in the active-source measurements using Array 2 (the longer array length) while no mode transitions observed either in the active-source measurements using Array 1 (the shorter array length) or in the ambient measurements. Lastly, at Site 3 and Site 5, both active and passive measurements show the transitions to dominant higher modes. The causes of the inconsistencies in the detection of dominant higher modes between the active and passive-source methods are not clear.

7.3 Factors Affecting the Performance of Passive $f-k$ Methods

As compared with active-source $f-k$ methods in the last section, passive-source $f-k$ showed poor performances on phase velocity estimates at Site 9. Local site conditions and ambient wavefield characteristics are two possible factors influencing the performances of the passive $f-k$ methods. Estimated soil lithologies at Sites 1, 3, 5, 9 and 10 are presented in Figures 3.28a, 3.28c, 3.28e, 3.28i and 3.28j in Chapter 3. From these figures, it can be observed that there is nothing dramatically different in soil profiles between Site 9 and the other sites. Therefore, local site conditions do not

appear to be the cause of the poor performances of passive f - k methods at Site 9.

As discussed in Section 6.4 of Chapter 6, ambient wavefield characteristics at Site 9 were quite different from the other sites. Unlike the other sites, Site 9 showed the presence of multiple energy sources at low frequencies. This feature is a possible factor influencing the performance of the different passive f - k methods. A simple simulation is performed in Section 7.3.2 to examine how a multiple-source wavefield influences the dispersion estimates using conventional and high-resolution f - k methods. In Section 7.3.1, the definition of the array pattern is introduced, which is important for the simulation discussed in Section 7.3.2.

7.3.1 Array Pattern

The array pattern of one array describes the array's filtering capability in the spatial spectral domain. It is also sometimes termed the array response (Aki and Richards, 1980) or array smoothing function (Zywicki, 1999). The normalized array pattern in the (k_x, k_y) plane is given as:

$$G(k_x, k_y) = \frac{1}{N^2} \left| \sum_{i=1}^N \exp[j(k_x \cdot x_i + k_y \cdot y_i)] \right|^2, \quad (7.1)$$

where, N is the number of receivers in the array, and (x_i, y_i) are their coordinates.

For the conventional FDBF method, the ability to separate multiple sources is directly related to the array pattern. That is, the FDBF method can separate two energy sources when the distance between their propagating wavenumbers is greater than half of the mainlobe width (diameter at the bottom of the mainlobe) of the array pattern. Array geometries and the corresponding array patterns of Array A, B and C

are presented in Figures 7.4a, 7.4b and 7.4c, respectively. From these figures, half of the mainlobe width is equal to 0.0239, 0.0364, and 0.0414 rad/m for Array A, B and C. Using different beamforming techniques, MUSIC and Capon's methods are able to decrease the mainlobe width and suppress the sidelobe heights, as shown in Figures 4.11, 4.12 and 4.13 in Chapter 4. As a result, the high-resolution methods provide an improved ability to separate multiple sources.

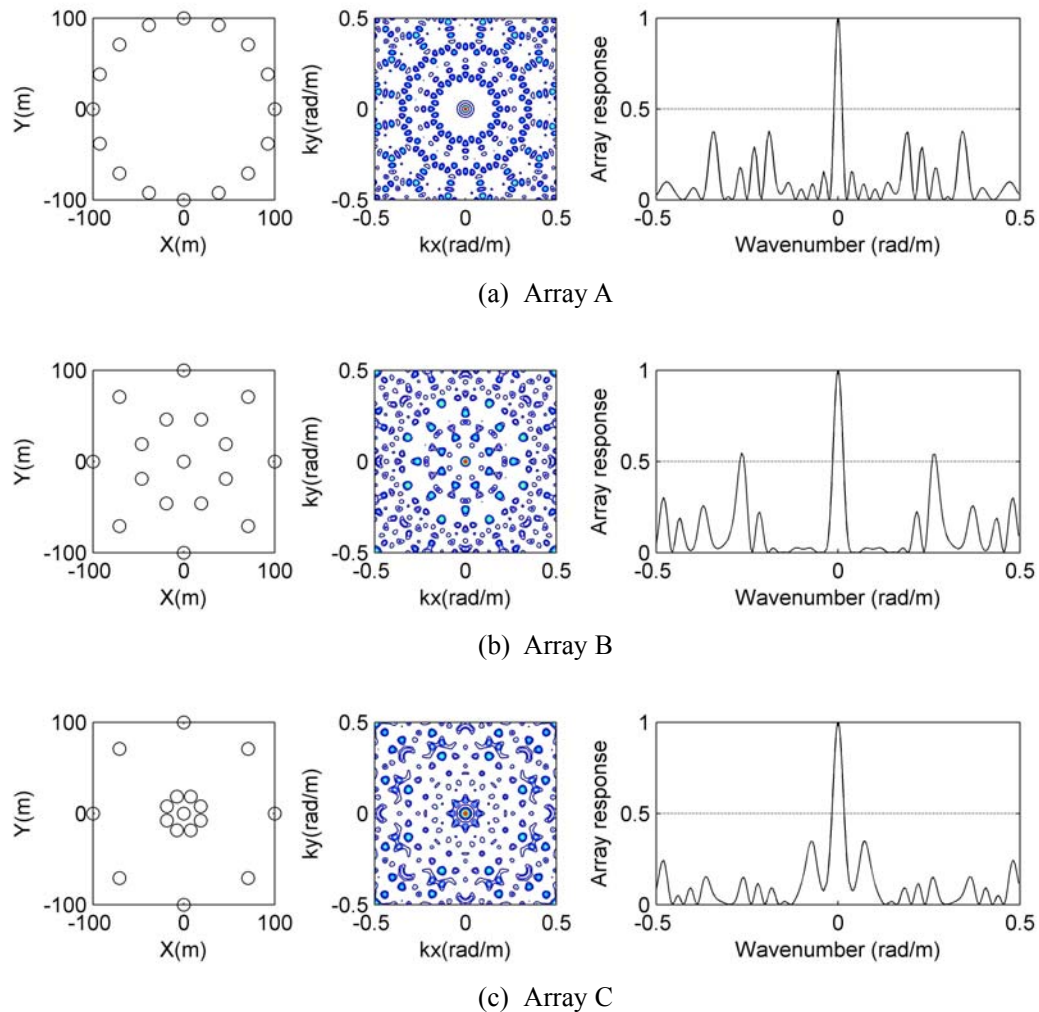


Figure 7.4 Normalized array patterns for (a) Array A, (b) Array B and (c) Array C. Left: Array geometries. Middle: Normalized array patterns in the (k_x, k_y) plane. Right: Cross-section of array patterns at $k_y = 0$.

7.3.2 Effect of Multiple-Source Wavefield

The effect of a multiple-source wavefield on the dispersion estimates from the conventional FDBF method can be investigated using a simulation approach. The basic procedures of this approach are: (1) simulating a multiple-source wavefield in the frequency domain, and (2) performing the conventional FDBF method on the simulated wavefield. The simulation results can be used to explain the different performance for estimating experimental dispersion curves of the conventional FDBF method and high-resolution methods.

Assuming multiple plane waves with the same velocity but different back azimuths are arriving at the array, the phase at the i th array sensor can be expressed as:

$$F_i = \sum_{g=1}^n a_g \exp[-j(k_x^{(g)} x_i + k_y^{(g)} y_i)] \quad (7.2)$$

where, n is the number of energy signals, $k_x^{(g)}$ and $k_y^{(g)}$ are assigned wavenumbers for g th signal, and a_g is the amplitude of g th signal. The auto-power spectrum at the i th sensor can be calculated by $F_i \cdot F_i^*$, and the cross-power spectrum between the i th and j th sensor can be calculated by $F_i \cdot F_j^*$. As defined in Section 4.3.1, the spatio-spectral correlation matrix can be formed by these auto-power spectra and cross-power spectra.

A two-source wavefield and a three-source wavefield travelling across Array B were simulated, as described in Table 7.1. The conventional FDBF method was then performed on these two simulated wavefields. The resulting power plots from the FDBF method are presented in Figure 7.5. The actual wavenumbers are also shown in

Table 7.1 Description of two simulated multi-source wavefield.

Cases	Description
Two-source wavefield	Two waves with equal amplitude travelling with wavenumbers: (0.0151 rad/m, -0.0151 rad/m) and (0.0051 rad/m, -0.0207 rad/m). These two wavenumbers have the same magnitude but different back-azimuth angles.
Three-source wavefield	Three waves with equal amplitude travelling with wavenumbers: (-0.0100 rad, -0.0086 rad/m), (-0.0110 rad/m, -0.0073 rad/m), and (-0.0120 rad/m, -0.0055 rad/m). These three wavenumbers have the same magnitude but different back-azimuth angles.

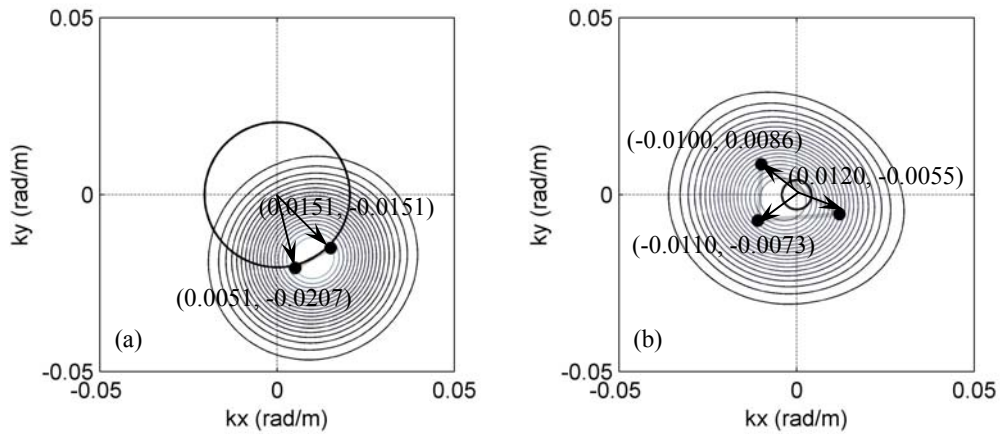


Figure 7.5 FDBF contour power plots for (a) simulated two-source wavefield and (b) simulated three-source wavefield.

this figure. Since the distance between every two wavenumbers in both cases is less than 0.0364 rad/m (half of the mainlobe width of Array B discussed in Section 7.3.1), the FDBF method is unable to separate individual sources. As a result, multiple energy sources are superposed to yield a spurious peak, as observed in Figure 7.5. For the two-source wavefield, the resulting peak corresponds to a wavenumber of (0.0100 rad/m, 0.0179 rad/m), which is equal to the average of two actual wavenumbers. For the three-source wavefield, the resulting wavenumber is (-0.0039 rad/m, -0.0014 rad/m), which is located inside the area formed by three actual wavenumbers, as

shown in Figure 7.5b.

When multiple sources can't be separated, the conventional FDBF overestimates the velocity estimate. This point can be demonstrated using a simulated two-source wavefield. If two incoming plane waves are assumed with wavenumbers $(k_x^{(1)}, k_y^{(1)})$ and $(k_x^{(2)}, k_y^{(2)})$, and $|\mathbf{k}|^2 = (k_x^{(1)})^2 + (k_y^{(1)})^2 = (k_x^{(2)})^2 + (k_y^{(2)})^2$, the detected wave using FDBF method has the wavenumber (\bar{k}_x, \bar{k}_y) , and $\bar{k}_x = (k_x^{(1)} + k_x^{(2)})/2$, $\bar{k}_y = (k_y^{(1)} + k_y^{(2)})/2$ (as observed in Figure 7.5 (a)). Therefore, the magnitude of the resulting wavenumber $|\bar{\mathbf{k}}|^2$ is:

$$|\bar{\mathbf{k}}|^2 = \bar{k}_x^2 + \bar{k}_y^2 = \frac{(k_x^{(1)} + k_x^{(2)})^2 + (k_y^{(1)} + k_y^{(2)})^2}{4} = \frac{|\mathbf{k}|^2}{2} + \frac{2k_x^{(1)}k_x^{(2)} + 2k_y^{(1)}k_y^{(2)}}{2} < |\mathbf{k}|^2 \quad (7.3)$$

That $|\bar{\mathbf{k}}|^2 < |\mathbf{k}|^2$ can be also shown for wavefield having more than two energy sources. Equation 7.3 indicates that $|\bar{\mathbf{k}}|^2$ of superposed peak is smaller than $|\mathbf{k}|^2$ of the actual propagation waves, thus yielding a higher estimate of velocity using Equation 4.23.

From above simulation, it also can be seen that the error, caused by the inability to separate sources using the FDBF method, is influenced by the distribution of multiple sources. As shown in Figure 7.5a, when two waves propagate at very close back-azimuth angles, the resulting velocity is 306.3 m/sec, just about 4% higher than true velocity of 294.1 m/sec. But when three waves travel with quite different directions as in Figure 7.5b, the estimated phase velocity is 1515.6 m/sec, which is over 3 times the actual velocity of 476.1 m/sec. These phenomena can also be inferred from Equation 7.3. When two actual waves have similar source directions, the resulting $|\bar{\mathbf{k}}|^2$ is closer to the actual $|\mathbf{k}|^2$.

The results from this simple simulation can be used to explain the

experimental velocities observed from the FDBF method at the experimental sites. For example, Figure 7.6 compares the power plots estimated at 1.68 Hz from FDBF and MUSIC methods using field measurements at Site 10. Two power peaks are detected by MUSIC, but only one peak from the FDBF method. This experimental result is similar to the simulation result for the two-source wavefield. In the experimental result, the resulting wavenumber is not exactly equal to the average of two actual wavenumbers but closer to the wavenumber of Source 1 because Source 1 has higher amplitude energy than Source 2.

Site 9 showed the poorest dispersion comparisons. Site 9 also differed from the other sites in that multiple sources were present at low frequencies (less than 1.5 Hz), as shown in Figure 6.14 and 6.16 of Chapter 6. These energy sources propagated from very different directions, which is similar to the simulated case in Figure 7.5b. As shown in Figure 7.7, experimental results from the FDBF and MUSIC methods at a frequency of 1.40 Hz for Site 9 also exhibit characteristics similar to the simulation

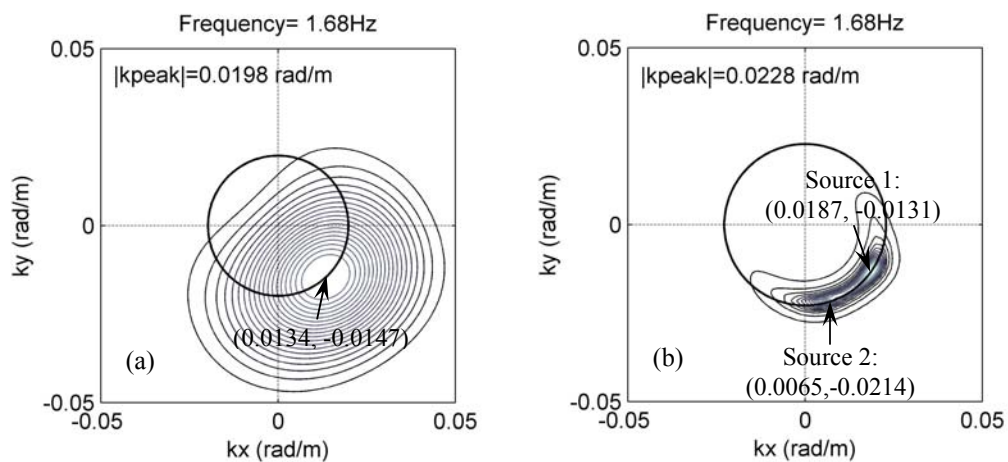


Figure 7.6 Power plots estimated from (a) FDBF and (b) MUSIC method at 1.68 Hz for Site 10.

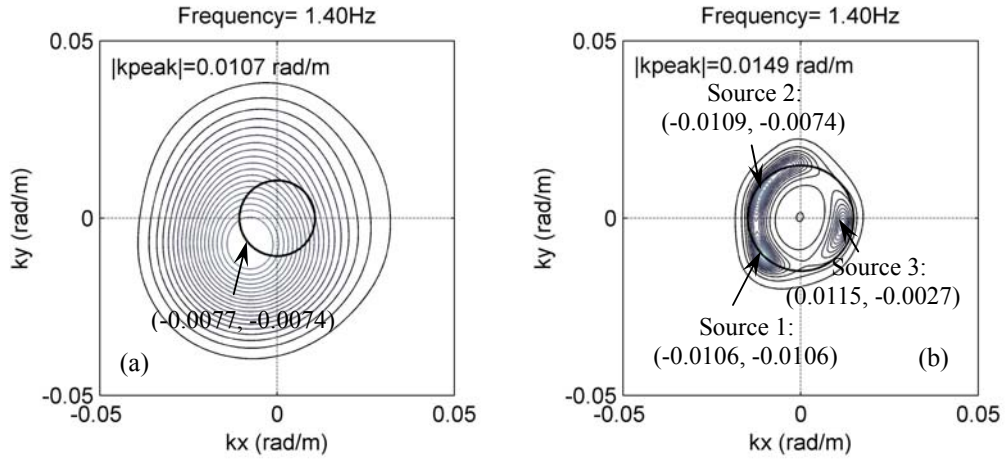


Figure 7.7 Power plots estimated from (a) FDBF and (b) MUSIC method at 1.40 Hz for Site 9.

results that the superposed peak greatly overestimates the velocity. With this, it can be concluded that the very difference performances between the conventional FDBF and high-resolution methods at Site 9 are caused by the wavefield characteristics at Site 9, where multiple energy sources from three very different directions were present at low frequencies.

7.4 Wavelength Resolution Criteria

Several different criteria to determine the longest resolvable wavelength, λ_{\max} , have been proposed for passive f - k methods. Based on the comparisons of dispersion curves developed from active and passive f - k methods in this chapter, three commonly-used empirical criteria are examined. These three criteria are: (a) $\lambda_{\max} = 2 \times D_{\max}$ (Liu, 2000), where D_{\max} denotes the maximum aperture of the array; (b) $\lambda_{\max} = 3 \times D_{\max}$ (Tokimatsu, 1997), and (c) Wathelet (2005) criterion. Wathelet (2005) defined the wavenumber resolution k_{\min} measured at the mid-height of the

mainlobe of array pattern. The λ_{\max} is calculated as $\lambda_{\max} = 2\pi/k_{\min}$ (Equation 4.12). As described in Chapter 3, Arrays A, B and C were used in this study, with the largest aperture (diameter) of 200 m. The resolvable λ_{\max} using each of the three arrays are presented for these three criteria in Table 7.2. From this table, it can be seen that the λ_{\max} from Wathelet's criterion is less than $3 \times D_{\max}$, and varies with the different array configurations used.

Table 7.2 The λ_{\max} estimated by three empirical criteria.

	$2 \times D_{\max}$	Wathelet's		$3 \times D_{\max}$
Array type	λ_{\max} (m)	k_{\min} (rad/m)	λ_{\max} (m)	λ_{\max} (m)
A	400	0.0113	556	600
B	400	0.0151	416	600
C	400	0.0170	369	600

The criteria of $\lambda_{\max} = 2 \times D_{\max}$, Wathelet's criterion and $\lambda_{\max} = 3 \times D_{\max}$ are shown in Figures 7.1, 7.2 and 7.3., using the dotted line, dashed line and dotted-dashed line, respectively. As observed from these figures, the $3 \times D_{\max}$ criterion appears to be unconservative, overestimating λ_{\max} in most cases. The $2 \times D_{\max}$ criterion works very well in most cases, though it gives conservative results. Wathelet's criterion has different performances dependent on array configurations used. For measurements using Array A, Wathelet's criterion overestimates λ_{\max} , much like the $3 \times D_{\max}$ criterion. For measurements using Arrays B and C, it gives similar results with the $2 \times D_{\max}$ criterion. It should be noted that none of these three criteria works well for Site 9, as shown in Figures 7.1d and 7.1e. The $2 \times D_{\max}$ criterion appears to be a conservative and is recommended for practical applications.

7.5 Summary

A comparative study of active-source $f-k$ and passive-source $f-k$ methods has been presented by comparing dispersion curves out to wavelengths of 600 m at 5 field measurement sites. A simulation procedure was used to study the effect of multi-source wavefield characteristics on passive-source $f-k$ estimates. Based on these studies, the following conclusions can be made:

1. At Site 1, 3, 5 and 10, the dispersion curves developed from the active and the conventional FDBF methods are generally very consistent out to wavelengths of about 500 m. Beyond 500 m, the phase velocities obtained by the conventional FDBF method tend to be overestimated. At one site, Site 9, major differences in dispersion curve estimates from the active-source and the conventional FDBF methods were observed at wavelengths from about 200 to 600 m.
2. Application of high-resolution approaches (MUSIC and Capon's methods) showed mixed results at Sites 1, 3, 5, 10, but produced much improved dispersion curve estimates at Site 9.
3. Detection of higher mode surface wave energy was not consistent between the active and passive methods.
4. Using a simple simulation procedure, poor performance at Site 9 was shown to be caused by different wavefield characteristics at this site where multiple-source energy was present at low frequencies and arrived at the array from different directions.

5. Three commonly-used empirical criteria of the largest resolvable wavelength were examined. The $2 \times D_{\max}$ criterion was found to be acceptable but conservative at 4 of the sites. At Site 9, none of these criteria worked well.

CHAPTER 8

DISPERSION CURVE COMPARISON BETWEEN ReMi AND ACTIVE f - k METHODS

8.1 Introduction

The refraction microtremor (ReMi) method (Louie, 2001) is a new method to perform passive microtremor measurements using a linear array. Due to the use of a linear receiver array and the lack of a need for an active source, ReMi is fast becoming a common method in geotechnical practice. The ReMi method has been extensively used to develop V_s profiles to depths of 50 to 100 m. In many applications, ReMi has been used together with active-source measurement to extend the penetration depth of active-source measurements. In a recent published study, the SASW method and ReMi method were combined to develop surface wave dispersion curves out to wavelengths of about 1000 m (Liu et al., 2005). The ReMi method is based on two assumptions regarding the characteristics of the ambient wavefield. First, the ReMi approach assumes that surface wave energy impinges on the array equally from all directions. Secondly, it assumes that the lowest edge of dispersion image is the fundamental mode propagating along the receiver array.

In this chapter, dispersion curve estimates from ReMi and active f - k methods are compared for eight test sites where equal-spacing linear arrays were used. ReMi was not applied at the three sites where unequal-spacing arrays were used because these arrays are not ideal for ReMi measurements. The data processing procedures

associated with ReMi analysis were described in Chapter 4. Using the ambient wavefield characteristics discussed in Chapter 6 and the dispersion comparisons, the validity of the basic assumptions of the ReMi method are examined in this chapter.

8.2 Slowness-Frequency (p - f) Spectral Ratio Images

ReMi analyses, discussed in Section 4.5.1 to 4.5.3, were performed on ambient vibrations recorded using Array 1 (short array) and Array 2 (long array) at eight sites (Site 1, 5, and Site 8 through 11). As described in Table 3.5 of Chapter 3, the configurations of Array 1 and Array 2 are consistent with those used in previous ReMi studies (Louie, 2001; Liu et al., 2005). The resulting slowness-frequency (p - f) spectral ratio images at each site obtained from Array 1 and Array 2 are presented in Figures 8.1 and 8.2, respectively. Higher spectral ratios are indicated with lighter shades in these images.

From these figures, it can be observed that a clear lower bound dispersion trend (bounded by the dark noise floor) is evident in each case. For measurements using Array 1, this dispersion trend is distinct at higher frequencies (from about 3 to 4 Hz up to 8 to 12 Hz) but becomes blurred at low frequencies (less than 3 Hz). On the other hand, the images obtained using Array 2 show a more distinct lower bound dispersion trend at lower frequencies (down to frequencies of about 1 to 2 Hz). The improved ReMi image at low frequencies using Array 2 is due to the larger length of Array 2 which results in a narrower array mainlobe, and thus increases the resolution. Also, due to the narrower mainlobe, the band of the dispersion trend from Array 2 is

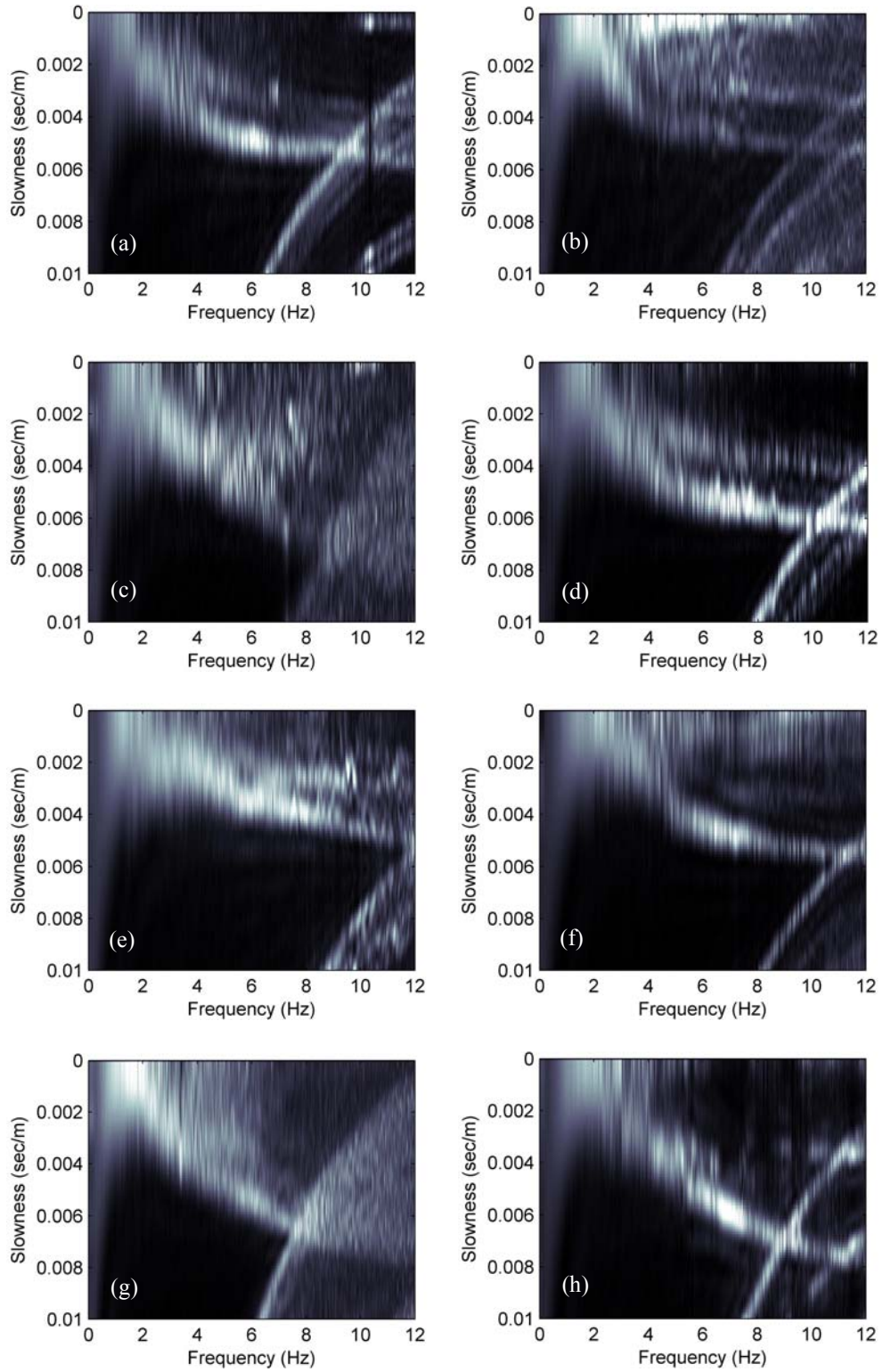


Figure 8.1 Slowness-frequency (p - f) spectral ratio images estimated using Array 1 (short arrays) for (a) Site 1, (b) Site 5 and (c)-(h) Site 6-Site 11.

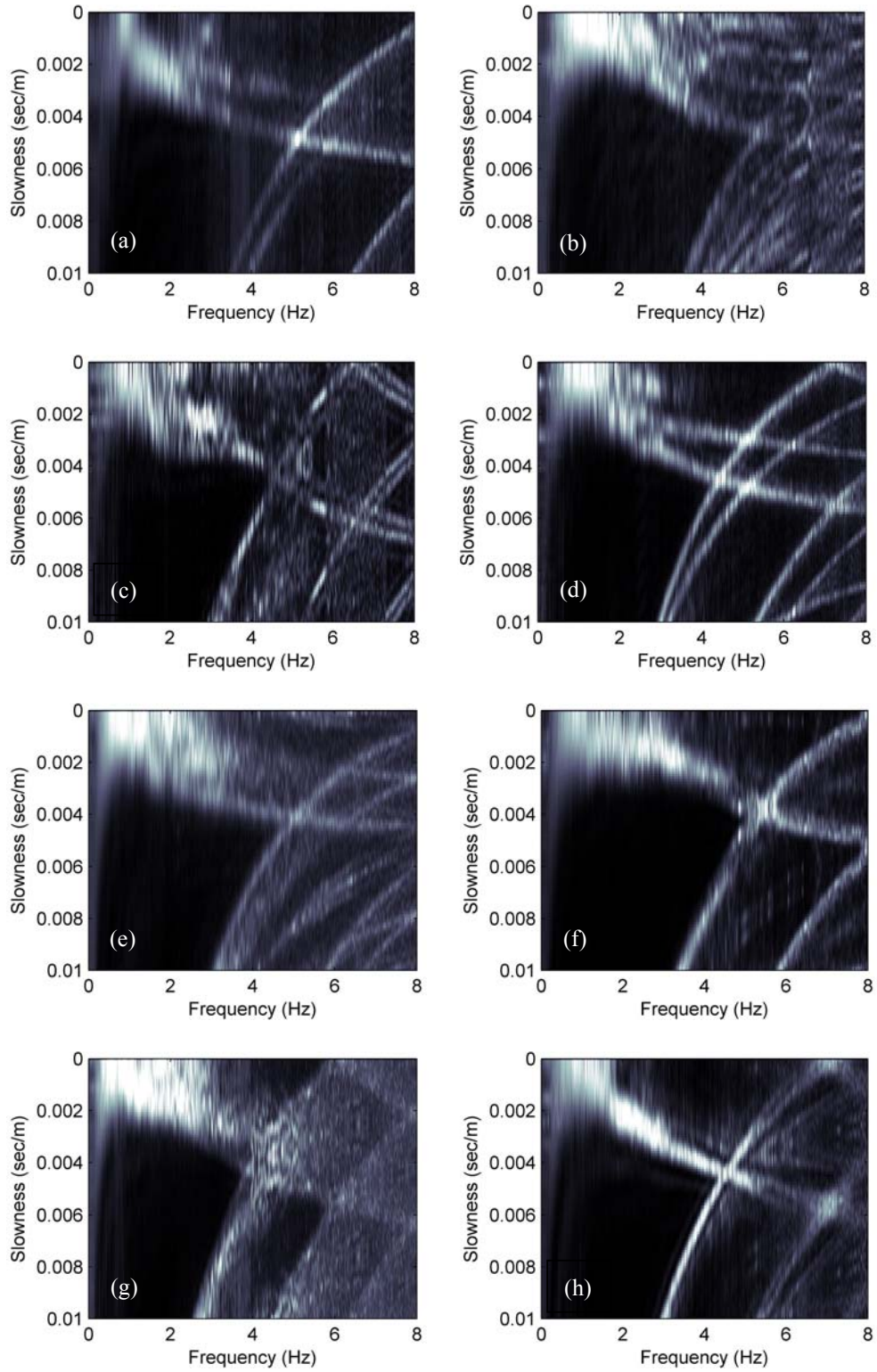


Figure 8.2 Slowness-frequency (p - f) spectral ratio images estimated using Array 2 (long arrays) for (a) Site 1, (b) Site 5 and (c)-(h) Site 6-Site 11.

narrower than that from Array 2 at each site, as shown in Figure 8.1 and 8.2. From these figures, it is also observed that Array 1 shows the dispersion image extending to higher frequencies than Array 2. This is due to the closer spacing used in Array 1, thus producing a higher aliasing limit. The bands running from the bottom of the image to the upper right in Figure 8.1 and 8.2 represent aliased signals which are ignored in the interpretation. The ReMi images shown in Figure 8.1 and 8.2 were used to develop dispersion curve estimates for each site.

8.3 Comparison of Dispersion Curves Developed from ReMi and Active f - k Methods

For each p - f image in Figures 8.1 and 8.2, two slowness picks were made at spectral power ratios corresponding to the peak and the steepest slope for each frequency, as described in Section 4.5.4 of the Chapter 4. In order to directly compare the ReMi dispersion curve with the active f - k dispersion curves, the frequencies for dispersion picking were chosen to be the same as those used for the active-source measurements. At some of these frequencies, no clear peaks were produced in the ReMi image. Therefore, slowness picks were not made for those frequencies. After the slowness picks were made, phase velocity values were calculated as the inverse of the slowness values. As a result, a total of four dispersion curves were produced for each site, with two for Array 1 and two for Array 2.

The surface wave velocity dispersion curves produced from the ReMi method are compared with active-source f - k dispersion curves in Figures 8.3a through 8.3h, for Sites 1, 5 and 6 through 11, respectively. The same dispersion data are presented in

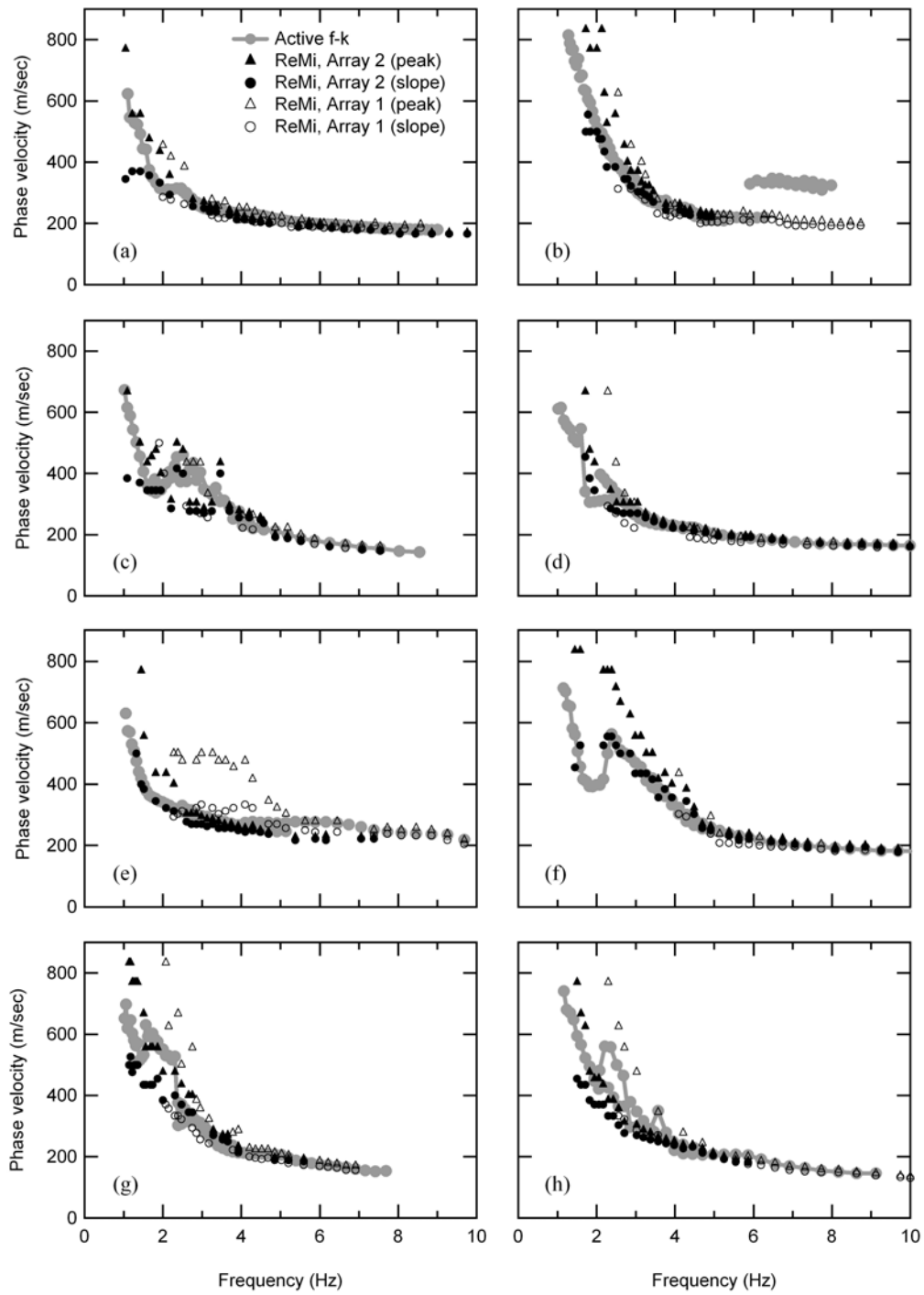


Figure 8.3 Comparison of dispersion curves developed from ReMi and active f - k methods shown in terms of frequency for (a) Site 1, (b) Site 5 and (c)-(h) Site 6-Site 11.

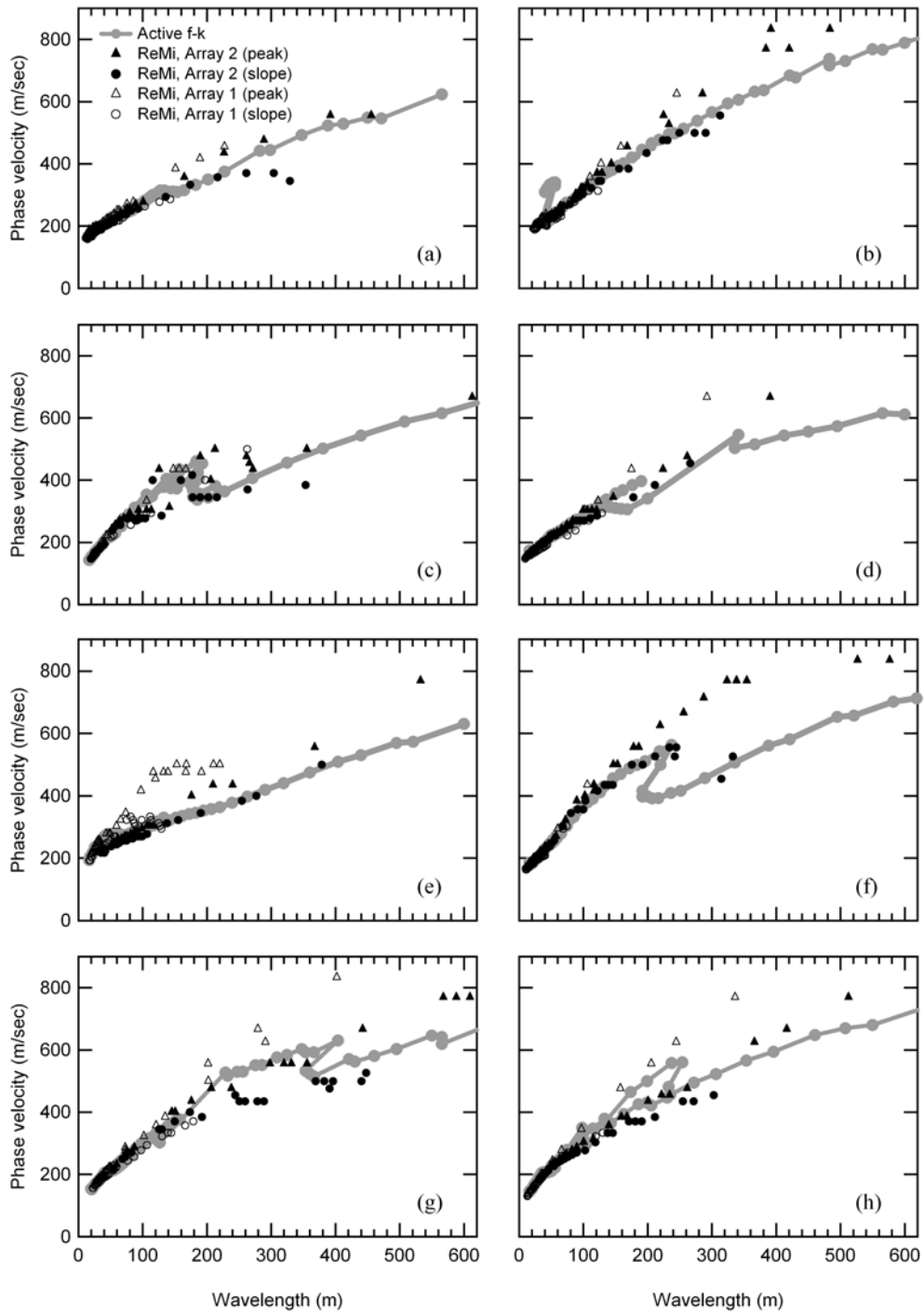


Figure 8.4 Comparison of dispersion curves developed from ReMi and active $f-k$ methods shown in terms of wavelength for (a) Site 1, (b) Site 5 and (c)-(h) Site 6-Site 11.

terms of wavelength in Figure 8.4 (a) through 8.4 (h), for Site 1, 5 and 6 through 11, respectively. A general observation from these comparisons is that the agreement between dispersion curves estimated from the ReMi measurements and active-source measurements are significantly different at high frequencies (> 3 to 4 Hz) as compared to lower frequencies at all eight sites.

At all eight sites the estimated phase velocities from the ReMi measurements are in good agreement with phase velocities from the active-source measurement at frequencies from about 8 to 10 Hz on the high end to about 3 to 4 Hz on the low end. This range in frequencies corresponds to wavelengths from about 10 to 20 m out to about 100 to 150 m, as shown in Figure 8.4. Expanded views of dispersion curves in this wavelength range are presented in Figure 8.5. Also presented in Figure 8.5 are the active-source $f-k$ dispersion curves shown with $\pm 5\%$ error bars. The 5% bound is a typical error value assumed for dispersion curve uncertainty (Joh, 1996). As can be observed from this figure, the variation between ReMi and active $f-k$ dispersion curves is within $\pm 5\%$ to the wavelength of 100 to 150 m, with the exception of Sites 6 and 8. Typically, dispersion curves with a maximum wavelength of 100 to 150 m can be used to develop V_s profile to depths of about 50 to 75 m.

At frequencies below 3 to 4 Hz (wavelength range of about 150 m to 600 m), the agreement between the active-source measurements and the ReMi measurements is much poorer, as shown in Figure 8.3. At these lower frequencies, the scatter between the Array 1 and Array 2 results, and between the two ReMi dispersion picks (peak versus slope) is significantly. As mentioned before, the longer receiver array

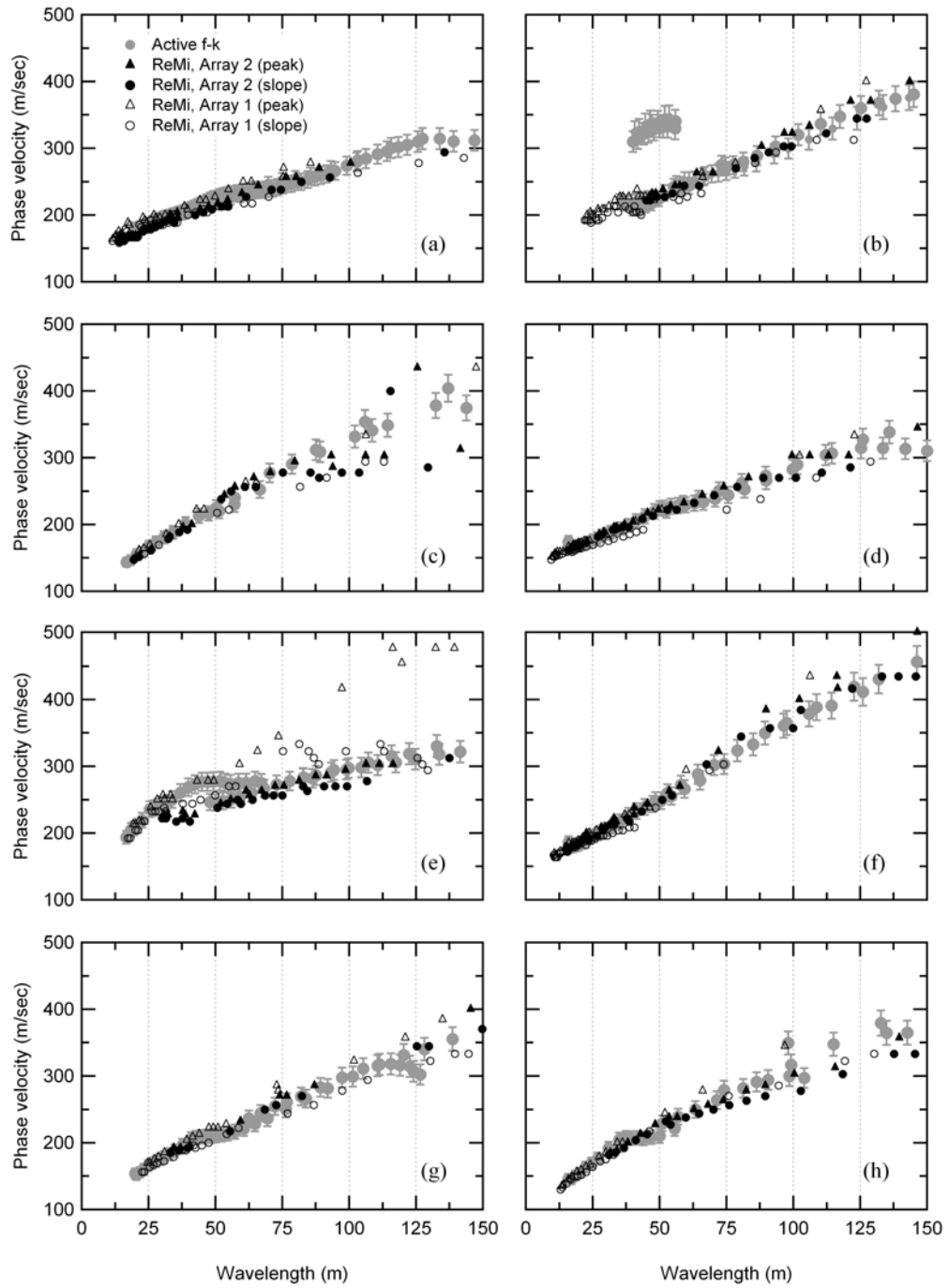


Figure 8.5 Expanded view of ReMi dispersion curves along with active f - k dispersion curves (with estimated 5% error bars) for (a) Site 1, (b) Site 5 and (c)-(h) Site 6-Site 11.

(Array 2) should provide a better result than the shorter array (Array 1) at low frequencies, but it still exhibits substantial variability from the active-source measurements. There is no consistent agreement from site-to-site between either of the two ReMi picks and the velocity estimate from the active-source measurements. For example, at Sites 5, 8 and 9 the “slope” picks generally agree well with the $f-k$ velocity estimates while the “peak” picks overestimate the velocities by about 30 to 50% (Figure 8.3b, 8.3e and 8.3f). At Sites 1 and 6, on the other hand, the “peak” picks are consistent with the active-source velocities while the “slope” picks are about 30 to 40% lower than the active-source measurements (Figure 8.3a and 8.3c). At the other sites (Site 7, 10 and 11), neither the “peak” nor the “slope” picks are in good agreement with $f-k$ results, with a deviation of about 30% or more at the lowest frequencies.

The differences between these methods are further demonstrated using the power-slowness plot (cross-section of slowness-frequency ReMi image) at the lowest frequency for each of eight sites, as presented in Figure 8.6. In each power-slowness plot, the two ReMi slowness picks and the slowness value determined from the active-source measurements (calculated as the inverse of the phase velocity) are presented. Although in most cases the ReMi picks bracket the active $f-k$ value, the ReMi slowness picks represent a very broad range in velocities. For example, for Site 9 (Figure 8.6f), the “peak” pick corresponds to a slowness of 0.0012 sec/m and the “slope” pick corresponds to a slowness of 0.0022 sec/m. When inversed, these values give a range in velocities of 454 m/sec on the low end and 833 m/sec (83% higher) on

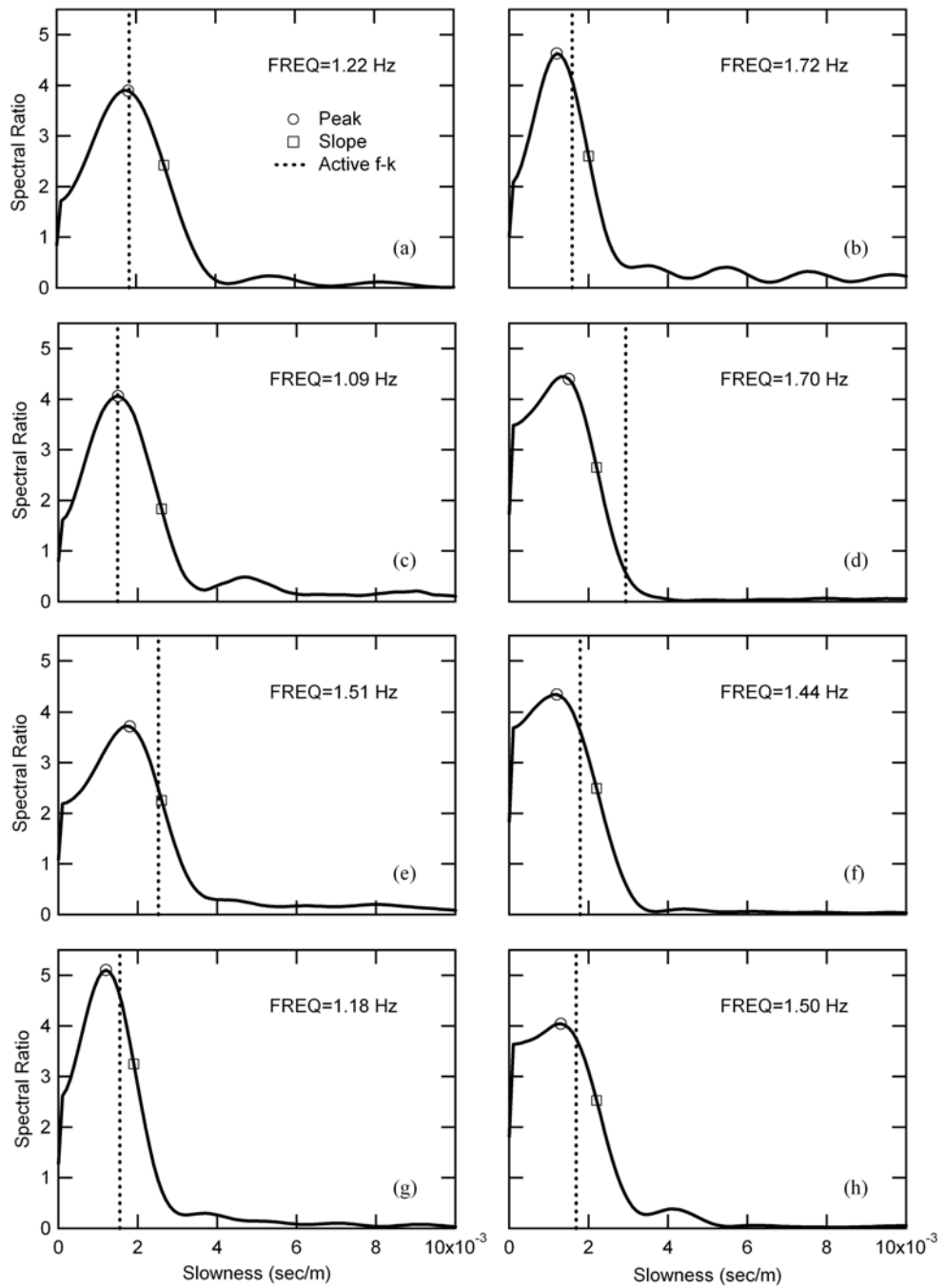


Figure 8.6 Power-slowness profiles of slowness-frequency images (Figure 8.2) at selected low frequencies for (a) Site 1, (b) Site 5 and (c)-(h) Site 6-Site 11.

the high end. It should be noted that the shape and quality of power-slowness plots in Figure 8.6 are consistent with ReMi data used to develop dispersion curves in other published studies (for example, Pancha et al., 2008).

As mentioned in the introduction, one of the basic assumptions that ReMi is predicated on is that the lowest edge of the dispersion image can be interpreted as the fundamental mode propagating along the length of receiver array. From these comparisons, it can be observed that this assumption may not always be valid. As seen in Figures 8.3c, 8.3f and 8.3g, at Sites 6, 9 and 10, the active-source dispersion curve transitions to a higher velocity over a portion of the frequency range. As discussed in Chapter 5, this transition is due to the dominant higher mode energy associated with a shallow soft soil layer over a stiff layer. This feature is most evident at Site 9 where the f - k dispersion curve follows a higher mode in a frequency range of about 2.5 to 4.0 Hz. In Figure 8.7, for example, the power-slowness profile is shown at a frequency of 2.38 Hz for Site 9. This frequency is located within the frequency range where higher mode dominates, as seen from Figure 8.3f. It is also can be anticipated from Figure 8.3f that the velocity of fundamental mode wave should be roughly 300 m/sec (a slowness of 0.0033 sec/m). But from Figure 8.7, no energy peak is evident around this slowness (marked by an arrow). As a result, the lower-bound ReMi picks identify this higher mode dispersion curve as the fundamental mode. This dispersion pick, therefore, is inconsistent with the above assumption of fundamental mode energy and will lead to an erroneous V_s model when a fundamental mode inversion is used.

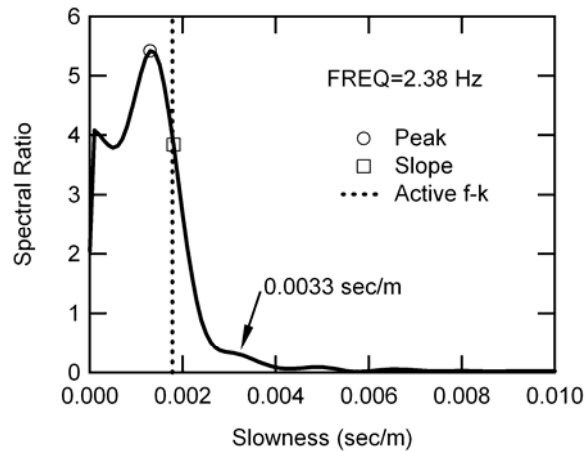


Figure 8.7 Power-slowness profile through slowness-frequency images (Figure 8.2f) at 2.38 Hz for Site 9.

8.4 Factors Influencing ReMi Performance

Factors such as low ambient energy levels, local site conditions, array length and wavefield characteristics can contribute to the poor performance of the ReMi method at low frequencies. In this study, a lack of ambient energy at low frequencies cannot be the reason for the poor performance based on the following reasons. First, high ambient noise levels were recorded as shown in Figure 6.1 of Chapter 6. Secondly, the dispersion curves developed from the passive f - k measurements using the circular array are in good agreement with active f - k results down to frequencies of 1 to 1.5 Hz for Sites 1, 5, 9 and 10, as shown in Figure 7.2a, 7.2c, 7.2d and 7.2f. This illustrates that sufficient low-frequency ambient energy was available at these sites for the passive measurements.

The poor ReMi performance also does not appear to be due to local site conditions because similar performance was observed at all eight sites, though they

have slightly different soil lithologies (as shown in Figure 3.28 of Chapter 3). Lastly, a longer array should improve the performance of the ReMi estimates. However, array length alone does not appear to be the primary factor causing the poor performance at low frequencies. For example, poor performance was observed both for Array 2 at Site 10 which had a length of 450 m, and for Array 2 at Site 1 which had a length of 300 m, indicating no good benefit from using a longer array.

Therefore, the good agreement achieved with ReMi at high frequencies and the poor performance at low frequencies is likely due to the characteristics of the ambient wavefield. Using the passive f - k data collected from the circular receiver arrays at Sites 1, 5, 9 and 10, it is possible to examine the influence of the ambient wavefield. Although the passive f - k measurements were performed one day after the ReMi measurements, and therefore do not necessarily show the same conditions as occurred during the ReMi measurements, they do provide valuable insight into the nature of the ambient wavefield at these sites and its influence on the ReMi dispersion estimates.

As discussed in Section 6.4 of Chapter 6, different wavefield characteristics were observed at low frequencies (below about 3 Hz) as compared to higher frequencies. To illustrate these differences, power plots developed from passive f - k measurements are presented in Figure 8.8 at a low frequency near 1.5 Hz (Figure 8.8a, 8.8d, 8.8g and 8.8j) and at a high frequency around 3.5 Hz (Figure 8.8b, 8.8e, 8.8h, 8.8k) for Sites 1, 5, 9 and 10, respectively. These power plots were also shown in Figures 6.8, 6.12, 6.14 and 6.18 in Chapter 6. The orientation of the ReMi receiver

array is also presented in the last column of Figure 8.8, with the same coordinate system as the power plots. As previously mentioned, the ReMi method is based on the assumption of a wavefield with energy propagating equally from all directions. From Figure 8.8, it can be observed that only at Site 5 (the urban site) did the higher-frequency measurements (Figure 8.8e) exhibit a wavefield that was consistent with the above assumption. At other sites, multiple energy sources were present at higher frequencies. Although these sources were not distributed in all directions as at Site 5, the presence of multiple energy sources increased the chance that the array aligned with some energy source. This explains the good performance of the ReMi method for velocity estimates at high frequencies (> 3 to 4 Hz).

The wavefield characteristics at low frequencies were quite different, showing only one or two dominant energy sources at most of the sites. This is not consistent with the above omni-directional wavefield assumption. In this case, array orientation will determine the performance of the ReMi measurements. As shown in Figure 8.8a and 8.8c, major energy happens to propagate along the array alignment at low frequencies for Site 1. As a result, the “peak” ReMi pick at this site matched well with the active f - k estimates at frequencies below 3 Hz, as shown in Figure 8.3a. At the other sites where the array alignment was oblique to the dominant energy, the “peak” picks overestimated the phase velocities when compared to the active-source velocities.

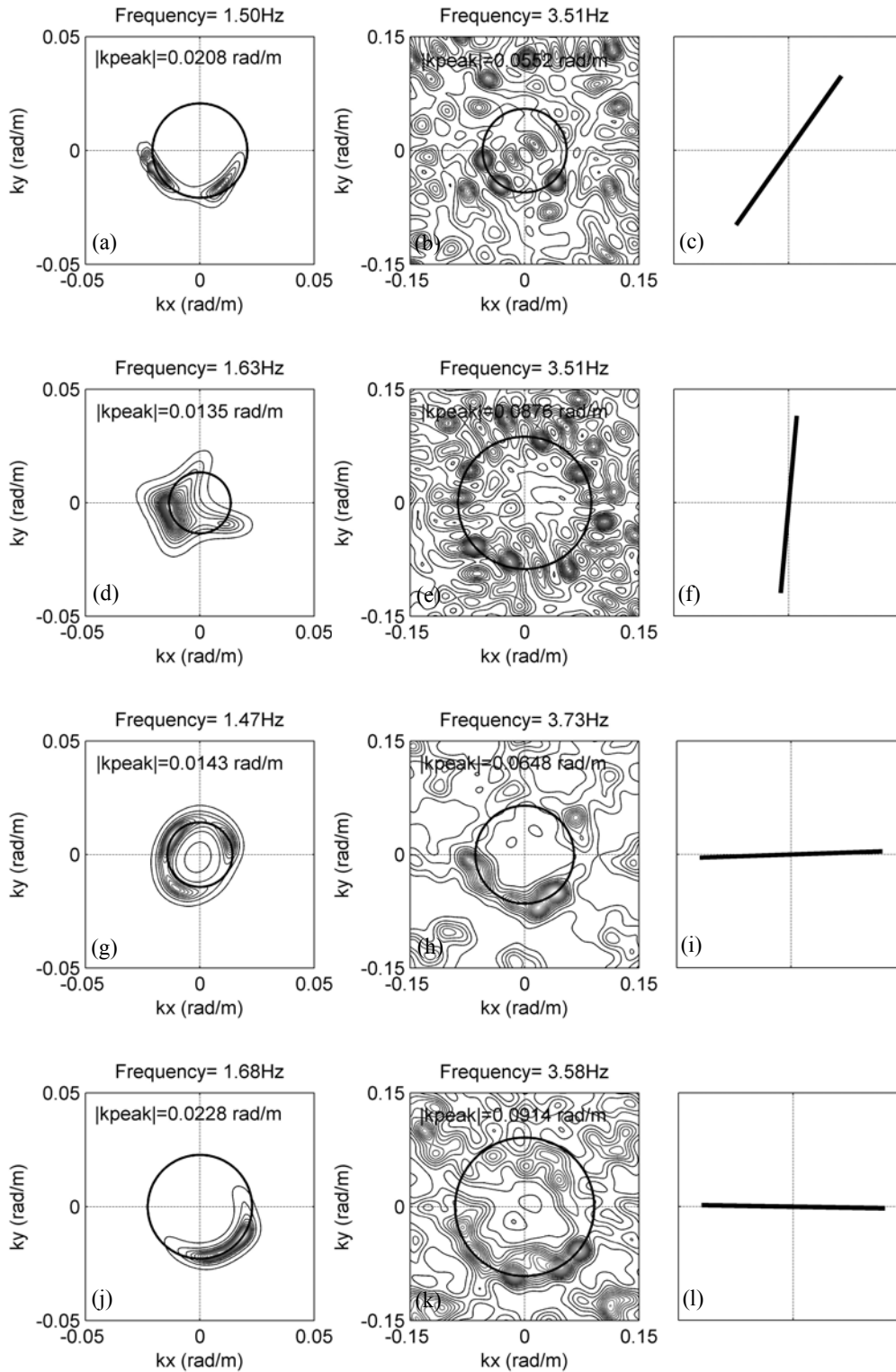


Figure 8.8 Power plots from passive f - k measurements at Site 1, 5, 9 and 10 (from the top row to the bottom shown in (a), (d), (g) and (j) for low frequencies, (b), (e), (h) and (k) for high frequencies, along with array orientation shown in (c), (f), (i) and (l).

8.5 Summary

From the observations in this study, the surface wave dispersion curves obtained using the ReMi method agreed well with active-source $f-k$ results down to frequencies of about 3 to 4 Hz at all 8 sites. This frequency range corresponds to wavelengths out to about 100 to 150 m. Typically, measurements out to this wavelength range can be used to develop V_s profiles to the depths of 50 to 75 m (assuming a profile depth of about one-third to one-half the maximum wavelength).

At frequencies below 3 Hz, the dispersion comparison between the ReMi and active $f-k$ methods was poor at each of eight sites. Although the ReMi estimates bracketed the active $f-k$ value, the “peak” and “slope” picks bound a very broad range in velocities, with variations of over 80% in the worst case. In addition, there is no way to determine which pick (slope or peak) presents a better estimate because there was no consistent agreement from site-to-site between either of the ReMi picks and the active-source velocity.

The poor performance of ReMi at low frequencies was shown to be primarily due to wavefield characteristics that violate the primary assumption used in ReMi data interpretation, namely an omni-direction, multi-source wavefield. Based on these results it appears that ReMi is best used in urban environments for shallow V_s profiling and should not be considered as a viable method for deep V_s profiling applications.

CHAPTER 9

COMPARISON OF DEEP V_s PROFILES FROM FUNDAMENTAL MODE AND EFFECTIVE VELOCITY INVERSION

9.1 Introduction

The focus of the work thus far has been on the reliability of the experimental dispersion curve estimate. The final step in surface wave measurements is the application of an inversion procedure to develop a shear wave velocity (V_s) profile for the site. This iterative procedure seeks to find a V_s profile by fitting the theoretical dispersion curve of the profile to the experimental dispersion curve. Two general approaches have been commonly used in surface wave inversion methods. The first approach is called a fundamental mode inversion. This approach uses the fundamental mode dispersion curve in the forward calculation. It is based on an assumption that the fundamental mode is measured in the field procedures. This fundamental mode approach is the most commonly used method for multi-channel active-source measurements and is almost always used in passive and ReMi measurements.

The second inversion approach is based on an “effective-velocity” dispersion curve, which is usually used for the inversion of SASW data. This approach does not calculate separate modes of the dispersion curve, but instead evaluates the displacements at each receiver location and calculates the resulting dispersion curve, hence simulating the actual SASW measurement. A similar approach has been suggested for multi-channel measurements (O’Neill, 2003).

In this chapter, the deep V_s profiles developed from active f - k dispersion

curves using the fundamental mode inversion approach are compared with the V_s profiles developed from the SASW dispersion curves using the “effective-velocity” inversion approach for eight sites where continuous $f-k$ dispersion curves were observed over a broad frequency range. The fundamental mode approach was not attempted at 3 sites (Sites 3, 6 and 9) where clear velocity transitions to higher modes were observed and the fundamental mode could not be identified. A simulation approach is also introduced to investigate the validity of the assumption of fundamental mode dominance in active $f-k$ measurements.

9.2 Data Inversion Procedures

Shear wave velocity (V_s) profiles for the eight sites (Site 1, 2, 4, 5, 7, 8, 10, 11) were developed from the measured dispersion curves by using the program WinSASW2, created at the University of Texas at Austin (Joh, 1996). Inversion of SASW dispersion curves using the “effective-velocity” approach was completed by a former Master’s student of the University of Missouri (Bailey, 2008). The inversion of the active-source $f-k$ dispersion curves using the fundamental mode forward model were performed as part of this study.

The required input parameters to WinSASW2 are: layer thickness, V_s , Poisson’s ratio (or compression wave velocity, V_p), mass density and material damping ratio. To be consistent, the parameters used for inversion of the active-source $f-k$ data are the same as those used in the SASW inversion approach. Above the water table (depth of 4 m or less), the soil was assumed to have a Poisson’s ratio of 0.25.

Below the water table, the V_p was assumed to be 1600 m/sec for soils with V_s less than or equal to 650 m/sec, but 1800 m/sec for soils with V_s greater than 650 m/sec. These values are consistent (within 10%) with V_p values measured over a similar depth range from well logs in the embayment (Cramer et al. 2004). Mass density values of 1.9 g/cm^3 and material damping ratios of 2% were assumed for all the soil layers. Similar mass density values were also applied in other studies (Romero and Rix, 2001; Cramer, 2006) and damping ratio values are consistent with those reported by Chen et al. (1996).

In this study, a generic profile layering (the number of layers and the thickness of each layer) was used for each site, starting with layer thickness of less than 1 m at the shallow depths and incrementally thicker layers at depth. The thicker layers were used at greater depths to account for the decreased sensitivity to layer thickness with depth. The initial layered profiles had 20 layers, extending to a depth of 400 m (two-thirds of the maximum wavelength). No *a priori* information on soil stratigraphy was used to develop the profile layering at any of the sites.

With the above input parameters, the inversion analysis includes three basic steps. The first step is to determine a preliminary V_s model for the given generic layered profile based on the measured dispersion data. This procedure involves constructing a temporary layered profile with the number of layers equal to the number of points in the experimental dispersion curve plus one. The thickness of the i th layer is estimated by multiplying the difference of wavelengths related to the i th and $(i-1)$ th dispersion points by a depth-to-wavelength ratio, α . The V_s of the layers

are determined, one by one, starting at the top layer. The first layer is assumed to be a single-layer system corresponding to the shortest wavelength in the dispersion data and the dynamic stiffness matrix is assembled according to the procedures described in Kaussel and Roesset (1981). The V_s is initially assumed equal to the phase velocity for the shortest wavelength and varied to make the determinant of the stiffness matrix equal to zero. For the determination of the V_s of the second layer, a two-layer system is assumed. In a similar way, the V_s for the second layer is solved as the value that gives a zero determinant of the stiffness matrix for the 2-layer system. The same scheme is used for the remaining layers. From this temporary layering, the preliminary V_s of the given generic layered profiles for each layer thickness is determined by calculating a weighting average of the V_s of this temporary profiles over layer thicknesses of the generic profile. The forward model is then performed using this preliminary V_s model and the root-mean-square (RMS) error is calculated. The entire process is repeated for five α values typically ranging between 0.51 and 0.59 in order to find the best-fitting preliminary V_s model.

The second step is to conduct the inversion procedure using the approach implemented in WinSASW2, which is based on a maximum likelihood approach (Menke, 1989; Tarantola, 1987). Once the theoretical dispersion curve is calculated using the preliminary V_s model with the lowest RMS error, the misfit between the experimental and theoretical dispersion curves is calculated as indicated by the root-mean-square (RMS) error. The model parameters are then updated using the sensitivity matrix calculated from the forward equation. This procedure is iterated

several times until an acceptable fit is achieved as indicated by a low RMS error and negligible changes in RMS with additional iterations. Prior to the inversion process, the uncertainty of the data values and the model values are estimated and input to the program in the form of standard deviations in order to provide stability in the inversion analysis. The standard deviations of the data and models values were set at 5% for this study, and for the SASW study performed by Bailey (2008). The inversion approach is described in detail by Joh (1996).

After the inversion analysis, the V_s model that produced the best agreement between the theoretical and experimental dispersion curves was used to perform a depth resolution analysis. This analysis was performed to determine the maximum resolvable depth of the selected V_s profile. For this study, a manual depth resolution study was performed to examine the sensitivity of the theoretical dispersion curve to changes in the V_s of the deepest layer. Using this procedure, the velocity of the deepest layer and halfspace was changed by $\pm 25\%$ while keeping all other layer velocities the same. The theoretical dispersion curve was then recalculated based on this adjusted profile. If there was no major change in the phase velocity (less than 5%) at the maximum wavelength, the deepest layer was removed and the half-space velocity was assigned to the next deepest layer. The same procedure was repeated until a change of about 5% was observed at the maximum wavelength. The final V_s profile was presented to the depth determined from this procedure.

9.3 Comparison of Deep V_s from Fundamental Mode and Effective Velocity Inversions

Based on the inversion procedures described above, the V_s profiles were developed for the eight sites from the active-source $f-k$ dispersion curves and a fundamental-mode forward model. The experimental dispersion curve at each site and the matching theoretical dispersion curve that were used for the development of the final V_s profile are presented in Figure 9.1a through Figure 9.8a. The final RMS error is also presented for each fit and indicates a low misfit between the experimental and theoretical data. For Sites 1, 2 and 4, no active-source $f-k$ measurements were performed at high frequencies to obtain dispersion data of the very shallow soils (less than 20 m). Therefore, the short-spacing SASW data were combined with the active $f-k$ data to develop a dispersion curve over the full range in wavelengths. At all of the other sites, active-source $f-k$ measurements were performed with a hammer source to obtain near-surface information. These dispersion curves were in good agreement with the SASW curves over the same wavelength range, indicating that the procedure used at Sites 1, 2 and 4 was reasonable.

The final V_s profiles from the active-source $f-k$ data (based on the fundamental-mode inversion) are presented along with the V_s profiles from SASW data (based on the effective phase velocity inversion) in Figures 9.1b through 9.8b. The V_s profiles from the SASW analyses are taken from Bailey (2008). Bailey (2008) showed that the SASW profiles were consistent with the soil stratigraphy information and provided V_s values that were in good agreement with past studies of the soil formation velocities. For most of the sites, the resolvable depths obtained from the $f-k$

fundamental mode analyses were greater than those obtained from the SASW data. To better compare the V_s values, the SASW profiles are presented to the same depth as the $f-k$ profiles, using a dashed line to represent the half-space velocity, as shown in Figures 9.2b through 9.5 b, 9.7b and 9.8b.

As observed from Figures 9.1 through 9.8, most of the sites show generally good agreement between the V_s profiles obtained from the two inversion approaches. In general, the fundamental mode inversion produced a slightly higher velocity at depth. The only site with poor agreement between these methods is Site 5 (Figure 9.4b), where the fundamental mode inversion produced a V_s profile that was as much as 22% and 40% higher at the two deepest soil layers (below 160 m). To illustrate that these higher layers are required in the fundamental mode inversion, the higher velocities were assumed to be equal to velocities obtained from the “effective-velocity” inversion at the same layers (as shown in Figure 9.9a), and the forward model was recalculated on the revised profile to generate the theoretical dispersion curve. In Figure 9.9b, the theoretical dispersion curves of the inverted and revised V_s profiles are compared. It can be observed that the profile with lower velocities assumed at depth shows a theoretical dispersion curve that significantly diverges from the experimental data at wavelengths beyond 300 m, thus demonstrates that these deep high velocities are necessary to fit to the experimental dispersion curve if a fundamental-mode forward model is used.

These high velocities are not consistent with the expected values for the Memphis Sand, the deposit present in the depth range of about 40 to 250 m at Site 5

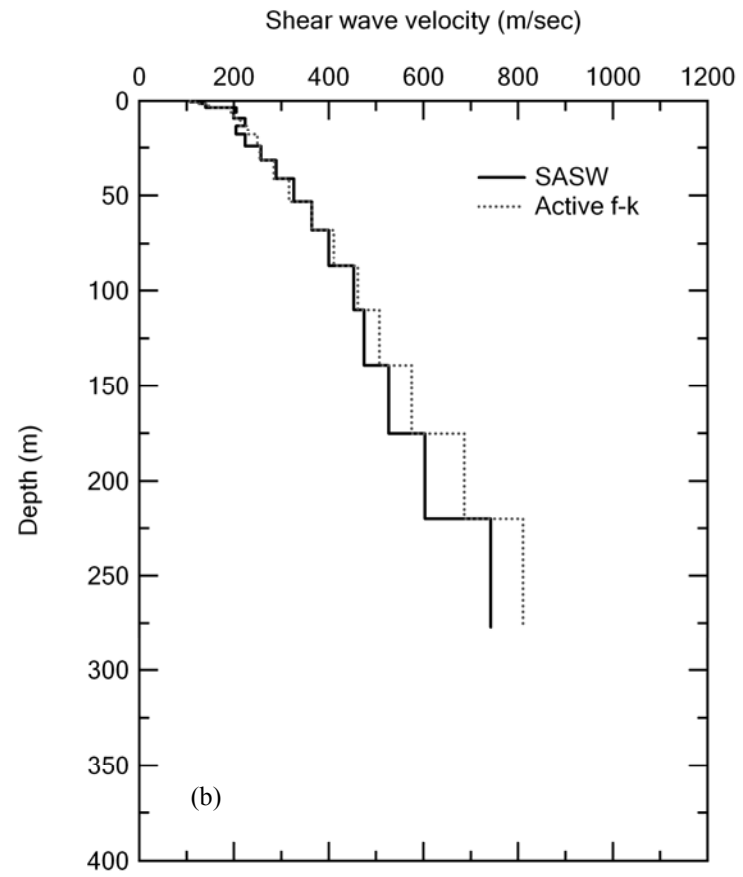
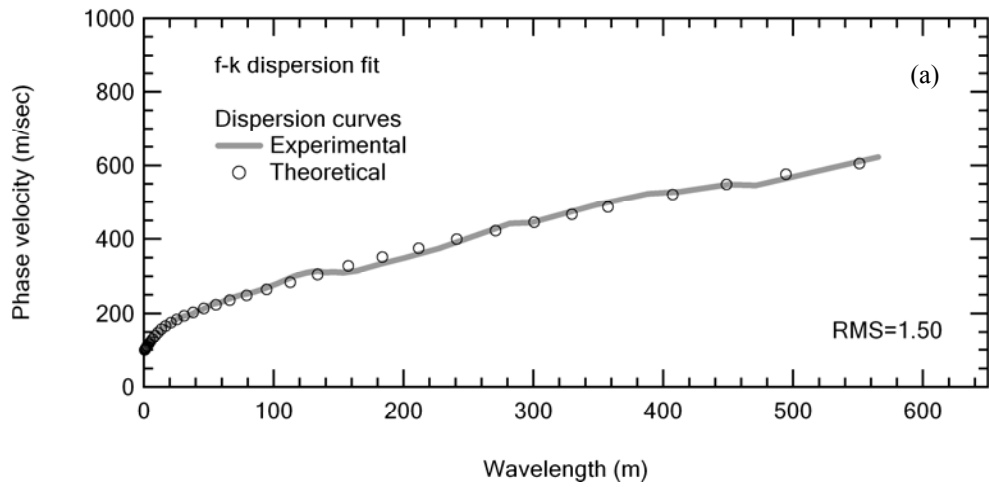


Figure 9.1 Inversion results for Site 1 showing (a) experimental and theoretical dispersion curves and (b) V_s profiles based on SASW (Bailey,2008) and active $f-k$ dispersion curves.

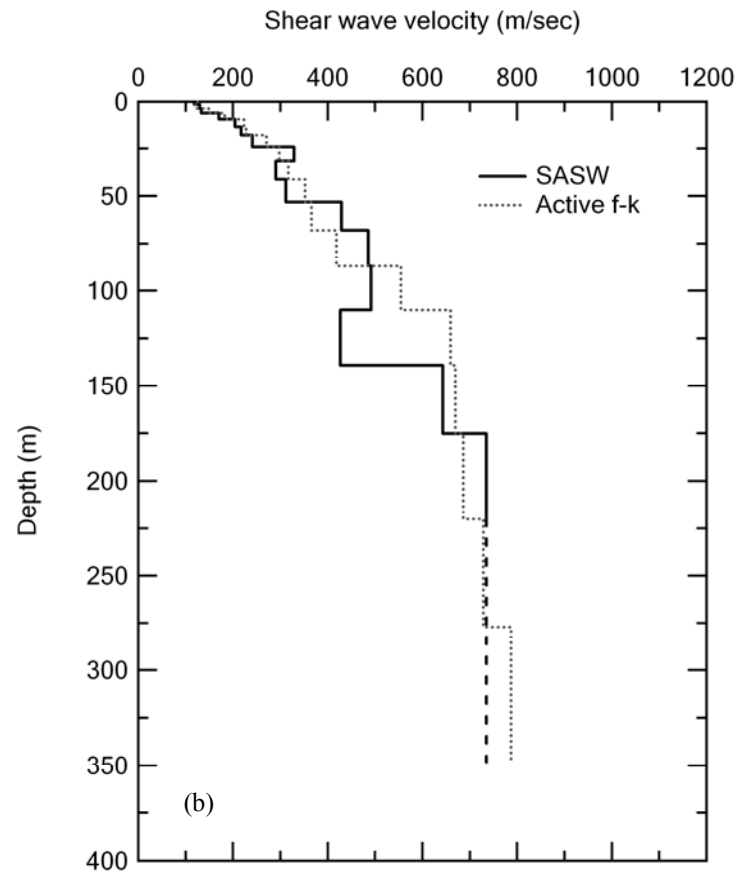
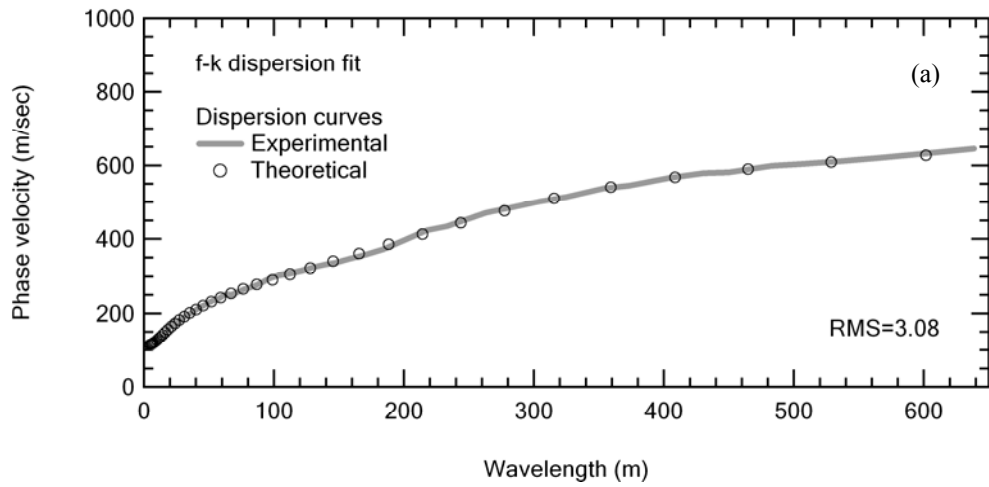


Figure 9.2 Inversion results for Site 2 showing (a) experimental and theoretical dispersion curves and (b) V_s profiles based on SASW (Bailey,2008) and active $f-k$ dispersion curves.

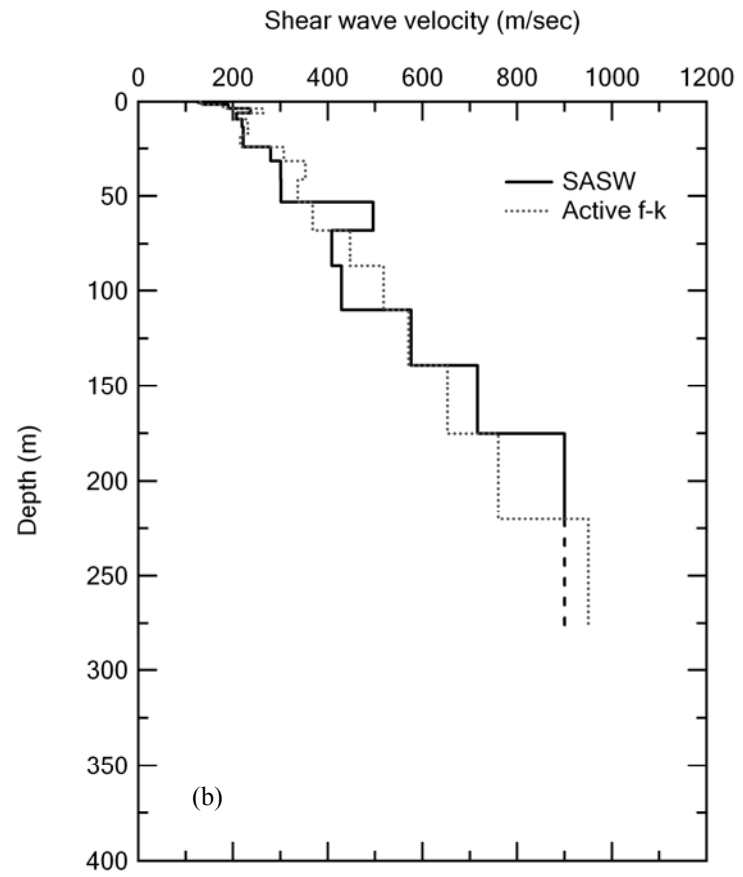
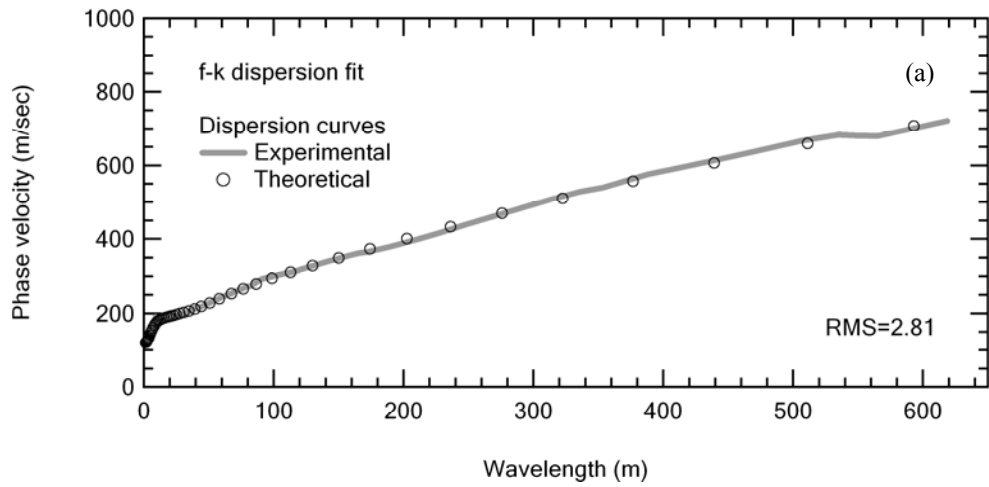


Figure 9.3 Inversion results for Site 4 showing (a) experimental and theoretical dispersion curves and (b) V_s profiles based on SASW (Bailey,2008) and active $f-k$ dispersion curves.

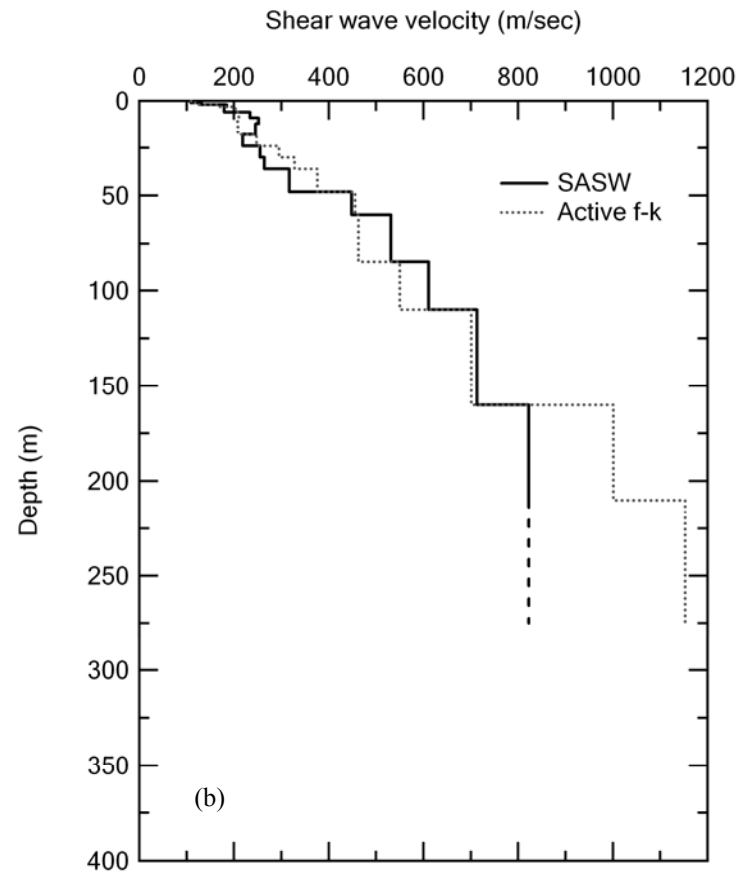
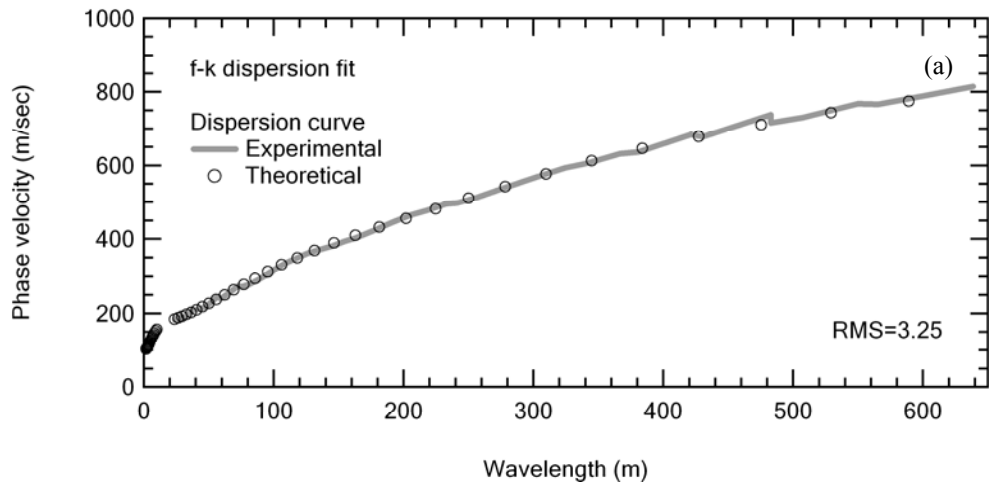


Figure 9.4 Inversion results for Site 5 showing (a) experimental and theoretical dispersion curves and (b) V_s profiles based on SASW (Bailey,2008) and active $f-k$ dispersion curves.

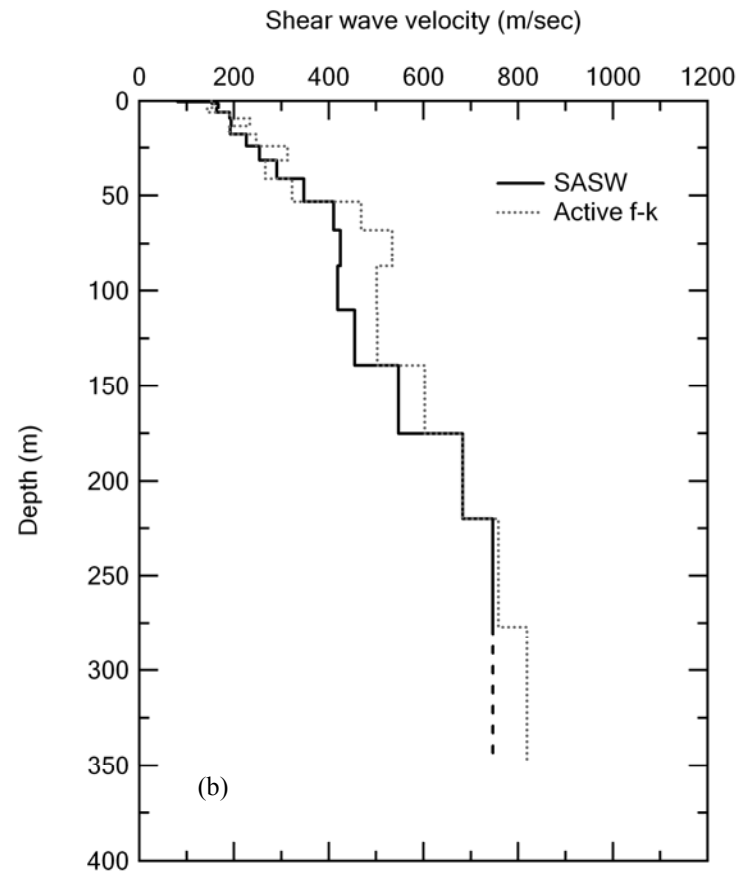
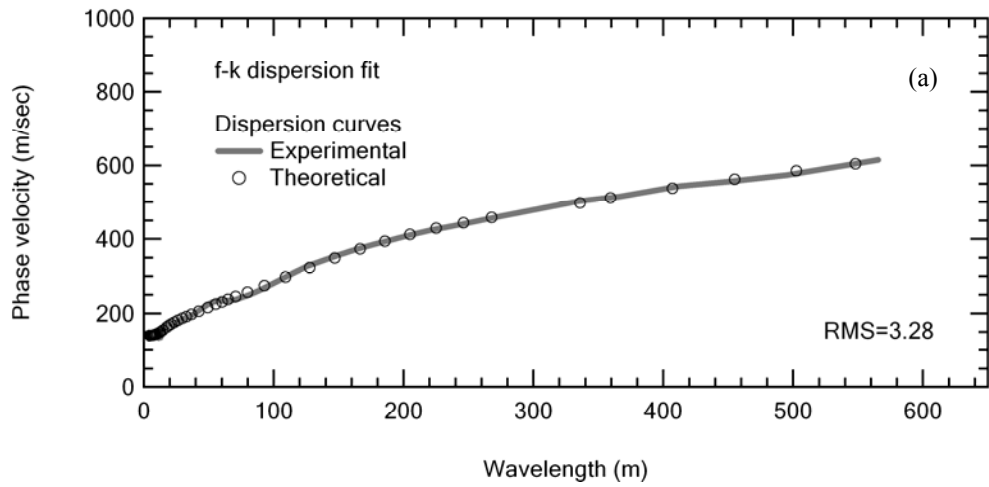


Figure 9.5 Inversion results for Site 7 showing (a) experimental and theoretical dispersion curves and (b) V_s profiles based on SASW (Bailey,2008) and active $f-k$ dispersion curves.

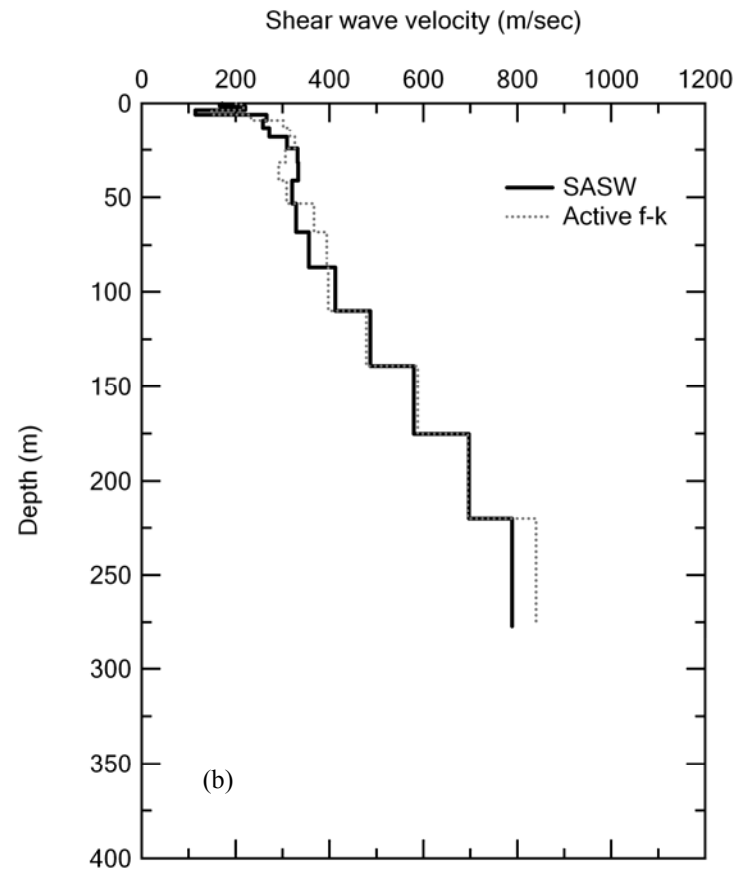
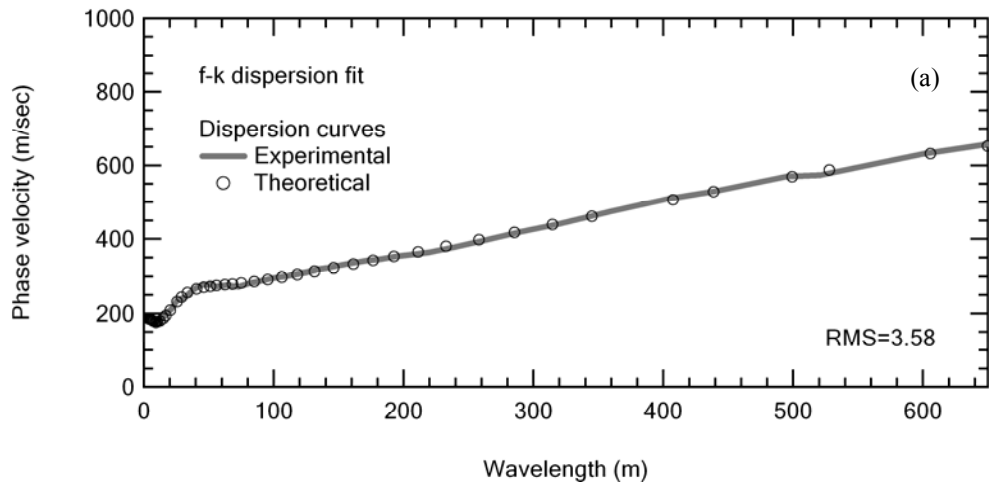


Figure 9.6 Inversion results for Site 8 showing (a) experimental and theoretical dispersion curves and (b) V_s profiles based on SASW (Bailey,2008) and active $f-k$ dispersion curves.

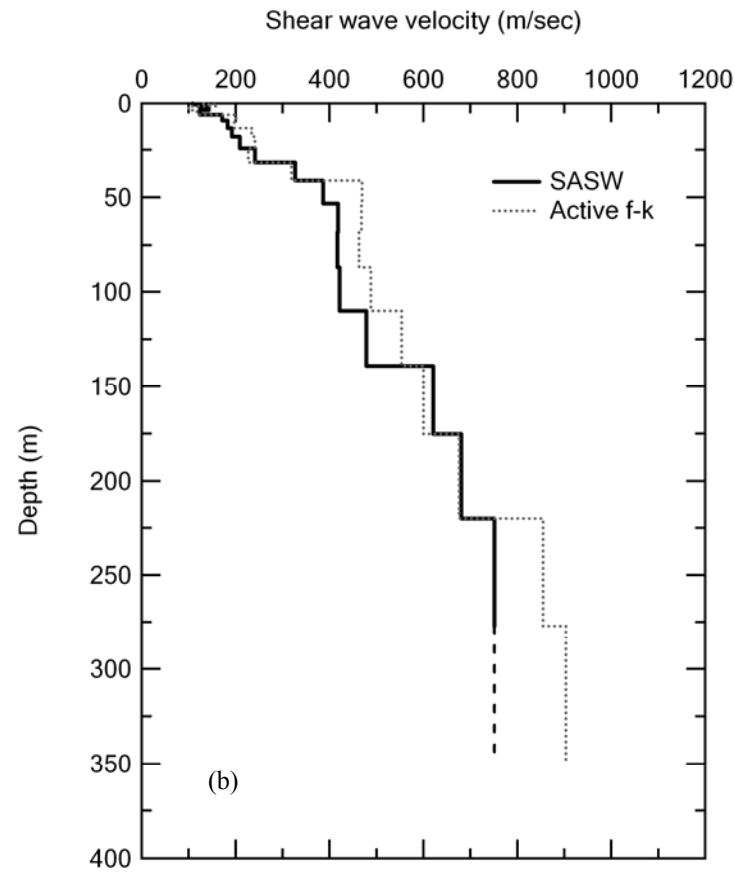
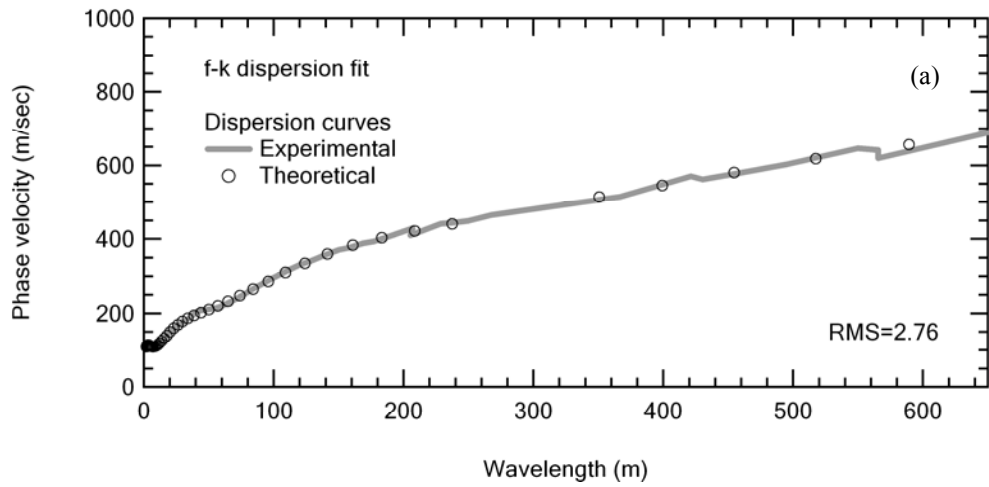


Figure 9.7 Inversion results for Site 10 showing (a) experimental and theoretical dispersion curves and (b) V_s profiles based on SASW (Bailey,2008) and active $f-k$ dispersion curves.

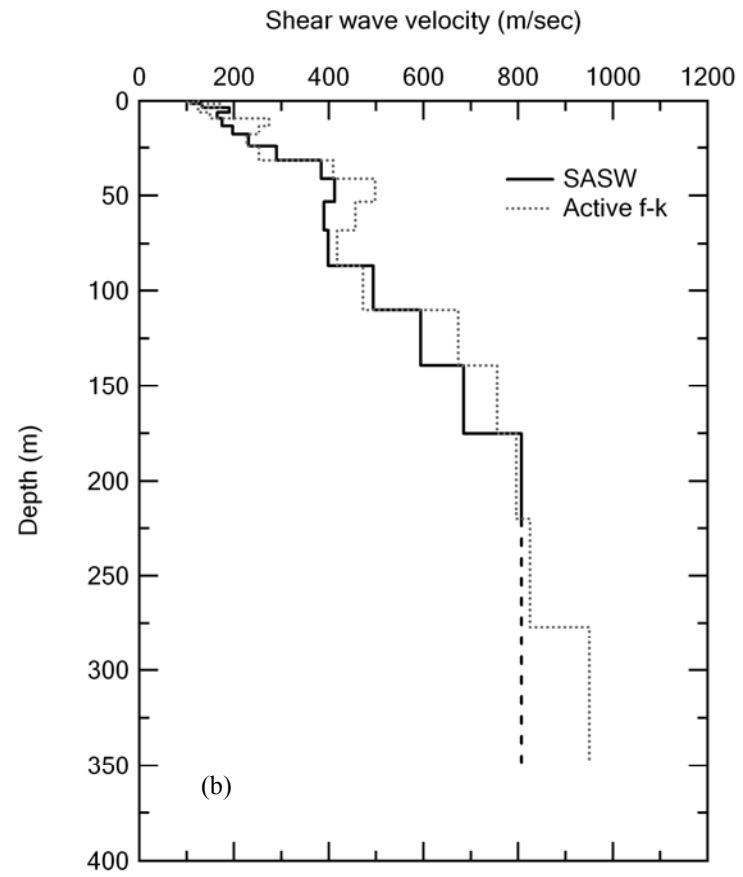
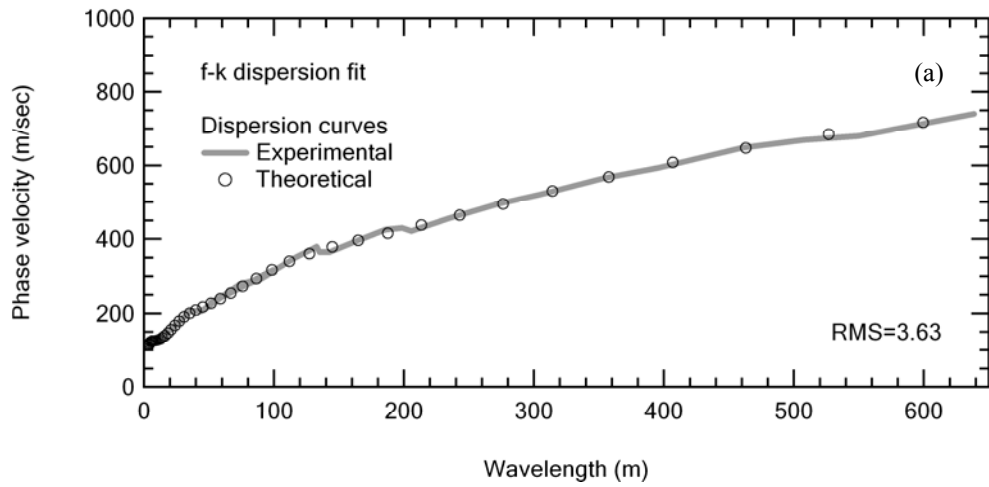


Figure 9.8 Inversion results for Site 11 showing (a) experimental and theoretical dispersion curves and (b) V_s profiles based on SASW (Bailey,2008) and active $f-k$ dispersion curves.

(as shown in Figure 3.28e). One of the few deep V_s profiles in the Mississippi embayment was measured at a Memphis Light, Gas, and Water (MLGW) well #236, which is located about 5.5 km from Site 5. This profile shows that the Memphis Sand has a V_s range of about 600 to 800 m/sec at depths of 160 to 240 m. There is no indication of V_s values of 1200 m/sec as was obtained with active-source $f-k$ method. The velocity values from the MLGW well are consistent with the SASW V_s profile, but not with the profile obtained from $f-k$ fundamental-mode analysis.

The comparison results from Site 5 are particularly interesting because the experimental dispersion curves obtained from the SASW and the active-source $f-k$ measurements were in very good agreement, especially at long wavelengths, as shown in Figure 9.11. The poor comparison of V_s profiles suggests a problem with the inversion procedures. The next section will investigate this issue by comparing simulated $f-k$ measurements for Site 5 and Site 8, where a very good comparison between dispersion curves was observed.

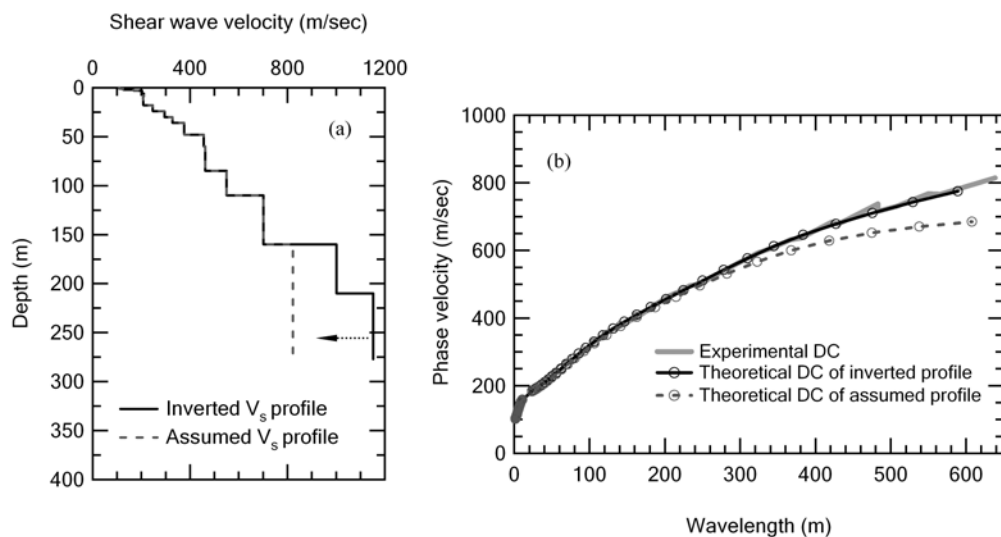


Figure 9.9 Plots showing (a) inverted and modified V_s profiles for Site 5, and (b) comparison of theoretical dispersion curves for inverted and modified V_s profiles.

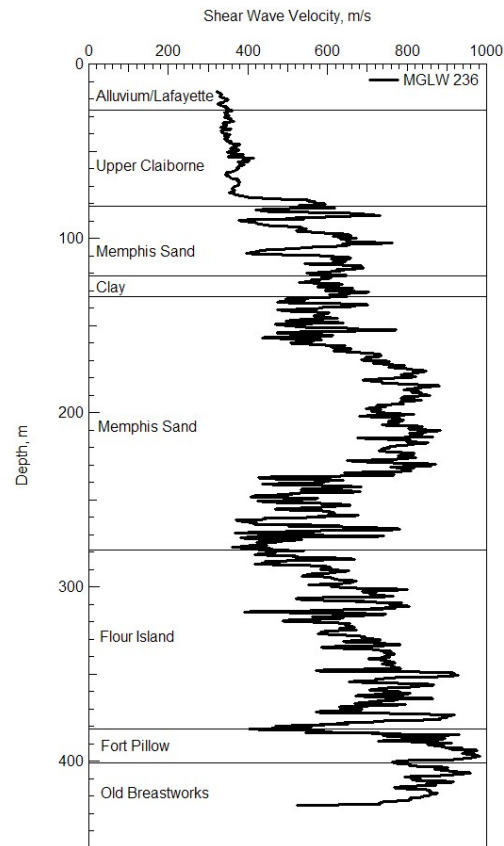


Figure 9.10 V_s profile in the Memphis, Tennessee area from geophysical logging at deep well MLGW 236, located about 5.5 km from Site 5.

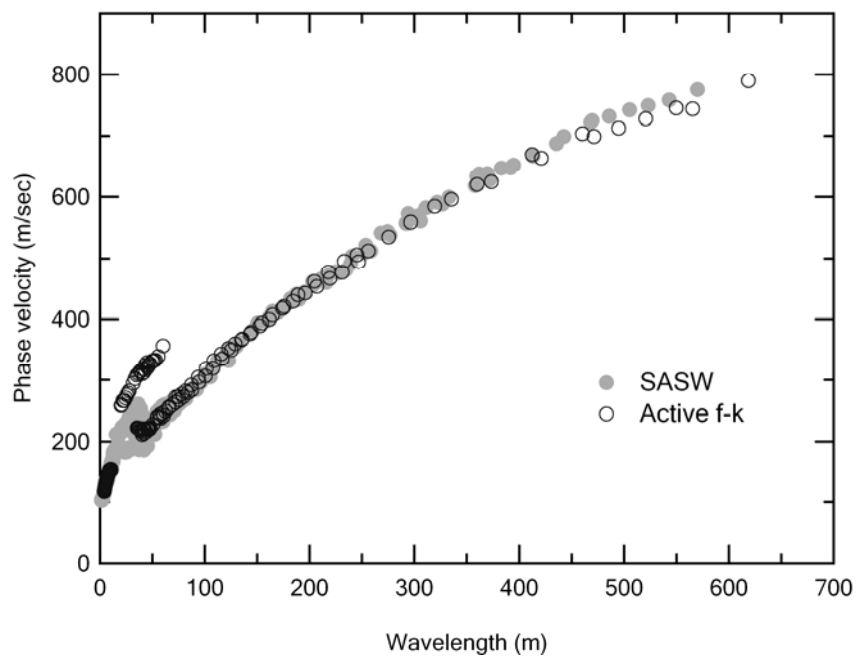


Figure 9.11 Comparison of experimental dispersion curves developed from SASW and active f-k methods presented in terms of wavelength for Site 5.

9.4 Inversion Model Compatibility

As observed from Figures 9.4 and 9.6, comparison of the V_s profiles from the two inversion approaches show quite different results for Site 5 and 8, with a poor comparison for Site 5, but a good comparison for Site 8. To better understand the performances of these two inversion approaches, a simulation procedure was performed for Site 5 and Site 8. This procedure sought to simulate the active $f-k$ measurements using the V_s profile determined from the SASW “effective-velocity” approach. The objective of these simulations was to investigate the consistency between the fundamental mode dispersion curve and the dispersion curve developed from actual $f-k$ measurements (e.g. the issue of model compatibility for the fundamental mode inversion)

9.4.1 Simulation Procedure

The simulation procedure involved calculating vertical ground displacements at each of the actual receiver locations due to a vertical point source located on the ground surface for a given V_s profile. The V_s profile obtained from the SASW analyses was used in the simulation calculations. A publically-available MATLAB program developed by Lai (1998) was used to calculate the displacements based on the following approach. When a harmonic unit point source is vertically applied on the free surface of the given layered system, the vertical displacement at each sensor can be computed by superposing the contributions of all the Rayleigh modes of propagation as:

$$u(x, z, \omega) = \sum_{j=1}^M [A(x, z, \omega)]_j \exp[i(\omega \cdot t - k_j \cdot x - \pi/4)], \text{ and} \quad (9.1)$$

$$[A(x, z, \omega)]_j = \frac{F_0 \cdot r_2(z_s, k_j, \omega)}{4V_j \cdot U_j \cdot I_j \cdot \sqrt{2\pi x k_j}} \cdot r_1(z, k_j, \omega), \quad (9.2)$$

in which x and z indicate the coordinates of one sensor along the horizontal or vertical direction ($z = 0$ here), j denotes the generic j -th mode, M is the total number of modes, k_j is the wavenumber corresponding to the j -th mode for the given frequency, $\omega = 2\pi f$, z_s is the source depth (equal to 0 in this case), $[A(x, z, \omega)]_j$ is the modal amplitude of the modal displacement, F_0 is the amplitude of the vertical harmonic force (equal to 1 in this case), and V_j , U_j , I_j , $r_1(z, k_j, \omega)$ are the modal phase, group velocities, the first energy integral, and displacement eigenvectors, respectively, which are computed or defined in Lai (1998). According to Lai (1998), Equation 9.1 was developed by only considering Rayleigh wave propagation and neglecting body wave contribution. With the vertical displacements simulated for the linear array, the f - k dispersion curve for the given layered profile was developed in the same way as the experimental data, as described in Section 4.3 of Chapter 4.

The contribution of each mode to the superposed displacement (or the resulting dispersion curve) can be indicated by the relative importance of each mode. Equation 9.1 can be rewritten as:

$$u(x, z, \omega) = \sum_{j=1}^M [\bar{A}(x, z, \omega)]_j \exp[i(\omega \cdot t)], \quad (9.3)$$

in which,

$$[\bar{A}(x, z, \omega)]_j = [A(x, z, \omega)]_j \exp[i(-k_j \cdot x - \pi/4)]. \quad (9.4)$$

The normalized relative contribution of the j th mode at a given frequency, ω_1 , can be computed by:

$$\left| \frac{[\bar{A}(x, z, \omega_1)]_j}{\max\{[\bar{A}(x, z, \omega)]_i\}} \right|, \text{ for } i = 1, 2, \dots, M \text{ and all } \omega. \quad (9.5)$$

9.4.2 Simulation Results for Site 5 and Site 8

In this section, the active-source f - k measurements in the field are simulated for Sites 5 and 8 using the V_s profile developed from the SASW measurements. For the simulation, the array configurations and frequency points were the same as those used at Sites 5 and 8 in the field, as listed in Table 3.5 and 3.6. The simulation results based on the SASW V_s profile are presented in Figures 9.12a and 9.12c for Site 8, and Figures 9.12b and 9.12d for Site 5. The modal velocities (dotted lines) are also presented in Figure 9.12a and 9.12b. As observed from these figures, the simulated active f - k measurements agree very well with the actual measurements for both of the sites, indicating that the SASW V_s profile is a reasonable V_s profile for the sites. Slight differences between the two results for Site 8 (from 2.6 to 5.0 Hz) and for Site 5 (from 2.3 to 4.0 Hz) may be due to local variability in the local soil conditions.

The consistency of the simulated dispersion curves with the fundamental mode dispersion curves is quite different for these two sites. For Site 8, the simulated f - k dispersion curve follows the fundamental mode down to a frequency of 1.1 Hz, and then diverges to higher velocities between the fundamental and the first higher mode at lower frequencies. In Figure 9.12c, it can be observed that the fundamental mode (mode 1) energy dominates down to 1.1 Hz, and below this frequency the energy from first two modes is almost equal, indicating similar contributions to the simulated

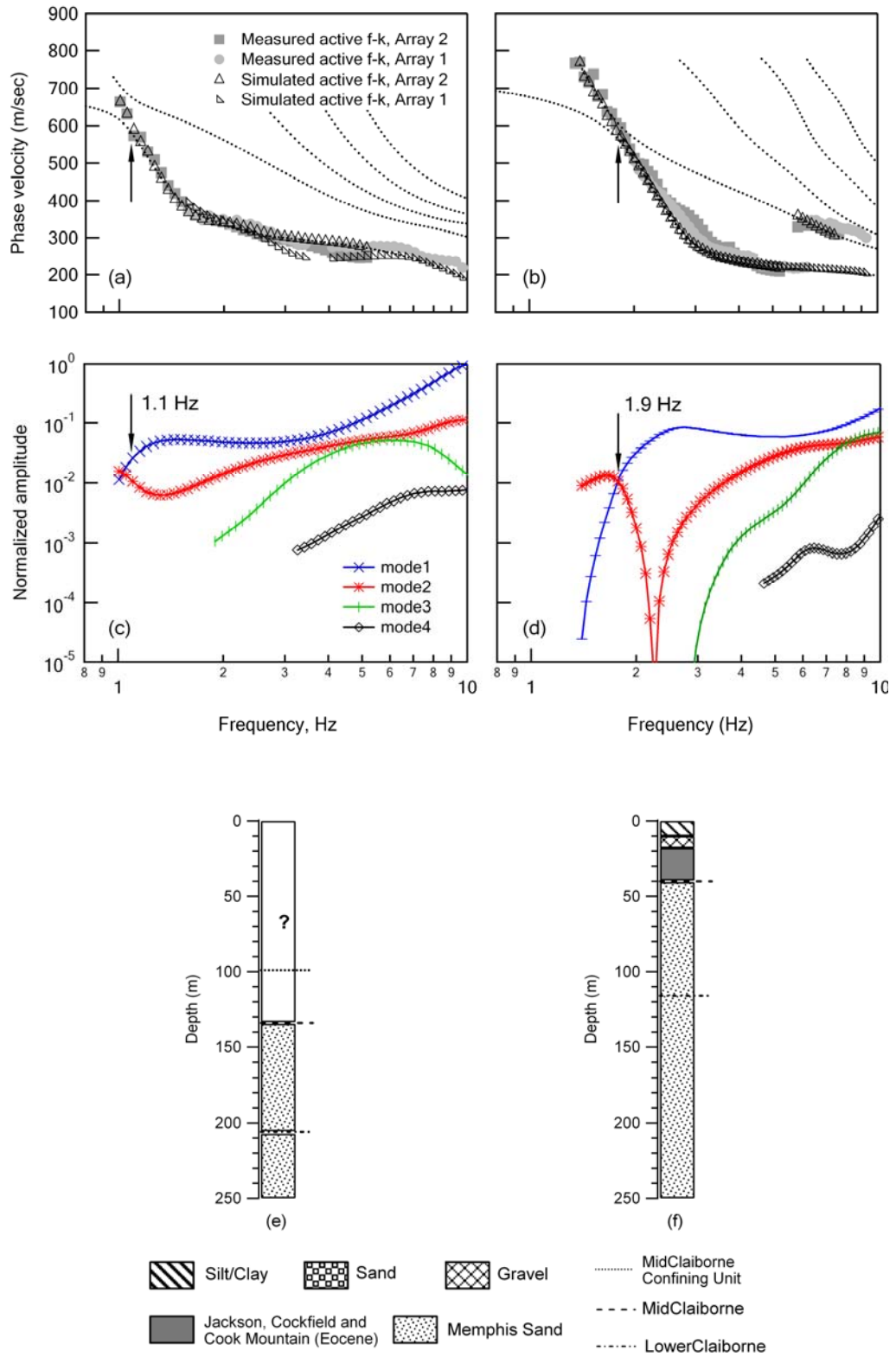


Figure 9.12 Simulation results for Site 8 (left column) and Site 5 (right column) showing (a) (b) measured and simulated $f-k$ dispersion curves, (c) (d) relative importance of first four Rayleigh modes, along with (e) (f) estimated soil stratigraphy.

displacements (or dispersion curve).

For Site 5, on the other hand, the simulated active $f-k$ dispersion curve follows the fundamental mode down to a frequency of about 1.9 Hz, where it then rapidly transitions to a higher mode. Corresponding to this observation, Figure 9.12d shows that the energy from the fundamental Rayleigh mode (mode 1) dominates until 1.9 Hz, then drops dramatically while the second mode becomes dominant until its cutoff frequency of 1.4 Hz. This abrupt mode transition over a broad range of low frequencies (1.9 to 1.0 Hz which corresponds to about 300 to 600 m in wavelength) appears to be the cause for the overestimate of the V_s profile from the $f-k$ data at depths below 160 m (Figure 9.4b) when the active-source $f-k$ dispersion curve was assumed to be the fundamental mode during the inversion. That is, the assumption of fundamental dominance, which the fundamental mode inversion relies on, was clearly not valid for this case.

It should be noted that the SASW V_s profile used in the simulation for Site 5 is consistent with previous studies conducted at two nearby sites. These two sites are located about 800 m south of Site 5. At Site W14 (35.129N, 89.841W), Williams et al. (1999) conducted S-wave refraction measurements to depths of about 120 m. At Site M7 (35.129N, 89.840W), seismic cone penetration tests (SCPT) were performed by Mayne (2000) in the top 30 m. Profiles from these two sites are compared with the profile obtained by Bailey (2008) from the SASW analyses, as shown in Figure 9.13. It can be seen that the profiles developed from these different approaches match very well. In particular, the SASW profile is very consistent with the refraction profile

from a depth of 10 m to about 120 m. As observed in Figure 9.10, the top of Memphis Sand formation is a strong velocity contrast as compared to the overlying alluvial deposits. As shown in 9.12f, the estimated soil lithology at Site 5 shows a very shallow Memphis Sand deposit at a depth of about 40 m. This feature can be observed also in the SASW V_s profile and the refraction profile, with a distinct velocity transition from 250 m/sec to around 500 m/sec at a depth of about 40 to 50 m.

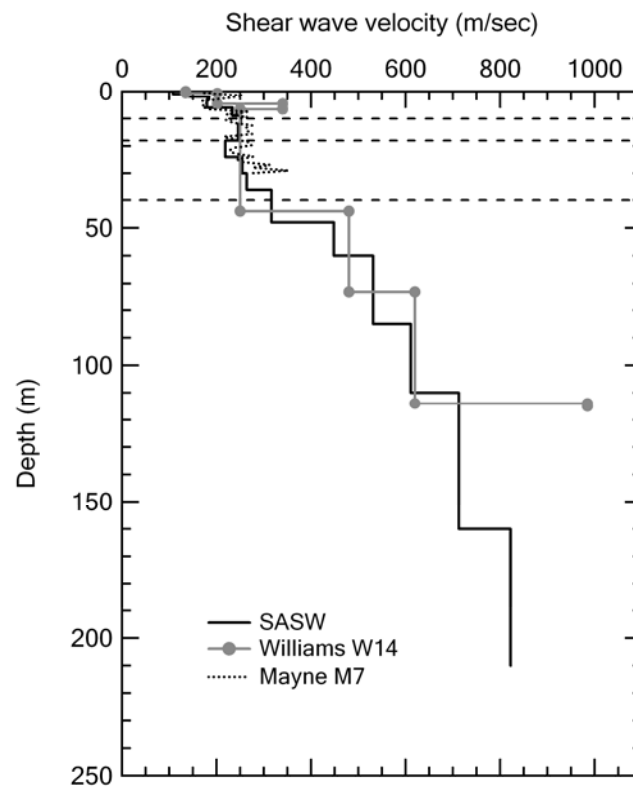


Figure 9.13 Comparison of V_s profiles from SASW measurements, refraction measurement (Williams et al, 1999) and SCPT (Mayne, 2000).

The primary difference between Sites 8 and 5 is the depth to the Memphis Sand deposit, as seen in Figure 9.12e and 9.12f, respectively. For Site 5, this depth is shallow at a depth of 40 m while it is at 130 m for Site 8. Based on the above

simulation results, it is hypothesized that the depth to the Memphis Sand deposit may be the primary factor causing the different comparison results between the fundamental mode and the actual f - k dispersion curve for Sites 5 and 8. In the following section, this hypothesis will be studied, using assumed profiles representative of the conditions in the Mississippi embayment.

9.4.3 Influence of Depth to Stiffer Soil Layer on Dispersion Curve Estimates

The objective of this section is to investigate the hypothesis that the depth to the Memphis Sand impacts the viability of the fundamental mode inversion procedure. To achieve this objective, three soil profiles were assumed for the numerical simulation, as listed in Table 9.1. Case 1 represents a normally dispersive soil profile, where the V_s of layers gradually increase with depth. Case 1 was created in the following way. A common empirical equation for the shear modulus of soils, G_{\max} , is:

$$G_{\max} = A \cdot F(e) \cdot (\bar{\sigma}_0)^n, \quad (9.1)$$

where, A is a soil constant, $F(e)$ is a function of the void ratio, e , $\bar{\sigma}_0$ denotes the mean efficient confining stress, which is equal to $\frac{2}{3}\bar{\sigma}_v$ for normal soil consolidation (the ratio of the horizontal stress to the vertical stress, $K_0 = 0.5$), and n is an exponent that is typically equal to 0.5 (Hardin & Black, 1968). V_s can be related to G_{\max} by:

$$V_s = \sqrt{G_{\max}/\rho}, \quad (9.2)$$

in which, ρ , denotes the mass density. Hence, V_s can be estimated by:

$$V_s = c \cdot (\bar{\sigma}_0)^{0.25}, \quad (9.3)$$

where, c is a constant (assuming e and ρ are constant). Over the top 40 m, the V_s assumed for Case 1 was fit to the V_s of SASW profile at Site 5 with c set to 107 and $\rho = 1.92 \text{ g/cm}^3$. Case 2 and Case 3 were developed from Case 1 by adding a stiffer layer (representative of the Memphis Sand) at different depth, representing the soil conditions estimated for Sites 5 and 8, respectively. As indicated in Table 9.1, Case 2 was created by increasing V_s by 200 m/sec starting at layer 11 (a depth of 36 m), which is similar to the condition at Site 5. Case 3 was created with a greater depth to the stiffer layer of 110 m. The purpose of using Case 2 and Case 3 was to examine how different depths to the stiffer layers influence the simulated results. The V_s profiles assumed for Case 1, Case 2 and Case 3 are plotted in Figures 9.14a, 9.14b and 9.14c, respectively.

Active f - k measurements were simulated using these three soil profiles. The simulated array consisted of 24 sensors with an equal spacing of 20 m. Simulation results for Case 1, Case 2 and Case 3 are presented in Figures 9.15, 9.16 and 9.17, respectively. As shown in Figure 9.15, the fundamental mode is dominant over the entire frequency range for the normally dispersive profile (Case 1). Therefore, the common assumption of fundamental mode dominance appears to be valid for this soil profile conditions. In contrast, for both Case 2 and Case 3 with the presence of stiffer layers, a transition to a higher mode occurs, but to a different extent. As seen from Figure 9.16, the modal dispersion curves for Case 2 are very similar to those observed at Site 5 (Figure 9.12b). In both cases, the first two modes are separate at high frequencies but converge at a lower frequency, and then separate again. The simulated

Table 9.1 Soil profiles for Case 1, Case 2 and Case 3

Layer	Depth (m)	Thickness (m)	Case 1		Case 2		Case 3	
			V _s (m/s)	V _p (m/s)	V _s (m/s)	V _p (m/s)	V _s (m/s)	V _p (m/s)
1	0	1	124.7	216.4	124.7	216.4	124.7	216.4
2	1	1	136.5	236.4	136.5	236.4	136.5	236.4
3	2	1	156.2	270.6	156.2	270.6	156.2	270.6
4	3	3	175.1	1600	175.1	1600	175.1	1600
5	6	3	192.2	1600	192.2	1600	192.2	1600
6	9	3	203.5	1600	203.5	1600	203.5	1600
7	12	6	217.2	1600	217.2	1600	217.2	1600
8	18	6	232.6	1600	232.6	1600	232.6	1600
9	24	6	245.4	1600	245.4	1600	245.4	1600
10	30	6	256.4	1600	256.4	1600	256.4	1600
11	36	12	270.4	1600	470.4	1600	270.4	1600
12	48	12	286.6	1600	486.6	1600	286.6	1600
13	60	25	306.6	1600	506.6	1600	306.6	1600
14	85	25	329.3	1600	529.3	1600	329.3	1600
15	110	50	355.6	1600	555.6	1600	555.6	1600
16	160	60	386.7	1600	586.7	1600	586.7	1600
17	220	80	417.7	1600	617.7	1600	617.7	1600
HS	300	∞	433.6	1600	633.6	1600	633.6	1600

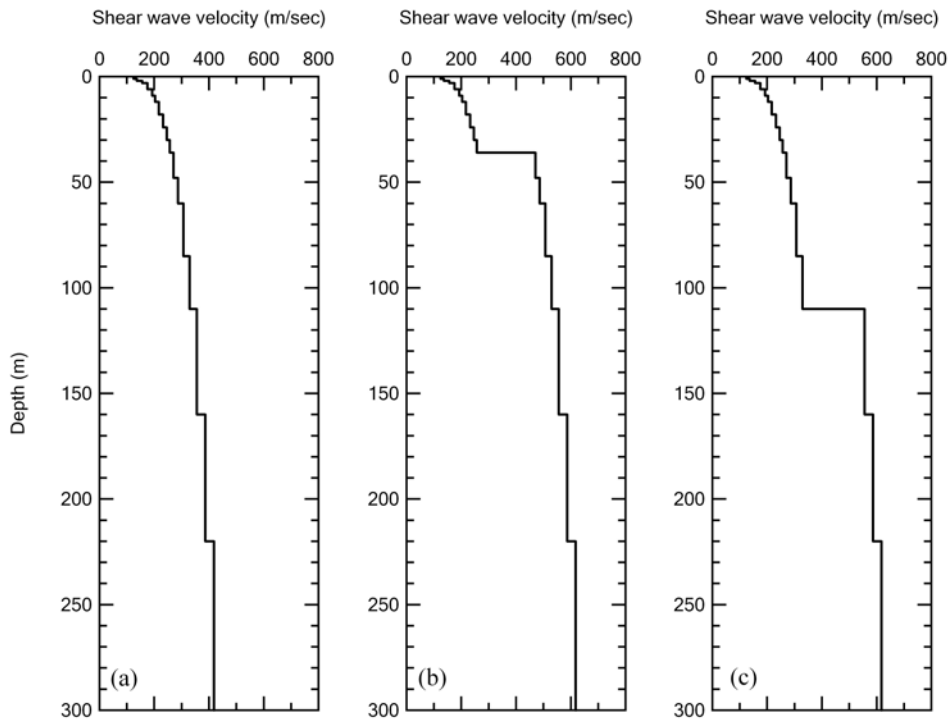


Figure 9.14 V_s profiles assumed for (a) Case 1, (b) Case 2 and (c) Case 3.

$f-k$ dispersion curves transition to the second mode at this convergence frequency. Correspondingly, the contribution from the second mode dominates and the contribution from the fundamental mode drops dramatically, as shown in Figure 9.12d and 9.16b. For Case 2, the $f-k$ dispersion curve follows the second mode to the cut-off frequency and returns back to the fundamental mode. This return transition was not observed in the field measurements which is likely due to undetectable energy levels at these frequencies.

For Case 3, a similar mode transition also occurs, as seen from Figure 9.17a and 9.17c. However, the transition frequency decreases from 2.4 Hz in Case 2 to about 1 Hz for Case 3. The mode transition at Case 3 is similar to that observed of Site 8 (Figure 12 (a)). This frequency (about 1 Hz) is near the lower bound of frequencies recorded in the field study, so for sites with deep Memphis Sand deposits (most of the sites in this study), this transition was not a problem over the frequency range of this study.

From the numerical simulations using these three cases, it can be concluded that the presence of a stiff soil layer can cause a transition of the dispersion curve from the fundamental mode to a higher mode. The transition frequency is strongly influenced by the depth of the stiffer layer, occurring at lower frequencies with increasing depth to the stiffer layer. The assumption of fundamental mode dominance for the inversion of $f-k$ dispersion curves is not valid for soil profiles with shallow stiffer layers. This is a very important finding for interpretation of surface wave measurements, particularly around Memphis, Tennessee area, where the depth to the Memphis Sand deposit is typically shallow (Gomberg, et al., 2003).

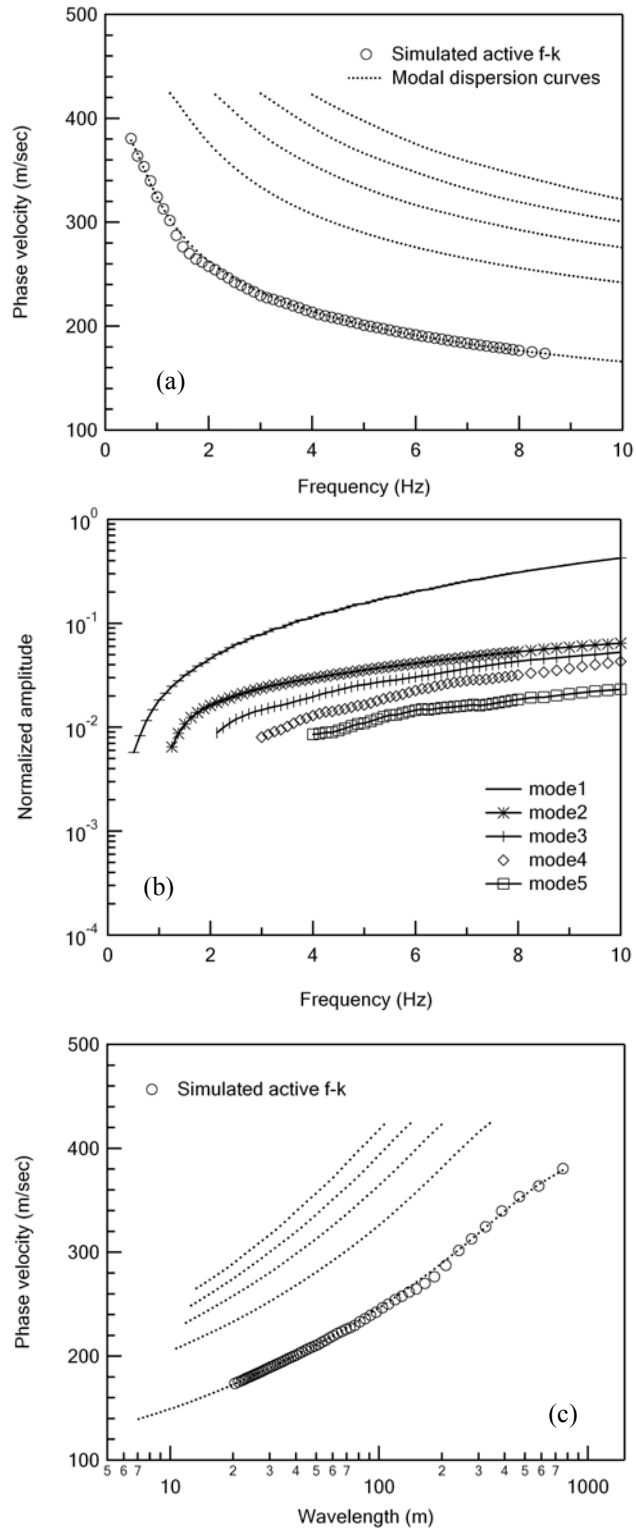


Figure 9.15 Simulation results for Case 1 showing (a) simulated f - k dispersion curve in terms of frequency, (b) relative importance of first five Rayleigh modes and (c) simulated f - k dispersion curve in terms of wavelength.

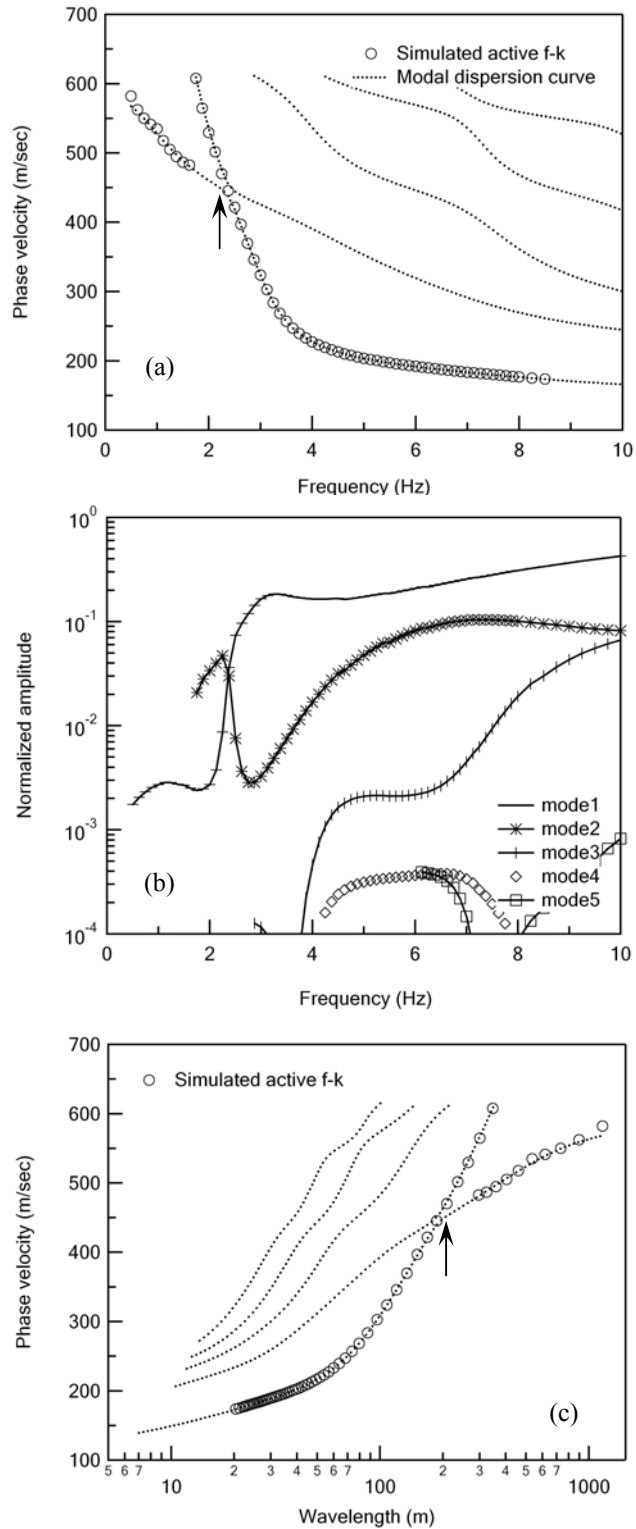


Figure 9.16 Simulation results for Case 2 showing (a) simulated f - k dispersion curve in terms of frequency, (b) relative importance of first five Rayleigh modes and (c) simulated f - k dispersion curve in terms of wavelength.

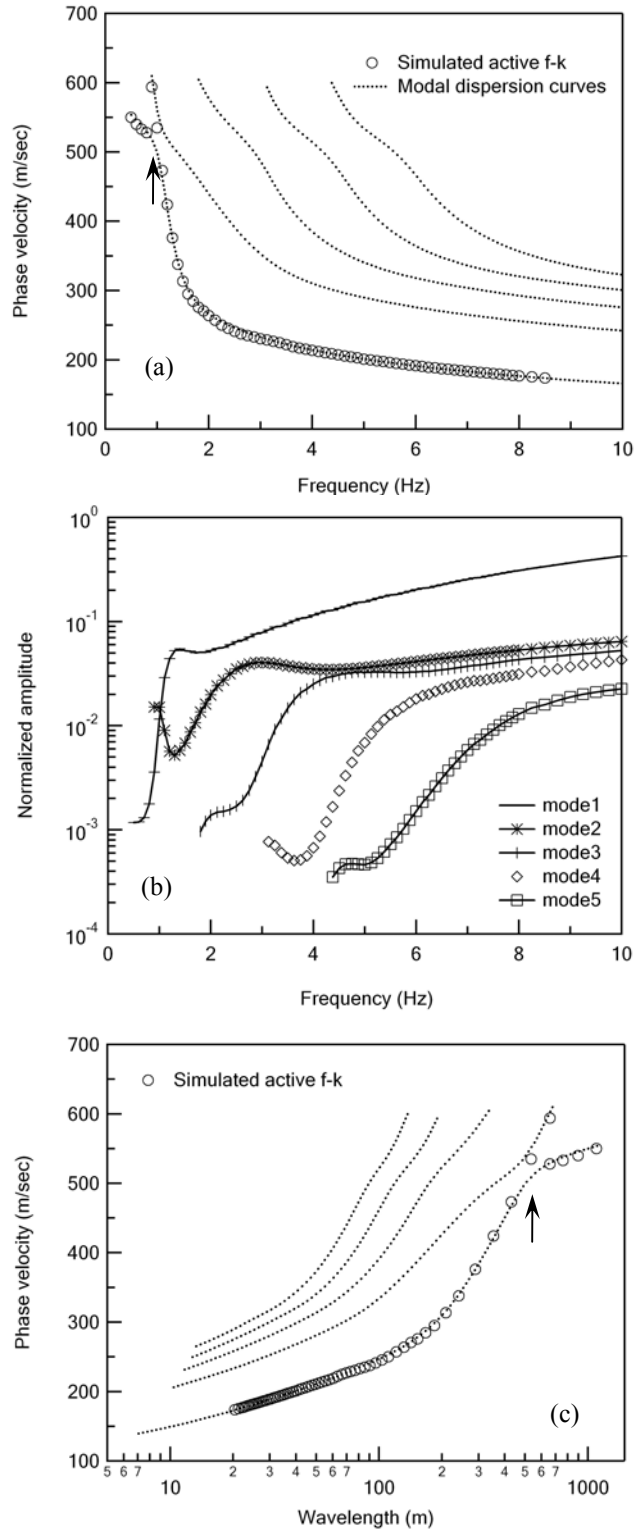


Figure 9.17 Simulation results for Case 3 showing (a) simulated $f-k$ dispersion curve in terms of frequency, (b) relative importance of first five Rayleigh modes and (c) simulated $f-k$ dispersion curve in terms of wavelength.

9.5 Consequence of Inversion Model Incompatibility

An erroneous V_s model is a direct consequence of the incompatibility between the measured dispersion curve and the fundamental mode inversion model. Due to this incompatibility, the V_s estimates from active-source $f-k$ data were overestimated by 40% variation at the bottom layer of Site 5. For shallow applications, this model incompatibility problem could yield erroneous values of the average V_s in the top 30 m ($V_{s(30)}$). The $V_{s(30)}$ value is an important parameter used in the IBC building code to determine site classification for building design.

According to Cramer et al. (2004), the site response analyzed for Memphis is sensitive to uncertainties in V_s for soil up to a depth of 300 m, and most sensitive to depths of about 80 m. Therefore, these erroneous V_s values may impact site response calculations in this region. A thorough investigation of the impact of the changes in V_s on site response are beyond the scope of this project, but should be studied in the future.

9.6 Summary

In this chapter, deep V_s profiles were developed from active-source $f-k$ dispersion curves using a fundamental mode inversion procedure and were compared with V_s profiles developed from SASW dispersion curves using the “effective-velocity” inversion approach. Good agreement between the V_s profiles was obtained from the two inversion approaches at all sites except Site 5. At Site 5, the V_s values below a depth of 160 m were greatly overestimated from the fundamental mode

inversion approach.

The inconsistencies observed at Site 5 were shown to be caused by model incompatibility from the fundamental mode inversion of the active-source $f-k$ dispersion curve. Simulation results showed that the $f-k$ dispersion curve transitioned to a higher mode over a low frequency range at Site 5, indicating that the basic assumption of fundamental mode dominance in the inversion was not valid for this case. Simulation studies also demonstrated that the validity of this assumption was impacted by the local soil conditions, specifically the depth to the Memphis Sand deposit.

Based on this study, it can be concluded that the assumption of fundamental mode dominance in the inversion of $f-k$ dispersion curves is not valid for soil conditions with stiff layers at shallow depths.

CHAPTER 10

CONCLUSIONS AND RECOMMENDATIONS

10.1 Introduction

The objective of this research was to provide a comprehensive comparative study of the performance of active and passive surface wave measurements for developing deep V_s profiles (200 to 250 m) at soil sites. Two active-source and two passive-source surface wave methods were performed at eleven sites distributed in the upper Mississippi embayment. For the active-source measurements, the unique Network for Earthquake Engineering Simulation (NEES) low-frequency vibrator was used to excite the surface wave energy. Experimental dispersion curves developed from these four methods were compared out to the wavelengths of 600 m and factors affecting the performance of these measurements were identified and investigated. Lastly, deep V_s profiles developed from active $f-k$ dispersion curves using the fundamental mode inversion were compared with the profiles developed from SASW dispersion curves using the “effective-velocity” inversion.

10.2 Conclusions

10.2.1 Conclusions on Active-Source Measurements

The performance of the low-frequency NEES vibrator for generating low-frequency energy (less than 1 Hz) needed for developing deep V_s profiles has been successfully demonstrated in this study. This was the first application of this

unique equipment to surface wave measurements at deep soil sites. The successful demonstration of the NEES vibrator for this application is one contribution of this study.

SASW and active-source $f-k$ measurements were performed at all eleven test sites. Through the dispersion curve comparisons between the SASW and active $f-k$ measurements, the following conclusions can be made:

1. The active $f-k$ method is a more effective and foolproof method to estimate phase velocities than the SASW method. The SASW method may produce erroneous dispersion curves in some cases due to potential phase unwrapping errors. Due to these errors, the SASW method may yield erroneously low velocities over a portion of the frequency range. These errors are difficult to identify without the dispersion curve comparisons between the two active-source methods.
2. These phase unwrapping errors were found to be associated with an abrupt mode transition caused by a soft-over-stiff site condition at shallow depths. These errors could be corrected by separating the SASW phase plot with the problematic interpretation into two sections, and unwrapping them independently. These experimental results supported the observations of Bertel (2006) based on simulation studies.
3. Near-field effects can cause lower $f-k$ velocity estimates at long wavelengths (low frequencies) when a close source-to-first-receiver offset is used. The near-field effects were greatly mitigated by increasing

the offset of the first array receiver to the energy source. However, the cylindrical beamforming approach appeared to have limited effect.

4. The maximum wavelengths that the active-source f - k method detected without near-field effects were observed to be 4 to 9 times the near-receiver offset distance from the source. For this study, a lower range of 3 to 4 was used.

10.2.2 Conclusions on Passive-Source Measurements

Valuable information on the ambient wavefield characteristics in the Mississippi embayment has been developed from this study, which is an important contribution of this work for future surface wave measurements in this region. The general characteristics can be summarized as:

1. The amplitudes of the ambient vibrations are highly variable from site-to-site, but the frequency content showed a consistent trend with significant amplitudes in the frequency range of 1 to 4 Hz. Ambient vibration levels at some rural sites were higher than at the urbanized site.
2. At most sites the directions of dominant signals are relatively constant at low frequencies (less than 3 to 4 Hz). At higher frequencies, the source direction was generally more scattered. At most of the sites the direction of dominant energy is generally consistent with the location of major roadways, and in some cases the Mississippi River.
3. The ambient wavefield is generally dominated by one or two sources at low frequencies (below 3 Hz), but exhibited multiple distributed sources

at higher frequencies.

Passive f - k measurements were performed at five of the eleven test sites where sufficient space or access to deploy the large circular array was available. Experimental dispersion curves were developed using the conventional FDBF, MUSIC and Capon's methods, and then compared with the active-source f - k results. The following conclusions from the passive f - k measurements can be made:

1. The conventional FDBF method and two high-resolution (MUSIC and Capon's) methods provided good dispersion estimates out to wavelengths of about 500 m at four of five test sites. At one site, the conventional FDBF performed very poorly at wavelengths from about 200 to 600 m, while the two high-resolution methods at this site performed better.
2. The variable performance was shown to be attributable to the inability of the conventional FDBF method to separate multiple energy signals arriving from different directions.
3. Three commonly-used empirical criteria of the largest resolvable wavelength were examined. The $2 \times D_{\max}$ criterion was found to be acceptable but conservative in most cases, and is recommended for future passive-source f - k measurements.

ReMi measurements were performed on eight of the eleven sites, where two equal-spacing linear arrays were used. Through the dispersion curve comparison between ReMi and the active f - k measurements, the following conclusions about

ReMi measurements can be made:

1. The ReMi method showed quite different performance at high frequencies and at low frequencies at all eight sites. ReMi measurements yielded phase velocities in very good agreement with active $f-k$ measurements at frequencies greater than 3 to 4 Hz (wavelengths out to about 100 to 150 m). However, very poor performance of the ReMi method was observed at low frequencies (less than 3 Hz).
2. The poor performance of ReMi at low frequencies was shown to be primarily due to the wavefield characteristics at low frequencies, where one or two energy sources were dominant. This condition is not consistent with the fundamental assumption of ReMi analysis, namely, energy arriving equally from all directions. The effect is the overestimation of the surface wave velocity.
3. The ReMi measurements showed that this approach may not be an effective method for developing deep V_s profiles.

10.2.3 Conclusions on Fundamental Mode and Effective-Velocity Inversion

Deep V_s profiles developed from active $f-k$ dispersion curves using the fundamental-mode inversion were compared with V_s profiles developed from SASW dispersion curves using the “effective-velocity” inversion for eight test sites. This comparison has led to the following conclusions:

1. The “effective-velocity” inversion using SASW data is a more reliable approach than the fundamental mode inversion using active $f-k$ results.

At one site, the V_s profile at depth was greatly overestimated using the fundamental mode inversion. The SASW method provided results that were consistent with other independent measurements in the area.

2. The poor performance at one site was shown to be due to the model incompatibility of the fundamental-mode inversion. The active $f-k$ dispersion curves transitioned to a higher mode at low frequencies, which violated the assumption of the fundamental mode dominance used in the fundamental-mode inversion. This is an important finding as it impacts the standard practice of assuming fundamental-mode dominance which is used in most active-source surface wave interpretations and nearly all passive measurements (including ReMi).
3. The validity of the fundamental-mode assumption was found to be influenced by the depth to the stiff Memphis Sand deposit. Simulations demonstrated that the surface wave transitions to a higher mode at low frequencies when a shallow, stiff layer (such as the Memphis Sand) is present. This has implications for surface wave studies in Memphis where the Memphis Sand deposit is very shallow in some locations.

10.3 Recommendations

The findings from this study show some limitations of each of the four surface wave methods used. From these findings, several recommendations can be made regarding procedures to be used for deep V_s profiling at soil sites:

1. The active-source surface wave methods like SASW and active-source $f-k$ methods are more reliable than passive-source methods for deep V_s profiling due to the single-source nature of the measurements. Multi-channel linear arrays are recommended over the 2-channel SASW approach due to potential phase unwrapping problems. The maximum wavelength that active-source $f-k$ method can detect without near-field effects is recommended to be 3 to 4 times the near source offset.
2. Though not as reliable as active-source measurements, the passive-source measurements based on two-dimensional receiver arrays remain a reasonable choice for deep V_s profiling. Circular arrays with large diameters are recommended for recording of ambient vibrations. Multiple high-resolution $f-k$ methods (such as MUSIC or Capon's method) should be used to develop the experimental dispersion curves. Care should be exercised when a multi-source environment is anticipated. To increase the confidence in passive-source measurements, a conservative criterion such as twice the maximum array aperture is recommended to determine the largest resolvable wavelength.
3. Given the problems associated with SASW phase unwrapping, and model incompatibility observed with the fundamental-mode inversion of multi-channel measurements, it is recommended that a robust "effective-velocity" inversion approach should be developed to simulate the actual $f-k$ multi-channel measurements.

Since no such program is readily available, another alternative could be to use multi-channel linear arrays during the active-source measurement and analyze the data using both the SASW and $f-k$ approaches to develop the experimental dispersion curves. The potential phase unwrapping errors of SASW measurements could be identified and corrected easily with the comparison to the active $f-k$ measurements. Then, the current “effective-velocity” inversion approach (Joh, 1996) could be used with the SASW dispersion curves.

REFERENCES

- Aki, K. & Richards, P.G. (1980). *Quantitative Seismology*, Freeman and Co., New York.
- Anderson, N., Thitimakorn, T. (2004). "Determination of SASW shear-wave velocity along a segment of interstate 70 in St. Louis, Missouri." U.S. Department of Transportation, Report No. UTC R100.
- Atkinson, G.M. and Hanks, T.C. (1995). "A high-frequency magnitude scale." *Bulletin of the Seismological Society of American*, 85(3), 825-833.
- Bailey, J.P. (2008). "Development of shear wave velocity profiles in the deep sediments of the Mississippi Embayment using surface wave and spectral ratio methods." M.S. thesis, the University of Missouri-Columbia.
- Beaty, K. S. (2000). "Determination of Near-Surface Variability Using Rayleigh Waves." Master's Thesis, University of Alberta.
- Bergstrom, J. (1999). "Non-destructive testing of ground strength using the SASW-method." *The Symposium on the Application of Geophysics to Engineering and Environmental Problems, Conference Proceedings*, Oakland, CA, 57-65.
- Bertel, J.D. (2006). "Analytical study of the Spectral-Analysis-of-Surface-Waves method at complex geotechnical sites." M.S. thesis, the University of Missouri at Columbia.
- Boore, D.M. (2006). "Determining surface shear-wave velocities: a review." *Proceedings of the 3rd International Symposium on Effects of Surface Geology on Seismic Motions, Grenoble, France*, 103-124.
- Bozdag, E. and Kocaoglu, A.H. (2005). "Estimation of site amplifications from shear-wave velocity profiles in Yesilyurt and Avcilar, Istanbul, by frequency-wavenumber analysis of microtremors." *Journal of seismology*, 9, 87-98.
- Brahana, J.V., Parks, W.S. and Gaydos, M.W. (1987). "Quality of Water from Freshwater Aquifers and Principal Well Fields in the Memphis Area, Tennessee." USGS Water Resources Investigations Report 87-4052.
- Braile, L.W., Keller, G.R., Hinze, W.J., and Lidiak, E.G. (1982). "An ancient rift complex and its relation to contemporary seismicity in the New Madrid seismic zone." *Tectonics*, 1, 225-237.

Brown, L. T., Boore, D. M. and Stokoe, K. H. II (2002). "Comparison of shear-wave slowness profiles at 10 strong-motion sites from Noninvasive SASW measurements and measurements made in boreholes." *Bulletin of the Seismological Society of American*, 92(8), 3116-3133.

Capon, J. (1969). "High-resolution frequency-wavenumber spectrum analysis." *Proc. IEEE*, 57, 1408-1418.

Chen, K.C., Chiu, J.M. and Yang Y.T. (1996). "Shear-wave velocity of the sedimentary basin in the Upper Mississippi Embayment using S-to-P converted waves." *Bulletin of the Seismological Society of America*, 86, 3, 848-856.

Cramer, C.H. (2001). "A seismic hazard uncertainty analysis for the New Madrid seismic zone." *Engineering Geology*, 62, 251-266.

Cramer, C.H., Gomberg, J.S., Schweig, E.S., Waldron, B. A. et al. (2004). "The Memphis, Shelby county, Tennessee, seismic hazard maps." USGS open-file report 04-1294.

Crone, A.J. (1981). "Sample description and stratigraphic correlation of the New Madrid test well 1-X, New Madrid County, Missouri." USGS open-file report 81-426, 26.

Cushing, E.M., Boswell, E.H., and Hosman, R.L. (1964). "General geology of the Mississippi Embayment." *U.S. Geological Survey Professional Paper*, 448-B.

Foti, S. (2000). "Multistation methods for geotechnical characterization using surface waves." Ph.D. dissertation, Politecnico di Torino, Italy.

Gabriels, P., Snieder, R., and Nolet, G. (1987). "In situ measurements of shear-wave velocity in sediments with higher-mode Rayleigh waves." *Geophysical Prospecting*, 35, 187-196.

Giulio, G.D., Cornou, C., Ohrnberger, M., Wathelet, M., and Rovelli, A. (2006). "Deriving wavefield characteristics and shear-velocity profiles from two-dimensional small-aperture arrays analysis of ambient vibrations in a small-size alluvial basin, Colfiorito, Italy." *Bulletin of the Seismological Society of American*, 96(5), 1915-1933.

Gomberg, J., Waldron, B., Schweig, E., Hwang, H., et al. (2003). "Lithology and Shear-Wave Velocity in Memphis, Tennessee." *Bulletin of the Seismological Society of America*, 93, 3, 986-997.

Hardin, B.O. and Black, W.L. (1968). "Vibration modulus of normally consolidated

clay.” *Journal of the Soil Mechanics and Foundations Division*, 92, 27-42.

Hashash, M.A. and Park, D. (2001). “Non-linear one-dimensional seismic ground motion propagation in the Mississippi embayment.” *Engineering Geology*, 62, 185-206.

Hebeler, G.L. (2001). “Site characterization in Shelby County, Tennessee using advanced surface wave methods.” M.S. Thesis, Georgia Institute of Technology.

Horike, M. (1985). “Inversion of phase velocity of long-period microtremors to the S-wave-velocity structure down to the basement in urbanized areas.” *J. Phys. Earth*, 33, 59-96.

Ishida, H., Nozawa, T., and Niwa, M. (1998). “Estimation of deep surface structure based on phase velocities and spectral ratios of long-period microtremors.” *Proceedings of the 2nd International Symposium on Effects of Surface Geology on Seismic Motions*, Tokyo, Japan, Vol. 2, 697-704.

Joh, S. (1996). “Advances in interpretation and analysis techniques for spectral-analysis-of-surface-waves (SASW) measurements.” Ph.D. dissertation, the University of Texas at Austin.

Johnson, D.H. and Dudgeon, D.E. (1993). *Array signal processing-concepts and techniques*, PTR Prentice Hall, Inc.

Johnston, A.C. and Kanter, L.R. (1990). “Earthquakes in stable continental crust.” *Scientific American*, 262, 68-75.

Kausel, E., and Roesset, J.M. (1981). “Stiffness matrices for layered soils.” *Bulletin of the Seismological Society of America*, 71 (6), 1743–1761.

Kavazanjian, E. Jr., Matasovic, N., Stokoe, K. H. II, and Bray, J. D. (1996). “In-situ shear wave velocity of solid waste from surface waves.” *Proceedings of the 2nd Int. Congr. on Envir. Geotechnics, IS-Osaka '96*, A.A. Balkema, Rotterdam, The Netherlands, 1, 97-102

Kawase, H., Satoh, T., Iwata, T. and Irikura, K. (1998). “S-wave velocity structures in the San Fernando and Santa Monica areas.” *Proceedings of the 2nd International Symposium on Effects of Surface Geology on Seismic Motions*, Tokyo, Japan, Vol. 2, 733-740.

Lai, C.G. (1998). “Simultaneous inversion of Rayleigh phase velocity and attenuation for near-surface site characterization.” Ph.D. dissertation, the Georgia Institute of Technology.

Liu, H.P., Boore, D.M., and Joyner, W.B., et al (2000). "Comparison of phase velocities from array measurements of Rayleigh waves associated with microtremor and results calculated from borehole shear-wave velocity profiles." *Bulletin of the Seismological Society of American*, 90(3), 666-678.

Liu, Y., Luke, B., Pullammanappallil, S., Louie, J.N. et al. (2005). "Combining active- and passive source measurements to profile shear wave velocities for seismic microzonation." *Earthquake Engineering and Soil Dynamics*, edited by Boulanger, R. W., Dewwolkar, M., Gucunski, N., Juang, C. et al, Geotechnical Special Publication 133, American Society of Civil Engineers, Reston, VA, 977-990.

Louie, J. N. (2001). "Faster, better: shear-wave velocity to 100 meters depth from refraction microtremor arrays." *Bulletin of the Seismological Society of American*, 91(2), 347-364.

Luke, B., Stokoe, K. H., II (1998). "Application of the SASW Method Underwater." *J. Geotech. Geoenviron. Eng.*, 124(6), 523-531.

Mayne, P. (2000). "Results of seismic piezocone penetration tests performed in Memphis, TN." GTRC Project Nos. E-20-F47/F34 submitted to USGS/MAE hazard mapping program central region by Geogia Tech research corporation, geosystems engineering group, civil and environmental engineering, Atlanta, GA.

McMechan, G.A. and Yedlin, M.J. (1981). "Analysis of dispersive waves by wave field transformation." *Geophysics*, 46, 869-874.

Menke, W. (1989). *Geophysical data analysis: discrete inverse theory*, Academic Press, New York.

Miller, R.D., Xia, J., Park, C.B. (1999). "MASW to investigate subsidence in the Tampa, Florida area." Kansas Geological Survey, Open-file Report No. 99-33.

Miyakoshi, K., Kagawa, T., Kinoshita, S. (1998). "Estimation of geological structures under the Kobe area using the array recordings of microtremors." *Proceedings of the 2nd International Symposium on Effects of Surface Geology on Seismic Motions*, Tokyo, Japan, Vol. 2, 691-696.

Nazarian, S., and Stokoe, K. H., II (1984). "In situ shear wave velocities from Spectral Analysis of Surface Waves." *Proceedings of the 8th World Conference on Earthquake Engineering*, Prentice-Hall, Inc., Englewood Cliffs, New Jersey, Vol. III, 31-38.

O'Neill, A. (2003). "Full-waveform reflectivity for modelling, inversion and appraisal of seismic surface wave dispersion in shallow site investigations." Ph.D.

dissertation, University of Western Australia.

Pancha, A., Anderson J.G., Louie, J.N., Pullammanappallil, S. (2008). "Measurements of shallow shear wave velocities at a rock site using the ReMi technique." *Soil Dynamics and Earthquake Engineering*, 28, 522-535.

Parks, W.S., Carmichael, J.K. (1990). "Geology and Ground-Water Resources of the Memphis Sand in Western Tennessee." U.S. Geological Survey Water Resources Investigation Report 88-4182.

Park, C.B., Miller, R.D., Miura H. (2002). "Optimum field parameters of an MASW survey." *SEG-J*, Tokyo, May.

Park, C.B., Miller, R.D., Xia, J. (1999). "Multichannel analysis of surface waves." *Geophysics*, 64, 800-808.

Pei, D., Louie, J.N., Pullammanappallil, S. (2005). "1-D inversion of shallow surface wave dispersion curves using a simulated annealing optimization method." *75th Annual International Meeting, Soc. Explor. Geophys.* (expanded abstracts), 1172-1175.

Pei, D., Louie, J.N., Pullannamappallil, S. (2007). "Inversion of phase velocities of high-frequency fundamental-mode Rayleigh waves using simulated annealing approach." *Geophysics*, 72(5), R77-R85.

Pullannanappallil, S., Honjas, B., Louie, J.N., Siemens, J.A. et al. (2003). "Comparative study of the refraction microtremor method: using seismic noise and standard P-wave refraction equipment for deriving 1D shear-wave profiles." *Proceedings of the 6th international SEG-J conference*, Tokyo, Japan.

Rix, G., Hebel, G.L., Orozco, M.C. (2002). "Near-surface Vs Profiling in the New Madrid Seismic Zone Using Surface-Wave Methods." *Seismological Research Letters*, 73, 3, 380-392.

Romero, S.M. and Rix, G.J. (2001). "Ground motion amplification of soils in the upper Mississippi embayment."

Rucker, M. L. (2003). "Applying the refraction microtremor (ReMi) shear wave technique to geotechnical characterization." *Proceedings of the 3rd international conference on the application of geophysical methodologies and NDT to transportation and infrastructure*, Orlando, Florida, USA, December 8-12.

Sanchez-Saliner, I. (1987). "Analytical investigation of seismic methods used for engineering applications." Ph.D. dissertation, University of Texas at Austin.

Satoh, T., Kawase, H. and Matsushima, S. (2001). "Estimation of S-wave velocity structures in and around the Sendai Basin, Japan, using array records of Microtremors." *Bulletin of the Seismological Society of American*, 91(2), 206-218.

Scherbaum, F., Hinzen K., and Ohrnberger, M. (2003). "Determination of shallow shear wave velocity profiles in the Cologne, Germany area using ambient vibrations." *Geophys. J. Int.* 152, 597-612

Schmidt, R.O. (1986). "Multiple source DF signal processing: an experimental system." *IEEE Trans. Ant. Prop.*, AP-34(3), 281-290.

Schneider, J.A., Mayne, P.W. (1999). "Soil Liquefaction Response in Mid-America Evaluated by Seismic Piezocone Tests." Mid-America Earthquake Center, Report MAE-GT-3A, 273 pp.

Schneider, J.A., Mayne, P.W., and Rix, G. (2001). "Geotechnical site characterization in the greater Memphis area using cone penetration tests." *Engineering Geology* 62, 169-184.

Stephenson, W.J., Louie, J.N., Pullanamappallil, S., Williams, R.A. et al. (2005). "Blind shear-wave velocity comparison of ReMi and MASW results with boreholes to 200m in Santa Clara Valley: implications for earthquake ground motion assessment." *Bulletin of the Seismological Society of American*, 95(6), 2506-2516.

Stokoe, K. H. II, Rix, G. J., and Nazarian, S. (1989). "In situ seismic testing with surface waves." *Proceedings of the 12th Int. Conf. on Soil Mechanics and Foundation Engineering*, Rio De Janiero, 331-334.

Stokoe, K. H., II, Wright, S. G., Bay, J. A., and Roësset, J. M. (1994). "Characterization of geotechnical sites by SASW method." *Geophysical Characterization of Sites*, ed. R. D.Woods, Oxford & IBH Pub. Co., New Delhi, India, 15-25.

Stokoe, K. H. II, Rathje, E. M., Wilson, C. R., and Rosenblad, B. L. (2004a). "Development of large-scale mobile shakers and associated instrumentation for in situ evaluation of nonlinear characteristics and liquefaction resistance of soils." *Proceedings of the 13th World Conference on Earthquake Engineering*, Vancouver, B.C., Canada.

Stokoe, K. H. II, Rosenblad, B. L., Wong, I. G., Bay, J. A., Thomas, P. A., and Silva, W. J. (2004b). "Deep Vs profiling along the top of Yucca mountain using a vibroseis source and surface waves." *Proceedings of the 13th World Conference on Earthquake Engineering*, Vancouver, B.C., Canada.

Street, R., Woolery, E.W., Wang, Z., and Harris, J.B. (2001). "NEHRP soil

classifications for estimating site-dependent seismic coefficients in the Upper Mississippi Embayment.” *Engineering Geology*, 62, 123-135.

Street, R.L. and Woolery, E. W. (2003). “Shear-wave velocities of the post-Paleozoic sediments in the upper Mississippi Embayment: collaborative research between the University of Kentucky and the University of Memphis.” University of Kentucky, Report for USGS, Award number: 02HQGR0023.

Suzuki, H., and Hayashi, K. (2003). “Shallow S-wave velocity sounding using the microtremors array measurements and the surface wave method.” *Proceedings of the Symposium on the Application of Geophysics to Engineering and Environmental Problems (SAGEEP)*, Environmental and Engineering Geophysical Society, Denver, CD-ROM, 1371-1376.

Tarantola, A. (1987). *Inverse problem theory: methods for data fitting and model parameter estimation*, Elsevier, New York.

Thelen, W.A., Clark, M., Lopez, C.T., Loughner, C. et al. (2006). “A transect of 200 shallow shear velocities profiles across the Los Angeles Basin.” *Bulletin of the Seismological Society of American*, 96(3), 1055-1067.

Thorson, J. R. and Claerbout, J.E. (1985). “Velocity-stack and slant-stack stochastic inversion.” *Geophysics*, 50, 2727-2741.

Tokeshi, J.C., Karlee, M.B. and Sugimura, Y. (2006). “Reliability of Rayleigh wave dispersion curve obtained from $f-k$ spectral analysis of microtremor array measurement.” *Soil Dynamics and Earthquake Engineering*, 26, 163-174.

Tokimatsu, K., Tamura, S., and Kojima, H. (1992a). “Effects of multiple modes on Rayleigh wave dispersion characteristics.” *Journal of Geotechnical Engineering*, ASCE, 118(10), 1529-1543.

Tokimatsu, K., Shinzawa, K., and Kuwayama, S. (1992b). "Use of short-period microtremors for Vs profiling." *Journal of Geotechnical Engineering*, ASCE, 118(10), 1544-1558.

Tokimatsu, K. (1995). “Geotechnical site characterization using surface waves.” *Proceedings of 1st International Conference on Earthquake Geotechnical Engineering, IS-Tokyo '95*, Balkema, Rotterdam, 1333-1368.

Tuttle, M.P., Schweig, E.S., Sims, J.D., Lafferty, R.H. et al. (2002). “The earthquake potential of the New Madrid Seismic Zone.” *Bulletin of the Seismological Society of American*, 92(6), 2080-2089.

Van Arsdale, R.B. and TenBrink, R.K. (2002). "Late Cretaceous and Cenozoic geology of the New Madrid Seismic Zone." *Bulletin of the Seismological Society of American*, 90(2), 345-356.

Wathelet, M. (2005). "Array recordings of ambient vibrations: surface-wave inversion." Ph.D. dissertation, Universite de Liege.

Williams, R.A., Odum, J.K., Stephenson, W.J., and Worley, D.M. (1999). "Surface seismic reflection/refraction measurements of P- and S-wave velocities in the Memphis, TN region." *Seismological Research Letters*, 71(1), 113.

Xia, J., Miller, R. D., and Park, C. B. (1999). "Estimation of near-surface shear-wave velocity by inversion of Rayleigh waves." *Geophysics*, 64, 691-700.

Xia, J., Miller, R.D., Park, C.B., Hunter, J.A., et al. (2002). "Comparing shear-wave velocity profiles inverted from multichannel surface wave with borehole measurements." *Soil Dynamics and Earthquake Engineering*, 22, 181-190.

Yoon, S. (2005). "Array-based measurements of surface wave dispersion and attenuation using frequency-wavenumber analysis." Ph.D. dissertation, the Georgia Institute of Technology.

Yoon, S. and Rix, G.J. (2005). "Active and passive surface wave measurements at the William Street Park Site, using F-K methods." USGS open-file report 2005-1169.

Zywicki, D.J. (1999). "Advanced signal processing methods applied to engineering analysis of seismic surface waves." Ph.D. dissertation, Georgia Institute of Technology.

Zywicki, D.J. (2007). "The impact of seismic wavefield and source properties on ReMi estimates." *Proceedings of Geo-Denver 2007*, Denver, Colorado, USA.

VITA

Jianhua Li was born on August 6th, 1975, in Wuzhong, Ningxia, China. He was the youngest in a seven-child family. He studied his primary and secondary education in his hometown, Wuzhong. In 1993, he attended Ningxia Institute of Technology at Yingchuan, Ningxia, China, and received his B.S. degree in Building Engineering four years later. He was titled as “Excellent College Graduate of Ningxia in Year 1997-1998”. Thereafter, Jianhua furthered his study in Qingdao Institute of Architecture and Engineering, Qingdao, Shandong, China. In 2000, he received his M.S. degree in Structural Engineering. Then, he worked in Shanghai for over three years.

In the fall of 2004, Jianhua began his Ph.D. study in the program of Geotechnical Engineering at the University of Missouri-Columbia. He has been working on his dissertation research under the guidance of Prof. Brent L. Rosenblad since 2005. He has co-authored several publications on his research and passed his dissertation defense on October 20th, 2008.